Graphenide solutions and graphene films

Yu Wang

université de BORDEAUX

THÈSE PRÉSENTÉE

POUR OBTENIR LE GRADE DE

DOCTEUR DE

L'UNIVERSITÉ DE BORDEAUX

ÉCOLE DOCTORALE DES SCIENCES CHIMIQUES

SPÉCIALITÉ : Chimie-Physique

Par

Yu WANG

Graphenide Solutions and Graphene Films

Sous la direction de Dr. Alain PENICAUD

Soutenue le 29 septembre 2014

Membres du jury :

M. Philippe RICHETTI	Directeur de recherche, CNRS	Président
M. Edward MC RAE	Directeur de recherche émérite, Institut Jean Lamour CNRS	Rapporteur
Mme. Catherine JOURNET-GAUTIER	Professeur, Université Lyon 1	Rapporteur
Mme. Nedjma BENDIAB	Chercheur, Institut NEEL CNRS	Examinateur
M. Alain PENICAUD	Directeur de recherche, CNRS	Examinateur
M. Kevin MCKEIGUE	Director Nanotechnology, Linde LLC	Examinateur

Titre : Solutions de graphenure et films transparent conducteur de graphene

Résumé : Les travaux de recherche effectués lors de cette thèse s'articulent autour de matériaux graphène. Une méthode est développée pour produire graphène en masse avec solution de graphenure. Les études effectuées les solutions de graphenure sont basées sur les composés d'intercalation du grpahite (GICs) synthétisé avec du potassium et l'exfoliation de GIC dans un solvant organique. Différentes techniques d'analyse ont été employées pour caractériser les graphène produits. Afin de tirer parti des propriétés électriques du graphène, les solutions de graphenure ont ensuite été utilisées pour produire des films transparents conducteurs. Des traitements de recuit à sous atmosphère d'argon ont été effectués pour améliorer les propriétés électriques du film. Les résultats de caractérisation montrent que l'élimination des groupes fonctionnels contenant des atomes d'oxygène et l'amélioration structurale peuvent largement améliorer les propriétés électriques des films de graphène avec ce traitement de recuit.

Mots clés : Solutions de graphenure, composé d'intercalation du graphite, film, transparent, conducteur, spectroscopie Raman

---

Title : Graphenide Solutions and graphene Films

Abstract: The graphene is promising materials in future industrial applications due to its excellent properties. In recent years, different production methods have been developed in order to pave the way for applications. One topic of this thesis focuses on graphenide solutions, which provide an efficient route to produce graphene. Using this method, graphite intercalation compounds (GICs) can be exfoliated into negativelz charged grapheme organic solvent under inert atmosphere. With its high conductivity and bendable feature, one of the promising applications of graphene is flexible transparent conductive films. The second main topic of this thesis consists in applying produced graphene to produce transparent conductive films. With mild thermal treatments, the electrical properties of graphene film can be largely improved.

Keywords : Graphenide solutions, graphite intercalation comprounds, film, transparent, conductive, Raman spectroscopy

---

Centre de Recherche Paul Pascal

115, Avenue Schweitzer, 33600 Pessac

Résumé

Le graphène est un cristal bidimensionnel de carbone, composé simplement d'une feuille d'atomes de carbone hybridés sp^2 formant un réseau d'hexagones. L'empilement de graphène constitue le graphite. Il a été isolé en 2004 par Andre Geim et Konstantin Novoselov de l'université de Manchester. Avec cette découverte, ils ont reçu le prix Nobel de physique en 2010. Depuis la découverte de graphène, les chercheurs ont étudié d'abord les propriétés du graphène. Les résultats expérimentaux ont montré que le graphène possède des propriétés spectaculaires, telle que la mobilité électronique qui peut atteindre 200 000 $cm^2/V{\cdot}s$; le graphène est l'un des matériaux mécaniquement le plus résistants testés jusqu'à maintenant, ayant un module d'Young de 1 TPa, etc. Ces propriétés excellentes font du graphène un composant potentiel dans divers domaines d'ingénierie de matériaux, d'électronique et de matériaux composites. Toutefois, l'exploitation du graphène bute sur la production de graphène qui reste encore onéreuse.

Les premiers échantillons de graphène ont été obtenus par exfoliation mécanique du graphène à l'aide de ruban adhésif. Cette méthode permet de produire des graphènes de grande qualité, mais son rendement faible restreint son utilisation à la recherche scientifique. Différentes méthodes ont ensuite été développées pour produire du graphène en masse, tel que la CVD (déposition en phase vapeur), la production de graphène à partir de carbure de silicium et des voies chimiques (solution de graphenure, graphène oxide, dispersion de graphène à l'aide de tensioactif ou superacide etc). Chaque méthode possède des avantages et des inconvénients; les graphènes produits ont des qualités différentes et en conséquence correspondent à différentes utilisations. Parmi ces méthodes, tenant compte de son avantage en termes de prix et la compatibilité avec des technologies existantes, la production de graphène par voie

chimique porte un très fort potentiel pour les applications du graphène dans le domaine de matériaux composites, stockage d'énergie et encore électronique etc.

En 2008, notre équipe a mis au point une méthode de production de graphène en s'inspirant de la solubilisation des sels de nanotubes de carbone dans le DMSO (Diméthylsulfoxyde). La méthode est effectuée en deux étapes sous atmosphère inerte. La première étape consiste à préparer un composé d'intercalation du graphite (GIC). La deuxième étape correspond à l'exfoliation de ce GIC dans un solvant organique afin de synthétiser la solution de graphenure (graphène chargé négativement). Les études effectuées précédemment sur les solutions de graphenure sont basées sur les GICs synthétisé avec du potassium, spécialement sur les GICs de stade 1 KC_8 et $K(THF)_xC_{24}$. Dans cette thèse, nous étendons les études systématiques au stade 2 KC_{24} et stade 3 KC_{36}. Avec l'objectif de mieux comprendre le système, les matériaux de départ, graphites issue de différent fournisseurs, ont été étudiés par différentes techniques afin d'analyser précisément leur nature chimique et structure cristallographique. La synthèse en phase vapeur a été employée pour préparer KC_8, KC_{24} et KC_{36}. Deux types de solvant organique, le NMP (N-méthyl pyrolidone) ayant une température d'ébullition de 202 °C et le THF (tétrahydrofurane) ayant une température d'ébullition de 66 °C, ont été utilisés pour dissoudre les GICs synthétisés. Les concentrations de chaque solution ont été déterminées par extrait sec. L'absorption UV-visible a été employée pour caractériser les solutions de graphenure. Les spectres d'absorption montrent que les solutions de graphenure présentent une bande caractéristique à 300 nm pour les solutions KC_x (x = 8, 24, 36) dans le solvant NMP quel que soit le nombre de stade. Pour les solutions KCx (x = 8, 24, 36) dans le solvant THF, on observe deux bandes d'absorption situées à 280 nm et 328 nm. Les graphènes synthétisés via les solutions de graphenure, spécialement KC_8 dans THF, ont été caractérisés par microscopie à force atomique (AFM), microscopie électronique à haute résolution

(HRTEM) et Raman. Les résultats des caractérisations nous permettent d'avoir des informations sur le nombre de feuillets, la qualité du graphène et la morphologie du graphène déposé sur un substrat. En parallèle des études sur les solutions de graphène, une étude de résonance Raman a été effectuée pour les GICs synthétisés (KC_8, KC_{24} et KC_{36}) en variant l'énergie d'excitation de l'UV au proche infrarouge. Au cours de l'intercalation du potassium entre les couches de graphite, il y a transfert de charge entre la couche de graphite et celle du potassium. Cela change la structure électronique de graphite. On peut étudier ce changement avec la spectroscopie Raman. Dans le stade 3, nous avons observé une résonance à 2.5 eV. Par des calculs théoriques, cette résonance a été attribuée à la transition $\pi \rightarrow \pi^*$ pour les couches extérieures de graphène dans KC_{36}.

Les caractérisations effectuées sur les dépôts de graphène montrent que les graphites peuvent être exfoliés avec cette méthode pour produire du graphène sans produire trop de défauts. Par rapport aux autres méthodes chimiques, on peut produire de graphène ayant une relativement bonne qualité. Afin de tirer partie des propriétés électriques du graphène, on a ensuite utilisé les solutions de graphenure, KC_8 + THF, pour produire des films transparents conducteurs. Tout d'abord, la solution de graphenure, KC8+THF, a été filtrée sur membrane sous atmosphère inerte. Ce film est ensuite ré-oxydes sous air sec, puis transféré sur substrat flexible PET (Polyéthylène téréphtalate) en éliminant la membrane de filtration. En effet, avec cette méthode, le film de graphène peut être transféré sur tous les substrats désirés. Le film de graphène sur PET montre de bonnes propriétés électriques et propriétés optiques par rapport aux autres films de graphène synthétisés par voie-liquide. Les caractérisations de films avec SEM (microscopie électronique à balayage), AFM et TEM montrent que les graphènes sont empilés de façon aléatoire pour construire le film. Les résultats de XPS montrent que pour le film de graphène la teneur en oxygène s'augmente par rapport au graphite de départ. Des

traitements de recuit à 450 °C sous atmosphère d'argon ont été effectués pour diminuer la teneur en oxygène. Après le traitement, la teneur en oxygène diminue, et la résistivité surfacique du film diminue d'un facteur 4. La spectroscopie Raman a été utilisée pour étudier les films avant et après traitement. Le rapport I_D/I_G est en général employé pour évaluer les défauts de graphène. La cartographie Raman effectuée sur une large zone montre que le rapport I_D/I_G diminue de 1.13 à 0.73 après le traitement, ce qui signifie que le film est moins défectif après traitement. La technique de diffraction de rayons X a été utilisée pour étudier les changements structuraux après traitement. Les résultats montrent que le traitement thermique peut améliorer également la structure du film. L'élimination des groupes fonctionnels contenant des atomes d'oxygène et l'amélioration structurale peuvent largement améliorer les propriétés électriques des films de graphène. Un autre traitement de recuit effectué à 120 °C sous atmosphère d'argon montre que la résistivité surfacique du film diminue. Une étude de traitement effectué à l'aide de laser indique que l'on peut non seulement diminuer la résistivité surfacique du film, mais aussi augmenter la transmittance optique du film avec ce type de traitement.

Avec la solution de graphenure, on peut produire des graphènes en masse et de bonne qualité. La solution de graphenure peut ensuite être exploitée pour élaborer des films transparents conducteurs. Les propriétés électriques des films peuvent être améliorées significativement en faisant des traitements à température relativement basse. Avec ses propriétés électriques intéressantes, les films peuvent servir d'électrodes conductrices flexibles.

Abstract

Graphene, a one atom layer carbon material, has been studied theoretically for long time as a fundamental concept. In 2004, Geim et al. reported a simple and feasible way to exfoliate graphene from graphite. Since then, based on experimental results from exfoliated graphene, researchers have constantly reported that this two-dimensional material has unique properties, such as high charge carrier mobility, mechanical properties, field effect behavior, high thermal conductivity etc. Meanwhile, researchers and engineers have exploited this material in application studies and obtained exciting results, which make graphene materials promising in future industrial applications. Nowadays, graphene is one of the priority research areas both in theoretical and application research.

Despite the exciting properties reported and the high expectations that people have placed on this material, there are still challenges about the development of graphene and materials derived from it. First, to pave the way for applications, industrially scalable production methods have to be developed. One topic of this thesis focuses on graphenide solutions, which provide an efficient route to produce graphene.

In recent years, different production methods have been developed. Graphene materials produced from different methods possess different qualities and properties, thus different graphene materials will be applied in different fields according to their properties, accessibility, processability etc. Due to its high conductivity and bendable feature, one of the promising applications of graphene is flexible transparent conductive films. The second main topic of this thesis consists in applying produced graphene to produce transparent conductive films.

In chapter I, at first, the structure and properties of graphene will be presented; different graphene production methods will be described. Some general presentations about graphite and graphite intercalation compounds (GICs) which we have used to produce graphenide solutions (negatively charged graphene solutions), will also be given in this chapter. Finally, the state of the art concerning recently developed materials for transparent conductive electrodes is presented in this chapter.

Chapter II is dedicated to a description of common characterization techniques of graphene. Several techniques and methods have been developed for graphene characterization to investigate the structure, morphologies and properties of graphene produced. We present in this chapter the techniques we have used. These techniques have proven to be efficient. Some review of characterization results concerning graphene materials are presented at the end of each section. The measurement of surface conductivity is essential for investigating and evaluating transparent conductive materials. The techniques for measuring surface conductivity are also presented.

Chapter III is devoted to the production method of graphenide solutions. The production method have been developed by Pénicaud and coworkers since 2008 based on graphite intercalation compounds (GICs) formed by alkali metals and graphite. The previous works performed by Dr. Cristina Vallés and Dr. Amélie Catheline established a feasible and efficient way to produce graphenide solutions, which consists in dissolving GICs in organic solvent under inert atmosphere. In their work, $K(THF)_xC_{24}$ and KC_8 were used; both compounds are stage 1 GICs. In order to make a systematic work and understand further graphenide solutions, in this work, we have extended to higher stage GICs, stage 2 KC_{24} and stage 3 KC_{36}. The characterization work practiced with starting materials graphite and GICs are also included in

this chapter. The characterization studies of graphenide solution and graphene produced from graphenide solutions are one of the main subject in this chapter.

Chapter IV presents the study of graphene films produced from graphenide solutions by using vacuum-filtration method. The vacuum-filtration method is largely used to produce graphene films with graphene produced by solution-route methods. Thermal treatments were performed to improve the electrical properties of graphene film. Several techniques described in chapter II were applied to evaluate as-produced graphene and treated film. Beside thermal treatment, laser-assisted treatment was also performed to improve electrical and optical properties. Finally, an initial experiment concerning hybrid films made of graphene and carbon nanotubes is summarized in this chapter.

Acknowledgements

First, I would like to express my gratitude to Dr. Alain Pénicaud for giving me the opportunity to prepare my thesis in the group NTG “Carbon nanotubes et Graphène”, for being my daily advisor, and for giving me the chances to present our works at conferences, for spending his precious time on correcting my oral and written contributions and for being a great supervisor.

I would like to thank the jury members: Dr. Philippe Richetti, Dr. Edward Mc Rae, Prof. Catherine Journet-Gautier, Dr. Nedjma Bendiab and Dr. Kevin Mckeigue for their precious time reading my thesis and for their constructive comments. I am very grateful to Dr. Carlos Drummond and Dr. Alain Derré for their helps and fruitful discussion during my research. I am very grateful to Dr. Pascal Puech for enlightening discussions concerning Raman spectroscopy, for helping me to performing Raman experiments in CEMES Toulouse (Centre d'Elaboration de Matériaux et d'Etudes Structurales). I am also grateful to Dr. Iann Gerber for his helpful work concerning first-principle calculation for our samples. I would like to thank Dr. Amélie Catheline for teaching me hand by hand the techniques to preparer samples at the beginning of my thesis.

I would like to thank Dr. I am very grateful to Dr. Célia Castro and Dr. Marc Monthioux for their good works of characterizing our samples with high-resolution transmission electron microscopy (HRTEM). I also would like to thank Dr. Stéphan Rouzière and Pascale Launois for performing X-ray scattering on our graphene film and for their help in understanding and analyzing the results.

My appreciation is extended to Dr. Kai Huang and Dr. Hassan Saadaoui for their invaluable help and advice on AFM measurements. My sincere appreciations also go to Ms. Isabelle Ly for her lectures and helps of SEM and TEM characterizations. I want to thank also Dr. Jean-Paul Salvetat and Dr. Philippe Poulin for helpful discussions. I also would like to express my sincere thanks to colleges working in office chimie Dr. Frédérice Louerat, and Mr. Xavier Brilland for their helps and supplies of chemical products. I am also very thankful to Mr. Phillippe Barboteau, Mr. Emmanuel Texier, Mr. Jean-Yves Juanico and Mr. Pascal Merzeau for their indispensable works concerning the home-made devices with which my works become more efficient and experimental setup become effective. I also would like to thanks Mr. Ahmed Bentaleb and Mr. Mbolotiana Rajaoarivelo who not only helped me with problems concerning instruments but also helped and trained me on sports ground.

I also would like to express thanks to Dr. Christine Labrugène for performing XPS experiments and introducing me to XPS analyses. Sincere thanks are also to Dr. Philippe Négrier and Mr. Eric Lebraud for XRD measurements and advice concerning dates analyses.

I am grateful to colleges and friends in NTG group (Dr. Cécile Zakri, Mr. Wilfrid Neri, Dr. Christèle Jaillet-Bartholome, Dr. Brigitte Delord, Dr. Cintia Mateo, Dr. George Bepete, Dr. Jinkai Yuan, Jonathan Idier and Katerina Kampioti) for their helps and advices. My sincere thanks also go to Ms. Corinne Amengual, Ms. Béatrice Dupin, Ms. Elisabeth Hortolland, Ms. Josiane Parzych and Ms. Nadine Laffargue for their administrative support. I would also like to thank collegues working in IT section (Ms. Anne Facq, Mr. Philippe Hortolland, Mr. Jean-Luc Laborde and Ms. Sandrine Maillet) for their IT support. I really appreciate all friends in CRPP.

Finally, I would express a deep sense of gratitude to my parents who has always stood by me like a pillar in times of need and to whom I owe my life for their encouragements and moral

support. I would also like to extend my gratitude to my sister's familly for their supporting. Without their encouragement, I would not have a chance to pursue my studies in this beautiful country.

Contents

Chapter I: Introduction

Carbon is the 15th most abundant element on earth, and one of the few elements known since antiquity. 220 years ago, Lavoisier identified the versatility of carbon, because he determined that carbon was the elementary component of diamond and graphite. [1] Today, carbon materials are still among the most studied materials. Beside diamond and graphite, new carbon allotropes have been discovered, like fullerenes and carbon nanotubes. All those carbon materials share the same feature: they are formed by sp^2 carbon atoms, except diamond. Graphene, on the other hand, the basal plane of graphite, is composed of sp^2 carbon atoms. For many years this hexagonal array of carbon atoms, graphene, was considered a concept. It was thought that under normal conditions, graphene plane will stacked together to form the most thermodynamically stable form of carbon, graphite. However, in 2004, Andre Geim and Konstantin Novoselov from the University of Manchester reported that they succeed in producing graphene from highly oriented pyrolytic graphite (HOPG) with a simple method.[2] In parallel, in the same year, de Heer, Berger et al. showed that thermal reconstruction of SiC led to a carbon single layer that behaves electronically as graphene.[3] Since then, this new two-dimensional (2D) carbon nanomaterial has drawn tremendous attention both from the experimental and theoretical scientific aspects.

In a few years, by performing numerous studies, it was found that graphene demonstrates extraordinary electronic, thermal and mechanical properties. With those properties, graphene is expected to be one of the most promising candidates for future materials engineering. But for exploiting graphene in a variety of applications, a prerequisite is to find ways to produce processable graphene in large quantities.

Part 1 of this chapter will present graphene, its properties and production techniques. In part 2, graphite and graphite intercalation compounds will be introduced. With graphite intercalation compounds, an alternative production process to produce graphene in large quantities has been developed. Part 3 introduces transparent conductive films, including existing commercial materials, Indium Tin Oxide (ITO), and reviews different potential materials for ITO replacement.

1. Graphene

Graphene, a single atomic layer of sp^2 hybridized carbon atoms covalently bonded in a honeycomb lattice, is a building block for carbon materials of different dimensionalities shown in figure 1.1, including 0D fullerene, 1D nanotubes, and graphite.

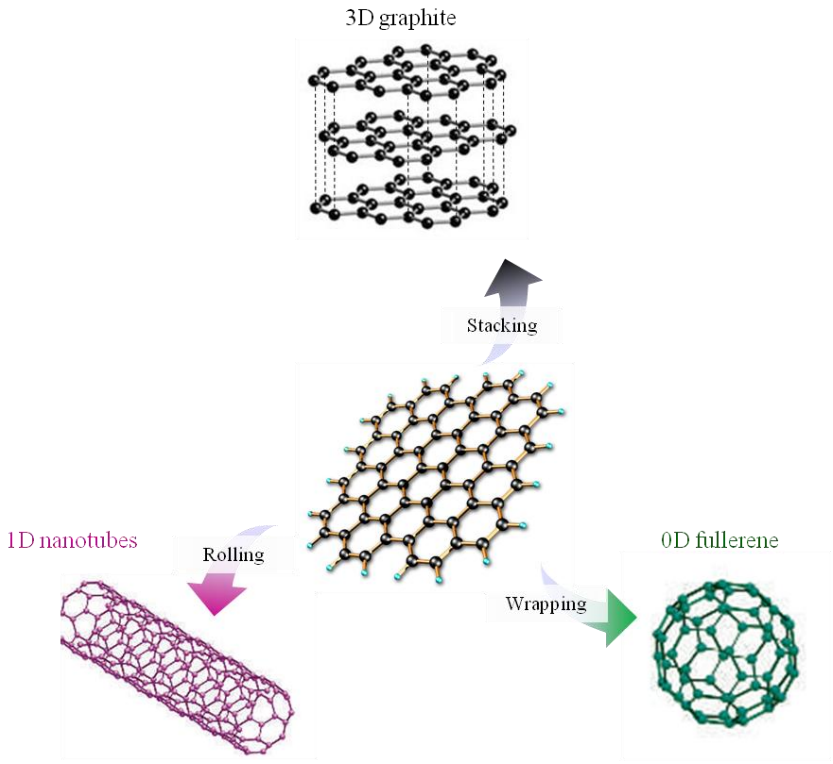

Figure 1.1: Conceptually, graphene is base for carbon materials of other dimensionalities. It can be wrapped up into 0D fullerene necessitating pentagons though, rolled into 1D carbon nanotubes or stacked into graphite.

1.1 Structure of graphene

Graphene has a simple two dimensional crystal structure. The unit cell for graphene contains two carbon atoms, A and B, each forming a triangular 2D network with 3 surrounding carbon atoms. Each carbon atom shares one σ bond with its 3 neighbors, which contributes to the stability of graphene plane. This unit cell can be characterized by carbon-carbon inter-atomic

length (a_{c-c}) of 1.42 Å and a degree of 120 ° between bonds. Perpendicular to the graphene plane, along the *z*-direction, there is a π orbital which can be visualized as a pair of symmetric lobes above and below the graphene plane. Each atom has one of these π-orbitals, which are then hybridized together to form a particular band structure, which are referred to as the π-band (valence band) and π*-band (conduction band). These bands are responsible for most of the peculiar electronic properties of graphene. [4] Since in benzene the bonding is the same, graphene can also be considered as a gigantic polycylic aromatic hydrocarbon.

For a given material, its band structure is often studied to better understand its electronic properties. Graphene has a remarkable band structure due to its crystal structure. With this kind of structure, graphene possesses a very special electronic band structure: the conduction and the valence bands are not separated by a gap, and do not overlap either. Indeed, they intersect in two in-equivalent points (K, K'), called Dirac points in the first Brillouin zone. Looking closely at the region near one of the Dirac points (K and K') as illustrated in figure 1.2, the cone-formed linear dispersion relation is evident. The Fermi energy for neutral graphene is at the Dirac energy. In graphene devices, the Fermi energy can be significantly different from the Dirac energy.

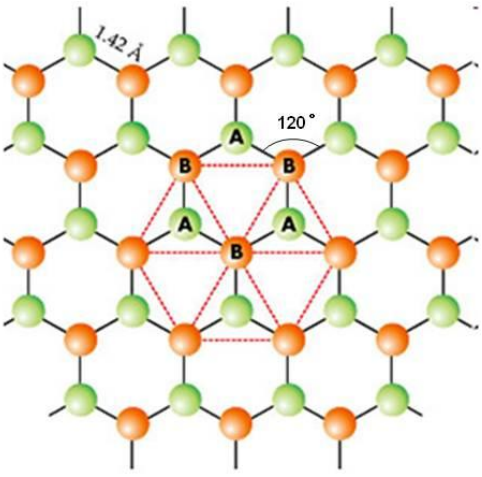

(a)

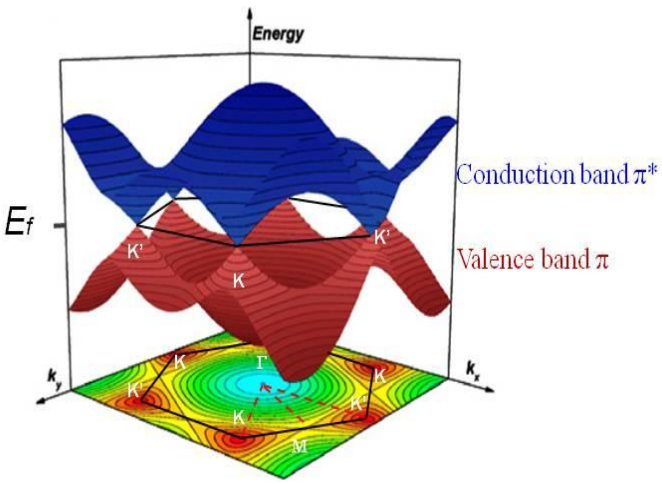

(b)

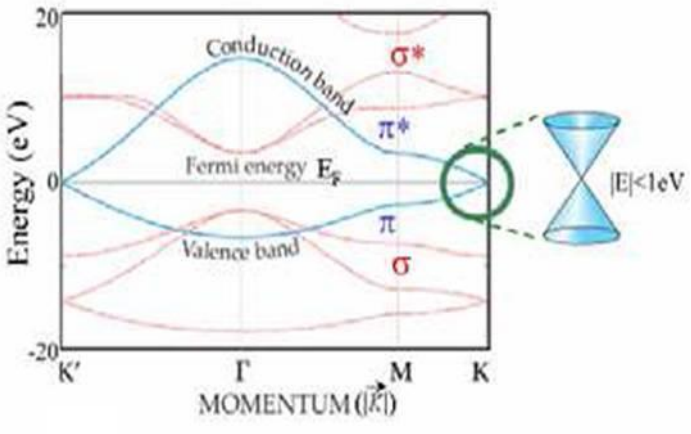

(c)

Figure 1.2: (a) Crystal lattice of graphene; (b) Full band dispersion over the whole Brillouin zone for valence band π (red surface) and conduction band π* (blue surface); (c) The energy of π (π*) band along the high symmetry directions in the first Brillouin zone.

In low energy region, electrons within about 1eV of Dirac energy have a linear dispersion relation. This dispersion relation near the K point can generally be expressed as follows: linear dispersion region is well-described by the Dirac equation for massless fermion. That is, the effective mass of the charge carriers in this region is zero. The dispersion relation near the K points is generally expressed as follow:

$$E_{\pm} \cong \pm \hbar v_F |k - K|$$

where $v_F \approx 10^6$ m/s is Fermi velocity, k is wavevector. Since at Dirac point, the energy is zero, the effective mass of the charge carriers in this region can be considered as zero. So in graphene, at low-energy region, this linear electronic band dispersion leads to the description of carriers in graphene as "massless Dirac fermions". Charge carriers in graphene behave like relativistic particles with an effective 'speed of light' ($c_* \approx 10^{-6}$ m/s) given by the Fermi velocity. [2] This behavior is one of the most interesting aspects in graphene, and is responsible for the remarkable properties that have been demonstrated in graphene.

For stacked graphenes, for example bilayer graphene shown in figure 1.3 (a) where the two monolayer stacks in the Bernal (AB) stacking arrangements (see section 2), due to the inter-plane interaction, the charge carriers is no longer featured by massless Dirac fermions; on the contrary, they can be described by massive chiral fermions. The interaction of the two π and π* bands of each graphene plane produces two parabolic bands illustrated in figure 1.3.

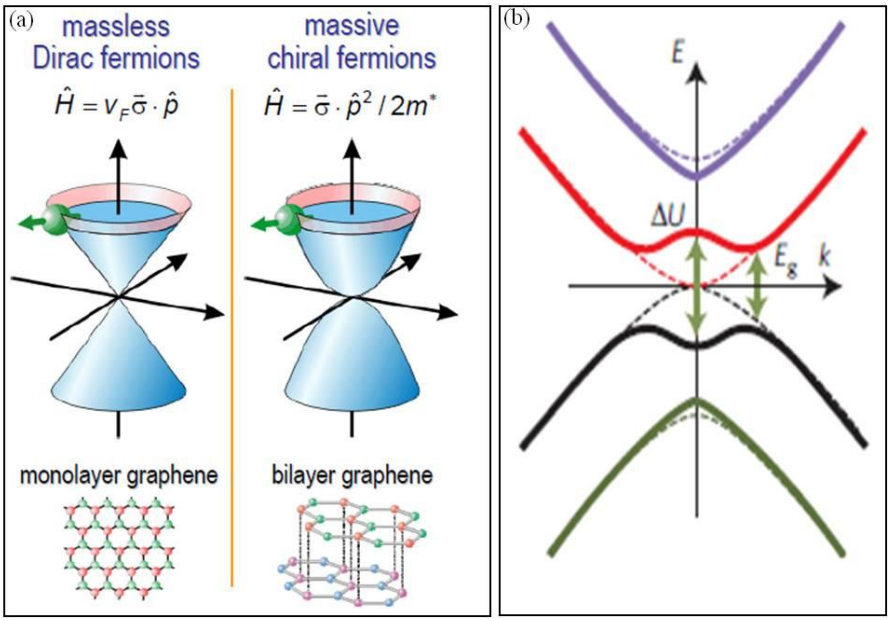

Figure 1.3: (a) Band structure of monolayer graphene and bilayer graphene. (b) Energy band diagram of bilayer graphene with (solid lines) and without (dashed lines) a bandgap. The electronic levels form Mexican-hat like energy bands with a potential energy asymmetry ΔU and a bandgap of E_g [4]

Unlike the zero bandgap in monolayer, in bilayer graphene theoretical calculations have predicted the possibility of a bandgap opening in bilayer graphene. [6] With the inter-plane interaction, the charge carriers can be described by massive chiral fermions as illustrated in figure 1.3 (a). The interaction of the two π and π* bands of each graphene plane produces two parabolic bands. In bilyer graphene with Bernal stacking structure, researchers have investigated a bandgap by breaking the symmetry of the bilayer stack with the application of a

transverse electrical field, which have demonstrated that the bandgap can reach values up to 250 meV. [7]

1.2 Properties of graphene

With this particular structure, graphene possesses various remarkable properties. It's noteworthy that there is no perfect graphene. In fact, there are always some kinds of defects in as-synthesized graphene, those kinds of disorders can reduce the properties of graphene, for example carrier mobility of graphene on 4H-SiC increases from 3000 cm^2/V-sec to > 11 000 cm^2/V-sec at 0.3 K after annealing under hydrogen which can eliminate Si dangling bonds. [8] In addition to those, monolayer, bilayer, few-layer graphene and even graphene oxide (see section 1.3.2) have different properties. It's not worth to make an exhaustive review for all kinds of graphene in the following section. Most of properties mentioned below were reported for monolayer graphene produced by mechanical exfoliation with which one can produce graphene samples with the best quality.

1.2.1 Electronic properties

In paragraph 1.1, the special band structure of graphene was mentioned, in the low energy region, electrons can be considered as massless Dirac fermions. Indeed, experimental results from transport measurements show that graphene has remarkably high electron mobility. The highest mobility was reported in suspended and annealed graphene device, the mobility can exceed 200 000 cm^2/V-sec. [9-11] In graphene, charger carrier mobility, for both electrons and holes, is temperature-independent between 10 and 100 K.[2] The extraordinary mobility of monomlayer graphene has only been observed on suspended graphene samples at low temperatures. However, supported graphene has limited mobility due to the scattering effects

of the underlying substrate that are still under investigation. [12] In neutral graphene, the Fermi level can easily be set by adjusting the doping level.

In addition to these properties found in graphene from mechanical exfoliation, thin films of CVD grown graphene as well as solvent exfoliated graphene or reduced graphene oxide possess high conductivity and good optical transparency. Graphene oxide is insulator but its conductivity can be improved by reduction treatment. Graphene grown by CVD method on nickel, and then transferred onto an insulating substrate can produce large area films with surface resistivity of ~ 280 Ω/sq and transparency beyond 80 % in the visible range. [13]

With these remarkable electrical properties, graphene has a high potential for high charge carrier mobility applications and transparent conductive materials.

1.2.2 Optical properties

For monolayer and bilayer graphene produced by mechanical exfoliation, the measured white light absorbance is 2.3 % and 4.6 % respectively. [14] In the visible range, thin graphene films have a transparency that decreases linearly with film thickness. The theoretical transmittance (T) of a free standing graphene can be given: [15]

$$T = (1+0.5\pi\alpha)^{-2} \approx 1 - \pi\alpha \approx 97.7\ \%$$

where α is the fine structure constant. It has been demonstrated that the transparency of graphene depends only on the fine-structure constant $\alpha = 2\pi e^2/hc = 1/137$, which describes the coupling between light and relativistic electrons. Thus the absorbance can be calculated as $A = 1-T = \pi\alpha = 2.3\ \%$, which is in excellent accordance with the measured value.

Graphene only reflects < 0.1% of the incident light in the visible region. The absorbance of few-layer graphene is simply the product of $\pi\alpha$ by the number of layers. The monolayer

graphene film produced by CVD has a similar optical transmittance, 97.6%. [16] Indeed, the transmittance of graphene depends on its crystal quality. And the transmittance linearly decreases when the number of layers increases.

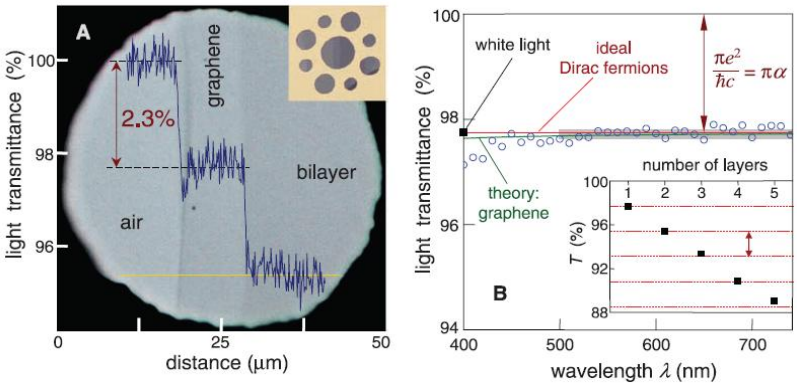

Figure 1.4: (a) Transmittance of mechanically exfoliated monolayer and bilayer graphene. [14] (b) Transmittance spectrum of mechanically exfoliated single-layer graphene. [14]

1.2.3 Mechanical properties

Graphite, diamond and carbon nanotubes have remarkable mechanical properties; especially they all have high Young's modulus. Both theoretical and experimental results show that graphene is not an exception in terms of mechanical properties. The reported breaking strength for graphene is about 42 N/m, which is 200 times higher than steel. [17] The elastic stiffness is in the order of 300-400 N/m; [17] the estimates of the Young's modulus yielded approximately 0.5-1.0 TPa which is very close to the accepted value for bulk graphite. [17] Even in graphene oxide sheets which contain defects, the Young's modulus can still be up to 0.25 TPa. [18]

1.2.4 Thermal conductivity

Since in graphene sheet, the carbon atoms based in-plane bonding is very strong, graphene exhibits a very high sound velocity, close to c_{ph} ~ 20 Km/S, due to the phonon dispersion relation in graphene. [19] This large sound velocity is responsible for the very high thermal conductivity of graphene that is useful in many applications.

The thermal conductivity due to phonons is given by $\kappa \sim c_{ph} C_V(T) \lambda$, where $C_V(T)$ is the specific heat per unit volume and λ is the phonon mean free path. This indicates that we can expect a large thermal conductivity because of very large c_{ph} in graphene. In fact, from experiments performed near room temperature, researchers obtain $\kappa \approx$ 3080-5150 W/mk and a phonon mean free path of $\lambda \approx$ 775 nm for graphene flakes. [20]

These results indicate that graphene is a good candidate for applications in electronic devices, since a high thermal conductivity facilitates the diffusion of heat to the contacts and allows for more compact circuits.

1.2.5 Chemical properties

Graphene has a large theoretical surface area of 2600 m^2/g for monolayer graphene, [21-22] while the surface area of multilay graphene is 270-1550 m^2/g. [22] Similar to the surface of graphite, graphene can absorb and desorb various atoms and molecules. Weakly attached adsorbates often act as donors or acceptors and lead to changes in the carrier concentration, so graphene remains highly conductive. This can be exploited for application as sensors for chemicals.

Other than weakly attached adsobates, graphene can be functionalized by several chemical groups, like -OH, -F, forming graphene oxide and fluorinated graphene. It has also been observeded that single-layer graphene is more reactive than 2, 3 or a higher number of layers

of graphene. [21] Also, the edge of graphene has been shown to be more reactive than the surface. [23] Unless exposed to harsh reaction conditions, graphene is chemically stable material.

1.3 Synthesis of graphene

With the above described significant properties, graphene could be applied in many engineering fields from flexible transparent electronics to high performance electronic devices. The development of this magic material could pave the way to future technologies featured as faster, thinner, stronger, flexible devices. However, a key for those applications is the development of production processes in industrial scale with a balance between fabricating cost and materials quality. In this section, the main production approaches are summarized.

1.3.1 Micromechanical exfoliation

Micromechanical exfoliation, called also micromechanical cleavage, was used in 2004 by Novoselov et al. to prepare single layer graphene with an adhesive tape to cleave. Actually, in 1999 scientists had reported a controlled way to cleave graphite in order to produce films with several layers of graphene. [24] Now, micromechanical exfoliation has been optimized to produce high quality graphene, which can currently reach millimeter lateral size. [25] This method can produce the graphene with best quality. As-produced graphene can be identified rather easily by optical microscope. The charge carriers mobility can reach up to 10^7 $cm^2/V \cdot s$ at 25 K for a monolayer graphene on the surface of bulk graphite. [26] At room temperature, for as-prepared monolayer graphene by micromechanical exfoliation, the charge carriers mobility is ~ 20 000 $cm^2/V \cdot s$.

Although this method produces graphene with the best quality, it's impractical for large scale applications. It still can be a method for fundamental studies. Beside the mechanical way, people have developed other kinds of method to exfoliate graphite via electrostatic forces [27] and photo-exfoliation (i.e. laser assisted) in air, vacuum or inert environment. [28]

1.3.2 Liquid phase exfoliation of graphite and graphite oxide

In liquid phase exfoliation, the starting material is graphite. The method consists in exfoliating graphitic materials in liquid environment with intensive energy assistance. In general, the liquid phase exfoliation involves the following steps: (1) dispersion and exfoliation of graphite or graphite oxide in a solvent with exploiting ultrasonic and/or surfactant; (2) centrifugation to separate exfoliated graphene layers from un-exfoliated flakes.

(a) Liquid phase exfoliation of graphite intercalaction compounds

Graphite intercalation compounds (GICs, see section 2.2) are formed by intercalation of atoms or molecules between the graphene planes. The intercalation process increases the graphite interlayer spacing, and can change dramatically the properties of pristine graphite.[29] The alkali metals intercalated graphite intercalation compounds (GICs), such as KC_8 and $K(THF)_xC_{24}$, are easy to exfoliation when they are exposed to organic solvents;[30-35] and these negatively charged graphene sheets form supple two dimensional polyelectrolytes. Cathelina et al. reported that the entropic gain from the dissolution of counterion and the increased degrees of freedom of grpahene in solution drives exfoliation process, which is spontaneous process without using sonication.

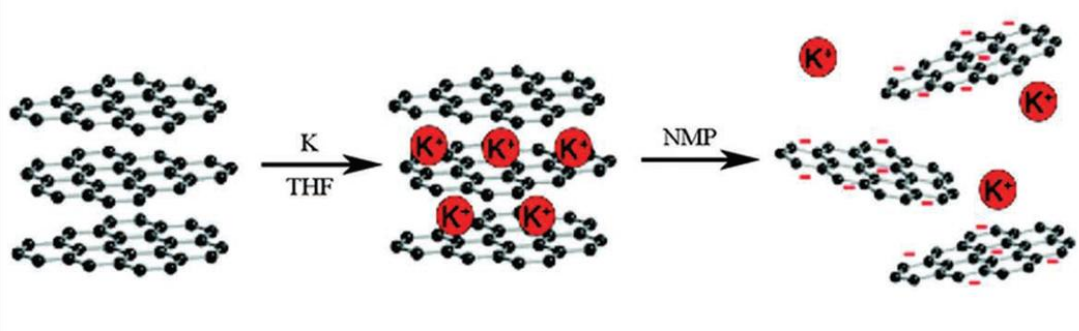

Figure 1.5: Negatively charged graphene layers from graphite intercalated compound spontaneously dissolved in NMP. [30]

Beside above presented alkali metals intercalated GICs, GICs can also be produced by intercalation of halogens and halogen mixtures. From these GICs, the expanded graphite can be produced by thermal shock by volatilizing intercalants. The as-produced expanded graphite can be used to produce graphene solutions with sonication. [36, 37] Strano et al. claimed that a predominance of bi- or trilayer graphene solutions can be produced from these GICs.

(b) Liquid phase exfoliation of graphite

In general, interfacial tension is an important factor when a solid surface is immersed in a liquid medium. [38] A high interfacial tension between solid and liquid will generally lead to a poor dispersion of the solid in the liquid. According to the research from Coleman's group, the best solvents for the dispersion of graphene have a surface tension, $\gamma \sim 40$ mN/m, since they minimize the interfacial tension between solvent and graphene flakes. [39] In reference 39, they list the main solvents, which possess $\gamma \sim 40$ mN/m like N-Methyl-2-pyrrolidone (NMP), Dimethylformamide (DMF), Benyl benzoate etc, they all have a rather high boiling point that makes it difficult to remove the solvent for successive processing. Thus, low boiling point solvents, such as acetone, isopropanol, and ethanol even water etc, can also be used. After exfoliation, the solvent-graphene interaction needs to counteract the attractive forces of graphene sheets dispersed in solvent. Thus, the surfactants sometimes have to be used for

stabilizing graphene flakes to avoid reaggregation of graphene sheets, especially for graphene dispersed in water which has $\gamma \sim 70$ mN/m too high for dispersing graphene. The most commonly used surfactants to disperse graphene are sodium deoxycholate (SDC), Sodium dodecylbenzenesulfonate (SDBS), polymer and bile salts, which are also used to disperse carbon nanotubes. It is noteworthy that the presence of surfactant or polymer may decrease the properties of graphene obtained (for example conductivity between graphene sheets), thus depending on the final application one should make a compromise.

(c) Graphene oxide and reduced graphene oxide

Beside liquid phase exfoliation of pristine graphite, exfoliation of oxidized graphite and then reduction of graphene oxide is another important method to produce graphene. The most commonly used method to produce graphitic oxide was developed by Hummers in 1958, and in this process graphite is oxidized by using a mixture of sulphuric acid (H_2SO_4), sodium nitrate ($NaNO_3$) and potassium permanganate ($KMnO_4$). [40] With these aggressive oxidation treatments, the sp^2 structure of graphene is highly disrupted and functional groups are created in the graphene plane, which results in insulating graphene oxide (GO). The introduction of these functional groups, which make GO flakes hydrophilic, is essential for the dispersion of GO in liquid after sonication of graphite oxide. Graphene oxide flakes can reach a several microns lateral size, [41] but they are defective and insulating. For example, the surface resistivity of a thin film produced with GO can be 10^{12} Ω/sq. [42] Thus, in order to repair the graphene structure, reduction treatments have to be done to eliminate the oxygen-containing groups. There are several methods to do the reduction, such as chemical reduction, like hydrazine, [43] hydride, [44] thermal reduction. [45, 46] Even after reduction treatment, the attached functional group cannot completely be removed, thus for reduced graphene oxide the electronic and thermal properties are not as good as pristine graphene.

(d) Liquid phase exfoliation of graphite with superacid

Superacids have been used to disperse single-walled carbon nanotube (SWNTs) due to protonation of the SWNT sidewalls. [47] Na et al. reported in 2009 that superacids can also be used to exfoliate graphite into graphene. [48] They claimed that superacid acid protonates the graphene, which induce repulsion between layers.

Although liquid phase exfoliation method has several kinds of disadvantage, but one can produce graphene with low cost, which can satisfy the scalable production of functional films and composites.

1.3.3 Chemical vapor deposition (CVD)

CVD is widely used in many industry sectors to produce thin films from solid, liquid and gaseous precursors. For producing graphene by CVD method, the metal substrate, like copper, nickel, ruthenium, that have different carbon solubility and catalytic effect, is exposed to hydrocarbon gas, such as methane, ethane or propane to produce high quality and large area graphene film.

The mechanism of graphene film growth on a substrate by CVD method can be explained by nucleation of carbon atoms decomposed from hydrocarbons and then growth of those nuclei into large domains. [49, 50] The nuclei density can be controlled by temperature and gas pressure. Thus by changing those factors, one can optimize the CVD process in order to produce good quality large area graphene film for a given substrate. In 2010, a graphene sheet, 30 inches in diagonal, produced by Low-pressure CVD (LPCVD) on Cu foil was made, with mobility μ ~7350 $cm^2V^{-1}s^{-1}$ at 6K. The transferred graphene on polyethylene terephthalate (PET) flexible substrate has a sheet resistance as low as ~125 Ω/□ with 97.4 % optical transmittance at 550 nm. [51]

For application of graphene produce by CVD on metal substrates, the catalytic metal substrate must be removed and graphene can be transferred onto arbitrary substrates. Figure 1.6 illustrates a typical process to transfer graphene from metal substrate. At first, graphene is coated by a thin layer of polymethyl methacrylate (PMMA), and then the metal layer is removed by etching, leaving only the PMMA/graphene film. This film can be transferred onto a desired substrate. [52] The transfer method can trap ionic species, located between graphene and substrate interface, which act as scattering sources; as a result, the electrical properties of as-produced graphene degrade. Furthermore, the etching process also results in loss of metal, which increases dramatically the production cost, especially if oriented single crystal substrate is used. These drawbacks limit to a certain extent the graphene production in large scale by CVD method. But CVD method is still one of the most promising ways to produce graphene with good quality in industrial mass production.

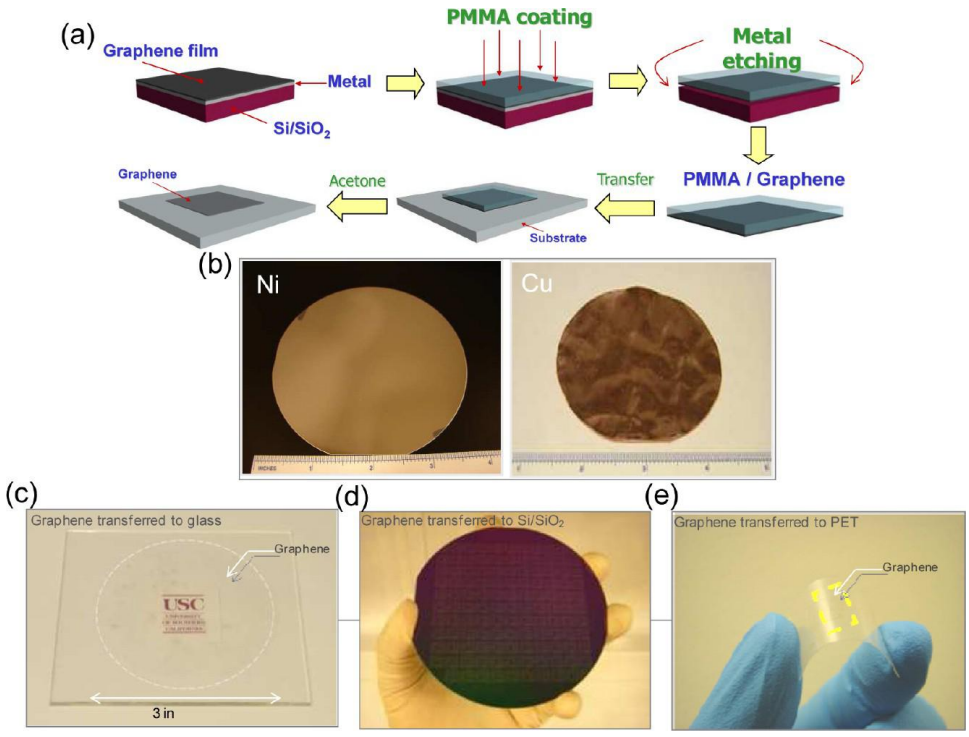

Figure 1.6: Transfer process of CVD produced graphene from substrate to desired substrate. (b) wafer-scale synthesis of graphene on evaporated Ni film and Cu foil. (c) graphene films on glass substrate; (d) graphene films on a Si/SiO_2; (e) graphene films on PET film. [53]

1.3.4 Thermal reconstruction

The production of graphene on SiC is also called "epitaxial growth". The method consists of production of graphene films by thermal decomposition of SiC above 1000 °C. For thermal decomposition production method, the control of layer number for large area is difficult. [54]

The growth rate of graphene on SiC substrate depends on the specific polar SiC crystal surface. Graphene grows faster on the C-face than on the Si-face. [54] Graphene grown on the Si-face has mobility up to ~500-2000 cm^2/V-sec, while higher values ~10 000 - 30 000 cm^2/V-sec are obtained on the C-face. [55, 56] The high mobility on C-face is attributed to rotational stacking faults whereas why the mobility on Si-face stays low is still under discussion. [56]

Since SiC substrate is well studied for modern high frequency electronics, light emitting devices, etc. a considerable advantage of this method is that there is no need for transferring graphene from insulating SiC substrates to another substrate. Furthermore graphene produced by this method is of high quality, but a challenge for this technology is to achieve large scale productions. Compared to Si technology in electronic applications, one drawback of this method is the production cost. SiC wafers cost almost 30 times higher than same size of Si wafer.

1.3.5 Chemical synthesis

Graphene can also be chemically synthesized with polycyclic aromatic hydrocarbons (PAHs), through surface-mediated reations. There are two approaches generally used in this method. The first is to use dendritic precursor transformed by cyclodehydrogenation and planarization [48]. This approach can produce small and almost pure graphenes with a molecular diameter of several nanometers, called nano-graphenes. Another approach is based on PAH (Polycyclic aromatic hydrocarbons) pyrolysis at high temperature to grow the PAH into larger graphene [57, 58]. Chemical synthesis may allow a true control at the atomic level, but the synthesis processes are complicated, which restrains its possibility for large scale production.

2. Graphite and Graphite Intercalation Compounds

2.1 Graphite

Graphite is an ordered carbon allotrope consisting of the stacking of hexagonal individual graphene layers in the direction perpendicular the graphene plane (*c*-axis). In the *c*-axis direction, the neighboring graphene planes interact by overlapping π-bands between the unhybridized carbon 2p orbitals.

The stacking sequence of the graphene planes along the c-axis follows a typical –ABAB– pattern (or Bernal stacking pattern) as shown in Figure 1.7 (c). In AB stacking graphite, the crystal unit cell consists of four carbon atoms A_1, A_2, B_1 and B_2 on the two layers shown in Figure 1.7. In basal plane, the carbon-carbon bond length is a = 1.421 Å, and the inter layer spacing is 3.354 Å. The AB stacking crystalline graphite is found in nature as a natural mineral.

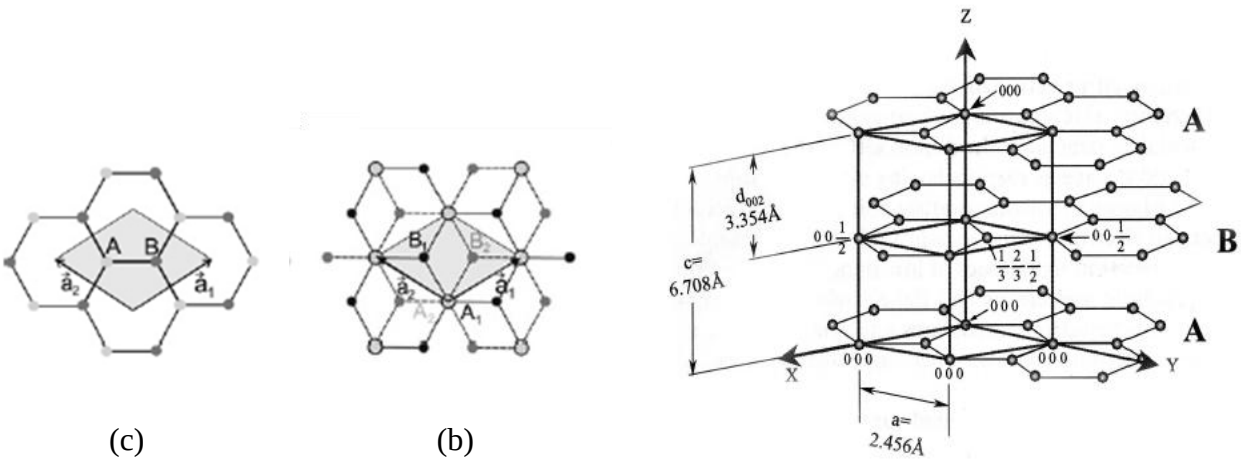

(c) (b) (c)

Figure 1.7: (a) A top view of the unit cell of monolayer graphene showing the two atoms A and B and unit vectors a_1 and a_2. (b) A top view of the AB stacking bilayer graphene. The light/dark gray dots and the black circles/black dots represent respectively the carbon atoms in the upper and lower layers in bilayer graphene. (c) The structure of AB stacking graphite

As mentioned in section 1, graphene is an excellent conductor of electricity. The bonding force between the graphene planes (van der Waals interaction) is almost 1/300th of C-C bond strength. It is this difference between the in-plane graphene bonding and the out-of plane interactions that cause the large anisotropic properties. The electrical resistivity of graphite is almost one thousand times higher along the *c*-axis than it is in any direction in the graphene basal plane where free electrons have greater mobility. [29]

Within the graphene plane, the binding energy is 7 eV/atom. Graphene is modeled as a zero band-gap semiconductor. The unit cell of graphite has a weak overlap of the π-bands, with around 0.02 eV/atom binding energy between the planes. Thus, in graphite the weak inter-plane interaction between AB stacked graphene planes modifies the electronic structure into a semimetallic structure. With is special semimetallic electronic structure, the graphite material possesses the same ionization potential and electron affinity (4.6 eV), which makes graphite an oxidant as well as a reducer in chemical reactions.

Besides the AB stacked graphite (also named 3D crystalline graphite), there is also turbostratic graphite in which there is no stacking order between adjacent graphene layers and the interlayer distance is larger than that of AB stacking graphite. Because of the absence of stacking order between the graphene planes, the turbostratic graphite has modified physical properties compared with 3D crystalline graphite. There is another common forme of crystalline graphite called HOPG (highly oriented pyrolytic graphite). HOPG is obtained from synthetic AB stacked graphite prepared from carbon-based precursors by heat treatment at high temperature (over 3200°C under high pressure). [59] Natural graphite exhibits imperfect structure due to defects. Pyrolytic graphite is a graphite material with a high degree of preferred crystallographic orientation of the *c*-axes. HOPG is a higly-ordered form of high-purity pyrolytic graphite. HOPG is characterized by the highest degree of three-dimensional

ordering. The density of HOPG is close to those of natural graphite. However, HOPG displays a better electric conductivity than that of the polycrystal graphite.

The graphite is three-dimensional (3D) layered material; it is nonporous with a surface area typically under $20m^2/g$. [60] The open structure between the layers in graphite is an interlamellar spacing that accepts rather easily guest species. It is often referred to as "galleries". Graphite can accepts a great number of different chemical elements, and many of them can stay stably inside the lattice under certain environment. This process is called intercalation. During the process of intercalation, graphite is "host" and accepts intercalated "guests". And the result of intercalation is called graphite intercalation compound, which will be presented in the following part.

2.2 Graphite intercalation compounds and synthesis

Graphite intercalation compounds, also abbreviated as GICs, are formed by the insertion of atomic or molecular species between graphene layers in graphite. The intercalated chemical elements are called the intercalant. The insertion of intercalants results in the increase of interlayer distance between graphene planes. During the intercalation, a charge transfer occurs between the graphene plane and the intercalant species. Electron can be transfered from graphite to intercalants, but also from intercalants to graphite (or graphene) planes. Those kinds of charge transfer can be described in the following reactions:

$$xC + D \rightarrow D^{+}C_x \qquad (1.1)$$

$$xC + A \rightarrow C_xA^{-} \qquad (1.2)$$

where C, D and A are respectively graphite, donor and acceptor. D and A are not always monovalents. There exist also higher valency compounds such as CaC_6 for example. [61]

The reactions above are called intercalation reaction. People have succeeded in intercalating a large number of species into the galleries of graphite. From the point of view of charge transfer, GICs can be classified into two types: donor and acceptor.

2.2.1 Donor Intercalation compounds

For donor type GICs, the electron is transferred from the intercalant species to graphite, which renders graphene planes negatively charged. The alkali metal, alkali earth metal and rare earth can be intercalated into graphite. Those can form typical donor type GICs. Alkali metal GICs are the best known and most intensively investigated donor type GICs, since they are easily prepared. In fact, the first discovery of GICs was made with potassium more than 160 years ago (Schaffäutl, 1841). [62] During our study, we have used potassium to synthesize different kinds of GICs.

GICs have the ability to accept further guest species, forming so-called ternary (or higher-order) GICs, for example hydrogen can be intercalated in the alkali metal GICs. Donor GICs with alkali metal, alkali earth metal and rare earth metal accept third intercalant elements to form ternary donor GICs. Usually these additional intercalants are organic compounds such as Tetrahydrofuran (THF).

2.2.2 Acceptor Intercalation compounds

For acceptor type GICs, the electron is transferred from graphite to the intercalant species. The graphene plane is thus positively charged in acceptor type GICs. The most well known acceptor GICs are acid GICs, like HNO_3, H_2SO_4 –GICs etc. Acid GICs can only form under reasonably oxidizing condition. Under intense oxidizing condition with acid, graphite is converted to graphite oxide in which the graphite π-bonds are broken. [41, 42] Besides acide

GICs, chloride, fluoride and halogen species (except iodine) can be acceptors and be intercalated into graphite to form acceptor type GICs.

Many GICs are unstable in air, with donor compounds being easily oxidized and acceptors being easily desorbed. For this reason, most intercalation compounds should be protected under inert atmosphere to ensure chemical stability. It is important to note that alkali metal - GICs are in general very sensitive to oxygen, moisture and other impurities. Exposing these GICs to air can result in rapid, irreversible degradation, sometimes even combustion. Even in atmospheres with a very low proportion of oxygen, oxidation and desorption of the intercalant are observed, resulting in the return of the coloured GICs sample to the grey tone of pristine graphite.

From the electronic structure point of view, for donor type GICs, the electron transfered from donor to graphite occupies the anti-bonding π*-band of graphene which is initially empty. For the acceptor type GICs, the electron transfers from graphite to the intercalant, emptying the top of the π-band of graphene.

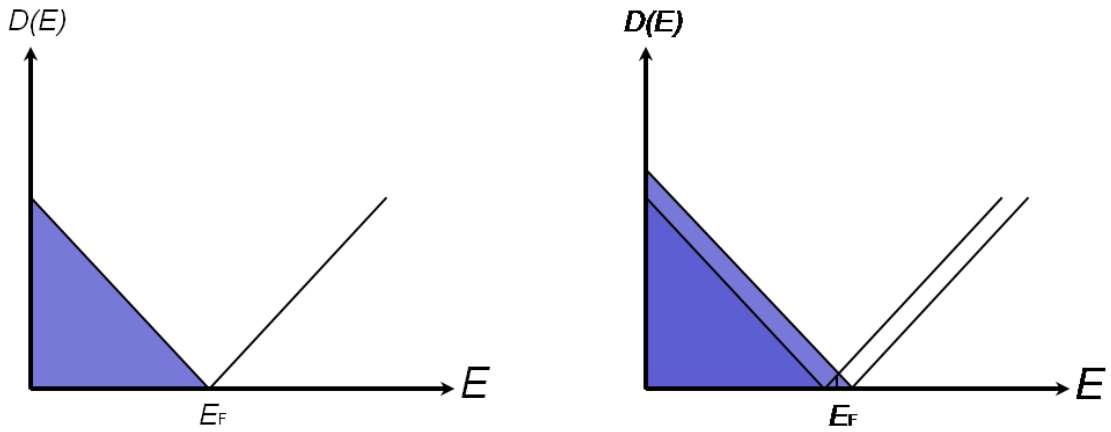

(a) (b)

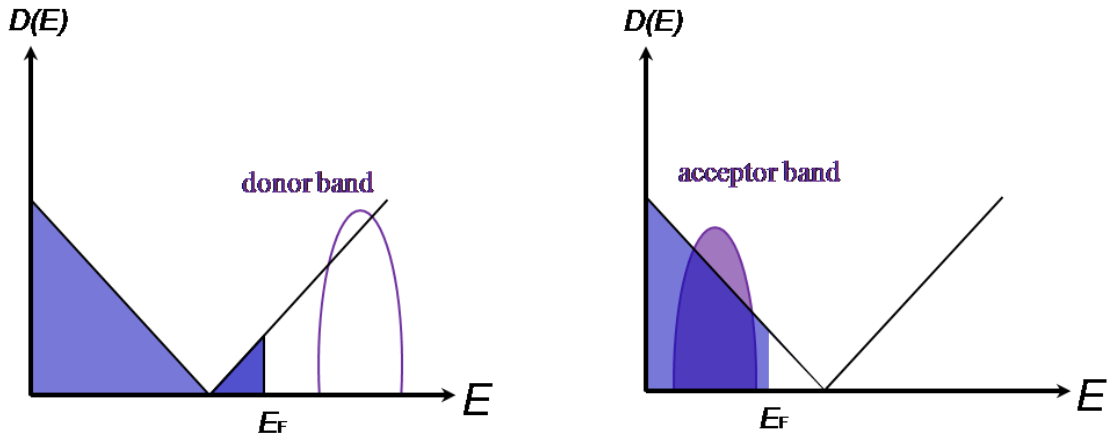

(c) (d)

Figure 1.8: The electronic structures of graphene (a), graphite (b), donor GICs (c) and acceptor GICs (d). $D(E)$ is the density of states and E_F is the Fermi energy in the neutral state. [63]

2.2.3 Structure of potassium intercalated graphite

We introduce principally potassium intercalated GICs in this part, but it is worth noticing that some conceptions, like staging phenomenon, stacking sequence etc, are similar to other kinds of GICs. A remarkable structural feature in intercalated graphite is a phenomenon called staging occurring in the *c*-axis direction. The potassium atoms can occupy galleries of graphite with some periodical way. When potassium atoms occupy every graphitic gallery, this is stage-1 KC_8. The stage number corresponds to the number of graphene layers between two adjacent intercalated atom layers. Figure 1.9 shows the staging phenomenon in graphite-potassium compounds for stages $1 \leq n \leq 3$.

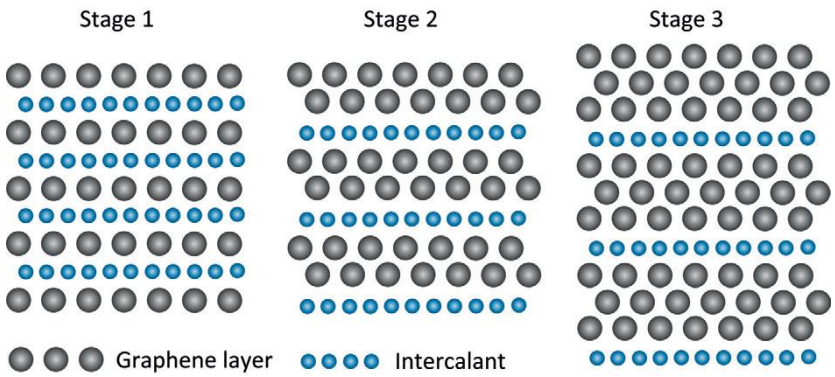

Figure 1.9: The staging phenomemon in graphite-potassium compounds

The stage dependenc of the *c*-axis lattice spacing I_c is given by

$$Ic(\text{Å}) = ds + 3.35(n\text{-}1) \qquad (1.3)$$

where n is the stage number, and d_s is the interlayer distance of a fully-intercalated gallery.

The charge transfer in different stage leads to characteristic colour properties of those compounds. These colours are related to the electronic band structure of the compounds and thus related to the charge density. Pure KC_8 is a golden-orange colour and KC_{24} a metallic blue. Higher stages become progressively greyer until indistinguishable from the grey of unadulterated graphite. The purity of the staging in a sample can easily be identified by observing the sample colour. If one sample is homogenous then the sample has a high degree of purity, especially for low stage compounds. This method was used to select the best quality samples for experimentation.

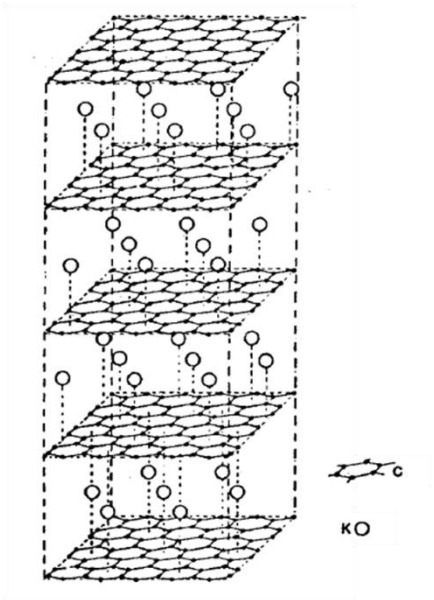

Figure 1.10: Model for KC8 according to Rüdorff showing the stacking of graphite layers (networks of small solid balls) and of potassium layers (networks of large hollow balls). The graphite and

intercalate layers are arranged in an AαAβAγAδ stacking sequence, where A refers to the graphite layers and the Greek letters to the intercalate layers. [29]

In potassium GICs, there are two competing forces. First, as illustrated in figure 1.10, the potassium atoms tend to be located at the hexagon centers due to the strong graphite corrugation potential. This would cause the opposing basal planes to overlap in an A│A sequence, where the vertical bar represents the potassium layer. Second, graphite planes tend to form its original stacking order, ABAB. It is the competition between these two driving forces that leads to the formation of discrete GIC stages. At low metal concentrations like KC_{24} and KC_{36}, it is energetically favorable for metal layers to only occupy every 2nd and 3rd graphite gallery, respectively. The non-intercalated layers can maintain a staggered AB sequence, while the intercalated layers have an A│A sequence. If the potassium concentration is increased further, the system will eventually reach KC_8 stoichiometry. The actual concentration of potassium within the GIC is determined by its relative chemical potential in the intercalated phase and in the vapor phase. By controlling the graphite temperature and the potassium vapor pressure (via the temperature of the melt), different potassium GIC stages can be synthesized (see Figure 1.11).

The stage 1 KC_8 has AαAβAγAδA stacking sequence. [64] For the stage-2 and higher stage, there is no well characterized stacking sequences. Nixon and Perry recommended the following stacking sequence: [65]

Stage 2 AB│BC│CA│A

Stage 3 ABA│ ACA│A

Stage 4 ABAB│ BCBC│CACA│

An in situ X-ray diffraction study of the potassium GICs allowed to identify stages 1 to 7, the investigation shows that there is no appreciable evidence of the intermediate state in which intercalants are passing through the phase boundary region so that the *c*-axis disorder occur.[66] When potassium is inserted into the host graphite, the interlayer spacing expands from 3.35 Å to 5.40 Å. Meanwhile the unintercalated galleries keep at 3.35 Å.

2.2.4 Synthesis of graphite intercalation compounds

In the long history of research on GICs, a number of different methods have been developed to prepare graphite intercalation compounds, such as the two-zone vapour transport technique, the liquid intercalation method, the electrochemical method and cointercalation techniques. [29] The objective is to bring the intercalant species in contact with graphite and have them sufficiently mobile in order to insert the intercalant into the galleries of graphite. For this reason, it is usually necessary to have the intercalant into either the gaseous or liquid state. For potassium GICs, the most common method is the vapour transport technique because this method allows us to obtain well-staged samples. In this method, the most important synthesis parameters are temperature and vapour pressure. Because we applied this method to make different stages of potassium GICs during our studies, we focus on the two-zone vapour transport technique in this part.

In the two-zone vapour transport technique, the intercalant metal potassium and graphite are placed separatively in a reactor. Then the reactor is sealed and evacuated as illustrated in figure 1.11. The sealed reactor is placed in an oven where the temperature can be carefully regulated. The intercalant is typically heated at some temperature T_i to vaporize the potassium. In the graphite zone, which is some distance away, the temperature T_g will be regulated in function of the desired stage of compound. The vapour is then taken up by the graphite. A

well controlled thermal gradient, T_g-T_i, is placed over the two zones. The compounds with desired stage are produced by the difference in vapour pressure over metal at temperature T_i and graphite at temperature T_g ($T_g > T_i$).

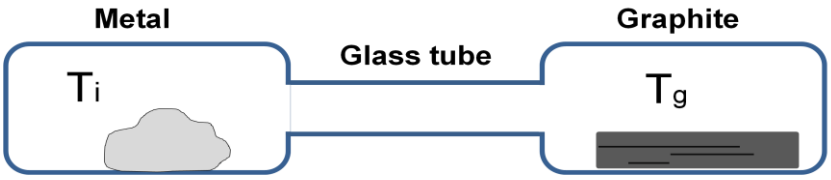

(a)

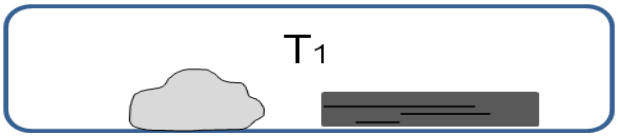

(b)

Figure 1.11: (a) Two-zone vapour transport technique. (b) One-zone vapour transport technique

An excess of intercalant can be used for two-zone vapour transport technique as in this method, the vapour pressure gradient/thermal gradient (T_g-T_i) is the key issue to determine the maximum amount of intercalation and thus the staging of the sample. The smaller values of T_g - T_i produce compounds with lower stage as shown in figure 1.11. It should be notice that with increase of stage number it becomes more difficult to produce homogenous staging samples. The time taken for intercalation to be finished completely depends strongly on the intercalant species, the amount of intercalant in the reactor and the microstructure of the host graphite. For example, small and thin graphite are easier to be intercalated and the resulting compounds are more well-staged and homogeneous. Also single crystal graphite flakes intercalate more readily than highly oriented pyrolytic graphite (HOPG) and carbon fibers. [67, 68] Typical time can range from a few seconds for easily-intercalated metals like potassium in graphite, to many weeks for the alkali-earth or rare-earth metals in HOPG. [67] Once the

intercalant enters in graphite, the intercalant must remain mobile in order to create a homogenous structure and so a process of annealing is used for a further period of time dependent on the temperature and the intercalant species. This allows the diffusion of intercalant ions and the creation of homogenous compounds. Beside this two-zone vapour transport technique, one can also use one-zone vapour transport technique shown in figure 1.11 to produce low stage compounds. Unlike two-zone vapour transport technique, the intercalant is sealed in the same space as graphite. In this way, there is no thermal gradient; the desired stage is produced by placing an accurate amount of intercalant and graphite in the reator and the amount is determined by their stoichiometry, as KC_{24}, KC_{36} etc. Cointercalation is a process where two or more species are intercalated at the same time. For example, lithium alloys can be used with other metals that do not intercalate alone; in this case, both lithium and other species can enter graphite. [63] Electrochemical techniques are also a commonly used technique to prepare GICs, especially for acid intercalants. Graphite serves as the working electrode, held by a platinum cap. The second platinum is employed as the counter electrode. In this method, the stage is controlled by the electrode voltage. [29, 63]

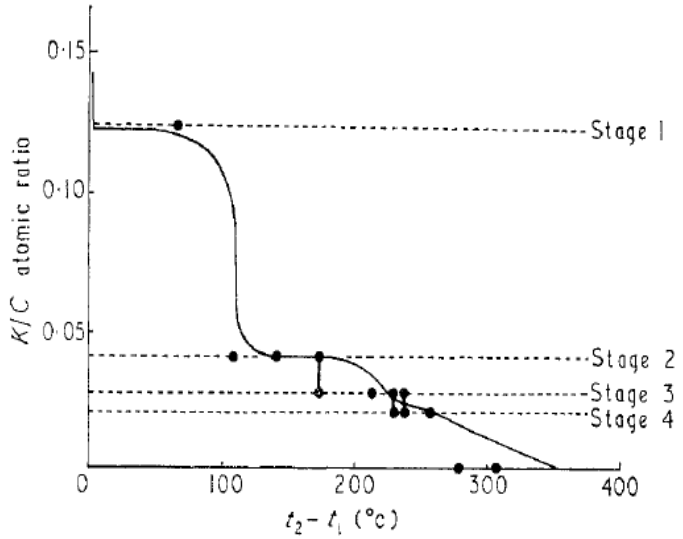

Figure 1.12: Isobar for growth of graphite-potassium GICs showing intercalant uptake versus temperature difference T_g-T_i between graphite and potassium. [29]

Liquid method is very useful technique to synthesize ternary GICs. In this method, graphite is immersed in solutions of the intercalant to produce GICs. For example, organic solvent tetrahydrofuran (THF) is a polar solvent with a strong affinity for donor metals. The solutions penetrate graphite very well, with the electrons going to the carbon layers and forming metal-THF-GICs. Another example is ammonia. I once used solution of potassium in THF, and then added pure degassed graphite to create ternary GIC $K(THF)_xC_{24}$ which is a stage 1 GIC.

3. Transparent conductive electrodes

Transparent conductive electrodes, being electrically conductive and optically transparent, play an important role in information and energy technologies. These materials, particularly for the current market of transparent conductive oxides, are widely exploited as transparent electrodes across technical fields from liquid crystal display (LCD), touch panels to electronic paper (e-paper), solar cells and low-emissivity coatings etc. LCD with annual growth of 9 % is still the largest usage of transparent conductive materials. But the rise and booming development of SmartPhone, which are always equipped of touch panel (annul growth of 20 %), and thin film solar cells enhance strongly the demand of those materials in foreseeable future. Over the last decade, the increasing demand in electronic devices, which require transparent conducting electrodes, draw researchers both from industry and academic research world into this field.

The most commonly used transparent conducting materials today are transparent conducting oxides. Those kinds of materials have been studied for over half century, especially indium tin oxide (ITO) and Zinc oxide. Those materials have been widely used in industry, and they are still the first choice because of many good properties they offer. However, they do have certain drawbacks. Since the increasing demand for raw materials, especially indium which suffers from its scarcity of supply, as consequence the price of indium have increased rapidly (from 100 $/kg in 2002 to 600 $/kg in 2012), scientists are currently searching for alternatives to indium tin oxide. Moreover, due to brittleness feature of ITO the current devices are typically built on rigid substrates, such as glass. And the new trend is lean to the development of flexible devices, even wearable electronic devices. ITO is apparently unsuited for such applications. Thus, the next generation of transparent electrode materials listed in table 1.1, such as conducting organic materials, carbon nanotube, graphene and metal nanowire

networks, as well as regular metal grids, have been rapidly developed and investigated. In this section, a summary of those materials will be made.

	Thickness (nm)	**Transparency (%)**	**Sheet resistance (Ω/□)**	**Failure strain (%)**	**Cost**
ITO	100-200	>90	10-25	1.4	120 $/m^2
PEDOT:PSS	15-33	80-88	65-176	3-5	2.3 $/ml
Silver NWs	~ 160	92	100	~ 1.2	40 $/m^2
CNT	7	90	500	~ 11	35 $/m^2
Graphene	0.34	90	~ 35	~ 7	45 $/m^2

Table 1.1: Properties of different materials for transparent conducting electrodes [69]

3.1. Transparent conducting oxide

Glass fibers are electrical insulators, but they are almost lossless light conductors. Whereas, depending on dopant, silicon and semiconductors can be electrical conductors, but they are generally optical resistor. Transparent conducting oxides (TCOs) can be tuned from insulating via semiconducting to conducting as well as their transparency adjusted. They can be produced as n-type and p-type conductors. In transparent conducting oxides, the nonmetal part, B, consists of oxygen, while by combining with different metals, A, they lead to semiconductors, A_yB_z, with different opto-electrical characteristics which can be changed by doping, like A_yB_z:D (D=dopant, like metals, metalloids or nonmetals). [70] Up to this time, for TCOs compounds, tin-, indium- and zinc oxides, which means A can be tin, indium and zinc, have provided outstanding good optical characteristics, hence, those compounds have been

largely developed and studied. The well known examples are indium tin oxide (ITO) and the zinc oxide doped with aluminum (ZnO:Al). [70]

3.1.1 Indium Tin oxide (ITO)

Indium tin oxide (ITO) is a solid solution of 90 %wt indium oxide (In_2O_3) and 10 %wt tin oxide (SnO_2). ITO is the most widely used transparent conductive oxide materials not only because of its excellent properties both in electrical conductivity and optical transparency, but also its production techniques are very mature after its development for about half a century. [72] Several methods can be used to deposit the yellowish colored ITO bulk materials onto desired substrate to form transparent and colorless thin film, such as ion assisted plasma evaporation, low temperature electron beam evaporation, radio frequency magnetron sputtering, and thermal evaporation or pulsed laser deposition. [72-76]

ITO has some drawbacks associated with its properties and economic issues. ITO is a ceramic materials, it can crack at relatively low strains of 2-3 %. [75] Furthermore, salts or acids present in the environment can cause corrosion of ITO layer, thus the application range of ITO are limited. [76] And another important threat is coming from its high cost due to materials supply and deposition process. In ITO, nearly 75 %wt of elements are indium, and indium is a rare metal. All of those disadvantages lead scientist and engineers to find new materials for its replacement.

3.1.2 Aluminum Doped Zinc Oxide

As transparent conducting thin film material, aluminum doped zinc oxide thin film contains different dopants and can be produced by different techniques, such as electron deposition, plasma enhanced chemical vapor deposition, atomic layer deposition etc. Normally, pure zinc

oxides are with aluminum, it can also be doped with other metals such as Cu, Ag, Cd, Sn etc. Those dopants can change properties of produced zinc oxide. The substrate also have an influence on the grown structure of zinc oxide, thus the opto-electronic properties of the thin film can be changed.[70] With its properties, beside transparent electrodes, zinc oxide can also be used as varistors, piezoelectric devices and transparent oxide thin film transistors.

3.2 Conducting polymer

Polymers are typically used in electrical and electronic applications as insulators because of their high resistivity. However, there are several semiconducting polymers that have been developed so far, including conjugated conducting polymers, charge transfer polymers, ionically conducting polymers and conductively filled polymers. Each polymer has already found widespread use in many applications, mainly optical and electronic applications, such as batteries, displays, solar energy conversion and optical signal processing etc…

In this section, we will focus on electrically conducting polymers. Polyacetylene was the first reported polymer to demonstrate high conductivity with addition of p or n-dopants.[77] In the 1980s, scientists found electrical conductivities in some commonly used polymers, such as polyprrole, polythiophene and polyaniline etc, via chemical doping. Among those polymers, two main polymers, polythiophene and polyaniline, gain much attention both in fundamental and application level due to the ease of manipulation and their stabilities after dopant. The most commonly used polythiophene materials, PEDOT stabilized by polystyrenesulfonic acid (PSS), has received the largest technical and application success. PEDOT: PSS can exhibit a resistivity as low as 7×10^{-4} Ω·cm. [78] The conducting polymer's electronic conductivity results from polaron and soliton species formed from the charge doping in the polymer

backbone. The PSS performs two critical roles in that it stabilizes the positive charges as well as adding aqueous solubility to the PEDOT oligomers.

Even though the conductivity of conducting polymer is lower than that of transparent conducting oxides, conducting polymers can still be used in transparent conductive devices, displays and organic light-emitting diodes (OLED). The expectation that electronics will gradually move towards flexible formats requires non-brittle transparent conductors. The non-brittle nature of polymer films can minimize defect generation during fabrication process. Conducting polymers are often used as a thin coating over ITO in many devices for enhanced charge injection. And conducting polymers can be used in flexible transparent electrodes, but for widespread application of conducting polymer there is still one important issue to be overcome, its stability. The properties of conducting polymer electrodes can degrade with exposing the materials to high temperature, humidity and UV light. [79]

3.3 Metal thin film and nanogrids

Metals possess a very high conductivity at room-temperature; however, ultrathin metal films demonstrate poor sheet conductance due to electron scattering from the surface and grain boundaries. Over last decades, several metal based nanostructures have been developed for achieving high performance in optical transparency and sheet resistance. Like many other materials, metals become more transparent as the thickness decreases down to nanometers ranges, however, their sheet resistivity increase sharply at this thickness. Scientists have succeeded in producing ultrathin continuous metal film with a thickness of less than 10 nm with nickel, which demonstrates sheet resistance between 30-1200 Ω/sq and transmittance between 40-80 %. [80]

To exploit the performances of metal based transparent electrode, one approach is metal nanogrid with periodic metal lines. Because the thickness of the metal lines is much larger than that of metal films, electron scattering due to the substrate and grain boundaries decrease, therefore the conductivity increase. But one consideration should be taken account; the line width of the metal mesh is subwavelength to provide sufficient transparency. [81] Different methods have been developed to enhance the performance of metal based nanostructure, like metal grid and solution-processed silver nanowire network. The transparent conductive film prepared from solution-processed Ag nanowire demonstrates excellent performances with a ρ_s value of 13 Ω/sq and transmittance of 85 %. [82] In an effort to decrease cost, solution processed copper nanowire and nanofibre have been studied, which show good performances in terms of transmittance and sheet resistance, ~20 Ω/sq with transmittance of 60 % for copper nanowires and 200 Ω/sq with transmittance of ~96 % for copper nanofibre. [83, 84] Metal nanostructure-based transparent electrodes exhibit good performance in terms of optical transparency, electrical conductance and relatively good flexibility; they can fin applications in many optoelectronic devices such as displays, touch screens and solar cells. With its particular performance, the metal based nanostructures are promising candidates for next-generation transparent electrodes. However, to fully integrate these new electrodes into commercial devices, challenges such as long-term environmental stability, contact resistance, uniformity, defects, must be overcome.

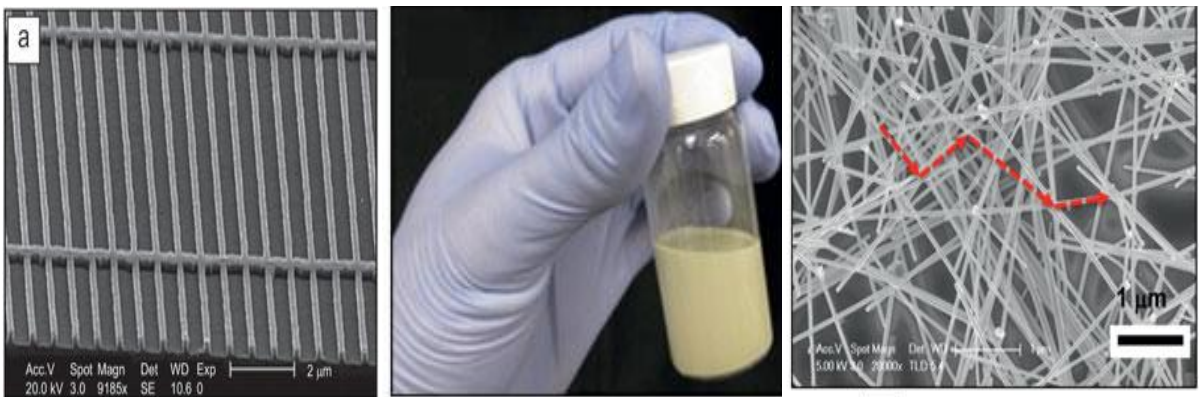

Figure 1.13: (a) Scanning electron microscopy image of an as-fabricated metal electrode, [81] (b) Ag nanowire (NW) ink in ethanol solvent with a concentration of 2.7 mg/mL; (c) Scanning electron microscopy images of an Ag NW mesh on a plastic substrate. The red dashed line indicates the electron transport path. [85]

3.4 Carbon nanotubes

Carbon nanotubes (CNTs), with their cylindrical nanostructure, have shown very exciting properties. They have a high aspect ratio of typically 1000 or greater with a diameter of a few nanometers. It is well known that CNTs have a high elastic modulus of 1-2 TPa. The charge carrier mobilities of individual CNTs can be in excess of 100 000 cm^2/Vs. [86] After extensive studies performed on CNT synthesis, purification and dispersion, CNT can finally be used to produce thin film. Unlike conventional ITO film, CNT films exhibit excellent flexible characteristics, which make CNTs premising materials for producing transparent conducting films.

Many techniques can be used to produce transparent conductive CNT films, including both dry and solution processing methods. In most dry processing methods, a nanotube film is first grown on substrate by CVD method, and then the nanotube film is transferred from the substrate to a flexible substrate. There are a number of reported methods to transfer CVD-grown CNTs. Commonly, a metal layer is deposited on top of the CNTs film and a "transfer substrate" such as PDMS or heat release tape is used to transfer the Metal/SWNT layer from the original to the receiving substrate. [87] Then the metal layer is removed by using chemical etchants, see figure 1.14. Although CVD-grown nanotubes generally yield better electrical performance, the CNTs film fabrication processing is relatively complicated. Thus, solution based methods are preferred because of their simplicity and compatibility with existing coating processes. The production of transparent conductive film with CNTs includes

generally three steps: (i) CNTs treatment; (ii) CNT-solution preparation, and (iii) film preparation.

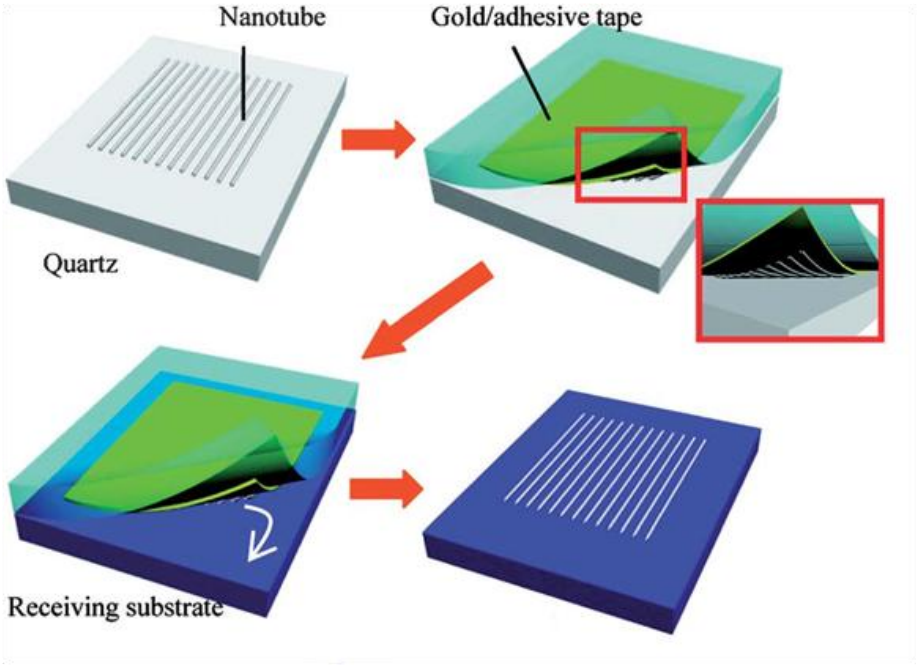

Figure 1.14: Schematic diagram of CVD-grown SWNT film transfer from quartz substrate to glass or PET substrate. [87]

In 2004, Wu et al. found that the CNTs were capable of forming robust random network in a transparent film and provide low sheet resistance and high transmittance with a few of CNTs. [88] They used filtration method to filter surfactant-based suspension of purified nanotube onto a filtration membrane. After washing away the surfactant, the film can be transferred onto the desired substrate by dissolving the filtration membrane in solvent. The as-prapered SWNT film with thickness of 50 nm displays a sheet resistant of 30 Ω/sq and transmittance of 70 %.

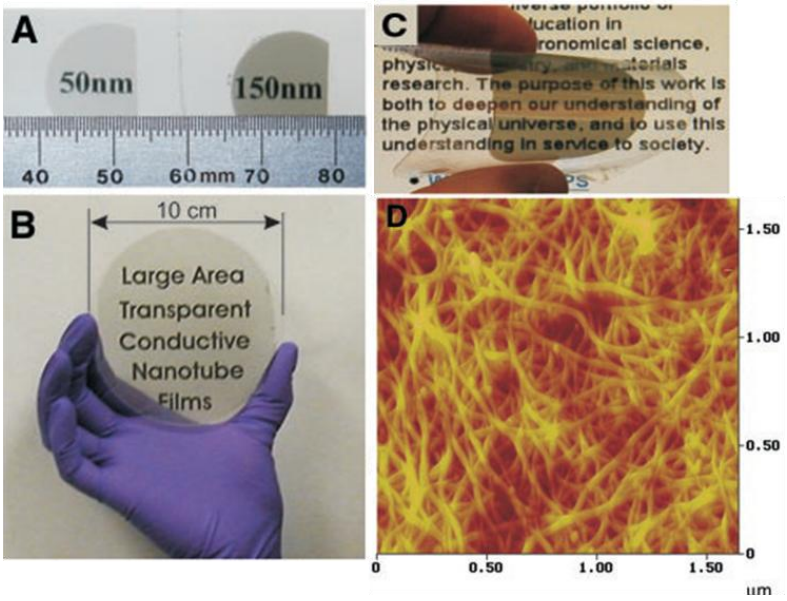

Figure 1.15: Transparent single wall carbon nanotube films. (A) Films of the indicated thickness on quartz substrates. (B) A large, 80nm thick film on a sapphire substrate 10cm in diameter. (C) Flexed film on a Mylar sheet. (D) AFM image of a 150-nm-thick SWNT film surface (color scale: black to bright yellow, 30 nm). [88]

In addition to vacuum filtration, there other simple deposition techniques which are useful for CNTs transparent film production. From well dispersed CNT solutions, transparent conductive CNTs film can be produced by spray coating, [89] spin coating, [90] dip coating, [91] and draw-downs using a Mayer rod coating bar. [92] Spray coating consists in spraying CNT solutions onto the surface of a heated substrate. For spray method, heating the substrate is important so that the sprayed droplets dry immediately when they reach the substrate surface, thus avoiding the "coffee ring" effect which effects homogeneity of film. Mayer bar coating is one of the most popular coating techniques in paint industry. The Mayer rod is a stainless steel rod that is wound tightly with stainless steel wire of varying diameter. The rod is used to remove the excess coating solution and control the coating weight. The coating thickness is controlled by the diameter of the wire used to wind the rod. By controlling the solution concentration and quantity of CNTs solution used, the film density can be easily controlled.

Another advantage of these methods is that after formation of large-area continuous CNTs film, conventional photolithography and reactive ion etching can be applied to remove the unwanted SWNTs materials on the surface, which enable the produced transparent electrode to satisfy the end application that requires some patterning in the transparent conducting film.

Beside those methods, CNT ink can be deposed onto large area of plastic substrate by roll to roll coating. This technique can coat film of 2 m wide with a speed of 500 m/min. [94] The ink printing methods can obviously increase throughput of large-area CNTs films, and with this lithographic technique, one can also avoid the wasting of material, then reduce the production cost. In this regard, several groups have studied ink-jet/aerosol printing method to make SWNT film for application in flexible electronics.[95] Kordas et al. reported large-area CNTs film printed on paper and on flexible polymer substrates by using a commercially available ink-jet printer. [96]

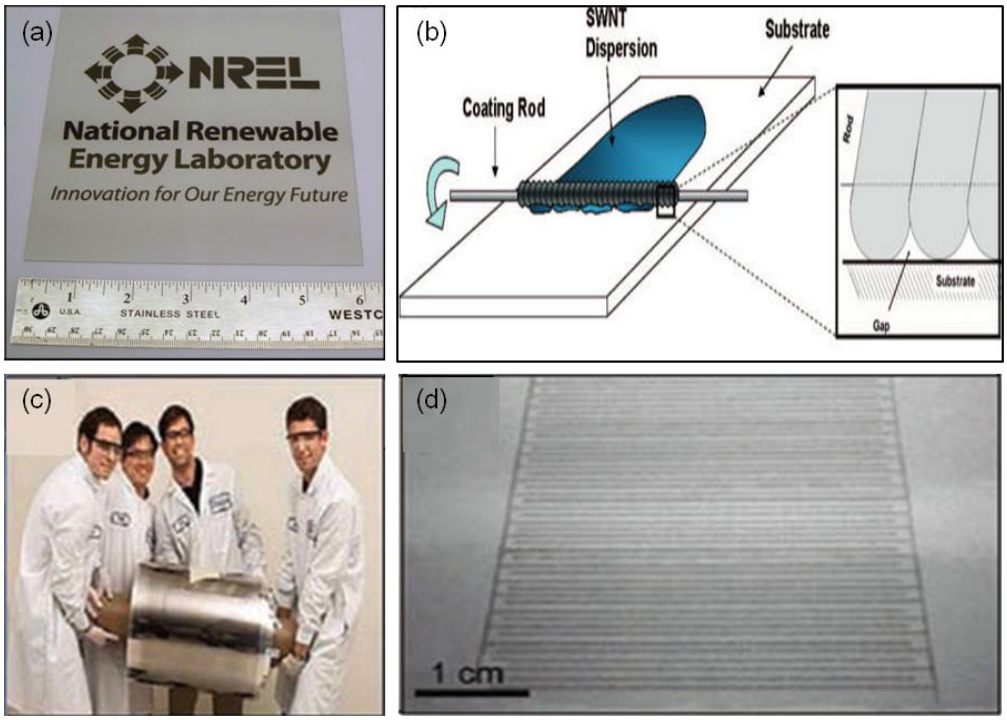

Figure 1.16: a) CNT film spray coated onto large area plastic substrate. [89] b) Mayer rod coating [92].c) roll-to-roll technique printed CNTs film. d) Inkjet printed CNT lines. [93]

For CNTs film, its conductivity is the most important factor. And this property of CNT transparent film is limited by the large junction resistance between nanotubes. The magnitude of this inter-tube resistance is typically on the order of 200 KΩ~20 MΩ, [97] while the resistance along a single tube one micrometer is ~ 6 KΩ/μm. [98] Therefore, in CNTs films the resistance is dominated by the inter-tube resistance. One can conclude that longer CNTs could produce high performance CNTs film, but it will be more difficult to disperse longer CNTs in solvent. Another method to reduce the inter-tube junction is to control the alignment of SWNTs. The alignment of SWNTs is achieved either by the application of an external force such as electric field, liquid flow, centrifugal force, or by self-assembly methods such as convective flow. [99, 100] From current development of emerging transparent conductive materials, CNT, graphene and metal based nanostructures, CNTs are perhaps the most promising and mature technology for application in transparent conductive electrodes.

3.5 Graphene

Graphene is an emerging material being studied both for fundamental science and application. Recent advances in the synthesis and characterization of graphene indicate that it would be suitable for future electronic applications including as a transparent conductor. Graphene can be produced by several methods, but not every method is adequate for producing transparent conductor. Graphene produced from liquid-phase route could be ideal for coating because this would enable the relatively low-cost methods, like spin-coating, and spray coating to be used. Graphene synthesis by chemical vapor deposition are also promising candidates for transparent conductor, especially for large area and high quality demand.

Among all graphene production method, it seems that CVD technique is one of the most promising routes to synthesize near perfect graphene. The decomposition of carbonaceous sources at high temperature and growth on metallic substrates leads to high quality graphene films which are comparable to the pristine graphene exfoliated from HOPG. Once graphene is grown on metal substrates, one can use the method illustrated in figure 1.6 to transfer graphene on flexible substrates. The properties of as-transferred film can be varied from 280 Ω/sq with transmittance of 80 % to 350 Ω/sq with transmittance of 90 %. [101, 102] Researchers have found optimal catalysts and conditions to produce large area monolayer graphene by the CVD method. The recent record is 30 inch graphene producd by CVD on copper substrates, and then graphene was transfered onto PET substrate. This large area graphene films demonstrate outstanding properties with ρ_s ~ 275 Ω/sq for single layer and ~ 40 Ω/sq for four layer graphene films after p-type doping with HNO_3. [51]

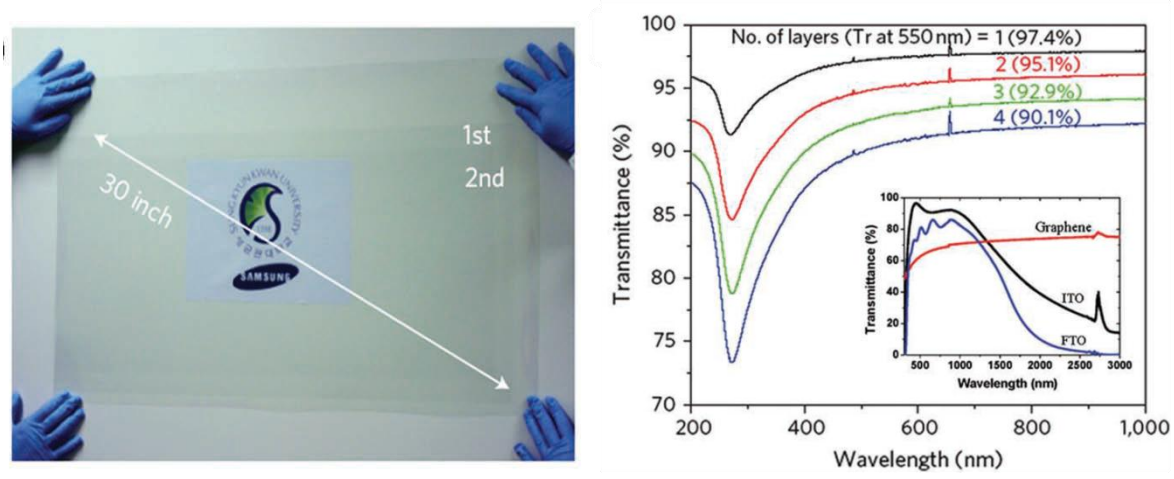

Figure 1.17: (a) A transparent, 35-inch flexible PET sheet supported ultralarge-area graphene film, which was synthesized by chemical vapor deposition (CVD); (b) Ultraviolet–visible (UV–vis) spectra of the CVD graphene films with 1 to 4 layers. The inset in (d) is the comparison of transmittance of a 10 nm thick thermal reduced graphene film (red), ITO (black) and fluorine tin oxide (FTO, blue). [51]

Liquid phase route provide another way to produce graphene films. The sonication and/or surfactant involved exfoliation of graphite in organic solvents has been shown to be efficient and low cost method to produce suspended graphene. Due to the nature of dispersion of exfoliated graphene, vacuum filtration, spray coating, Langmuir-Blodgett (LB) techniques can be used to produce graphene films. By using graphene dispersed in DMF (Dimethylformamide) solvent without surfactant, Novoselov et al. reported spray-coated graphene film with ρ_s ~5 KΩ/sq and transmittance of ~ 90 %. [103] For surfactant stabilized graphene dispersions, small graphene flakes can assemble to form a monolayer graphene film at the water/air interface. By repeating LB cycles, Dai et al. reported graphene film with ρ_s ~8 KΩ/sq and transmittance of 80 %. [104] Compared to spray-coated film, they claimed that the higher resistance of these LB method produced films could be attributed to the small size of the graphene sheets and the presence of surfactant molecules between the graphene flakes. Vacuum filtration can also be applied to produce homogenous films with surfactant stabilized graphene dispersions. In this way, graphene films with ρ_s ~ 4 kΩ/sq and transmittance of ~ 80 % after 500 °C thermal annealing have been obtained. [105] Even though the liquid exfoliation methods can produce graphene in large scale and low cost, the resistance of these films is still quite high when compared to pristine graphene because of the large contact-resistance between the adjacent graphene sheets and the presence of adsorbed solvent molecules and surfactants. [39,103]

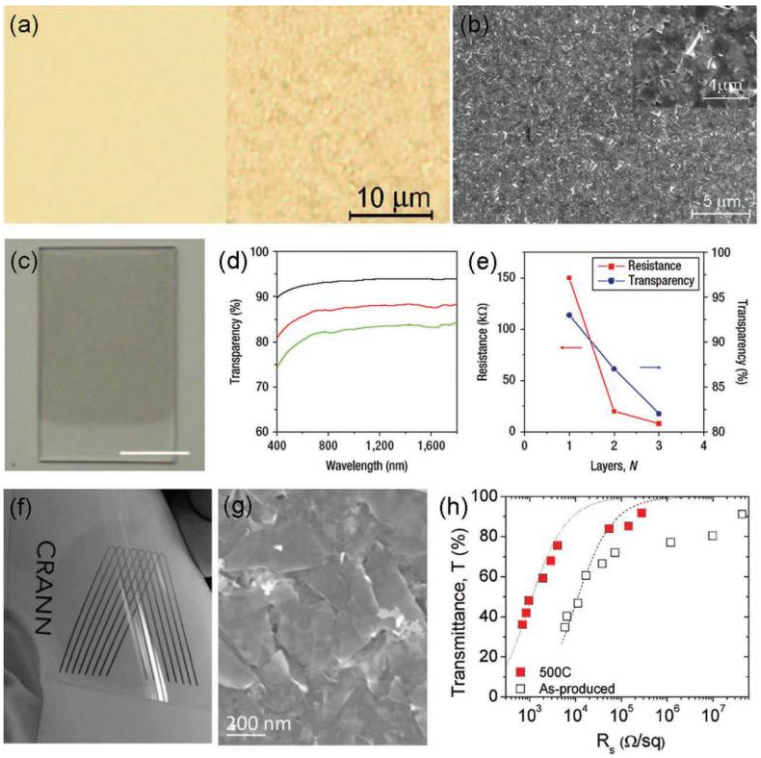

Figure 1.18: (a) Light transmittance through an original glass slide, the right side covered with graphene film. (b) Scanning electron micrograph (SEM) of a thin graphene fi lm obtained by spray-coating from a liquid phase exfoliated graphene dispersion. [103] (c) Photograph of a two- layer graphene film fabricated by the Langmuir-Blodgett (LB) technique from the surfactant stabilized graphene dispersion (scale bar is 10 mm). (d) Transmittances of one-, two-, and three-layer graphene films. (e) Resistance and transparencies of one-, two- and three-layer LB graphene films. [104] (f) Photograph of 6 nm thick graphene film on PET substrate prepared by filtration and transfer process from the surfactant stabilized graphene water dispersion. (g) SEM image of the surface of graphene film. [105] (h) Transmittance plotted as a function of Rs for both as-produced and annealed films. [105]

Reduced graphene oxide (rGO) is another low cost method to produce graphene on a large scale. Due to its low cost and easy solution processing, a great number of studies have been made to improve the electronic properties of rGO. Using well dispersed graphene oxide (GO) and reduced graphene oxide is another way to the production of graphene based transparent conductor. Graphene oxide film can be easily prepared by spray-coating, dip-coating, spin-

coating, vacuum filtering and LB techniques. With oxygen-containing groups presented on graphene oxide flake, the suspended GO flakes can form monolayer on desired substrate by using LB technology. [106] Spin-coating is also a convenient way to produce GO transparent film, and with this method the thickness of the film can be easily adjusted by the spin-coating speed and the concentration of the GO dispersion [107]. The in-plane conductivity in reduced graphene oxide film is much higher than that in the vertical direction because of the large resistance in the junction between two rGO sheets. [108] Therefore, the preparation of ultra-large GO flakes is interesting because of the reduction of inter-junction resistance.

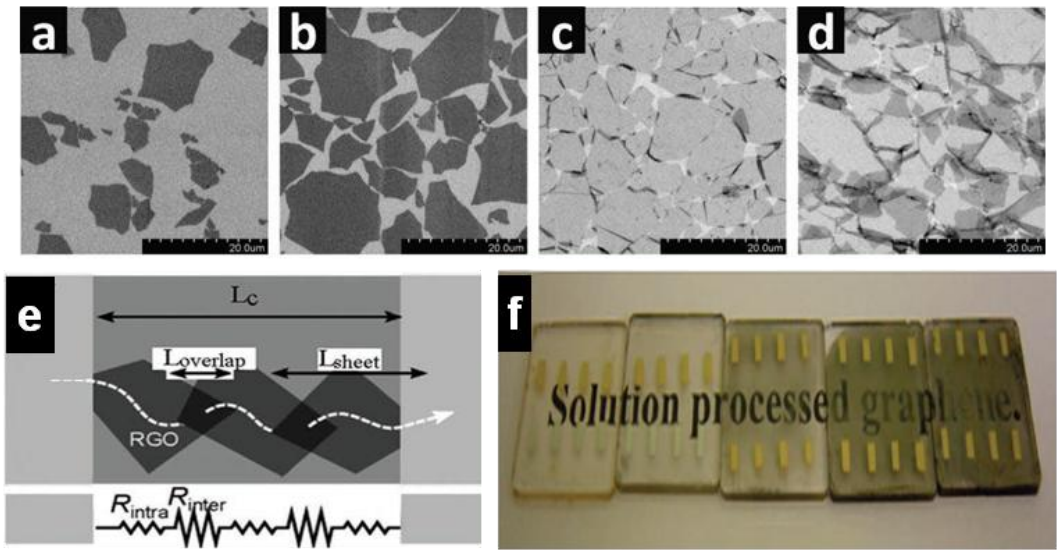

Figure 1.19: (a-d) SEM images showing the collected GO monolayers on a silicon wafer at different regions of the isotherm. Scale bars in (a-d) represent 20 μm. [106] (e) Schematic of the resistance of RGO nanosheets between two electrodes and the corresponding resistor network model (bottom). [108] (f) Photograph of an unreduced (left most) and a series of high temperature reduced GO films prepared by spin coating with increasing thickness. [109]

The oxygen content in insulating GO is as high as ~ 40 wt%, which can strongly disrupt the pristine sp^2 structure. In order to increase the conductivity, the sp^2 structure has to be repaired.

Thermal and chemical reductions have been used to improve the electrical properties of GO films.

Beside the methods mentioned, a method to improve the conductivity of graphite oxide films is to fill the graphene oxide film with conductive filler material. Watcharotone et al. reported a film produced from mixture of silica matrix and GO. Then the film was thermally annealed. The film demonstrates a conductivity of 0.45 S/cm with transmittance of 94 %. [110] Since carbon nanotubes are being actively studied for use of transparent conductors, the films produced with mixture of graphene oxide and carbon nanotube were also reported. [111] Their properties are shown in table 1.2.

Graphene Material	Sheet resistivity	Transmittance	Reference
exf-graphite	5KΩ/sq	90%	[103]
exf-graphite	8KΩ/sq	83%	[104]
exf-graphite	1K-1MΩ/sq	35-90%	[105]
rGO	1.8KΩ/sq	70%	[112]
rGO	1 KΩ/sq	80%	[113]
rGO	5 KΩ/sq	80%	[114]
rGO	11 KΩ/sq	96%	[115]
rGO	70 KΩ/sq	65%	[116]
rGO-silica	0.45S cm^{-1}	94%	[110]

rGO-CNT	240Ω/sq	85%	[111]
rGO-CNT	151KΩ/sq	93%	[117]

Table 1.2: Resistivity and transmittance for graphene film.

Graphene-based transparent conductors are listed in table 1.2. From these results, for solution processed graphene, the graphene-CNTs hybrid seems to be the most promising way for producting transparent conductive film. This method is relatively low-cost and scalable, and prepared films can be deposed on flexible substrate.

4. Conclusion

Graphene, a one atom thick layer of carbon material, is the basal plane of graphite. It is mechanically stable, optically transparent, chemically inert and an excellent electrical and thermal conductor. These properties make graphene a promising candidate for various applications, like transparent conductor, electrodes with high surface area and very low electrical resistance for energy device, transistors operating at higher frequency, composite, chemical sensors etc.

The production of graphene is essential for its applications. Currently, there are several methods being developed and used to prepare graphene of different shapes and quality. For example liquid phase methods can produce scalable and low-cost graphene with lateral dimension of micrometer and nanometer, CVD method can produce large area and high quality graphene films. But it's worth to notice that each kind of produced graphene corresponds to different applications. Graphene or reduced graphene oxide flakes, which contain more defects, can be exploited for composite materials, conductive paints etc. High quality graphene can be used for high-performance electronic devices. The application depends very much on the quality of the material which is determined by the production method.

Transparent electrodes are one necessary component in many modern electronic devices, such as touch screens, LCD, solar cells etc. ITO is still dominant in the transparent electrodes market. Since the market of transparent electrodes is rapidly growing and scarcity of indium, there is need to find a replacement for ITO. Currently, several materials have been developed for application in transparent electrodes, like CNTs, metal-base nanomaterials. Up to now there have been a great number of reports which suggest that graphene is indeed a promising transparent conductor. Novel graphene-based transparent electrodes on flexible substrates for

organic electronics show excellent flexibility. Depending on applications, the industry requires different kinds of transparent electrodes, which means that graphenes with different performances can be used in different kinds of electronic devices. Although the liquid-phase produced graphene films have significantly lower conductivity than that of CVD graphene, it still works in certain applications, like OFET (organic field-effect transistor) and LCDs. The availability and esay processbility of graphene on substrates or on liquid phase have already shown to be premising as transparent electrodes in organic electronics. There will be many improvements in this direction in the near future. Carbon is once more paving the way toward new advanced materials, this time towards light, flexible, resilient and efficient directions.

References

[1] AL. Lavoisier. Traité élémentaire de chimie. Paris; 1789.

[2] K.S. Novoselov, A.K. Geim, S.V. Morozov, D.Jiang, M.I.Katsnelson, I.V. Grigorieva, S.V.Dubonos and A.A.Firsov. Two-dimensional gas of massless Dirac fermions in graphene. Nature. 2005, 438, 197.

[3] C. Berger, Z. Song, T. Li, X. Li, A. Y. Ogbazghi, R. Feng, Z. Dai, A. N. Marchenkov, E.H. Conrad, P. N. First, W. A. de Heer. Ultrathin Epitaxial Graphite : 2D Electron Gas Properties and a Route toward graphene based nanoelectronics. J. Phys. Chem. B. 2004 (108), 19912–19916.

[4] B.T. Kelly. Physic of graphite. London: Applied Science Publishers; 1981

[5]G.M. Rutter, S. Jung, N.N. Klimov, D.B. Newell, N.B. Zhitenev, J.A. Stroscio. Microscopic polarization in bilayer graphene. Nature Physics, 2011, 7, 649

[6] E. McCann, Physical Review B.2006, 74, 161403.

[7] T.Ohta, A. Bostwick, T. Seyller, K. Horn, and E. Rotenberg, Science. 2006, 313, 951.

[8] E.Pallecchi, F.Lafont, V.Cavaliere, F.Schopfter, D.Maily, W.Poirer, A.Ouerghi. Higer Electron Mobility in epitaxial graphene on 4H-SiC (0001) via post-growth annealing under hydrogen. Scientific Reports, 2014, 4, Doi:10.1038/srep04558

[9] K.I. Bolotin, K.J. Sikes, Z. Jiang, M. Klima, G. Fudenberg, J. Hone. Ultrahigh electron mobility in suspended graphene. Solid. State. Commun. 2008,146, 351.

[10] K.I. Bolotin, K.J. Sikes, J. Hone, H.L. Stormer, P. Kim. Temperaturedependent transport in suspended graphene. Phys. Rev. Lett. 2008,101, 096802.

[11] X. Du, I. Skachko, A. Barker, E.Y. Andrei. Approaching ballistic transport in suspended graphene. Nature Nanotechnol 2008, 3, 491.

[12] M. Bruna, A. Vaira, A. Battiato, E. Vittone, S. Borini. Graphene strain tuning by control of the substrate surface chemistry. Appl. Phys. Lett. 97, 021911, 2010.

[13] K.S. Kim, Y. Zhao, H. Jang, S.Y. Lee, J.M. Kim, J.H. Ahn. Large-scale pattern growth of graphene films for stretchable transparent electrodes. Nature 2009, 457, 706.

[14] R. R. Nair, P. Blake, A. N. Grigorenko, K. S. Novoselov, T. J. Booth, T. Stauber, N. M. R. Peres, A. K. Geim. Fine Structure Constant Defines Visual Transparency of Graphene . Science 2008, 320, 1308

[15] A. B. Kuzmenko , E. van Heumen , F. Carbone , D. Van Der Marel. Universal Optical Conductance of Graphite. Phys. Rev. Lett. 2008, 100, 117401

[16] J. Suk, A.Kitt, C. Magnuson, Y. Hao, S. Ahmed, J. An, A. Swan, B. B. Goldberg, and R. S. Ruoff. Transfer of CVD-Grown Monolayer Graphene onto Arbitrary Substrates. ACS. Nano. 2011, 59, 6916.

[17] C. Lee, X. Wei, J.W. Kysar, J. Hone. Measurement of the elastic properties and intrinsic strength of monolayer graphene. Science 2008, 321, 385.

[18] C. Gomez-Navarro, M. Burghard, K. Kern. Elastic properties of chemically derived single graphene sheets. Nano Letters, 2008, 8, 2045.

[19] V. Adamyan, V. Zavalniuk, Journal of Physics-Condensed Matter. 2011, 23, 015402.

[20] A. A. Balandin, S. Ghosh, W. Bao, I. Calizo, D. Tewelde-brhan, F. Miao, C. N. Lau. Nano Letters. 2008, 8, 902.

[21] Y.Zhu, S.Murali , W.Cai , X.Li , J. Suk , J.R. Potts , and R.S. Ruoff. Graphene and graphene oxide: synthesis, properties and applications. Adv. Mater. 2010.

[21] C. N. R. Rao, A. K. Sood, R.Voggu, and K. S. Subrahmanyam. Some Novel Attributes of Graphene . J. Phys. Chem. Lett. 2010, 1, 572.

[23] Q. Wu, Y. Wu, Y. Hao, J. Geng, M. Charlton, S. Chen, Y. Ren, H. Ji, H. Li, D.W. Boukhvalov, R.D. Piner, C.W. Bielawski, R.S. Ruoff . Selective surface functionalization at regions of high local curvature in graphene. Chem. Commun., 2013,49, 677-679.

[24] X. Lu, M. Yu, H. Huang, R.S. Ruoff. Tailoring graphite with the goal of achieving single sheets. Nanotechnology, 1999, 10, 269.

[25] A. K. Geim. Graphene: Status and Prospects. Science. 2009, 324, 1530;

[26] P. Neugebauer, M. Orlita, C. Faugeras, A.-L. Barra, M. Potemski. How Perfect Can Graphene Be? Phys. Rev. Lett. 2009,103, 136403.

[27] A.Shukla, Rakesh Kumar, J.Mazher, A. Balan. Graphene made easy: High quality, large-area samples. Solid. State. Communications. 2009, 149, 718.

[28] M. Lenner, A. Kaplan, Ch. Huchon, R. E. Palmer. Ultrafast laser ablation of graphite. Phys. Rev. 2009, 79, 184105.

[29] M. S. Dresselhaus and G. Dresselhaus. Adv. Phys. 2002, 51, 1.

[30] C. Vallés, C. Drummond, H. Saadaoui, C. A. Furtado, M. He, O. Roubeau, L. Ortolani, M. Monthioux, A. Pénicaud, J. Am. Chem. Soc., 2008, 130, 15802.

[31] A. Catheline, C. Vallés, C. Drummond, L. Ortolani, V. Morandi, M. Marcaccio, M. Iurlo, F. Paolucci, A. Pénicaud, Chem. Commun., 2011, 47, 5470.

[32] A. Catheline, L. Ortolani, V. Morandi, M. Melle-Franco, C. Drummond, C. Zakri, A. Pénicaud, Soft Matter 2012, 8, 7882–7887.

[33] Alain Pénicaud, Carlos Drummond. Deconstructing Graphite: Graphenide solutions. Acc. Chem. Res., 2013, 46, 129.

[34] E.M. Milner, N.T.Skipper, C.A. Howard, M.S.P.Shaffer, D.J.Buckley, K.A. Rahnejat, R.J.Cullen, R.K.Heenan, P.Lindner, R.Schweins. Structure and morphology of charged graphene platelets in solution by Small-Angle Neutron Scattering. J. Am. Chem. Soc. 2012, 134, 8302−8305.

[35] J.M.Englert, C.Dotzer, G.Yang, M.Schmid, C.Papp, J.M. Gottfried, H.P. Steinruck, E.Spiecker, F.Hauke, A.Hirsch. Covalent bulk functionalization of graphene. Nature Chem. 2011, 3, 279-286.

[36] X. L. Li , G. Y. Zhang , X. D. Bai , X. M. Sun , X. R. Wang , E. Wang , H. J. Dai , Highly conducting graphene sheets and Langmuir-Blodgett films. Nat. Nanotechnol. 2008, 3, 538-942.

[37] C. Shih, A. Vijayaraghavan, R. Krishnan, R. Sharma, J. Han, M. Ham, Z. Jin, S. Lin, G.L.C. Paulus, N. F. Reuel, Q.Wang, D. Blankschtein, M.S. Strano. Bi- and trilayer graphene solution. Nature Nanotech. 2011, 6, 439-445.

[38] Jacob Israelachvili, Intermolecular and surface force. Boston: Academic Press third edition (2011).

[39] Y. Hernandez, V. Nicolosi, M. Lotya, F.M. Blighe, Z. Sun, S. De, I.T. McGovern, B. Holland, M. Byrne, Y. K. GunKo, J. Boland, P. Niraj, G. Duesberg, S. Krishnamurthy, R. Goodhue, J. Hutchison, V.Scardaci, A.C. Ferrari, J.N. Coleman. Nature Nanotechnology, 2008, 3, 563.

[40] W.S. Hummers, R.E. Offeman. J Am Chem Soc, 1958, 80, 1339.

[41] C. Su, Y. Xu,W. Zhang, J. Zhao, X. Tang,C. Tsai, L. Li. Electrical and spectroscopic characterizations of ultra-large Reduced Graphene Oxide Monolayers. Chem. Mater. 2009, 21, 5674.

[42] H.A. Becerril, J. Mao, Z. Liu, R.M. Stoltenberg, Z. Bao, Y. Chen. Evaluation of Solution-Processed Reduced Graphene Oxide Films as Transparent Conductors. ACS Nano. 2008, 2, 463.

[43] C. Gomez-Navarro, R. Thomas Weitz, A. M. Bittner, M. Scolari, A. Mews, M. Burghard, K. Kern. Electronic Transport Properties of Individual Chemically Reduced Graphene Oxide Sheets. Nano Lett. 2007, 7, 3499

[44] Y. Si, E.T. Samulski. Synthesis of water soluble graphene. Nano Lett. 2008, 8, 1679.

[45] R. Trusovasa, K. Ratautasa, G. Račiukaitisa, J. Barkauskasb, I. Stankevičienėb, G. Niaurac, R. Mažeikienėc. Reduction of graphite oxide to graphene with laser irradiation. Carbon. 2013, 52, 574.

[46] J.T. Robinson, M. Zalalutdinov, J.W. Baldwin, E. S. Snow, Z. Wei, P.Sheehan, B.H. Houston. Wafer-scale Reduced Graphene Oxide Films for Nanomechanical Devices. Nano Lett. 2008, 8, 3441.

[47] V.A. Davis et al. True solutions of single-walled carbon nanotubes for assembly into macroscopic materials. Nature Nanotech. 2009, 4, 830.

[48] N. Behabtu, J.R. Lomeda, M.J.Green, A.L. Higginbotham, A.Sinitskii, D.V.Kosynkin, D. Tsentalovich, A.N.G.Parra-Vasquez, J.Schmidt, E.Kesselman, Y.Cohen, Y.Talmon, J.M. Tour, M.Pasquali. Nature Nanotech. 2010, 5, 406.

[49] X. Li, C.W. Magnuson, A.Venugopal, J. An, J.W. Suk, B. Han, M. Borysiak , W. Cai, A.Velamakanni, Y.Zhu, L.Fu, E.M. Vogel, E.Voelkl, L. Colombo , R.S. Ruoff . Graphene Films with Large Domain Size by a Two-Step Chemical Vapor Deposition Process. Nano Lett., 2010, 10, 4328.

[50] X. Li, C.W. Magnuson, A.Venugopal, R.M. Tromp, J.B. Hannon, E.M. Vogel, L. Colombo, and R.S. Ruoff. Large-Area Graphene Single Crystals Grown by Low-Pressure Chemical Vapor Deposition of Methane on Copper. J. Am. Chem. Soc., 2011, 9, 2816.

[51] S. Bae, H. Kim,Y. Lee, X. Xu, J. Park, Y. Zheng, J. Balakrishnan, T. Lei, H. Kim,Y.Song, Y. Kim, K.S. Kim, B. Özyilmaz, J. Ahn, B. Hong, S. Iijima. Roll-to-roll production of 30-inch graphene films for transparent electrodes. Nature Nanotech, 2010, 4, 574.

[52] W.Regan, N.Alem, B. Alemán, B. Geng, Ç. Girit, L. Maserati, F.Wang, M. Crommie, A. Zettl. A direct transfer of layer-area graphene. Appl. Phys. Lett. 2010, 96, 113102.

[53] Y.Zhang, L.Zhang, C.Zhou. Acc. Chem. Res., 2013, 46, 2329-2339.

[54] K.V. Emtsev, A.Bostwick, K. Horn, J.Jobst, G. L. Kellogg, L. Ley, J. L. McChesney, T. Ohta, S. A. Reshanov, J. Röhrl, E.Rotenberg, A. K. Schmid, D. Waldmann, H.B.Weber and T.Seyller. Towards wafer-size graphene layers by atmospheric pressure graphitization of silicon carbide.

[55] W.A. de Heer, C. Berger, M. Ruan, M. Sprinkle, X.Li , Y. Hu, B. Zhang, J. Hankinson, and E. Conrad. Large area and structured epitaxial graphene produced by confinement controlled sublimation of silicon carbide. PNAS 2011, 41, 16900.

[56] J. Hass, J. E. Millán-Otoya, P. N. First, and E. H. Conrad. Interface structure of epitaxial graphene grown on 4H-SiC(0001). Phys. Rev. B 78, 2008, 205424

[57] L. Zhi and K. Müllen. A bottom-up approach from molecular nanographenes to unconventional carbon materials. J. Mater. Chem., 2008, 18, 1472.

[58] L.Dössel, L.Gherghel, X. Feng, K. Müllen. Graphene Nanoribbons by Chemists: Nanometer-Sized, Soluble and Defect-Free. Angewandte Chemie int Ed., 2011, 50, 2540.

[59] A.W. Moore, in: P.L. Walker, P.A. Thrower (Eds.), Chemistry and Physics of Carbon, Marcel Dekker Inc., New York, 1981, 17, 233.

[60] F.Rouquerol, J.Rouquerol, and K. Sing. Adsorption by Powders and Porous Solids. Academic Press, London, 1999.

[61] N. Emery, C. Hérold, J.-F, Marêché, P. Lagrange, Synthesis and superconducting properties of CaC_6. Sci. Technol. Adv. Mater. 2008, 9, 044102.

[62] P. Schaffäutl, J. Prakt. Chem.1841, 21, 155.

[63] Toshiaki Enoki, Masatsugu Suzuki, Morinobu Endo. Graphite Intercalation Compounds and Application. Oxyford University Press, 2003.

[64] W. Rüdoff and E. Schulze. Über Alkaligraphitverbindungen. Z. anorg. Chem. 1954, 277, 156.

[65] D. E. Nixon and G. S. Parry. Formation and structure of the potassium graphites. Brit. J. Appl. Phys. (J. Phys. D.), 1968, 1, 291.

[66] R. Nishitani, Y. Uno, and H. Suematsu. In situ observation of staging inpotassium graphite intercalation compounds. Phys. Rev. B, 1983, 27, 6572.

[67] A. W. Moore. Chemistry and Physics of Carbon, 1973, Vol. 11, edited by P. L. Walker and P. A. Thrower (New York: Dekker)

[68] J.G. Hooley. Carbon. 1972, 10, 155.

[69] Y. Lee, J. Ahn. Graphene-based transparent conductive films.NANO 2013, 08, 1330001.

[70] K.Ellmer, A.Klein, B.Rech. Transparent Conductive Zinc Oxide-Basics and Applications in Thin Film Solar Cells. Springer Series in Materials Science, Vol. 104

[71] D.S. Hecht, L. Hu and G. Irvin. Emerging Transparent Electrodes Based on Thin Films of Carbon Nanotubes, Graphene, and Metallic Nanostructures. Adv. Mater. 2011, 23, 1482.

[72]S. Laux, N. Kaiser, A. Zöller, R. Götzelmann, H. Lauth, H. Bernitzki. Room-temperature deposition of indium tin oxide thin films with plasma ion-assisted evaporation. Thin Solid Films. 1998, 335, 1.

[73] L.J. Meng, M.P. Santos. Properties of indium tin oxide films prepared by RF reactive magnetron sputtering at different substrate temperature. Thin Solid Films 1998, 322, 56.

[74] H. Kim, A. Piqué, J.S. Horwitz, H. Mattoussi, H. Murata, Z.H. Kafafi, D.B. Chrisey. Indium tin oxide thin films for organic light-emitting devices. Appl. Phys. Lett. 1999, 74, 3444.

[75] D. R. Cairns , R. P. Witte , D. K. Sparacin , S. M. Sachsman , D. C. Paine , G. P. Crawford , R. R. Newton. Strain-dependent electrical resistance of tin-doped indium oxide on polymer substrates. Appl. Phys. Lett. 2000, 76, 1425.

[76] K. A. Sierros , N. J. Morris , K. Ramji , D. R. Cairns. Stress–corrosion cracking of indium tin oxide coated polyethylene terephthalate for flexible optoelectronic devices. Thin Solid Films 2009, 517, 2590.

[77] J.C.W. Chien, J.C.W. Polyacetylene, Chemistry, Physics, and Material Science, 1984, Academic Press, London.

[78] Y. H. Kim, et al. Highly conductive PEDOT: PSS electrode with optimized solvent and thermal post-treatment for ITO-free organic solar cells. Adv. Func. Mater. 2011, 21, 1076.

[79] A. M. Nardes, M. Kemerink, M. M. de Kok , E. Vinken , K. Maturova , R. A. J. Janssen , Conductivity, work function, and environmental stability of PEDOT:PSS thin films treated with sorbitol. Org. Electron. 2008, 9, 727.

[80] D. S. Ghosh , L. Martinez , S. Giurgola , P. Vergani , V. Pruneri , widely transparent electrodes based on ultrathin metals . Optics. Lett. 2009, 34, 325

[81] M.G. Kang , H.J. Park , S.H. Ahn , T. Xu , L.J. Guo , Toward Low-Cost, High-Efficiency, and Scalable Organic Solar Cells with Transparent Metal Electrode and Improved Domain Morphology. IEEE J. Sel. Top. Quantum Electron . 2010, 16, 1807.

[82] S. De, T.M. Higgins, P.E. Lyons, E.M. Doherty, P.N. Nirmalraj, W.J. Blau, J.J. Boland, J.N. Coleman. Silver Nanowire Networks as Flexible, Transparent, Conducting Films: Extremely High DC to Optical Conductivity Ratios. ACS Nano 2009, 3, 1767.

[83] A.R. Rathmell, S.M. Bergin, Y.L. Hua , Z.Y. Li , B.J. Wiley. The Growth Mechanism of Copper Nanowires and Their Properties in Flexible, Transparent Conducting Films. Adv. Mater. 2010, 22, 3558.

[84] H. Wu, L.B. Hu, M.W. Rowell, D.S. Kong, J.J. Cha, J.R. McDonough, J. Zhu , Y.A. Yang, M.D. McGehee, Y. Cui, Electrospun Metal Nanofiber Webs as High-Performance Transparent Electrode. Nano Lett. 2010, 10, 4242.

[85] J.Y. Lee, S.T. Connor, Y. Cui , P. Peumans. Solution-Processed Metal Nanowire Mesh Transparent Electrodes. Nano Lett . 2008, 8, 689.

[86] T. Durkop, S. A. Getty, E. Cobas, M. S. Fuhrer. Extraordinary mobility in semiconducting carbon nanotubes. Nano Lett. 2004, 4, 35.

[87] F. N. Ishikawa, H.-K. Chang, K. Ryu, P.-C. Chen, A. Badmaev, L. Gomez De Arco, G. Shen and C. Zhou. Transparent Electronics Based on Transfer Printed Aligned Carbon Nanotubes on Rigid and Flexible Substrates. ACS Nano, 2008, 3, 73.

[88] Z. C. Wu, Z. Chen, X. Du, J. M. Logan, J. Sippel, M. Nikolou, K. Kamaras, J. R.Reynolds, D. B. Tanner, A. F. Hebard, A. G. Rinzler. Transparent, conductive carbon nanotube films. Science, 2004, 305, 1273.

[89] R. C. Tenent, T. M. Barnes, J. D. Bergeson, A. J. Ferguson, B. To, L. M. Gedvilas, M. J. Heben, J. L. Blackburn. Ultrasmooth, Large-Area, High-Uniformity, Conductive Transparent Single-Walled-Carbon-Nanotube Films for Photovoltaics Produced by Ultrasonic Spraying. Adv. Mater. 2009, 21, 3210.

[90] S. Manivannan, J. H. Ryu, H. E. Lim, M. Nakamoto, J. Jang , K. C. Park. Properties of surface treated transparent conducting single walled carbon nanotube films. J. Mater. Sci. - Mater. Electron. 2010, 21, 72.

[91] Y. I. Song, C. M. Yang, D. Y. Kim, H. Kanoh, K. Kaneko. Flexible transparent conducting single-wall carbon nanotube film with network bridging method. J. Colloid. Interface Sci. 2008, 318, 365 .

[92] B. Dan, G. C. Irvin, M. Pasquali. Continuous and Scalable Fabrication of Transparent Conducting Carbon Nanotube Films. ACS Nano 2009, 3, 835.

[93] J. W. Song , J. Kim , Y. H. Yoon , B. S. Choi , J. H. Kim , C. S. Han , Nanotechnology 2008 , 19 , 6 .

W. R. Small , M. I. H. Panhuis , Small 2007 , 3 , 1500 .

[94] S.Suzuki. Syntheses and Applications of Carbon Nanotubes and Their Composites. Chaptre 14. InTech. 2013

[95] P. Chen, Y. Fu, R. Aminirad, C. Wang, J. Zhang, K. Wang, K. Galatsis and C. Zhou. Fully Printed Separated Carbon Nanotube Thin Film Transistor Circuits and Its Application in Organic Light Emitting Diode Control. Nano Lett., 2011, 11, 530.

[96] K. Kordas, T. Mustonen, G. T´oth, H. Jantunen, M. Lajunen, C. Soldano, S. Talapatra, S. Kar, R. Vajtai and P. M. Ajayan. Inkjet Printing of Electrically Conductive Patterns of Carbon Nanotubes. Small, 2006, 2, 1021.

[97] M. S. Fuhrer, J. Nygard, L. Shih, M. Forero, Y. G. Yoon, M. S. C. Mazzoni, H. J. Choi, J. Ihm, S. G. Louie, A. Zettl, P. L. McEuen. Crossed nanotubes junctions. Science 2000, 288, 494.

[98] S. D. Li, Z. Yu, C. Rutherglen, P. J. Burke. Electrical Properties of 0.4 cm Long Single-Walled Carbon Nanotubes. Nano Lett. 2004, 4, 2003.

[99] N. Rouhi, D. Jain and P. J. Burke. High-performance semiconducting nanotube inks: progress and prospects. ACS Nano, 2011, 5, 8471.

[100] T. Druzhinina, S. Hoeppener and U. S. Schubert. Strategies for Post-Synthesis Alignment and Immobilization of Carbon Nanotubes. Adv. Mater., 2011, 23, 953–970

[101] K.S. Kim, Y. Zhao, H. Jang, S.Y. Lee, J.M. Kim, J.H. Ahn, et al. Largescale pattern growth of graphene films for stretchable transparent electrodes. Nature 2009,457,706.

[102] X. Li,Y. Zhu,W. Cai, M. Borysiak, B. Han, D. Chen, R. D. Piner, L. Colombo, and R. S. Ruoff. Transfer of Large-Area Graphene Films for high-performance transparent conductive electrodes. Nano letters, 2009, 9, 4359

[103] P. Blake, P. D. Brimicombe, R. R. Nair, T. J. Booth, D. Jiang, F. Schedin , L. A. Ponomarenko, S. V. Morozov, H. F. Gleeson, E. W. Hill, A. K. Geim, K. S. Novoselov, Graphene-Based Liquid Crystal Device. Nano Lett. 2008, 8, 1704.

[104] X. L. Li, G. Y. Zhang, X. D. Bai, X. M. Sun, X. R. Wang, E. Wang, H. J. Dai, Highly conducting graphene sheets and Langmuir-Blodgett films. Nat. Nanotechnol. 2008, 3, 538 .

[105] S. De, P. J. King, M. Lotya, A. O'Neill, E. M. Doherty, Y. Hernandez, G. S. Duesberg, J. N. Coleman. Flexible transparent conducting films of randomly stacked graphene from surfactant-stabilized oxide free graphene dispersions. Small. 2010, 6, 458

[106] L.J.Cote, F.Kim, J.Huang. Langmuir-Blodgett Assembly of graphite oxide single layers. J. Am. Chem. Soc. 2009, 131, 1043.

[107] S. P. Pang, H. N. Tsao, X. L. Feng, K. Mullen, Patterned Graphene Electrodes from solution-processed graphite oxide films for organic field-effect transistors. Adv. Mater. 2009, 21, 3488.

[108] T. Kobayashi, N. Kimura, J. B. Chi, S. Hirata, D. Hobara. Channel Length Dependent Field-Effect Mobility and Carrier Concentration of Reduced Graphene Oxide Thin-Film Transistors. Small, 2010, 6, 1210.

[109] H. A. Becerril, J. Mao, Z. Liu, R. M. Stoltenberg, Z. Bao, Y. Chen. Evaluation of Solution-Processed Reduced Graphene Oxide Films as Transparent Conductors. ACS Nano 2008, 2, 463.

[110] S. Watcharotone, D.A. Dikin, S. Stankovich, R. Piner, I. Jung, G. H. B. Dommett, G. Evmenenko, S. Wu, S. Chen, C. Liu, S. T. Nguyen, R.S.Ruoff. Graphene−Silica Composite Thin Films as Transparent Conductors. Nano Lett. 2007, 7, 1888.

[111] V.C. Tung, L. Chen, M.J. Allen, J.K. Wassei, K. Nelson, R.B. Kaner, Y. Yang. Low-Temperature Solution Processing of Graphene-Carbon Nanotube Hybrid Materials for High-Performance Transparent Conductors. Nano Lett, 2009, 9, 1949.

[112] X. Wang, L. Zhi, K. Mullen. Transparent, Conductive Graphene Electrodes for Dye-Sensitized Solar Cells. Nano Lett, 2008, 8, 323.

[113] S.Biswas, L.T. Drzal. A Novel Approach to Create a Highly Ordered Monolayer Film of Graphene Nanosheets at the Liquid-Liquid Interface. Nano letters, 2009, 9, 167.

[114] J.Wu, H.A. Becerril, Z.Bao, Z.Liu, Y. Chen, P. Peumans. Organic solar cells with solution-processed graphene transparent electrodes. Appl. Phys. Lett., (2008) 92, 263302.

[115] Y.Zhu, W.Cai, R.D. Piner, A.Velamakanni, R.S. Ruoff. Transparent self-assembled films of reduced graphene oxide platelets. Appl. Phys. Lett., 2009, 95, 103104.

[116] G.Eda, Y.Lin, S. Miller, C. Chen, W.Su, M. Chhowalla. Transparent and conducting electrodes for organic electronics from reduced graphene oxide. Appl. Phys. Lett. 2008, 92, 233305.

[117] Y.K. Kim, D. Min. Durable Large-Area Thin Films of Graphene/Carbon Nanotube Double Layers as a Transparent Electrode. Langmuir, 2009, 25, 11302.

Chapter II: Characterization Techniques and Experimental Methods

In chapter I, we presented that graphene have attracted great interests in both fundamental sciences and industrial technologies due to its excellent electronic, mechanical and thermal properties. Only after a few years of study, graphene based materials have shown promising performances for high-performance nanoelectronis, transparent conductive electrodes, composites etc. To pave the way to applications, several production methods which can be scale-up have been developed to synthesize graphene and its derivatives materials such as graphene oxide (GO).

Different production methods can produce graphene materials with different quantities, properties and cost; in consequence, graphene produced from different methods corresponds to different applications. Before applying graphene materials, one key issue is to identify/characterize these thinnest two dimensional nano-materials. Especially for graphene produced by exfoliation methods, both their thickness and lateral dimension are in nano-scale, and the characterization studies of these graphene are therefore complex. Characterization is also crucial for studying the microstructures of graphene such as surface morphology, degree of wrinkles, overlaps, and folds of individual sheets, which heavily affect the properties of graphene. Meanwhile, the characterizations results can provide immediate feedback to improve production and processing methods. In general, there are several common techniques and methods that have been applied to characterize graphene: such as (i) optical microscopy; [1] (ii) AFM (Atomic Force Microscopy); [2] (iii) STM (Scanning Tunneling Microscopy); [3] (iv) TEM (Transmission Electron Microscopy); [4] (v) Raman spectroscopy; [5] (vi) SEM (Scanning Electron Microscopy) [6] etc. Each technique has its advantages and requirements.

In this chapter, we will not give a state-of-the-art concerning all characterization results obtained from graphene materials. Instead, we provide some general aspects about the techniques that we have largely used during our study. Some overview of current characterizations results concerning graphene will also be included in this chapter.

1. Atomic force microscope (AFM)

1.1 Principle of AFM

Unlike the traditional microscopes, such as optical or electron microscopes which rely on electromagnetic radiation, the AFM does not rely on photon or electron beams to create an image. The images obtained from optical and electron microscopes are typically in the plane horizontal to the surface of observed samples. These microscopes do not give information about vertical dimensions of a sample. AFM is a mechanical imaging instrument which can be used to measure three dimensional topography and physical properties of materials with a sharp probe. This sharpened probe is positioned close enough to the sample surface so that it can interact with the force fields associated with these studied surfaces. In AFM, an image of the surface is reconstructed by monitoring the precise motion of the probe as it is scanned over the surface. The probe of an AFM is typically less than 50 nm in diameter and the areas scanned by the probe are less than 100 μm in laterl size.[7] The atomic force microscope (AFM) was invented and introduced by Binning, Quate and Gerber in the mid-1980s. It was based on the scanning tunneling microscope (STM) and took advantage of the existence of strong inter-atomic forces between atoms from specimen surface and the scanning tip.

In AFM, the force between the nanoscopic probe and the surface is measured with a force sensor. The typical force sensor is constructed with light lever in which the laser beam is focused on the backside of a cantilever and reflected into a photo-detector. The interaction between the probe located at the end of cantilever and the sample can bend the cantilever. As a result, light path changes, which can cause the amount of light in the detector to change. The output of the force sensor is then sent to a feedback controller which can control a Z motion generator. The feedback controller uses the output of force sensor to maintain a fixed distance between the probe and surface of the observed sample. X-Y motion generators are applied to

move the probe over the surface in the X and Y direction. The motion of the probe is monitored and used to create an image of the surface.

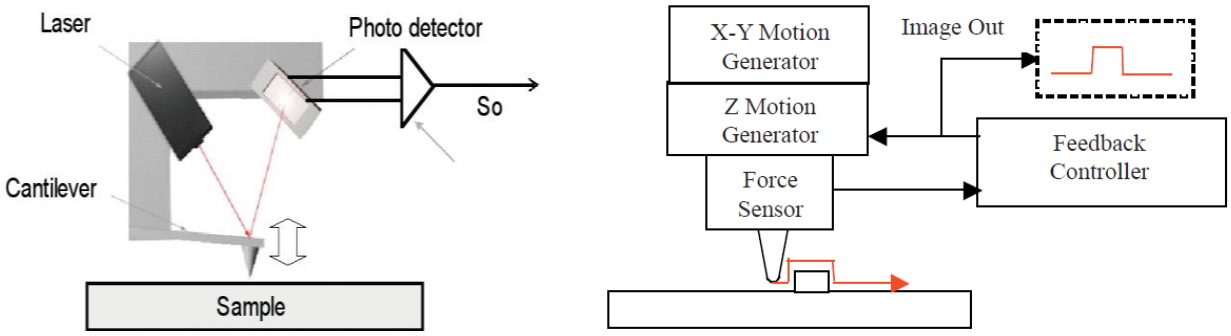

(a) (b)

Figure 2.1: (a) Illustration of cantilever force sensor; (b) Basic block diagram of AFM.

1.1.1 AFM tip

One of the most important parts in AFM is the probing tip, because AFM generates image with the aid of a sensing tool, the tip. The AFM tip is micro-fabricated, as shown in figure 2.2, as a particularly sharp point made of solid material, like Si, SiO_2 or SiC.

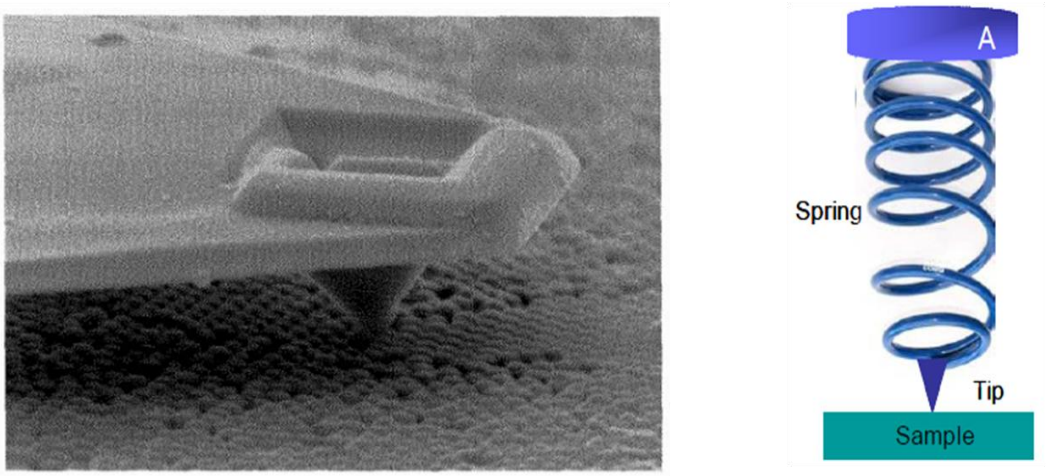

(a) (b)

Figure 2.2: (a). Scanning electron microscope (SEM) image of an AFM tip used to probe the structure of a sample surface; [7] Magnification approximately x 10,000; (b). Spring depiction of cantilever

The tip, which must have good elastic properties in the used range, is installed at the end of a cantilever. The cantilever allows the tip to move up and down in the z-direction. The force constant of the cantilever is suited to respond to the force between the tip and the sample. The resolution of an AFM depends strongly on the shape of the tip.The smaller and sharper the tip the better the AFM image. [8] The deflection of cantilever as a spring can be converted to force, according to Hooke's law：

$$F = - k_z \cdot d \tag{1.1}$$

Where k_z is the force constant of the cantilever (typically ~ 0.1-1 N/m) and d is its displacement. The minus sign indicates the force is opposite to the displacement of tip.

1.2 Modes of AFM

In general, AFM has three operating modes for imaging: the contact mode, semi-contact mode and non-contact mode. In these three modes, the cantilever scans across sample surface, and the topography of a sample is produced by cantilever deflections. As tip approaches the surface, an attractive force (non-contact region) is experienced on the tip due to the long-range atomic potential. The attractive force is exerted on the tip until equilibrium point where the attractive force reaches its maximum. Over this point the repulsive component of the atomic potential starts to be larger than the attractive part. This is the contact region. The region around the minimum is used in the intermittent contact mode (tapping mode).

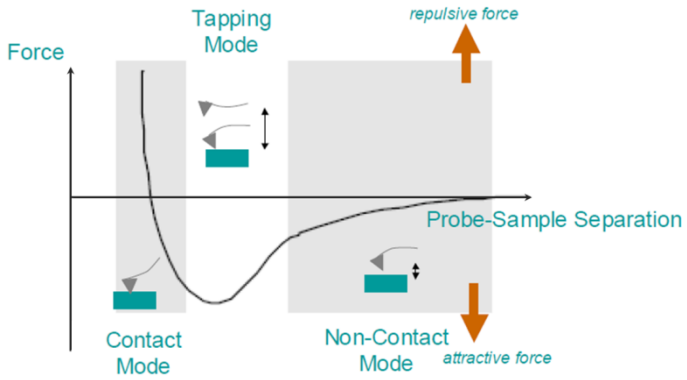

Figure 2.3: Plot of force as function of probe-sample separation

1.2.1 Contact mode

When the studied samples are sufficiently hard, i.e. metal and ceramic materials etc, using the tip in contact mode is appropriate, and the tip is in close contact with the sample surface. For softer samples, this mode may destroy the surface. An advantage of the scanning under contact mode is that it can be executed in air, vacuum and fluid environments.

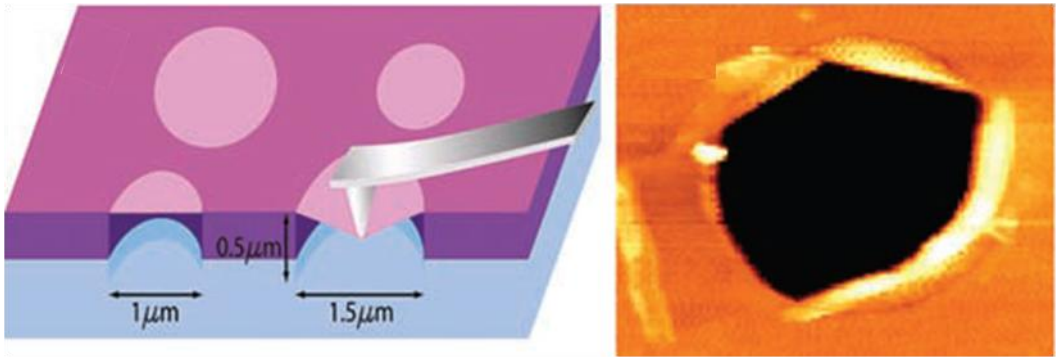

Figure 2.4: Schematic of nano-indentation performed with AFM in contact mode on suspended graphene membrane (left); AFM image of a fractured graphene membrane (right). [9]

In this mode, care must be taken to keep the tip always in close contact. This can be obtained by using an appropriate feedback to maintain the deflection signal at the set point value. The set point value should not be too far from the zero deflection level, for example the tip should not be pressed too much on the surface, because this might result in the destruction of the tip and of the surface. On the other hand, a too small difference between the value of set point

and the zero deflection level could cause instabilities in the tracking system. [7] The contact mode can also be a basis for the operation of other contact techniques, because the contact mode uses the tip deflection, which can be converted into a net force according to Hooks low. The net force is composed of a long range attraction and a short range repulsive interaction between the probe and sample. [7] With an appropriate detection system, lateral forces can be measured. Since the tip is in stable contact with the surface, the scanning motion results in some torsion of the tip in the lateral x-y plane that also reflects the frictional properties of a surface. [8] Indeed, Lee et al. reported elastic properties of free-standing monolayer graphene membranes by nanoindentation, shown in figure 2.4. These experiments were performed with AFM in contact mode. [9]

1.2.2 Non-contact mode

The non-contact mode of AFM is used to study long-range attractive forces. In this mode, the tip does not actually touch the sample surface during the scanning. However, the forces applied to the tip are extremely low, resulting in low deformation and shear. Thus, the non-contact mode is the most suitable method for soft samples. In non-contact mode, van der Waals forces would have little deflective effect on stiff cantilever, a flexible tip with a low resonant frequency is important. [7] The non-contact mode can also be used to characterize various tip-surface interactions, such as magnetic and electrostatic interactions. For some measurements, a special coating for the tip is necessary. For example, one can use an AFM tip coated with a thin magnetic film to study magnetic properties of sample. The obtained magnetic force imaging can provide information about the surface magnetization of the sample.

1.2.3 Semi-contact mode/Tapping mode

The semi-contact mode is also known as the "tapping mode". In the tapping mode, the tip is oscillating (frequencies in air 50 – 500 kHz) with amplitude of ~ 100 nm. This oscillation is driven by the cantilever piezodriver, so that the tip approaches the surface several thousands of times per second, slightly touching or "tapping" the surface. [8] The contact time between the tip and the sample is greatly reduced by using the tapping mode, and the friction force is minimized while the tip is scanning over the surface. This could prevent the tip form attracting the molecules on the surface. In tapping mode, because the various material properties lead to a phase shift of the tip oscillation, phase image can also be obtained. Therefore, using phase image we can also indentify the sample.

1.3 AFM of graphene

Measuring the atomic steps presented on surfaces with AFM is relatively easy. This ability to determine heights of specimens with atomic precision makes it suitable for characterizing the thickness of graphene and functionalized graphene flakes, for example graphene oxide. Graphene oxide has a variety of functional groups, such as epoxides, carbonyls (=CO), hydroxyls (-OH) groups etc, attached to its surfaces. The attachment of these functional groups makes the height of GO to be larger than pristine graphene. GO is thicher than a prinstine graphene sheet, which is only 0.34 nm, the typical thickness of a single graphene oxide sheet is within the range of 1-1.6 nm. It is expected that some water molecules could be trapped between the sheet and substrate or between the sheets, since the functional groups make graphene oxide strongly hydrophilic. [10-12]

AFM also turned out to be a useful tool with which one can investigate the mechanical properties of graphene. As presented in section 1.2.1, AFM was used to investigate elastic

properties of free-standing monolayer graphene. The tribological properties of few-layer graphene have also been studied by using AFM. The studies show that the frictional properties of graphene vary with the number of layers. The friction decreases as the number of layers increases. They attributed this variation of friction to the interlayer surface attractive forces between layers and to electron-phonon coupling. [13-15]

2. Raman spectroscopy

Raman spectroscopy has long been used as a powerful tool to analyze carbon materials. And many studies have been performed in order to understand Raman scattering effect and the origin of the different Raman bands present in graphitic materials. After several years of research on Raman spectroscopy of graphitic materials, both theoretical and experimental researchs about Raman spectroscopy of graphene have been well developed. Raman spectroscopy is becoming an indispensable characterization tool for graphene based materials and other two dimensional materials.

2.1 Raman scattering and Raman spectroscopy

Raman spectroscopy is based on vibrational and rotational modes of molecules in different states. This phenomenon was primarily observed by an Indian physicist Dr. Raman in 1928. Two years after, he won the Nobel Prize due to his ground breaking contribution in the field of Raman scattering. The Raman scattering can be simply understood as a frequency shift of the scattered photons, after incident photons (monochromatic light source) is applied onto materials. During this process, not only elastic scattering, but also some particular vibrational modes and additional scattered photons with different frequencies can be observed, as shown in figure 2.5.

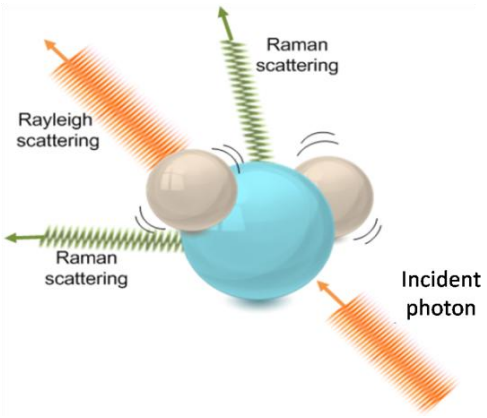

Figure 2.5: Schematic diagram of light scattering in molecule H_2O

The basic concepts of Raman spectroscopy can be introduced with classical electromagnetism theory. In crystal structures, the induced polarization *P* due to the electric field *E* produced from incident light can be expressed as following:

$$\vec{P} = a \cdot \vec{E} \tag{2.1}$$

where *a* is polarizability which is related to the vibration of the atom in the crystal lattice after being excited by the incident monochromatic light. When the incident light is a monochromatic source, the equation 2.1 can be rewritten as: [16]

$$\vec{P} = \left(a_0 + a_1 sin\left(\omega_q t\right)\right)\left(\overrightarrow{E_0}\sin(\omega_0 t)\right) = \overrightarrow{E_0}\, a_0 \sin(\omega_0 t) + \frac{1}{2}\overrightarrow{E_0}\, a_1 \cos\left(\left(\omega_0 - \omega_q\right) t\right)$$
$$-\frac{1}{2}\overrightarrow{E_0}\, a_1 \cos\left(\left(\omega_0 + \omega_q\right) t\right) \tag{2.2}$$

where ω_q is the vibrational frequency of the atom in the lattice when it is excited by an incident photon of frequency ω_0. Thus, we can see that incident light will be scattered both elastically and inelastically. From equation 2.2 the three terms are associated with three different scattering processes: the first one can be regarded as an elastic scattering process in which the scattered photon has the same frequency as the incident photon ω_0, this scattering process is also known as Rayleigh scattering. The second and third terms are inelastic scattering which can produce frequency shift. The frequency is down-shifted by the vibration frequency ω_q of the atom; this is the Stokes process for the emission of a phonon. While in anti-Stokes process the frequency is up-shifted for the absorption of a phonon. Figure 2.6 illustrates an energy diagram to explain these three different scattering processes.

For Rayleigh scattering, the molecule comes back to its original ground state after the transition, which means that the scattered photon has the same frequency as that of the incident one. This is the scattering process with higher probability to arise in light scattering process. In Stokes Raman scattering, electrons are excited from the ground state to a virtual

high energy state, and then electrons are back to a vibrational state which has a higher energy level than the ground state by a relaxation process associated with the emission of phonons. For the anti-Stock Raman scattering, corresponding to the third term, electrons first adsorb the phonon energy and are excited to virtual state by incident light. Then, the electrons are back to the ground state by a relaxation process. Generally, it is expected that most of the electrons stay at the ground state and shift to a higher energy level by light excitation, so stokes Raman scattering usually has larger intensity than that of anti-stokes as shown in figure 2.6.

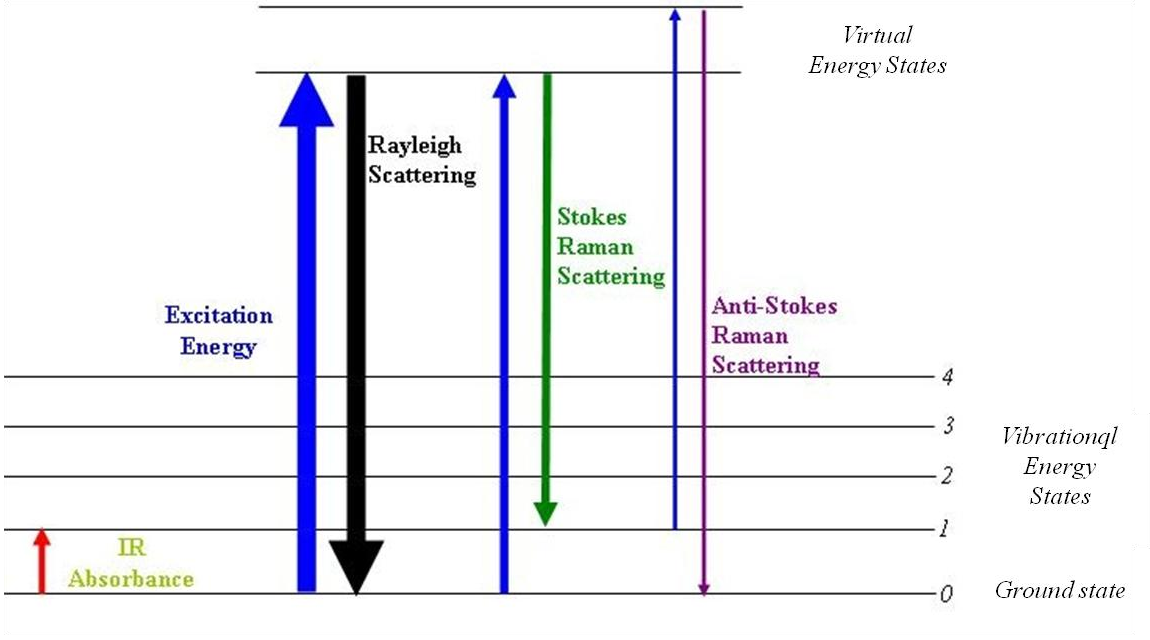

Figure 2.6: Energy-level diagram of Rayleigh and Raman scattering. The line thickness is roughly proportional to the signal strength from the different transitions.

2.2 Raman of graphene

As shown in figure 2.7 (top), in perfect graphene (without defects), Raman spectrum shows two main features: the G band the 2D band. In graphene containing defects, as shown in figure 2.7 (down), the D and D' bands become active, and in high Raman shift region, their combination mode D + D' is also active. [17] Raman is an inelastic scattering of light, which can be originated from different interactions between the light source and solids. In graphitic

materials the inelastic scattering is mainly resulting from electro-phonon interaction. [18, 19] For this reason, it is important to analyze the phonon dispersion of graphitic materials in order to analyze their Raman spectra.

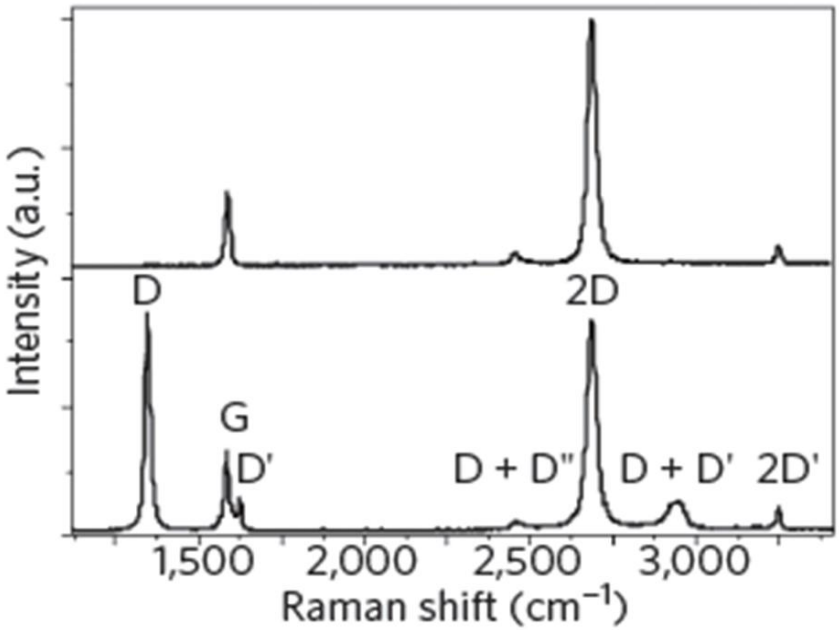

Figure 2.7: Raman spectra of pristine (top) and defected (bottom) graphene. The main peaks are labeled. [17]

As there are two carbon atoms in the unit cell of graphene, there are six possible phonon dispersion branches: three optical and three acoustic. The different vibrations are defined as in plane formed by the graphene lattice or vibrations perpendicular to graphene plane (or out of the plane). The in plane displacements can also be separated in two: longitudinal and transverse, which are related to atomic vibrations parallel or perpendicular to the vector formed between the two carbon atoms in the unit cell of graphene. [20, 21] Then, three optical branches are associated with the out-of-plane, in-plane longitudinal and in-plane transverse optical phonon dispersions; and in similar way we can find acoustic phonon dispersion. In figure 2.8, we can see the in-plane transverse (TO, TA) and the in-plane longitudinal (LO, LA)

branches, the out-of-plane branches are not displayed because they do not contribute to the Raman scattering. It should be noticed that this is established for a perfect and flat graphene sheet.

From figure 2.8, at the Γ point, the TO and LO branches located at ~ 1580 cm^{-1}, this is also called E_{2g} symmetry mode. At the K point, for the TO branch, we can find one A_1 symmetry mode. This degeneracy is called Kohn anomaly. The Kohn anomaly can give rise to a strong interaction between electrons and phonons. [23, 24] It is possible to define electron-phonon coupling (EPC) at the E_{2g} and A_1 symmetry points that are responsible for the main features of the Raman spectra of graphene.

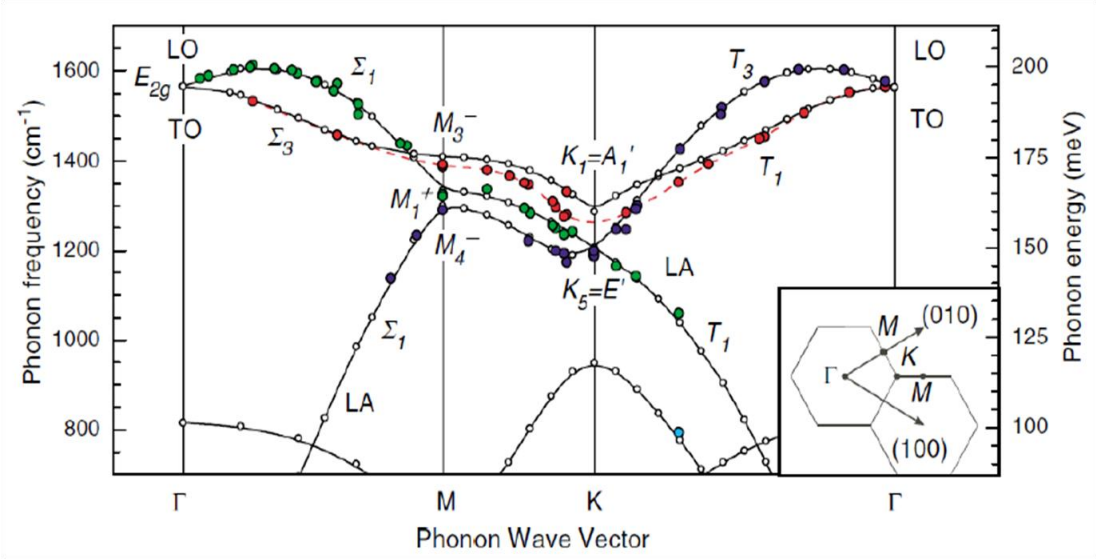

Figure 2.8: Phonon dispersion of graphite. [22]

2.2.1 The G band

The E_{2g} point symmetry give rise to the G band and this is due to the in-plane stretching of the carbon-carbon bonding as shown in figure 2.9. The G band is the signature of all sp^2 carbon allotropes (graphene, graphite, carbon fibers, CNTs etc). The G band is first-order stokes Raman scattering process in graphene, which means that only one scattering process occur

and it can be represented in figure 2.9 (b). In this process, the electrons are excited to the valence band, and then a phonon with a small momentum ($q \approx 0$) is emitted (G band in the Raman spectra), and finally it is the electron-hole recombination process. The G band is sensitive to changes of electronic structure of graphitic materials, thus both Raman shift and line-width of G band can be changed by doping, temperature and strain.

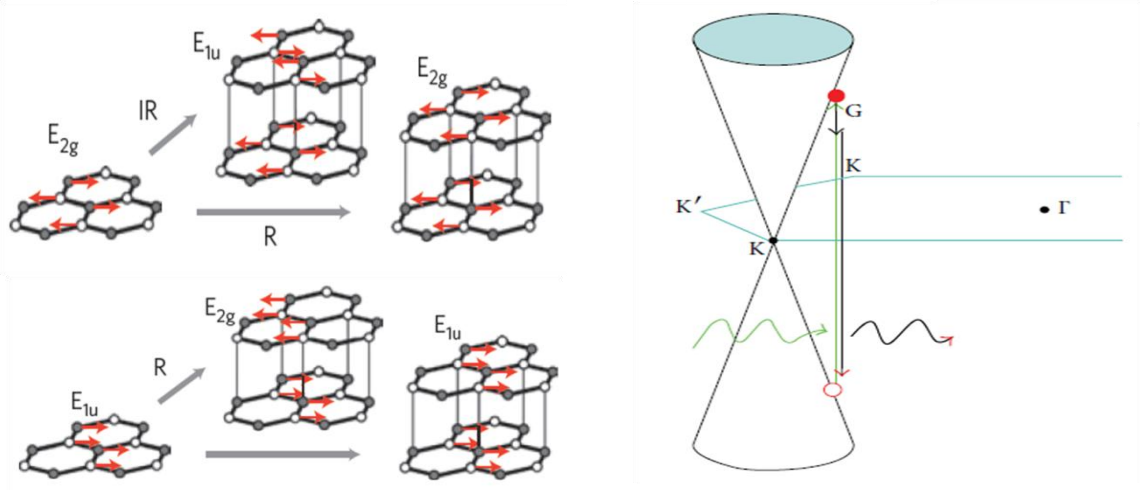

(a) (b)

Figure 2.9: (a) Γ-point phonon-displacement pattern for graphene and graphite. Empty and filled circles represent inequivalent carbon atoms in the unit cell of graphene. Red arrows show atom displacements. Grey arrows show how each phonon mode in graphene gives rise to two phonon modes of graphite, Raman-active (R), infrared-active (IR) and inactive (unlabelled) modes.[17] (b) Resonance process for the G band. The wavy arrows indicate the incoming (green) and outgoing (red) photons. The electronic transitions induced by the incoming photon (green), the G band phonon (black), and the outing photon (red) are indicated by the vertical arrows. [16]

2.2.2 The D band

The figure 2.10 demonstrates the atomic displacement associated with this vibration mode, which is called D band. This process is prohibited in perfect graphene, and the intensity is dependent on the amount of defects. The D band is a second-order Raman process where the

excited electrons are elastically scattered from *K* to *K'*, then the electron is scattered back, emitting a phonon of momentum *q* ($q \neq 0$), and finally the recombination process occurs, as shown in figure 2.10 (b). Because the electron scattering takes place between the two cones (*K* and *K'*), thus this is an inter-valley process. Like the D band, D' mode is the result of an elastic scattering (defect) and an inelastic scattering but takes place in the some cone and is called intra-valley process.

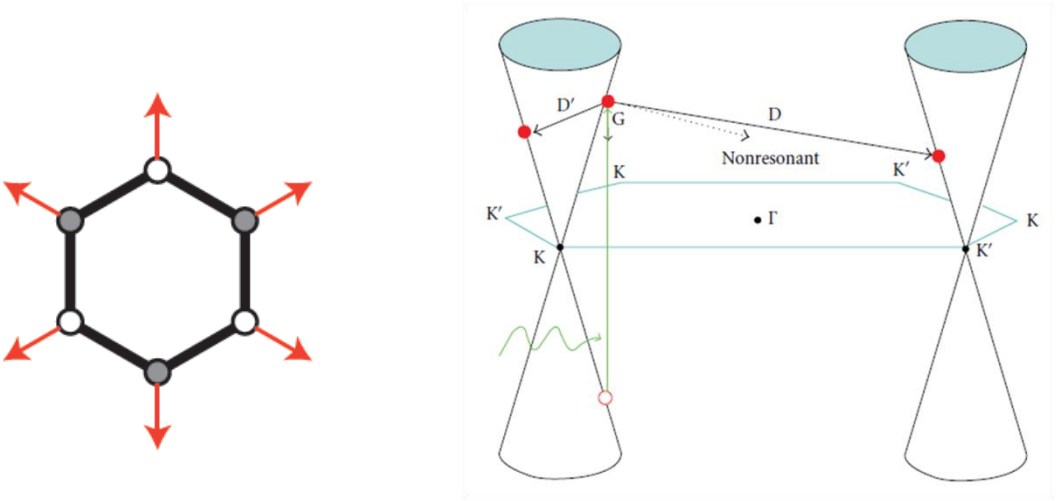

(a) (b)

Figure 2.10: (a) Atom displacements (red arrows) for the A_1 mode at *K*.[17] (b) multiple-resonance processes for the D and D' bands, the first Brillouin zone showing two electronic Dirac cones for the π electron dispersion in the nonequivalent *K* and *K'* points. The green wavy arrow indicates the incoming photon. The electronic transition induced by the incoming light is indicated by the green upward arrow. The phonon-induced transitions are indicated by black arrows: the G band phonon (vertical downwards), the D and D' band phonons (diagonal black solid arrows) and a nonresonant process (diagonal black dashed arrow). [16]

The D band is the main sp^2 Raman signature of disorder or defects. Unlike G band, the D band displays different properties. The Raman shift of D band, ω_D, changes with the change of laser excitation energy. The D band intensity can be used to quantify disorder. Because

absolute intensity measurement is difficult to acquire, the normalized intensity I_D/I_G ratio is largely used to measure the amount of disorder. This ratio depends not only on the amount of disorder, but also on the excitation laser energy, since $I_G \propto E^4_{laser}$, while I_D is E_{laser} independent. Being defects associated mode, the D band linewidth can change from several cm^{-1} to dozens even hundred of cm^{-1} (for very defective graphite materials). Compare to ω_D band, the Raman shift of D' band, $\omega_{D'}$ (~ 1620 cm^{-1}), demonstrates an E_{laser} independent feature.

2.2.3 The 2D band

The 2D band, also called G' in early articles, is the most intense band present in Raman spectrum of monolayer graphene. It is also an inter-valley process as the D band. The excited electrons are inelastic scattered from *K* to *K'* by emitting a phonon of momentum *q* and then inelastically scattered back to K by a phonon of momentum – *q* for momentum conservation. The Raman shift of 2D band, ω_{2D}, is approximately two time of D band. For this reason, the 2D band is considered as the overtone of D band. This second-order sp^2 Raman band is changing with E_{laser}.

The line shape of 2D band depends on the number of graphene layers: one-layer graphene demonstrates a single Lorentzian peak as shown in figure 2.11 (a). For bilayer graphene with AB Bernal stacking graphene, the 2D band exhibits four Lorentzian components. For AB Bernal stacking trilayer graphene, there are 15 possible scattering processes, but these 15 components locate so close in Raman shift that they cannot be distinguished from each other. In general, the 2D band of trilayer graphene can be fitted by 6 Lorentzian components. The 2D band of HOPG has two Lorentzian components. Care should be taken when 2D band is used to identify the number of layers. Turbostratic graphite, i.e. graphite with uncorrelated

layers (to be opposed to Bernal and hexagonal graphite), demonstrates only one single 2D band. Therefore, the shape (single or multi peaks) of 2D band feature can be used to assign the stacking order for graphitic materials. It is important to note that the high intensity of 2D band is one signature for good quality graphene.

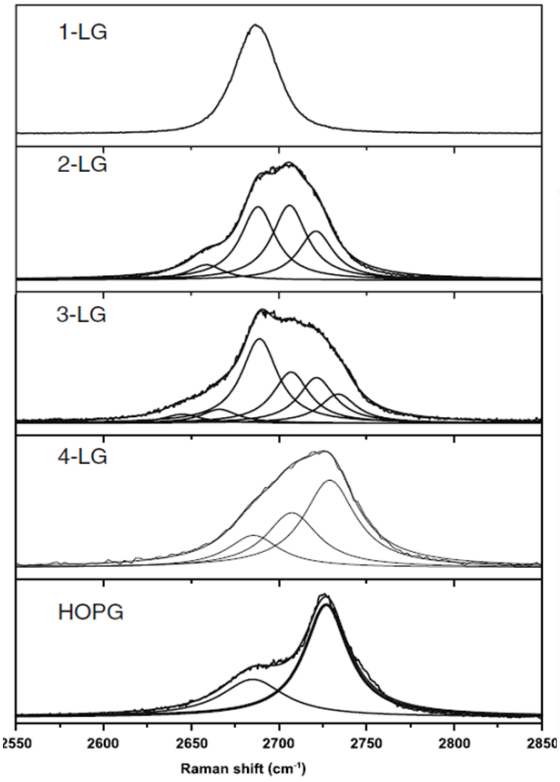

(a)

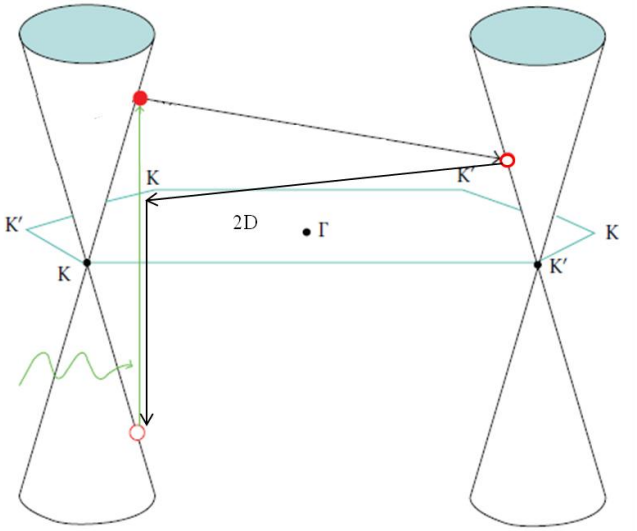

(b)

Figure 2.11: (a) The measured 2D Raman band with 2.41 eV laser energy for AB stacked graphite (Bernal stacking)1-LG, 2-LG, 3-LG, 4-LG, HOPG; [25] (b) Second-order resonance Raman spectral processes for the double resonance 2D band of monolayer graphene.[16]

3. X-ray photoelectron spectroscopy

Photoelectron Spectroscopy (PES) is based on the photoelectric effect in which electrons are emitted through electromagnetic radiation. In X-ray Photoelectron Spectroscopy (XPS), X-rays are used to generate the emission of photoelectrons (PE). The energy of X-rays is in the order of a few thousand eV. XPS can excite electrons from the outer and inner core shells of molecule. The information depth of XPS is roughly in the order of up to 10 nm (depending on the material), but is most sensitive in the first 4 nm. [26] Auger lines are also recorded during XPS measurements. Auger electrons are emitted by a three electron process shown in figure 2.13 (b). At first, under irradiation of X-ray, a core hole is created (e.g. in the K-shell). This hole is filled by a second electron from an outer shell (e.g. L_1). During this relaxation process, energy is released, which can be used to emit an electron (e.g. $L_{2,3}$) with a lower binding energy (E_B) than the second electron.

Development of XPS

More than a hundred year ago, in 1907, Innes recorded the velocity of electrons emitted from different metal surfaces when exposed to irradiation by X-rays.[27] The experimental setups that he used contain almost all the necessary parts that are still used today. Sixty years later technical improvements in the setup have been implemented mainly by Dr. Siegbahn and his group. Siegbahn's group also noted that the XPS spectra can be used for chemical analysis; therefore XPS is sometimes also called Electron Spectroscopy for Chemical Analysis (ESCA). Siegbahn received the Nobel Prize in 1981.

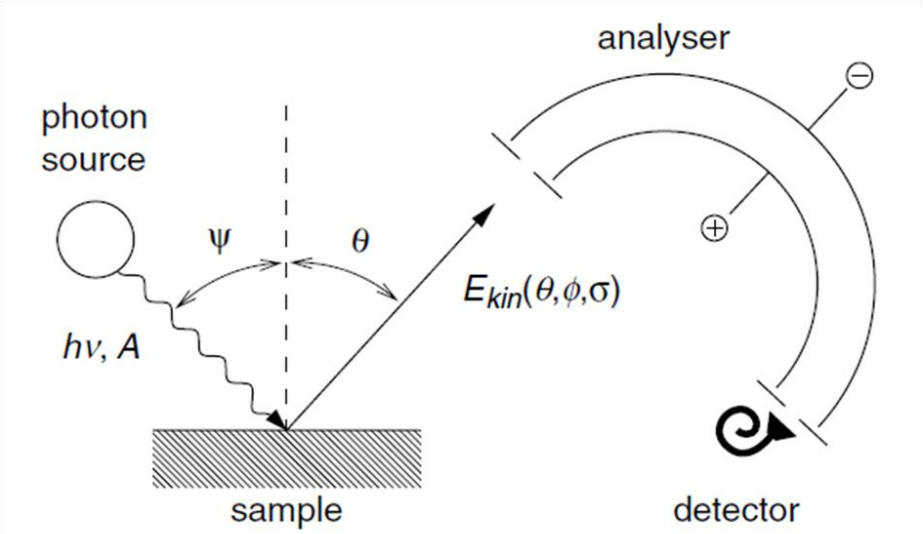

Figure 2.12: Principle of a modern photoemission spectrometer. Monochromatic photons with energy $h\nu$ and polarization (A is the vector potential of the electromagnetic field) are produced by a light source, e.g. an Al-K_α x-ray anode, and hit the sample surface under an angle ψ with respect to the surface normal. The kinetic energy E_{kin} of the photoelectrons can be analyzed by using electrostatic analyzer as a function of the experimental parameters, e.g. emission angle (θ,Φ), the electron spin orientation σ, or the photon energy or polarization. The whole setup is evacuated to ultra high vacuum (UHV, typically $p < 10^{-10}$ mbar). [28]

The modern photoemission spectroscopy, as shown in figure 2.12, is basically performing the same as 100 years ago. The sample is irradiated by photons from a monochromatic light source, which can be a laboratory source, ultraviolet (UV) or x-ray radiation. Compared to XPS, in ultraviolet photoelectron spectroscopy (UPS) the energy of radiation is only a few tens of eV, therefore UPS is only able to excite electrons from the outer valence band. XPS and UPS are both surface sensitive methods to probe the chemical elements for materials. Under photoelectric effect, the photons liberated from sample are analyzed with respect to emission angle and kinetic energy by an electrostatic analyzer. The properties of the photoelectrons basically reflect the electronic eigenstate of the investigated materials.

3.1 The photoemission process

In XPS, the photoelectric effect is used to investigate the binding energy (E_B) of the electrons in the sample. The studied materials are exposed to X-rays with a defined energy, *hv*. If the energy is high enough, electrons can be emitted from the sample (see figure 2.13). With XPS, not only are the intensity of emitted electrons detected, but also their kinetic energy E_{kin} can be studied. E_B can be calculated in a first approximation as the difference between the photon energy *hv*, *E* and Φ:

$$E_B = hv - E_{kin} - \Phi \qquad (3.1)$$

where Φ is the work function, i.e. a potential including surface potential of the sample and a correction factor to the actual referencing point for E_B.[26] The latter is characteristic not only for each element but also for its electronic surrounding. Therefore this method can be used to investigate quantitatively the elemental composition and its chemical environment. While it is easy to detect qualitatively the chemical elements, even traces of elements below 0.1 %, it is quite difficult to determine a quantitative concentration rates within the order of 1%.

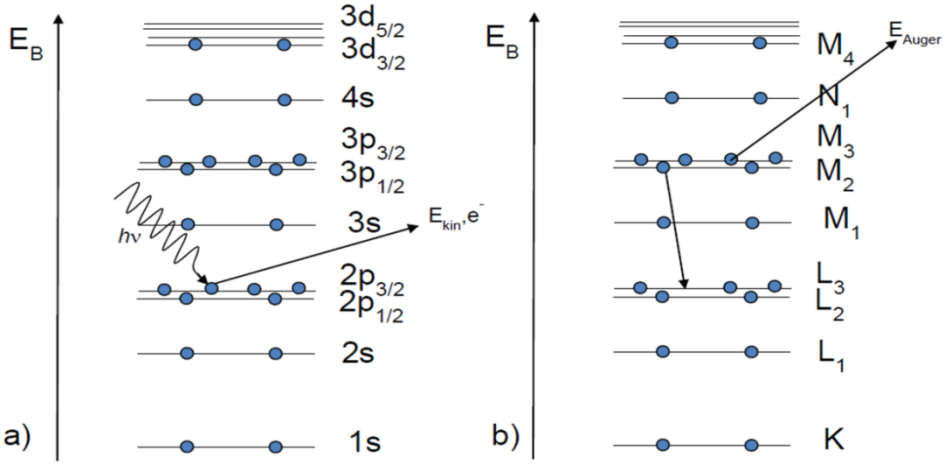

Figure 2.13: Schematics of XPS (a) and Auger electron spectroscopy (b) [28]

3.2 XPS analyses

The position and line shape of XPS spectrum contain important information concerning the detected elements and their origin. In photoelectron lines, main lines are caused by photoelectrons that are emitted either from any core level or the valence band. Auger lines are caused by a three electron process, first an electron is emitted due to the photoelectric effect, and secondly an electron from outer shells fills the created hole via photo emission and can transmit the gained energy to third electron which is emitted from the atom. The kinetic energy of Auger electrons is therefore much lower than the one of photoelectrons. Beside these peaks, there are other peaks, for example, X-ray satellites refer to peaks due to non-monochromatic radiation of an ideally pure X-ray anode; Plasmon peaks caused by the excitation of electrons of the conduction band. The oscillations are quantized and therefore the Plasmon peaks repeat in constant energy distances with decreasing intensity.

3.2.1 Line shapes analyses

The evaluation of the XPS spectra require a precise peak analysis, therefore it is essential to use the correct line shape to fit the peak. In order to find the correct line shape, a full understanding of what is causing the line shape is needed. Several groups initially studied theoretical core line shapes.[29-31] Among these theoretical studies, Mahan line shape have been largely applied to practice line shapes analyses.[32] The Mahan line shape is a combination of a Gaussian and a Lorentzian line shape.[33] The reason for the Lorentzian part is the lifetime broadening, while the Gaussian broadening originates from the response function of the instrument and from phonon or vibrational excitation.[34] In these theoretical studies of XPS line shape, they showed that there is an asymmetric shape term, which is caused by elastic scattering of the emitted photoelectrons in the conducting band.

3.2.2 Background

In every spectrum there is noise and, additionally, the intensity on both sides of the peak does not drop to zero. For peak analysis, this background (BG) has to be taken into account. To properly analyze a given spectrum, the BG subtraction is important. An incorrect BG subtraction can result in wrong peak intensities and consequently result in misinterpretation of XPS spectra. In order to select the correct BG, it is necessary to understand its origin. Photoelectrons are emitted from depth up to 10 nm. As they emit from sample, on their way to the surface they undergo inelastic and elastic scattering. During these inelastic processes, photoelectrons lose energy. Besides the inelastic scattering, excitation due to the created core hole participate also in the raise of the BG.[26] Therefore a background correction is always required. For simple BG subtraction, such as a linear BG or Shirley functions BG substraction are widely used. Most of these are available in common XPS evaluation programs.

Linear background This background simply gives a linear line between the limits of spectral region. The linear BG is often used for polymers and insulators, since it is hard to observe any increase in the BG for these materials. [26] Insulators have a big band gap and therefore show a low energy loss. [26]

Shirley background Probably the most commonly used BG type is the Shirley BG. [34, 35] The Shirley BG is an empirical background subtraction technique that iteratively adjusts the background as a function of the intensity of the photoelectron line. It is therefore proportional to the peak intensity and shows the highest slope at the peak center. For practical applications it has the advantage that only a short energy range of 20 eV has to be recorded. And this algorithm is suitable for spectra that show only a small intensity increase when going from the low to high binding energy side of a peak; it is conveniently used as a BG for one or two non-

overlapping peaks. The Shirley background corrected spectra (*F(E)*) of the kinetic energy *E* over an interval [E_{min}, E_{max}] is given as:

$$F(E) = I(E) - k \int_{E_{max}}^{E_{max}} F(E')dE' \quad (3.2)$$

where *I(E)* is the intensity at the kinetic energy E and *k* is adjusted in such a way that the BG adjusts to the spectrum at the lower energy side, $F(E_{min}) = 0$.

In this report, we have mainly used Shirley background subtraction. In some specific cases, Tougarrd background can also be used. [34, 36] Both background treatments are integrated in the XPS analysis software.

3.3 XPS of graphene

XPS is an excellent technique to carry out the compositional analysis for graphene based materials. Actually, XPS has been largely used to study graphene oxide. We summarize in this section the XPS results of graphene oxide.

XPS spectra can be used to reveal the presence of elements, such as carbon, oxygen, nitrogen etc. The spectra analysis can provide information about their relative content and the nature of the bonds. However, precautions should be taken when XPS is used to carry out compositional and structural analysis for graphene materials. Since monolayer graphene is only ~ 0.34 nm thick and monolayer graphene oxide is ~ 1 nm thick, in measured XPS spectra the presence of peaks from substrate is unavoidable. Additional measurements for substrates are suggested. To minimize the effects of substrate, a careful selection of the substrate can produce more precise measurement results. For XPS study of a graphene sample, a preferable substrate should not contain elements like carbon and/or oxygen. In most case, to carry out XPS analysis, the graphene oxide samples were collected to form multi-layer “paper-like”

sample. Figure 2.14 shows typical XPS spectra of C1s and O1s recorded from a graphene oxide film deposited on silicon nitride – on silicon substrate. [37] The graphene oxide film was annealed at different temperature under argon for oxygen reduction.

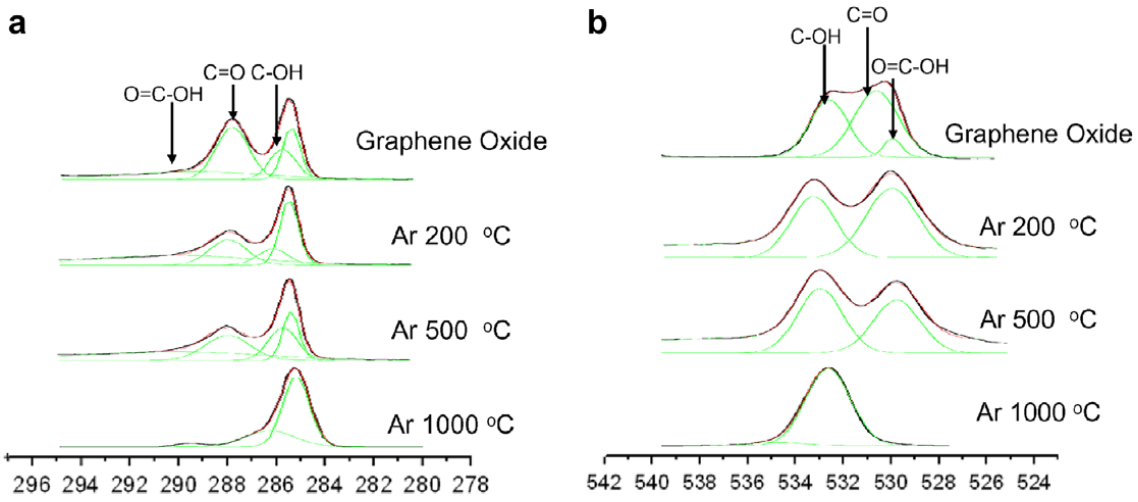

Figure 2.14 : XPS spectra for graphene oxide films on Si_3N_4-on Si substrate after 200, 500, and 1000 °C treatment in flowing Argon: (a) comparison of C1s peaks, (b). comparison of O1s peaks.[37]

The decomposition of XPS spectra allows us to identify different component. For quantitative analysis, the spectrum of C1s can be decomposed into individual components by fitting the entire spectrum with different component. As shown in figure 2.15 (a), the C1s peak of graphene oxide consists of several chemically shifted components: sp^2 carbon (284.6 eV), C-OH (286.4 eV), C=O (287.8 eV), O=C-OH (288.9 eV), and $\pi - \pi^*$ shakeup satellite peak (290.6 eV). [38-41] After thermal reduction, the intensities of oxygen containing groups decreases, even reduction at 1000 °C, there is still a sp^3 component around 289.7 eV. For high resolution of XPS spectra, the fraction of sp^2 and sp^3 functional groups can be estimated by evaluating the intensities of the corresponding components.

The C-O bonds in graphene oxide can be attributed to epoxy and hydroxyl groups in the basal plane. The XPS measurements of O1s, which includes typical contributions from C-OH (533

eV), C = O (531.2 eV), O = C-OH (530 eV), can be used to estimate the content of these groups.[39, 41] The disappearance of component located at 531.2 eV and 530 eV after 1000 °C reduction indicates loss of oxygen during the thermal reduction.

4. Surface conductivity measurements

In articles, surface resistance and surface resistivity are both used to characterize the electrical properties of materials. But from their definitions, there is difference between the two terms. Surface resistance is defined as the ratio of a DC voltage U to the current, I_s, flowing between two electrodes of specified configuration that are in contact with a thin film under test. The surface resistance can be calculated with:

$$R_s = \frac{U}{I_s} \tag{4.1}$$

On the other hand, surface resistivity is determined by the ratio of DC voltage U drop per unit length L to the surface current I_s per unit width D. [42]

$$\rho_s = \frac{\frac{U}{L}}{\frac{I_s}{D}} \tag{4.2}$$

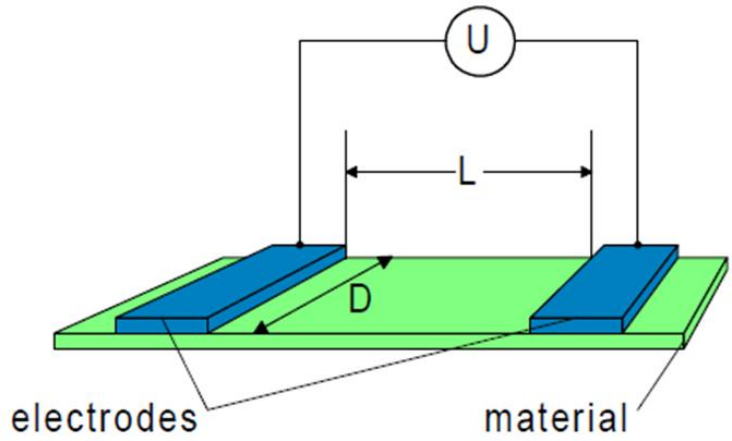

Figure 2.15: Basic conception of surface resistance and surface resistivity measurement.

Surface resistivity is a property of materials. In effect, the surface resistivity is the resistance between two opposite sides of a square. Thus, it should remain constant regardless of the method and configuration of the electrodes applied for the surface resistivity measurement. The surface resistance measurement depends on both the material and the configuration of the

electrodes applied in the measurement. The surface resistance is expressed in ohms (Ω). The surface resistivity is expressed by ohms/square (Ω/sq).

For surface resistance measurement with four-point probe, as shown in figure 2.16, there are several resistances. The probe has a probe resistance R_p. At the interface between the probe tip and the sample, there is a probe contact resistance, R_{cp}. When the current flows from the tip into sample and spreads out in the sample, there will be a resistance associated with current spreading, noted as R_{sp}. Finally the sample itself has a resistance R_s. The equivalent circuit for measurement of surface resistance of thin film by using four-point probe is shown in figure 2.16 (c). Two probes provide the current and the other two probes measure the voltage. Each probe has a probe resistance R_p, a probe contact resistance R_{cp} and a spreading resistance R_{sp}. However, there resistances can be neglected for the two probes associated with voltmeter as the voltage is measured with a high impedance voltmeter, which draws very little current. Thus, the voltage shown in voltmeter is approximately equal to the voltage drop across the measured sample.

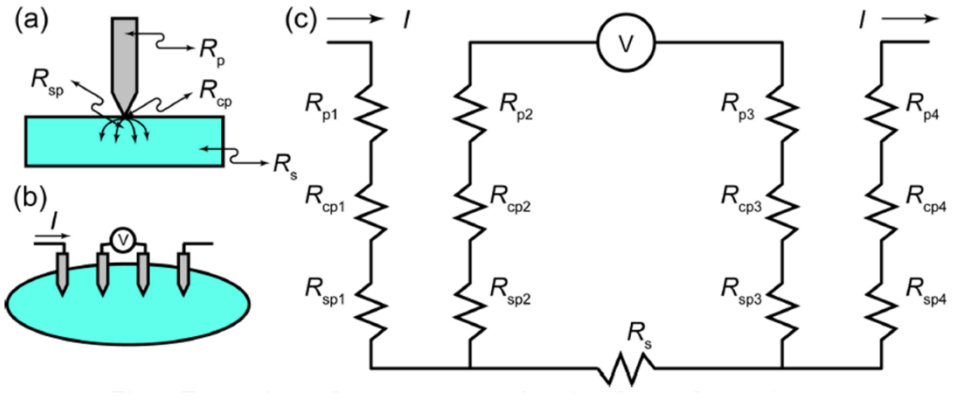

Figure 2.16: Four-point probe for surface resistance measurement of thin film

By contrast, the two-point probe system has relatively high measurement noise and as a consequence, this method has substantial uncertainty in resistance measurements. The four-

point probe system can decrease the effect introduced by the probe resistance, probe contact resistance and spreading resistance. Therefore it has more accuracy than the two-point probe method.

4.1 "four-point" surface resistivity measurement methods

4.1.1 The van der Pauw technique

The van der Pauw technique was reported for the first time in 1958. [43] The advantage of the van der Pauw technique is that this technique can be used to sample without knowing the geometry of sample. L.J.van der Pauw showed that the resistivity of a certain material with arbitrary shape can be determined without knowing the current pattern.

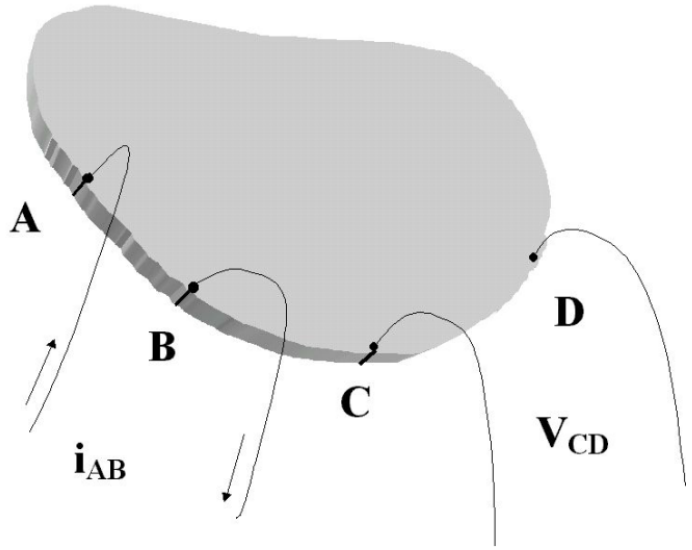

Figure 2.17: Contact disposition on the edge of an arbitrarily-shaped sample for van der Pauw technique.

As shown in figure 2.17, in van der Pauw technique, the current flows from A to B. The voltage is measured across C and D. Then current flows from B to C, and voltage is measured across A and D. The resistance $R_{AB,CD}$ can be expressed as:

$$R_{AB,CD} = (V_D - V_C)/i_{AB} \quad (4.3)$$

and i_{AB} is the current fed in the sample through contact A and drained from contact B. A similar relation defines $R_{BC,\,AD}$. $R_{AB,\,CD}$ and $R_{BC,\,AD}$ are related to the surface resistance R_s through the Van der Pauw equation:

$$e^{\left(-\frac{\pi R_{AB,CD}\, d}{\rho}\right)} + e^{\left(-\frac{\pi R_{BC,AD}\, d}{\rho}\right)} = 1 \tag{4.4}$$

where d is the thickness.

For a sample of arbitrary shape, it is possible to write resistivity in the form:

$$\rho = \frac{\pi d}{ln2}\frac{R_{AB,CD}+R_{BC,DA}}{2} f\left(\frac{R_{AB,CD}}{R_{BC,DA}}\right) \tag{4.5}$$

where *f* is the correction function, and can be numerically calculated by exploiting the relation:

$$\frac{R_{AB,CD}-R_{BC,DA}}{R_{AB,CD}+R_{BC,DA}} = \frac{f}{ln2} arccosh\left(\frac{\exp(ln2/f)}{2}\right) \tag{4.6}$$

4.1.2 One line four-point probe for surface resistivity measuring

The four-point probe measuring system is largely applied to measure the surface resistivity of thin films and semiconductors wafers. The measured surface resistivity values help us characterize the quality of produced thin films. This technique was firstly reported by L.Valdes in 1954. [44] The technique was further improved by F.M.Smits in 1957. [45] In this setup the sheet resistance is measured by sending a DC current to measured sample through the outer two probes. This connection completes an electrical circuit which then induces a voltage in the inner two probes. This voltage is read through a digital multimeter.

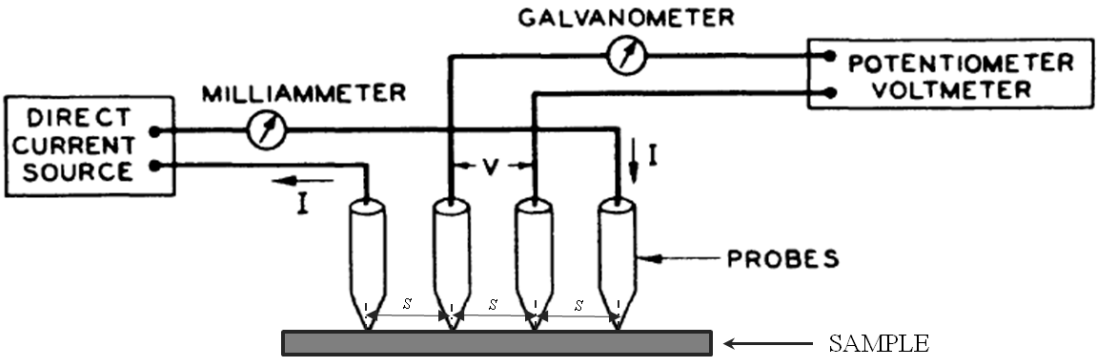

Figure 2.18: Circuit used for surface resistance measurements.

By applying measurement conception shown in figure 2.18 for sample having infinity dimension, the resistivity ρ_0 can be expressed by equation:

$$\rho_0 = \frac{V}{I} 2\pi s \tag{4.7}$$

where *s* is distance between electrodes shown in figure 2.18.

For a thin film with thickness of *e*, the resistivity can be calculated:

$$\rho = \frac{\rho_0}{f(\frac{e}{s})} \tag{4.8}$$

where *f(e/s)* is correction factor for applying the equation to the case of thin film.

In the case that thickness *e* is small enough compare to distance between electrodes, *e/s* → 0, then the correction factor can be expressed:

$$f\left(\frac{e}{c}\right) = \frac{2s}{e} ln2 \tag{4.9}$$

By introducing a correction factor associated with the dimensions of the samples, Smits developed the method for a material with finite dimension as shown in figure 2.20:

$$\rho_s = \frac{V}{I} e \cdot C \cdot F \tag{4.10}$$

where *C* and *F* are correction factor. *C* is related to dimension of sample, *a, d* and *s*. For small *d/s* the quantity *C'=(s/d)C* is close to unity. In these cases the sheet resistivity can be expressed as:

$$\rho_s = \frac{V}{I}\frac{d}{s} C' \approx \frac{V}{I}\frac{d}{s} \tag{4.11}$$

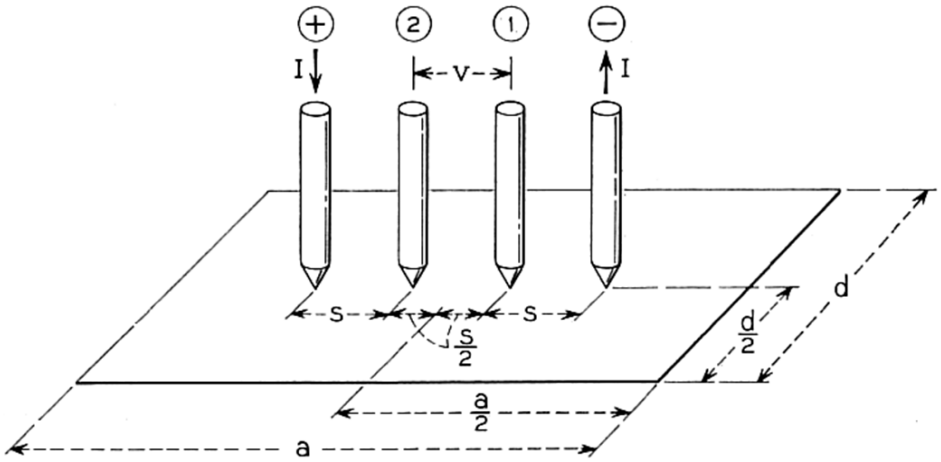

Figure 2.19: Arrangement of a four-point probe on a rectangular sample [45]

4.2 Four-point probe system applied

For surface resistivitance measurement of graphene film, the four-point probe is a common method. During our study concerning graphene film, one four-point probe system developed by Dr. Amélie Catheline was used. It is proved to be very useful for studying conductive CNTs films. As shown in figure 2.20 (a), four electrodes (gold) with equidistance were at first deposited onto the film by using a mask shown in figure 2.20 (b). The technique has the advantage to eliminate contact resistance as presented by Valdes and Smits.

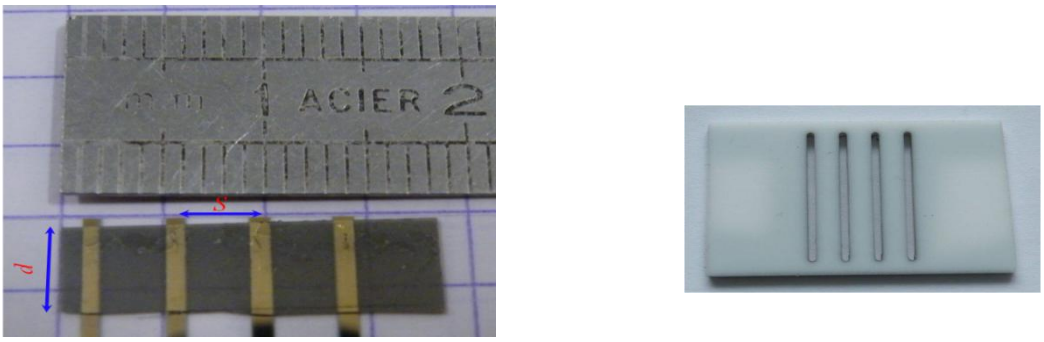

(a) (b)

Figure 2.20: (a) graphene film with four deposited electrodes. (b) Mask for electrodes deposition

The electrical measurement was realized by home-made four-point probe, as shown in figure 2.21. The current is applied between the two exterior electrodes and a tension is measured at inner electrodes. Surface resistivity is calculated by using equation 4.11. Electrodes are 1 mm width and are separated 3 mm from each other.

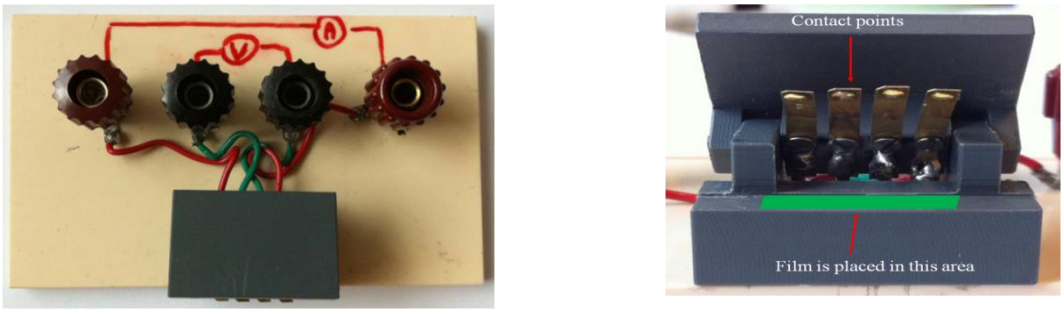

(a) (b)

Figure 2.21: (a) home-made four-point probe; (b) front view of four-point probe.

5. Scanning electron microscopy

Scanning Electron microscopy (SEM) is widely used to characterize microstructure and morphology of materials. SEM images are obtained by using backscattered electron which can reproduce difference in the brightness and contrast resulting from different phases and materials. In 1937, Von Ardrenne showed a prototype of a SEM. Further SEM development occurred in 1951; Charles Oatley and his colleagues obtained the first SEM images at Cambridge University. Since then there have been great improvements in the electron microscopes. At the present, SEM has been widely used for characterization of materials.

5.1 Principle of SEM

SEM is based on the emission of electrons onto the surface of a sample to generate signals. The schematic diagram with the main parts of a scanning electron microscopy is presented in figure 2.22. SEM can be divided into several sections with different vacuum levels. The highest vacuum is obtained at the electron gun section. An electron beam is generated in the top of the microscope's column where is the highest vacuum section. When a steady stream of electrons is generated, it is passing through the condenser lenses which adjust the beam current. And the objective lens determines the final size of electron beam. The scan coils control the beam scanning across the sample. As the electron beam traces over the specimen, it interacts with the specimen. As a result, the electrons can be backscattered or they can generate secondary electrons. [45, 46] Moreover some of the electrons can be absorbed or pass through the specimen.

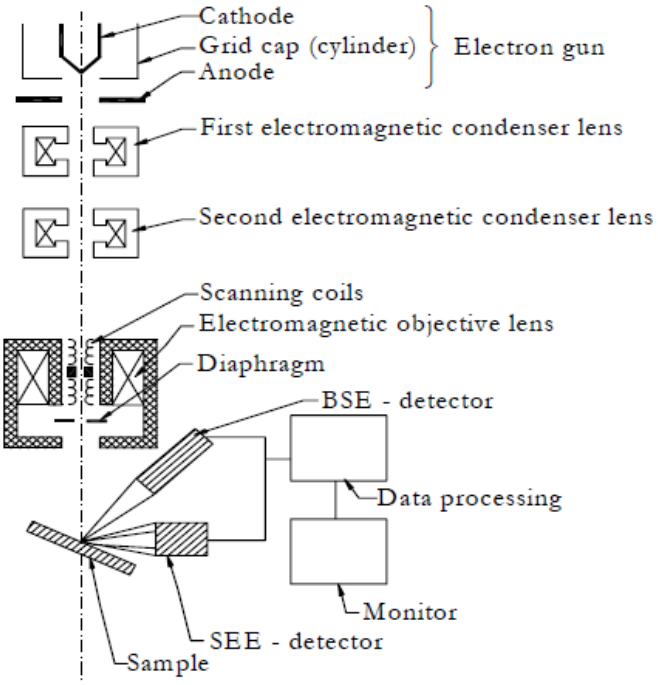

Figure 2.22: overview of Scanning Electron microscopy

The electron emitted (signal) from the surface is registered by different detectors: backscattered and secondary electron. The detector counts the number of electrons from each point of sample surface. The intensity of these emitted electrons is displayed as brightness on SEM image.

Electron interaction with atoms

For a better understanding of the SEM, it is important to know the interactions between the primary electrons (PE) beam and the atom. The primary electrons are charged particles and so they can interact strongly with the electrically charged particles of the atoms in the sample. When this electron beam reaches the sample, the electrons are scattered many times before they are deflected into different ways. The interaction between the electron and the sample's atoms may be inelastic or elastic.

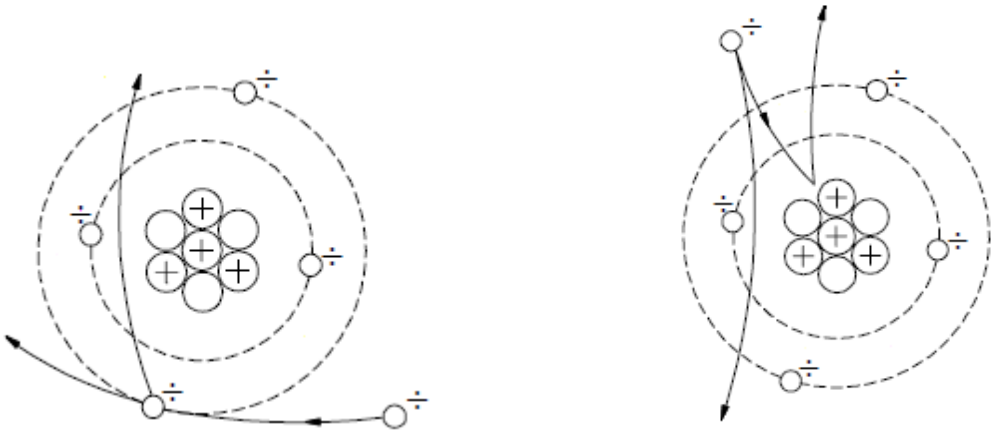

(a) (b)

Figure 2.23: Schematic illustration of inelastic (a) and elastic (b) interaction between electron and atom

As shown in figure 2.23, in inelastic interaction, some of the energy of the primary electron is lost during the interaction; while in elastic interaction, no energy is lost during the interaction. The area where the elastic or inelastic interaction takes place is called the “interaction volum” as shown in figure 2.24 (a). The size of the interaction volume depends on the electron’s energy and the atomic number of sample. For an element with lighter atomic number, the penetration depth of the primary electrons is higher than that observed for a heavier atomic number.

Emitted lower-energy electrons resulting from inelastic scattering are the secondary electrons (SE). Secondary electrons can be formed by inelastic collision which results in the emission of lower energy electrons. They are detected by a SE detector. SE is abundant and they are used to give topological and morphological information of the sample. High-energy electron is come from elastic collision of an incident electron, typically with atom’s nucleus of sample, are referred to as backscattered electrons (BSE). The energy of BSE will be comparable to that of incident electrons. Compare to secondary electrons, these high-energy electrons can

escape from deeper areas. So surface topography produced from BSE is not as accurately resolved as image from secondary electrons. However, BSE are highly influenced by atomic number of the sample. And BSE is responsible for the phase contrast of image.

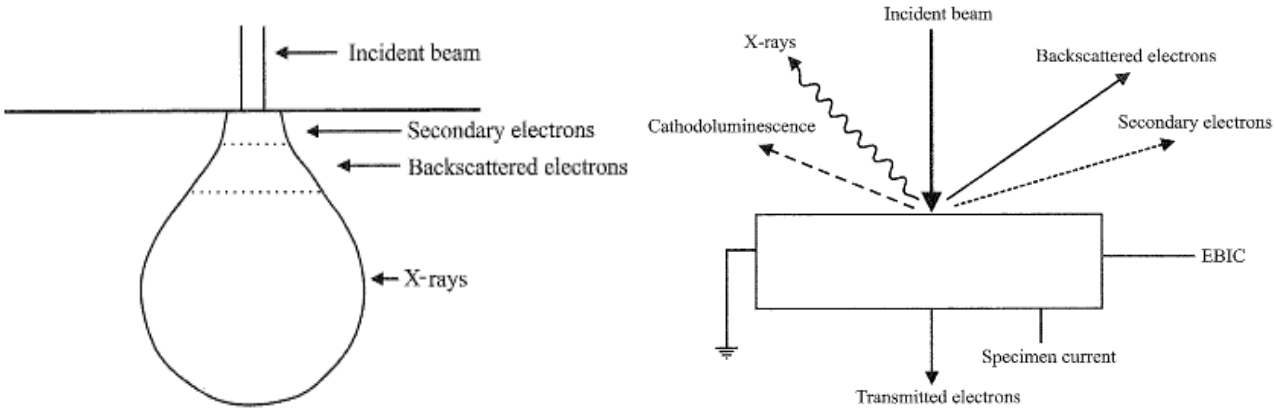

(a) (b)

Figure 2.24: (a) Interaction volume and (b) interaction diagram of SEM

The key to produce a good quality SEM image is to understand well the equipment's parameters (accelerating voltage, probe current, working distance) and their impact on the SEM image.

5.2 SEM of graphene

Although AFM and SEM can provide visual information by scanning the substrate surface containing graphene, SEM is still largely applied to characterize graphene based materials, especially for graphene films. SEM is faster in scanning samples surface for imaging the morphologies of materials. Moreover, SEM has the advantages in detecting rapidly impurities, folds and discontinuities for graphene film. However, it is difficult to make SEM image for an atomic thick graphene layer because of resolution limitation of SEM. Moreover, the ultra-thin graphene film is transparent to high energy electron beams. Therefore, SEM images sometime

display the morphologies of the substrate on which graphene films were deposited, not the graphene film itself. Thus the interpretation of SEM image of graphene film is sometimes complicated. In the following part, we will summarize some contrast study to understand SEM imaging of graphene films.

A perfect graphene film shoud be smooth and continuous, but in many cases, graphene film produced by CVD method are required to transfer the film onto substrates, this transfer process usually produces wrinkles, folds and ruptures. For graphene film produced from solution ways, the graphene flakes are assembled together to form continuous film. These wrinkles, folds and edges can create different contrast under electron scanning.

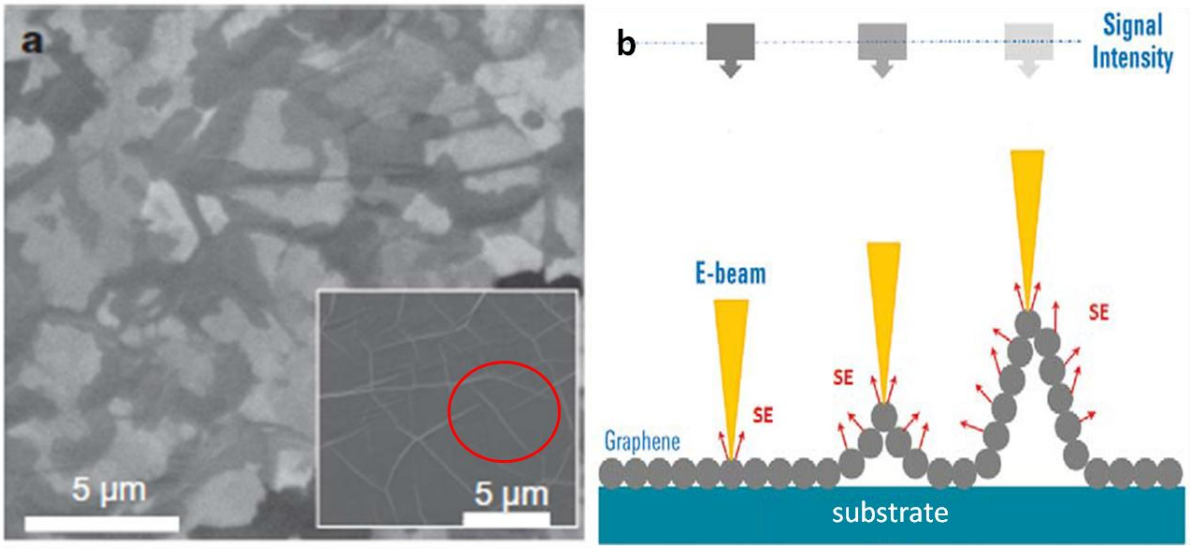

Figure 2.25: (a) SEM images of as-grown graphene films on thin (300-nm) nickel layers and thick (1-mm) Ni foils (inset); [47] (b) the roughness contrast for a corrugated graphene sheet.

The roughness contrast is the most common contrast that one can observe on SEM image. These contrasts have a complex origin and they depend on the intensity and trajectories of electrons (SE and BSE). [48] In a higher magnification image, a wrinkled structure can be seen clearly, shown in figure 2.25 (a). The contrast in the red circle represents roughness of film. In figure 2.25 (b), a schematic image indicates that roughness contrast of a graphene film comes

from different number of SE detected. For rougher surfaces, more SE will come from the graphene surface within the same area resulting in higher signal intensity than that from the background. [49] Thus, it is reasonable to relate the signal intensity with the height of the feature.

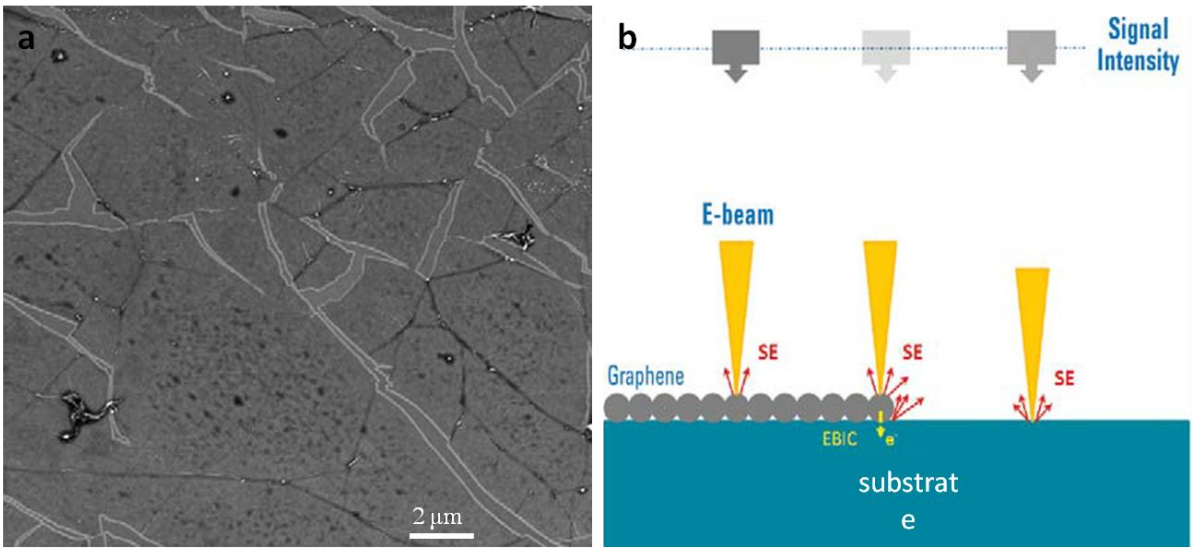

Figure 2.26: (a) SEM images showing bright contour lines around cracked graphene film; (b) edge contrast caused by both edge effect and EBIC.

Generally, the edge of grpahene can also be detected under SEM imaging. As shown in figure 2.26, at the edge area, a larger part of the beam/specimen interaction volume will be in the SE escape zone. Therefore more secondary electrons can emit from the side of the edge resulting in higher signal intensity than that from a flat surface. The contrast mechanism of electron beam induced current (EBIC) could be used to explain the observed edge of grpahene films as well.

SEM can be used to distinguish few-layer graphene as thickness contrast of graphene films can be observed in SEM images. [50] It was reported that the work function of graphene increases with the number of layers: from ~ 4.3 eV for monolayer to ~ 4.6 eV for quadrilayer,

and it saturates for more layers. [50, 51] The SE yield δ is related to the work function according to the following formula: [52]

$$\frac{\partial \delta}{\partial E_k} = \frac{F' E_k}{(E_k + \emptyset)} \tag{5.1}$$

Where Φ is the work function of graphene, E_k is the energy of SE and F' is a normalization factor. The equation indicates that the SE yield is in inversely proportional to the work function of the material. Hence a graphene with a lower work function produces more secondary electrons than a few layer graphene.

6. Conclusion

Graphene, a 2D material with a thickness of the order of a single atomic unit, have stimulated great interest due to its promising properties. Since the properties of graphene are influenced by the production method, and can be largely changed by its morphology and environment, such as doping, temperature, strain, stacking order etc, thus the characterization of graphene is crucial for further study and applications of graphene and its derivatives materials.

Several characterization techniques are presented in this chapter. Among these techniques, both atomic force microscopy (AFM) and scanning electron microscopy (SEM) can be applied to characterize the morphology of materials. AFM, with its atomic precision, can be used to determine the thickness of graphene, while SEM can rapidely display morphology of graphene. Since the theoretical and experimental Raman studies concerning sp^2 carbon materials, like carbon nanotube, graphite etc, have been well established, this technique have been quickly used to study graphene materials. Raman scattering is highly sensitive to the physical and chemical properties of the observed materials. Raman scattering can also be used to study any environmental effect that may change properties of graphene. Moreover, this technique is relatively simple to perform and it is a nondestructive characterization tool. For these reason, the Raman spectroscopy is now evolving into one of the most useful tools for studying graphene materials. X-ray photoelectron microscopy is a chemical elements analysis technique. This technique is largely used for studying functionalized graphene materials, such as graphene oxide and reduced graphene oxide materials. Surface conductivity measurement techniques were also introduced in this chapter.

Even though, the characterization studies with techniques introduced in chapter were well established for graphene materials, most of these characterization results were developed on mechanically exfoliated graphene, graphene produced from CVD, GO. One can of course use

these results to interpret characterization results obtained from graphene produced by different ways, but care should be taken. If it is necessary, several techniques should be used to elucidate correctly the observed graphene specimens.

References

[1] R. R. Nair, P. Blake, A. N. Grigorenko, K. S. Novoselov, T. J. Booth, T. Stauber, N. M. R. Peres, A. K. Geim. Fine Structure Constant Defines Visual Transparency of Graphene . Science 2008, 320, 1308.

[2] C. Lui, L. Liu, K.F. Mak, G. W. Flynn, T.F. Heinz. Ultraflat graphene. Nature, 2009 462, 339.

[3] E. Stolyarova, K. T. Rim, S. Ryu, J. Maultzsch, P. Kim, L. E. Brus, T. F. Heinz, M.S. Hybertsen, G.W. Flynn. High-resolution scanning tunneling microscopy imaging of mesoscopic graphene sheets on an insulating surface. Proc. Natl. Acad. Sci. 2007, 104, 9209.

[4] Y. Hernandez, V. Nicolosi, M. Lotya, F.M. Blighe, Z. Sun, S. De, I.T. McGovern, B. Holland, M. Byrne, Y. K. GunKo, J. Boland, P. Niraj, G. Duesberg, S. Krishnamurthy, R. Goodhue, J. Hutchison, V.Scardaci, A.C. Ferrari, J.N. Coleman. High-yield production of graphene by liquid-phase exfoliation of graphite. Nature Nanotechnology, 2008, 3, 563.

[5] D. Graf, F. Molitor, K. Ensslin, C. Stampfer, A. Jungen, C. Hierold, L. Wirtz. Raman imaging of graphene. Solid State Commun. 2007,143, 44.

[6] L.J.Cote, F.Kim, J.Huang. Langmuir-Blodgett Assembly of graphite oxide single layers. J. AM. CHEM. SOC. 2009, 131, 1043.

[7] V.J.Morris, A.R. Kirby, A.P. Gunning. Atomic Force Microscopy for Bilogists. Imperial College Press. 2001.

[8] K.D. Jandt. Atomic force microscopy of biomaterials surfaces and interfaces. Surface science. 2001, 491, 303.

[9] C. Lee, X. Wei, J.W. Kysar, J. Hone. Measurement of the elastic properties and intrinsic strength of monolayer graphene. Science 2008, 321, 385.

[10] A. Lerf, H. He, M. Forster, J. Klinowski, J. Phys. Chem. B,1998, 102, 4477.

[11] I. Jung, M. Vaupel, M. Pelton, R. Piner, D.A. Dikin, S. Stankovich, J. An, R.S. Ruoff, J. Phys. Chem. C. 2008, 112, 8499.

[12] A. Buchsteiner, A. Lerf, J. Pieper, J. Phys. Chem. B.2006, 110, 22328.

[13] C.G. Lee, X.D. Wei, Q.Y. Li, R.Carpick, J.W. Kysar, J.Hone. Elastic and frictional properties of graphene. Phys. Status Solidi B.2009, 246 (11–12), 2562–2567.

[14] C.G. Lee, Q.Y. Li, W. Kalb, X.Z. Liu, H. Berger, R.W. Carpick, J.Hone. Frictional characteristics of atomically thin sheets. Science, 2010, 328 (5974), 76–80.

[15] T. Filleter, J.L. McChesney, A. Bostwick, E. Rotenberg, K.V. Emtsev, Th. Seyller, K. Horn, R. Bennewitz. Friction and dissipation in epitaxial graphene films. Phys. Rev. Lett 2009,102, 086102.

[16] A.Jorio, M. Dresselhaus, R.Saito, G.F. Dresselhaus. Raman spectroscopy in graphene related systems. Wiley-VCH, 2011

[17] A.C. Ferrari, D.M. Basko. Raman spectroscopy as a versatile tool for studying the properties of graphene. Nature Nanotechnology, 2013, 8,235-246.

[18] R. Saito, A. Jorio, A.G. Souza Filho, G. Dresselhaus, M.S. Dresselhaus, M.A. Pimenta. Phys.Rev.Lett. 2001, 88, 027410.

[19] D.L. Mafra, G. Samsonidze, L.M. Malard, D.C. Elias, J.C. Brant, F. Plentz, E.S. Alves, M.A. Pimenta. Phys. Rev. B. 2007, 76, 233407.

[20] L.M. Malard, M.A. Pimenta, G. Dresselhaus, M.S. Dresselhaus. Physics Reports. 2009, 472, 51

[21] G.G. Samsonidez, E.B.Barros, R.Saito, J.Jiang, G. Dresselhaus, M.S. Dresselhaus. Phys.Rev.B. 2007, 155420, 75.

[22] J.Maultzsch, S.Reich, C. Thomsen, H.Requardt, P. Ordenjon. Phys.Rev.Lett. 2004, 92, 075501.

[23]W.Kohn. Phys. Rev.Lett. 1959, 2, 393-394.

[24] S.Piscanec, M.Lazzeri, F.Mauri, A. Ferrari, J. Robertston. Phys. Rev. Lett. 2004, 93, 185503.

[25] L.M. Malard, M.A. Pimenta, G. Dresselhaus, M.S. Dresselhaus. Raman spectroscopy in graphene. Physics Reports, 2009, 473, 51.

[26] D.Briggs, T. Grant. Surface analysis by Auger and X-ray photoelectron spectroscopy. IM-Publichation, 2003.

[27] J.G.Jenkin, R.C.G. Leckey, J. Liesegang. The development of X-ray photoelectron spectroscopy 1900-1960. J.Electron Spectrosc. Relat. Phenom. 1977, 12(1), 1-35.

[28] F.Reinert, S.Hüfner. Photoemission spectroscopy – from early days recent applications. Journal of Physics. 2005, 7(97), 1-27.

[29] S.Doniach, M.Sunjic. Many electron singularity in x-ray photoemission and x-ray line spectra from metals J.Phys.C. 1970, 3(2), 285-291.

[30] G.D.Mahan Collective excitations in x-ray spectra of metals Phys. Rev. B 1975, 11 4814-24.

[31] P.Minnhagen. Increased phonon broadening of XPS lines of metals due to finite core-hole lifetime. J.Phys.F:Metal Phys. 1976, 6(10), 1789-1800.

[32] F.Reinert, S.Hüfner. Photoemission spectroscopy-from early days to recent applications. Jour. Physi. 2005, 7, 1-25.

[33] G.D.Mahan. Theory of photoemission in simple metals Phys. Rev. B 1970, 2, 4334–50.

[34] S.Tougaard. Unviersality classes of inelastic electron scattering cross-sections surf.Interf.Anal. 1997, 25(3), 137-154.

[34] D. A. Shirley. High-Resolution X-Ray photoemission spectrum of the valence bands of gold. Phys. Rev. B, 1972, 5(12), 4709.

[35] J.Végh. The shirley background revised. J. Electron Spectrosc. Relat. Phenom., 2006,151(3),159–164.

[36] S. Tougaard. Composition depth information from the inelastic background signal in XPS. Surf. Sci., 1985,162(1-3), 875–885.

[37] D.Yang, A.Velamakanni, G. Bozoklu, S.Park, M.Stoller, R.D. Piner, S.Stankovich, I. Jung, D.A. Field, C.A. Ventrice Jr., R. S. Ruoff. Chemical analysis of graphene oxide films after heat and chemical treatments by X-ray photoelectron and Micro-Raman spectroscopy. Carbon, 2009, 47, 145-152.

[38] C. Mattevi, G. Eda, S. Agnoli, S. Miller, K.A. Mkhoyan, O. Celik, D. Mastrogiovanni, G. Granozzi, E. Garfunkel, M. Chhowalla, Adv. Funct. Mater. 2009, 19, 2577.

[39] C. Hontoria-Lucas, A.J.L. Peinando, J.D.D. Lopez-Gonzalez, M.L. Rojas-Cervantes, R.M. Martin-Aranda, Carbon 1995, 33, 1585.

[40] D.Q. Yang, E. Sacher, Langmuir 2006, 22, 860.

[41] D. Yang, A. Velamakanni, G. Bozoklu, S. Park, M. Stoller, R.D. Piner, S. Stankovich, I. Jung, D.A. Field, C.A. Ventrice Jr., R.S. Ruoff, Carbon 2008, 47, 145.

[42] ESD STM 11.11-2001 Standard. Surface resistance measurement of static dissipative planar materials, 2001.

[43] L. J. Van der Pauw, A Method of Measuring Specific Resistivity and Hall Effect of Discs of Arbitrary Shapes. Philips Res. Repts. 1958, 13, 1-9.

[44] L.Valdes. Resistivity measurements on germanium for transistors, Proceeding of the institute of radio engineers, 1954, 42, 420-427.

[45] F.M. Smits. Measurement of sheet resistivity with the 4-point probe, Bell system technical journal, 1958, 37, 711-718.

[45] P.J. Goodhew, J.Humphreys, R. Beanland. Electron Microscopy and Analysis, 2000, London.

[46]G.H. Michler. Electron microscope for polymers, Heidelberg, 2008, Springer-Verlag.

[47] K.S.Kim, Y.Zhao, H.Jang, S.Y. Lee, J.M.Kim, K.S. Kim, J.Ahn, P.Kim, J.Choi, B.H.Hong. Large-scale pattern growth of graphene films for stretchable transparent electrodes. Nature. 2009, 457,706-711.

[48] J. Goldstein, D. Newbury, D. Joy, C. Lyman, P. Echlin, E. Lifshin, L. Sawyer, J. Michael, Scanning Electron Microscopy and X-Ray Microanalysis, 3rd Edition, Springer (2003).

[49] X. Liang, B.A. Sperling, I. Calizo, G. Cheng, C.A. Hacker, Q. Zhang, Y. Obeng, K. Yan, H. Peng, Q. Li, X. Zhu, H. Yuan, A.R. Hight Walker, Z. Liu, L. Peng, C.A. Richter, ACS Nano 5, 9144 (2011).

[50] M.-H. Park, T.-H. Kim, C.-W. Yang. Thickness contrast of few-layered graphene in SEM. Surf. Interface Anal. 2012, 44, 1538-1541

[51] H. Hibino, H. Kageshima, M. Kotsugi, F. Maeda, F.Z. Guo and Y. Watanabe, Physical Review B 2010, 79, 125437.

[52] J. Cazaux, Material contrastinSEM: Fermienergyandworkfunctioneffects. Ultramicroscopy 2010,110, 242.

Chapter III: Graphenide solutions

Several graphene production methods via liquid-route exfoliation were introduced in chapter I including the dispersion of graphite in organic solvents and reduction of soluble graphite oxides. For reduced graphene oxide, there are still significant oxygen-containing groups on graphene plane, which degrades its electrical properties. For the dispersion of graphite in organic solvent, a great challenge one has to face is the stability of dispersed graphene flakes in a given solvent. Although added surfactant or polymer can improve the stability, dispersion of graphene is still instable and the system will aggregate which is a major disadvantage for further application.

Beside those methods, an alternative method has been developed in our group since 2008. The approach is to start with synthesis of potassium intercalated graphite intercalation compounds (GICs). Then, those GICs can be dissolved in aprotic organic solvents to produce thermodynamically stable graphenide solutions. The earlier studies concerning graphenide solutions in our group were performed with ternary GICs $K(THF)C_{24}$ in which both potassium and THF molecule are intercalated into the graphene galleries. [1] The result shows that a spontaneous dissolution of the ternary GICs in *N-methyl pyrrolidone* (NMP) can produce a stable solution which contains negatively charged monolayer graphene flakes and ribbons and K^+ ions. A further study was performed with stage-1 KC_8. [2] In both case, the charge on the graphene flakes and the counterions prevent aggregation of the graphene sheets, thus the obtained solutions are stable as long as they are protected from air. In this work, we have expanded our studies of GICs from stage-1 KC_8 to stage-2 KC_{24} and stage-3 KC_{36}, which hold different charge transfer between the graphene planes and intercalated potassium. These GICs were then used to produce corresponding graphenide solutions.

In this chapter, we will at first present a detail study of starting materials, different kinds of graphite from different suppliers. Several characterization techniques were used to help us to identify the best starting materials from five different graphite samples. Then we have synthesized and studied stage-1, stage-2 and stage-3 potassium intercalated graphite intercalation compounds (K-GICs) and the graphenide solutions produced from these compounds. To better understand properties of graphenide solutions, we have also studied the GICs with different techniques. Since there are few techniques which can characterize efficiently charged graphene in solution, several conventional techniques introduced in this chapter were developed and used to study depositions of graphenide solutions.

1. Potassium-graphite intercalation compounds stage-1, 2 and 3

Graphite has a layered structure, in which the carbon atoms are arranged in parallel planes. There is no covalent chemical bonding between the layers and so alkali metals can be inserted rather easily between the layers. Alkali-metal graphite intercalation compounds have been studied extensively as they are extremely interesting materials. The previous works were based on potassium intercalated compounds, in this work, we continue using potassium as intercalant to synthesize GICs and study the graphenide solutions prepared from these compounds.

Based on the intercalant density, GICs demonstrate different charging feature for 2D graphene sheets. They have long-distance homogeneity in the positioning of intercalated metal ions within graphite galleries. A stage-1 KC_8 contains metal ions between every graphene layer and is one of the most densely intercalated compounds under normal laboratory condition. It should be noticed that there is still another type of stage-1 potassium intercalated GICs with even higher contents of potassium. The general formula is KC_4, so it contains two times more alkali metal than KC_8, leading to a higher charge transfer than KC_8. But KC_4 is synthesized under high pressure 8-10 kbar at a temperature of 160 °C. [3, 4] The compound is unstable at ambient pressure; when the pressure is released at room temperature below 1.5 Kbar, the sample decomposes instantly to less saturated KC_8 and potassium. Because of its instability at ambient pressure, we didn't study this compound. Stage-2 KC_{24} has alternatively intercalated and empty galleries. KC_{24} contains less potassium than KC_8, and graphene layers are thus less charged. In stage-3 KC_{36}, there are three graphene layers between two adjacent intercalated potassium layers. Thus, those layers are not equivalent, which results in different electronic properties. The stage-1 KC_8, stage-2 KC_{24}, stage-3 KC_{36} were synthesized and studied during this work.

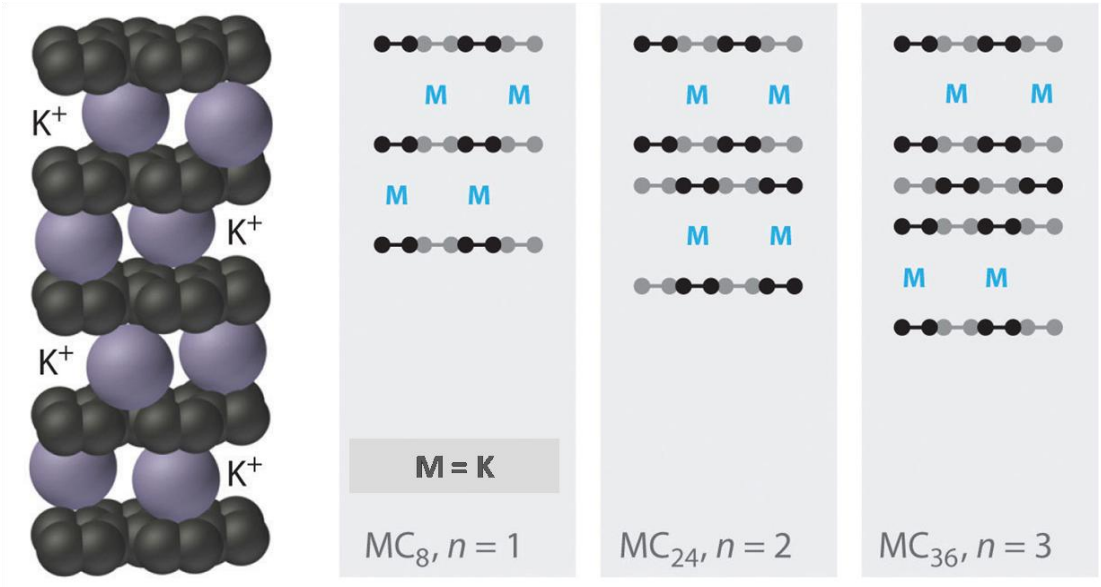

Figure 3.1: Layer arrangements and stoichiometries of K-GICs

1.1 Characterization of starting graphite

We have five different graphite samples from different suppliers. In order to produce K-GICs graphenide solutions with best quality, these graphite samples were all characterized by Scanning electron microscope (SEM), X-ray photoelectron spectrometry (XPS), Raman spectroscopy and X-ray diffraction (XRD).

1.1.1 Graphites morphologies

Among the five graphite samples, three samples are of flake form. The powder-form graphite samples come from Madagascar. SEM image shows the powder particles have dimension up to ~ 20 µm. The five graphite samples are listed in table 3.1.

Samples	Supplier	Morphology
Natural	Nacional de Grafite LTDA Brazil	small flake with micron dimension

SA	Sigma-Aldrich	small flake with micron dimension
TIMCAL	TICMAL Graphite	Powder
Expanded Graphite	Nacional de Grafite LTDA Brazil	Worm-like expanded graphite
Madagascar	Unknown	Powder

Table 3.1: Five graphite samples from different supplier

The expanded graphite was produced by thermal shock of acid intercalated GICs by the supplier. [5] The expanded graphite sample was intercalated by H_2SO_4. Then the prepared H_2SO_4-GICs were washed and dried for further heat treatment which was performed by inserting expandable H_2SO_4-GICs in a muffle furnace. Finally the thermal shock leads to removal of H_2SO_4 and formation of expanded graphite.

SEM was preformed for the five graphite samples to observe their surface morphologies. Figure 3.2 shows the SEM images of five graphite samples. Image (a) and (b) are SEM for natural graphite. This graphite sample is composed of small graphite platelets of ca. 300 micron size. Actually some have dimensions up to 1mm. From edge of these platelets, one magnified SEM image, figure 3.2 (b), shows the compact layers of graphene sheet. From naked-eye observation, the graphite from Sigma-Aldrich has the morphology as natural graphite, they are small flakes. Figure 3.2 (c) SEM image of Sigma-Aldrich, these platelets show similar dimension as natural graphite. Graphite from TIMCAL and Madagascar are both in form of powder. Figure (f) show the "worm-like" structure of expanded graphite. The intercalation of H_2SO_4 into graphite results in extension of the interlayer spacing of graphene plane, as shown in inserted SEM photo in figure 3.2 (f).

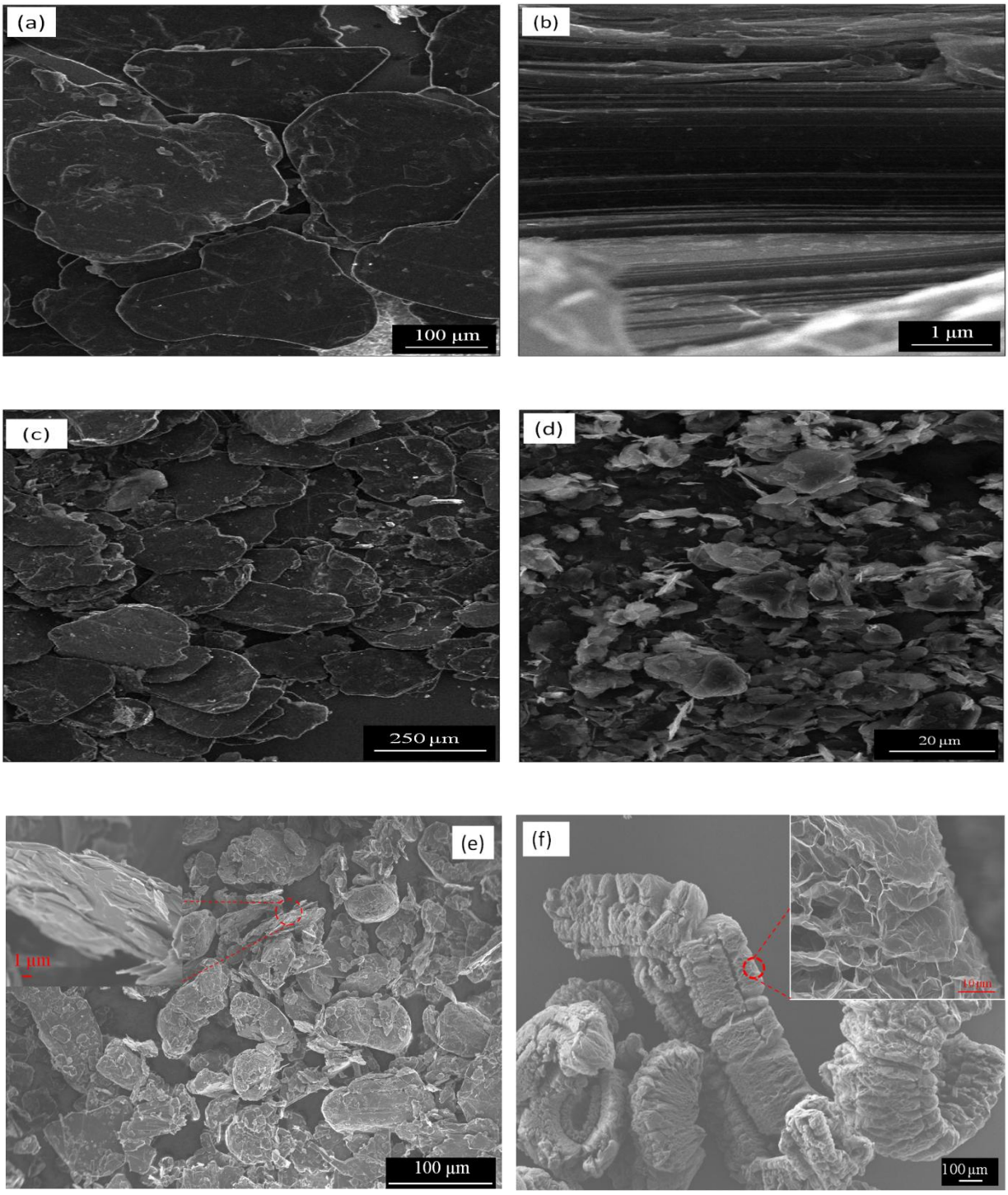

Figure 3.2: SEM micrograph of five graphite samples. (a-b) natural graphite; (c) graphite from Sigma-Aldrich; (d) graphite from TIMCAL; (e) graphite from Madagascar; (f) expanded graphite.

SEM images of those samples provide us information of surface morphologies and a three-dimensional appearance of the samples. To understand better their crystal structure, XRD were performed for the samples.

1.1.2 X-ray Diffraction analysis (XRD)

Characterization of structural parameters of graphite samples, such as crystallite size, is important for identifying the best starting graphite sample. X-ray diffraction line profile analysis was preformed to estimate crystallite sizes over large volumes.

a) Sample preparation

In order to increase the peak intensity at high 2θ, the sample size should not be too large. Since natural graphite and graphite SA are in platelet form, the samples were at first ground into powder in agate mortar, and then the ground samples were sieved through a 270mesh sieve for separating the small graphite particle from relatively larger graphite particle. The graphite TIMCAL and Madagascar graphites were just sieved through the sieve. For expanded graphite, the hand grind can turn samples into graphite foil, thus for XRD we used unground materials.

b) X-ray diffraction analysis

The X-ray diffraction line broadening analysis includes: 1) diffraction pattern acquisition, 2) profile fitting, 3) in-plane (L_a) and out-of-plane (L_c) crystallite sizes calculation. Figure 3.3 shows schematically an image of graphite and its sizes: in the basal plane/in-plane L_a and perpendicular to the basal plane/out-of-plane L_c.

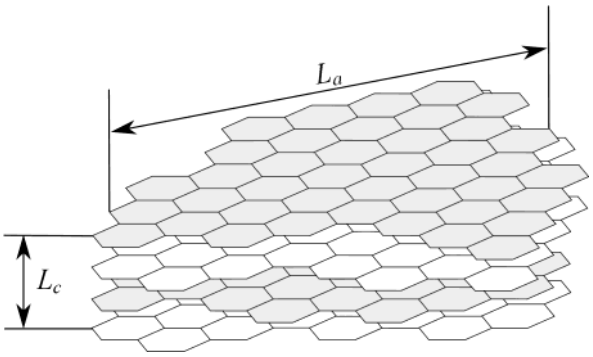

Figure 3.3: The schematic image of graphite

The diffraction patterns were acquired on a Philips 1050-diffracometer (Cu K_α radiation, from 8 ° to 79 °, 0.02 °/ step). All X-ray diffraction acquisitions were performed with Mr. Eric Lebraud in the Institut de Chimie de la Matière Condensée de Bordeaux (ICMCB). The obtained X-ray diffraction patterns were analyzed with a popular XRD data analysis package MDI Jade (Version 6.0), which can be used to perform empirical peak profile fitting and estimate of crystallite size. [6] These XRD patterns were carefully smoothed to avoid distortion of the line shape. The diffraction line widths were determined by fitting with Peason VII function. [6]

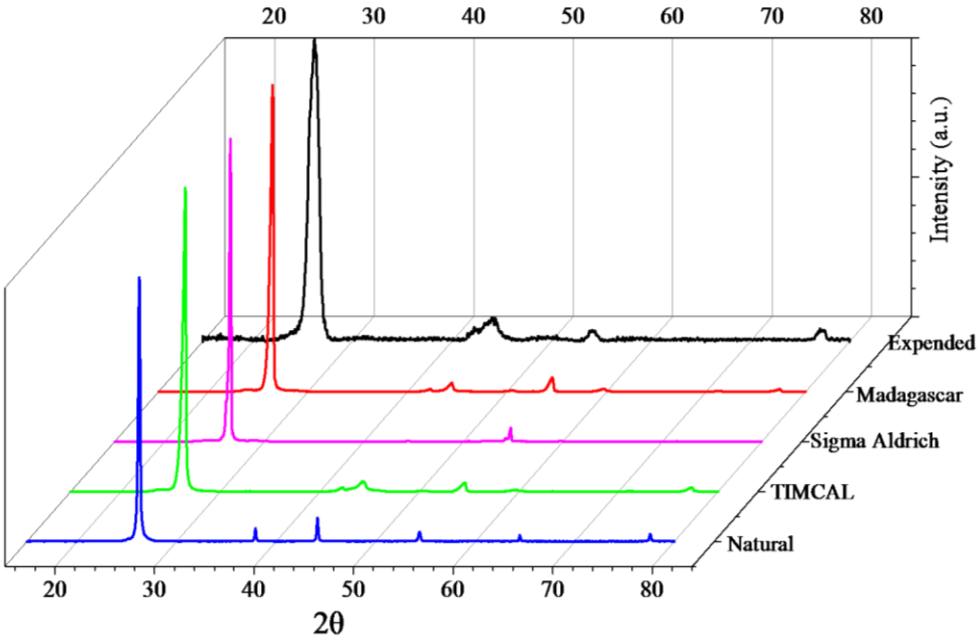

Figure 3.4: X-ray diffraction patterns of five graphite samples.

From XRD patterns of graphite samples, illustrated in figure 3.4, we can see two major peaks (002) and (004) located respectively around 26.5 ° and 54.5 °. These two peaks represent perpendicular direction (*c*-axis) to the graphene hexagonal planes. [7] With Bragg's law: $2d\sin\theta = n\lambda$, where d is the spacing between diffracting planes, 2θ is the incident angle (002) peak (26.2 °), λ is the wavelength of diffraction beam (Cu K_α, 1.5405 Å), we can calculate the basal spacing d_{002} = 3.36 Å.

The conventional way to obtain the average Crystallite size L_{hkl} of microscopic powder particle in the [*hkl*] direction is to apply the Scherrer equation: [8, 9]

$$L[hkl] = \frac{K\lambda}{\beta_{hkl} COS(\theta)}$$

- h,k, l are Miller indices;
- K: Scherrer constant;
- λ: the wavelength of the diffraction beam;
- $2\theta_{hkl}$: the position of the (*hkl*) line;
- β_{hkl} : the full width at half maximum (FWHM) of the (*hkl*) line;

This equation implies that the crystallite size varies inversely with the width of the diffraction peak; as the crystallite size gets smaller, the peak gets broader. The value for K is usually 0.89.

The average in-plane crystallite sizes (L_a) were determined from the FWHM values of (110) peak, whereas the out-of-plane crystallite sizes (L_c) were determined from the (002) FWHM by using Scherrer equation. The calculated values of the in-plane (L_a) and out-of-plane (L_c) crystallite sizes are listed in table 3.2.

	(002)		(110)	
	2θ	crystallite size L_c (nm)	2θ	crystallite size L_a (nm)
Natural	26.48	35.5	77.6	52.4
Sigma-Aldrich	26.60	36.3	77.41	27.8
TIMCAL	26.47	21.9	77.36	17.9
Expanded graphite	26.02	7.1	76.96	37.5
Madagascar	26.41	23.3	77.38	25.5

Table 3.2: Calculated average crystallite size L_a and L_c according to Scherrer equation

It should be noticed that the instrumental profile width should be corrected when one applies Scherrer equation for estimation of crystallite size. [10] This can be performed with standard silicon specimen described in "Standard Reference Materials" SRM 640c. Unfortunately, we don't have this standard silicon, so the calculated crystallite sizes are not accurate. They are smaller than estimated values with correction of instrumental broadening. Since the error caused by instrumental broadening presents in all XRD patterns, the calculated values can still be used to help us to evaluate microstructures of samples. The results show that except for expanded graphite all the graphite samples have similar crystallite size and natural graphite has the largest crystallite size L_a in graphene basal plan.

1.1.3 Study of Crystallite size with Raman Spectroscopy

Besides XRD, Raman spectroscopy can also be used to estimate crystallite size of graphitic materials. In the pioneering work of Tuinstra and Koenig in the 1970s, they performed

systematic Raman and x-ray diffraction characterizations. Their studies show that there is a proportional relationship between the intensity ratio of the D and G bands (I_D/I_G) and the inverse of crystallite size L_a. [11, 12] This work was based on a fixed excitation laser energy. Later work performed by Mernagh et al. showed that the ratio I_D/I_G depends strongly on the excitation laser energy (E_l). [13] In 2006, Pimenta et al. performed X-ray diffraction and Raman characterizations (varying excitation laser energy from 647 nm (1.92 eV) to 457.9 nm (2.71 eV)) to determine the crystallite size L_a from Raman spectrum. [14] They found that I_D/I_G is inversely proportional to the fourth power of the laser energy used:

$$L_a(nm) = (2.4 \times 10^{-10})\lambda_l^4 \left(\frac{I_D}{I_G}\right)^{-1}$$

where λ_l is the excitation laser used in nanometer units, and I_D/I_G is the integrated intensity ratio of the D and G bands.

We thus applied Raman spectroscopy to characterize our sample natural graphite. Raman scattering experiments were performed with JOBIN YVON Xplora Raman microscope at room temperature using the following excitation laser energies: 785 nm (1.58 eV), 638 nm (1.94 eV) and 532 nm (2.33 eV). The spectra were collected under a microscope (× 100 objectives). The Raman acquisition was performed by a holographic grating with 1800 lines/mm and detected by a charge-coupled device (CCD) camera. By using a laser filter, very low incident power (<1 mW) was used to avoid local heating and graphitization effects caused by incident laser. [15]

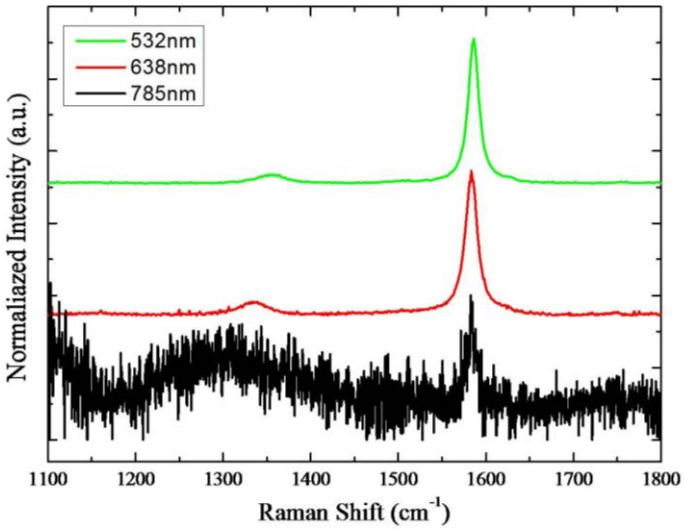
532nm
638nm
785nm
Normaliazed Intensity (a.u.)
1100 1200 1300 1400 1500 1600 1700 1800
Raman Shift (cm-1)

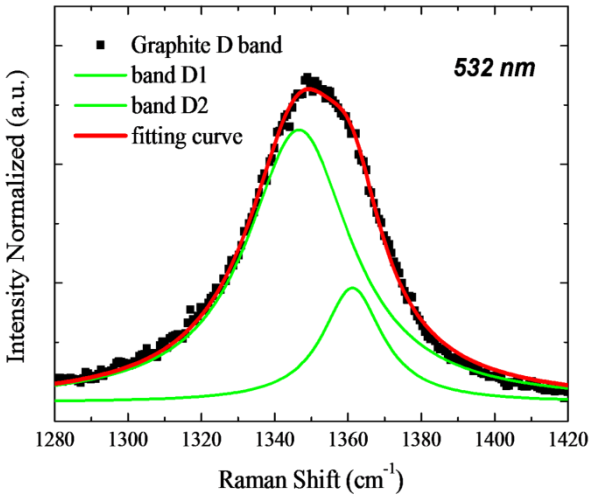
Graphite D band
band D1
band D2
fitting curve
532 nm
Intensity Normalized (a.u.)
1280 1300 1320 1340 1360 1380 1400 1420
Raman Shift (cm-1)

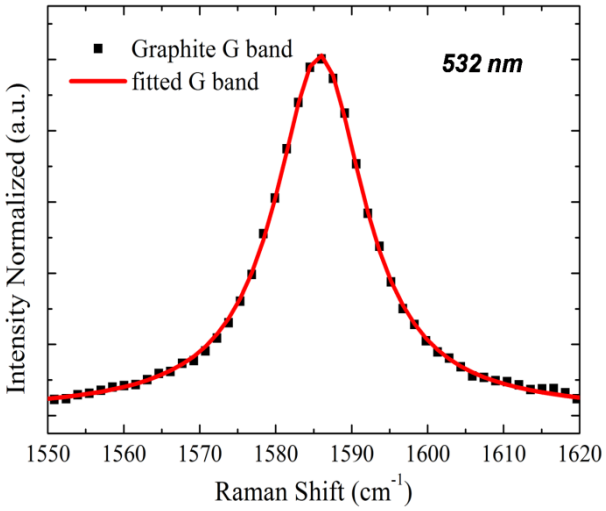
Graphite G band
fitted G band
532 nm
Intensity Normalized (a.u.)
1550 1560 1570 1580 1590 1600 1610 1620
Raman Shift (cm-1)

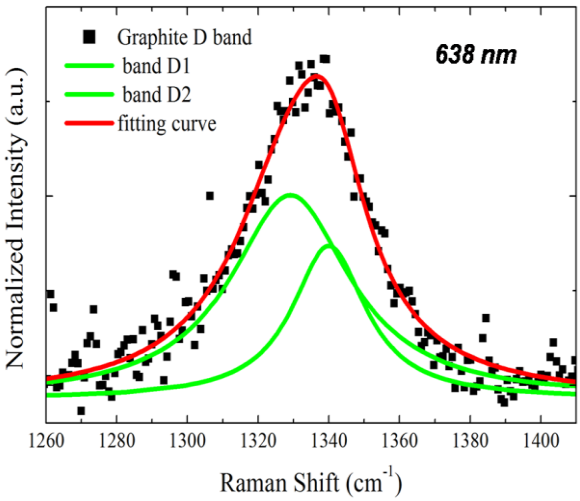
Graphite D band
band D1
band D2
fitting curve
638 nm
Normalized Intensity (a.u.)
1260 1280 1300 1320 1340 1360 1380 1400
Raman Shift (cm-1)

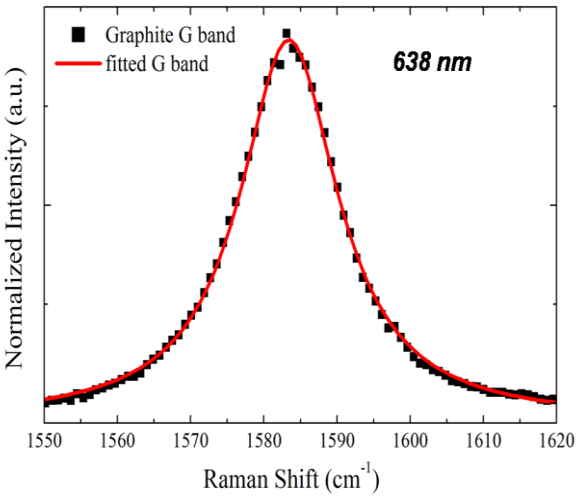
Graphite G band
fitted G band
638 nm
Normalized Intensity (a.u.)
1550 1560 1570 1580 1590 1600 1610 1620
Raman Shift (cm-1)

Figure 3.5: Raman spectra of graphite Nature 4 under three different excitation laser energy (2.33 eV, 1.94 eV and 1.58 eV). Fitted D band and G band for 532 nm (2.33 eV) and 638 nm (1.94 eV).

Raman spectra in figure 3.5 demonstrate an intens G band which doesn't change despite the change of excitation energy. And there is a smaller band around 1350 cm^{-1} called D band. However, for 785nm (1.58eV) laser energy, there is a large oscillation from 1200 cm^{-1} to 1500 cm^{-1}, which totally covers the D band, resulting in uselessness of this spectrum. Finally, the line-shape analyses were performed for 523 nm and 638 nm Raman spectra. D band were fitted by two Lorentizan function whereas G bands can be fitted with only one Lorentzian function.

	D band (cm^{-1})		G band (cm^{-1})	I_D/I_G	La (nm)
	D_1 band	D_2 band	G band		
532nm (2,33 eV)	1348	1360	1586	0.15	128
638nm (1,94 eV)	1330	1340	1585	0.25	159

Table 3.3: D and G band position (ω_D and ω_G) and intensity (I_D and I_G). L_a values estimated from equation

The results listed in table 3.3 show that the G band position don't change with excitation laser energy, whereas D band displays a red-shift when laser wavelength varies from green to red. From their ratios I_D/I_G and equation, the calculated crystallite sizes L_a from two laser excitation energy are shown in table 3.3. These estimated crystallite sizes are bigger than the crystallite size calculated from XRD pattern.

1.1.4 Elemental composition analyses

X-ray photoemission spectroscopy (XPS) is often used for surface analysis in order to obtain elemental composition information of carbon materials. XPS analyses of the five graphite samples were performed in PLACAMAT analysis centre by Dr. Christine Labrugère. The

graphite samples were fixed on a sample-holder by using double sided adhesive copper tape. In this way, samples could be smooth, flat and free from contamination, which ensure good quality data. XPS were performed with a VG Escalab 220i XL X-Ray Photoelectron Spectrometer under ultrahigh vacuum conditions. All spectra were taken using Mg non-monochromatized source (1253.6 eV) at 200 W. The spot size was approximately 25 µm. The acquired spectra were treated with Labspec 4.18. XPS analyses of all graphite samples are shown in figure 3.6.

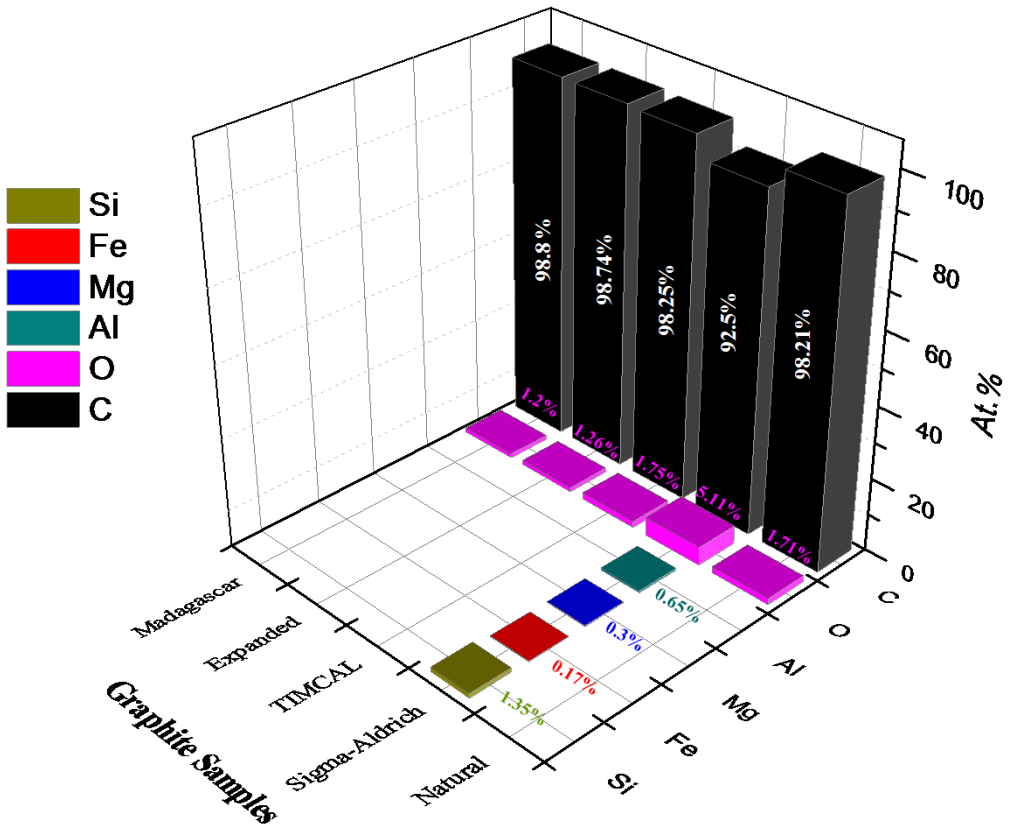

Figure 3.6: XPS Elemental composition analyses of graphite samples

From the results of XRD and XPS characterizations, we chose natural graphite which has the largest in-plan crystallite size and highest sp^2 graphitic carbon contents as our starting graphite material to synthesize GICs.

1.2 GICs synthesis

Since the potassium is very sensitive to oxygen and moisture, sample preparations were performed in a glove box where the ambient environment inside the box is filled with inert gas (Argon) and oxygen level is controlled as low as 5-10 ppm, as well as the moisture level. The starting materials are natural graphite and potassium metal (from Sigma-aldrich, 98% trace metals basis, potassium chunks stored in mineral oil). Before synthesis, the potassium was washed with ether to remove the paraffin oil and the oxide part was cut away. Graphite sample was degassed in anti-chamber under vacuum for ~12 hours to remove any residual water or solvent that may have been adsorbed on surface.

The GICs sample were prepared by using one-zone vapour transport technique for stage-1 KC_8 synthesis and two-zone vapour transport technique for stage-2 KC_{24} and stage-3 KC_{36}. With those two techniques we can produce GICs with well-defined stage. In one-zone vapour transport technique, the weighted graphite and potassium were placed together in Pyrex tubes; in two-zone vapour transport technique, graphite and potassium were placed separately in a Pyrex tube as illustrated in figure 1.11, and the tube was evacuated to 10^{-5} mbar and sealed. The sealed tube was then placed in a furnace for 3 day in order to get homogenous GICs samples. Since one-zone vapour transport technique was applied for stage-1 KC_8, the tube was placed in one furnace where the temperature is fixed at 250°C. For stage-2 KC_{24} and stage-3 KC_{36}, tube was placed in a two-zone furnace where graphite and potassium were maintained at different temperatures T_g and T_i ($T_g > T_i$). The temperatures used for synthesis are listed in figure 3.7. T_i is maintained at 250°C in order to have a high enough potassium vapour pressure and a satisfactory reaction rate for the intercalation reaction. By adjusting the temperature difference T_g - T_i, well intercalated stage-2 KC_{24} and stage-3 KC_{36} were obtained.

They can be qualitatively identified by their color: golden for stage-1 KC_8, blue for stage-2 KC_{24} and dark-blue for stage-3 KC_{36}, shown in figure 3.7. [16]

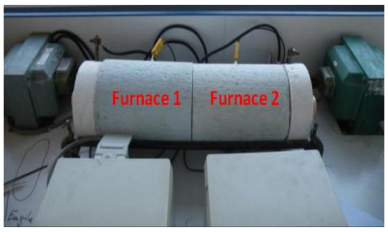

	K (T_i=250°C)
Stage	T_g (°C)
1 (KC_8)	250
2 (KC_{24})	350-400
3 (KC_{36})	450-480

 stage 1

 stage 2

 stage 3

Figure 3.7: "two-zone furnace" for GICs synthesis, T_i and T_g for the preparation of potassium-GICs by the two zone vapour transport method. [16]

After reaction, a thin film of potassium was typically plated onto the glass which meant that not all of the loaded potassium was necessarily intercalation into the sample.

1.2.1 XRD Characterization of GICs

X-ray diffraction measurements can be used to verify phase purity of GICs samples synthesized from graphite sample. Unlike the starting graphite, we can't use hand grinding to prepare the sample for XRD since potassium-GICs (K-GICs) are sensitive. Hand-grind will cause de-intercalation of K-GICs samples. So K-GICs were carefully sealed into 1.5 mm glass capillary tube in order to protect the sample from oxygen and moisture during XRD measurements. The XRD patterns were collected on a PANalytical X'Pert Pro diffractometer [Cu-Kα radiation (λ = 1.54056nm), X'Celerator detector] within the range 5 – 100 ° (2θ). All measurements were collected at room temperature in Laboratoire Ondes et Matière d'Aquitaine (LOMA) with Dr. Philippe Négrier.

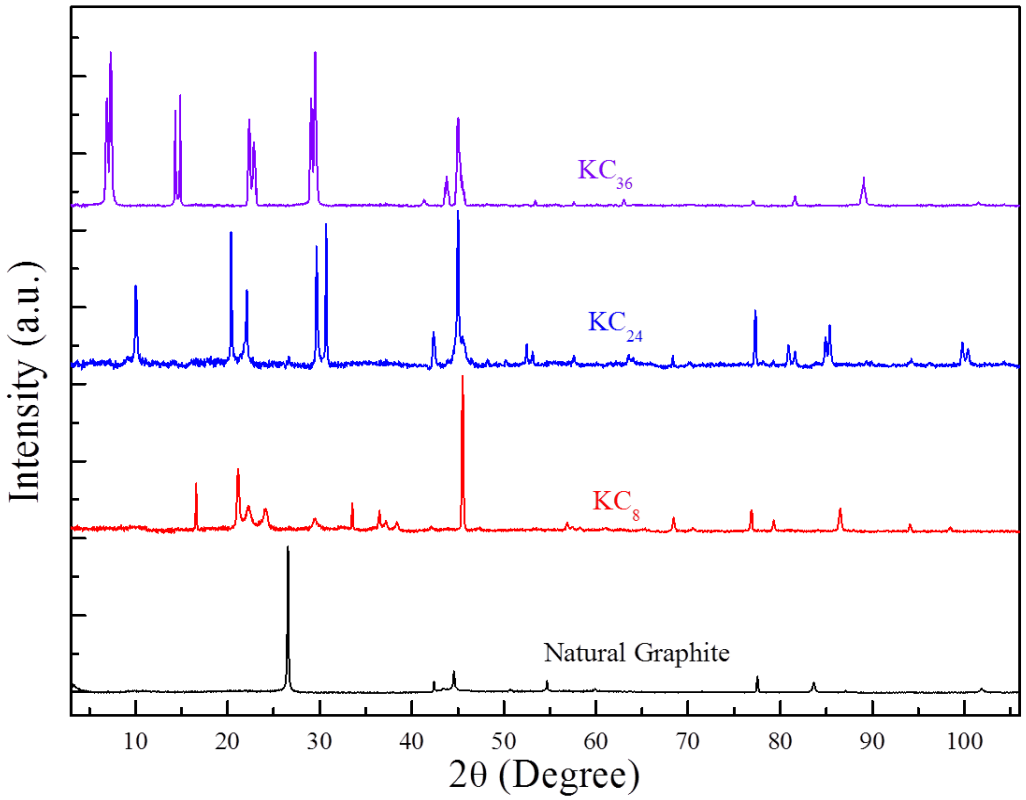

Figure 3.8: Comparison of the XRD patterns of stage-1 KC_8, stage-2 KC_{24} and stage-3 KC_{36} K-GICs

XRD patterns of the three K-GICs samples are shown in figure 3.8. A summary of lattice parameters for three synthesized K-GICs is listed in table 3.5. The lattice parameter refers to the distance between intercalated potassium layer.

Sample	[00*l*]	Lattice parameter (Å)
Natural	26.48°	3.36
KC_8	16.58°	5.34
KC_{24}	10.02°	8.81
KC_{36}	7.30°	12.09

Table 3.5: Lattice parameters of synthesized graphite intercalation compounds

Analysis of figure 3.8 and table 3.5 shows that graphite 002 peak located at 26.48° is disappeared in all XRD patterns of GICs. GICs XRD patterns show their characteristical diffraction peaks, which implies the synthesized compounds are desired GICs.

1.2.2 Raman spectroscopy

Raman spectroscopy was used as an alternative method to verify the phase of prepared GICs samples. The GICs were sealed into quartz cuvettes in a glove box for Raman characterizations. Raman measurements were performed with JOBIN YVON Xplora at room temperature by using 532 nm (2.33 eV) excitation laser. The spectra were collected under a microscope (× 50 objectives). The Raman-scattered light was dispersed by a holographic grating with 2400 lines/mm for high spectral resolution and detected by a charge-coupled device (CCD) camera. Since laser induced heating effect upon K-GICs samples can easily cause the de-intercalation, the special attention should be paid when the Raman study is performed for GICs samples. By applying a laser filter (1%) integrated in Raman spectroscopy, the laser power was always kept below the power values leading to de-intercalation. The laser power after the filter can decrease to 0.16 mW. It is important to mention that once the sample is highly intercalated, the spectra acquisition should be with low exposure time to avoid laser induced de-intercalation. During the whole experiment the samples were checked by verifying their color to ensure the samples were not de-intercalated. The studies of deintercalation caused by laser-induced heating effect are included in annex.

Raman spectrum for pristine graphite, KC_8, KC_{24} and KC_{36} are displayed in figure 3.9. In Raman spectrum of graphite, the peak around 1580 cm^{-1}, called G band, is typically assigned to the E_{2g} mode. Because, in KC_8 the graphene planes are heavily charged and surrounded by two potassium layers, both the line-shape and the position of the G band are thus strongly

affected. In stage-2 KC_{24}, the G band is located around 1600 cm^{-1} is assigned to the E_{2g} mode of graphite where the graphite layer is bounded by an intercalant layer on one side and a graphene layer on the other side. For stage-3 KC_{36}, the G band is split into two bands, one corresponds to boundary layer which is bounded by one potassium layer and graphene layer, another band corresponds to interior layer which is surrounded by two charged graphene layers.

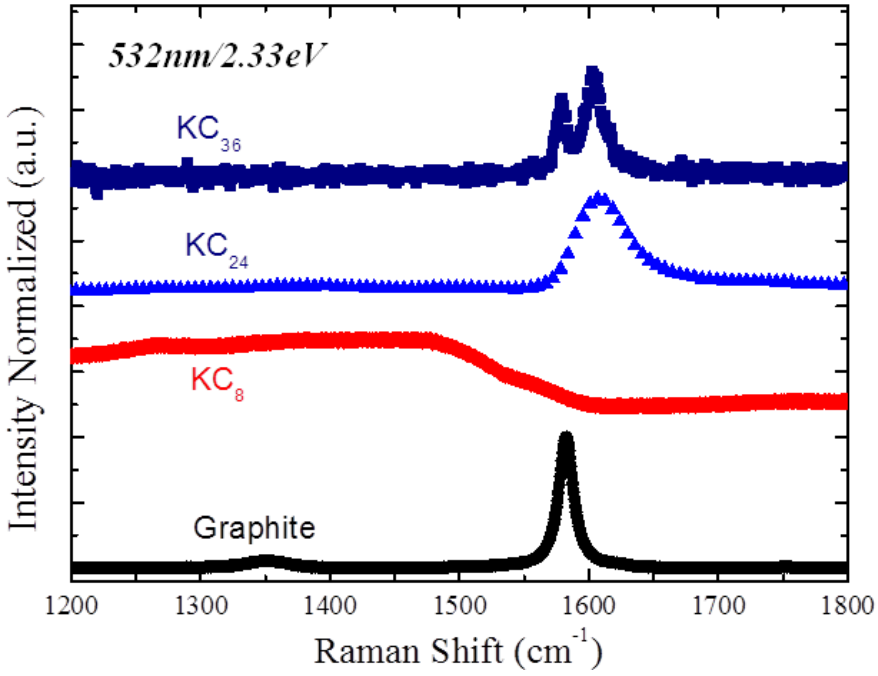

Figure 3.9: Raman scattering spectra G band of pristine graphite and three synthesized potassium-GICs: stage-1 KC_8, stage-2 KC_{24} and stage-3 KC_{36} at room temperature. Measured scattering was from individual flakes.

These G bands show a strong change in character with doping. To investigate these doping effects in more detail, line-shape analysis were performed for the G band of the three K-GICs samples. In the previous section, it has been noticed that the G peak of graphite can be fitted with a single Lorentizan function. However in GICs samples, regarding the line shape, the G

bands of three K-GICs samples have been fitted by a Breit Wigner Fano (BWF) function of the form:

$$I = I_0 \frac{\left(1 + \frac{\omega - \omega_0}{q\Gamma}\right)^2}{1 + (\frac{\omega - \omega_0}{\Gamma})^2}$$

where ω_{ph} is the phonon frequency, Γ is the full width at half maximum (FWHM) or damping, $\boldsymbol{q}$ the asymmetry parameter. Those special G peak line shapes are due to coupling between the phonon and an electronic continuum, [17] and it is commonly found in the Raman spectra of doped graphitic systems. The G band is split into two bands in stage 3 KC_{36}, and two BWF functions were employed to fit these G bands.

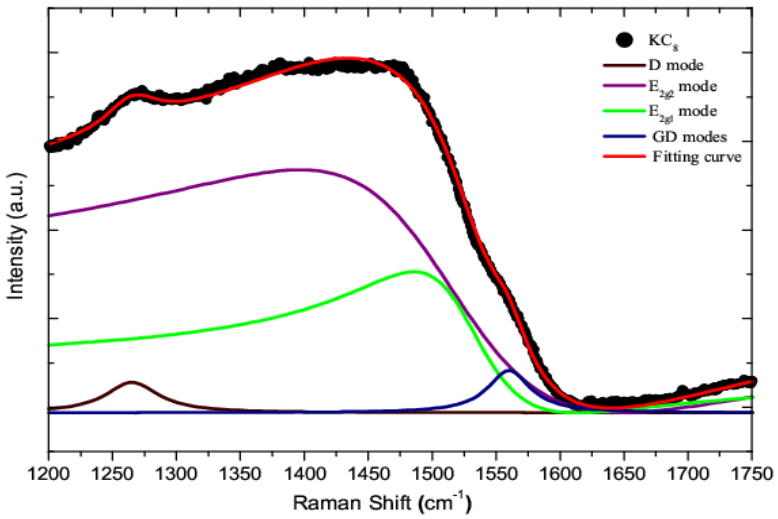

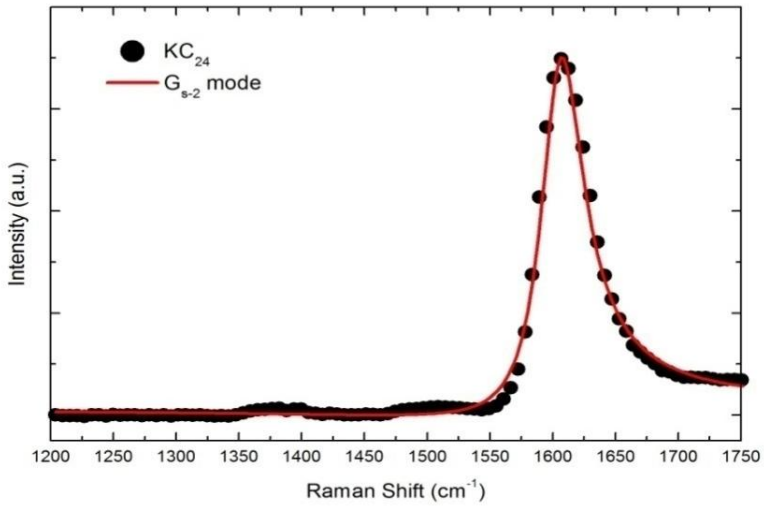

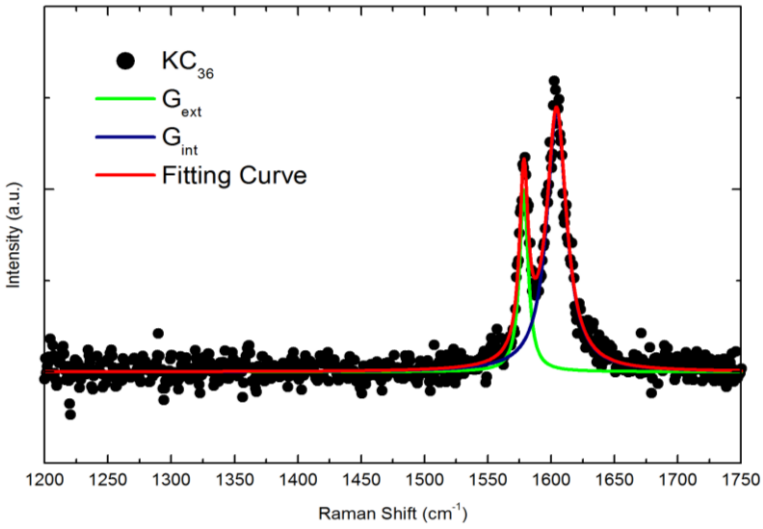

Figure 3.10: The detailed line-shape analysis of the three compounds: KC_8, KC_{24} and KC_{36}

In the Raman reponse of graphitc materials, optical vibration modes are presented in the following irreducible representation:

$$\Gamma = 2A_{2u} + 2B_{2g} + 2E_{1u} + 2E_{2g}$$

The E_{2g} mode is Raman active. Indeed, the common band present in Raman spectra of graphite materials, G band, corresponds to this first-order Raman active mode E_{2g}. Previous Raman studies in GICs confirmed that the presence of the E_{2g} mode is around 1600 cm^{-1}. [18, 19] For stage-1 KC_8 illustrated in figure 3.10, a detailed and accurate analysis of G peak analysis is illustrated by introducing four components named as: D, E_{2g2}, E_{2g1}, and $G_{s\text{-}2}$. Each individual component was fitted by using a BWF function. From fitted results, we can observe the E_{2g1} mode at ~1525 cm^{-1}, which is attributed to not homogeneous, de-intercalated or not complete intercalation in stage-1 compounds with asymmetry $\boldsymbol{q}$ = -1.5. [20] The E_{2g2} mode is around ~1510 cm^{-1} with a clear and strong Fano behavior ($\boldsymbol{q}$ = -1.1 and Γ = 125 cm^{-1}) which is the characteristic peak for stage-1 GICs. [18, 21, 22] The D mode at 1274 cm^{-1} is attributed to intrinsic defects on the edges and / or the presence of disorder due to high intercalation. [23, 24] The last mode GD is located ~ 1560 cm^{-1}. For stage-2 KC_{24} Raman

spectra illustrated in figure 3.10 shows an intrinsic G_{s-2} mode at 1606 cm^{-1} with Γ = 20 cm^{-1}, which is in agreement to experimental results previously reported. [24, 25]

	KC_8			KC_{24}			KC_{36}		
	ω	Γ	$\boldsymbol{q}$	ω	Γ	$\boldsymbol{q}$	ω	Γ	$\boldsymbol{q}$
D	1265	25	10^5	—	—	—	—	—	—
E_{2g2}	1510	125	-1.1	—	—	—	—	—	—
E_{2g1}	1525	58	-1.5	—	—	—	—	—	—
GD	1560	20	10^5	—	—	—	—	—	—
G_{s-2}	—	—	—	1606	20	6.5	—	—	—
G_{ext}	—	—	—	—	—	—	1578	8	10^5
G_{int}	—	—	—	—	—	—	1604	19	10^5

Table 3.6: Fitting parameters to the components of the G line in Raman spectra of stage-1 KC_8, stage-2 KC_{24}, stage-3 KC_{36}.

The parameters of fitting results are summarized in table 3.6. For stage-3 KC_{36}, the asymmetry of two bands was $\boldsymbol{q}$=10^5 approaching a Lorentzian function, which means we can also use two Lorentzian functions to fit two G bands of stage-3 KC_{36}. The detailed analysis of the G peaks in stage-3 KC_{36} and an intrinsic Raman resonance of stage-3 will be presented in next section.

2. Raman resonance of stage-3 KC_{36}

In GICs, due to the charge transfer between the layers of graphene and the intercalated potassium layers, the Fermi levels are strongly shifted. Thus, properties of GICs are highly dependent on the number of graphene layers between intercalant layers. Potassium is known to give its electron leading to a large charge transfer f_C close to −1/8 for stage 1 (KC_8) and −1/24 for stage 2 (KC_{24}).[26,27] Charge transfer per carbon atom f_C and density of charge σ of the graphene layer are related by:

$$f_C = 0.0026\ \sigma$$

with σ in 10^{12} cm^{-2}. Raman scattering is a powerful technique which has proven in-valuable for characterization of pristine graphene. For graphite, only E_{2g} represents the Raman-active modes, and there are two first-order doublet Raman-active optical modes of E_{2g} symmetry. [28] One of these represents an intra-layer vibration mode which involves an out-of-phase displacement for carbon atoms in adjacent layers, and the other one corresponds to rigid-layer vibration which is in-phase displacement, as illustrated in figure 3.11. [24]

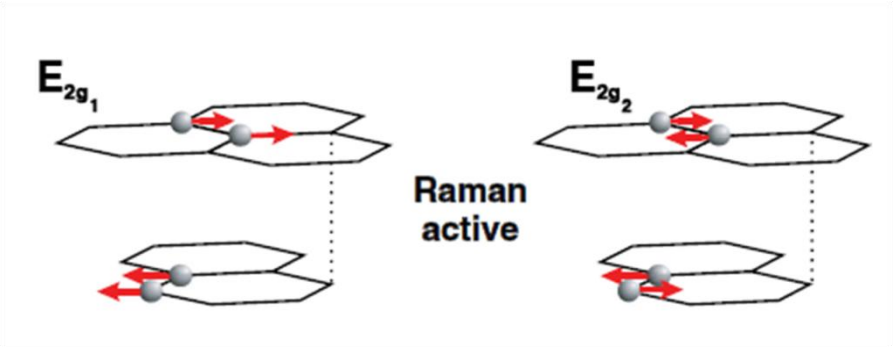

Figure 3.11: Optical modes of graphite

Due to the fabrication of graphene transistors, the electron-phonon coupling leading to non adiabatic effects has been accurately investigated. As a consequence, Raman spectra obtained on GICs have been revisited recently. [25] In previous section, the line-shape analysis of the

three K-GICs was presented for 532 nm laser excited Raman spectrum to understand the electron-phonon coupling. So far, resonant Raman scattering of potassium intercalated graphite with different excitation energies is still missing as several empirical laws show a linear behavior and consequently,[19, 29] one could suppose that nothing is expected by varying the excitation energy. Besides a better understanding of graphene physics, [30, 31] a thorough analysis of potassium GICs should prove invaluable as a comparative analysis tool for graphenide solutions, a choice method to exfoliate graphite in large quantities. [1, 2, 32, 33, 34]

The electron-phonon coupled mode, G band, is particularly interesting for investigating the doping effect.[35-38] Three effects are present: the lattice expansion softens the G band vibration, the carbon potassium interaction leads also to a decrease of the G band wave-number and finally the non adiabatic effects harden the G band. As the non adiabatic effects are modulated by the lifetime of the coupled state, determining the charge transfer from only the Raman shift is nearly impossible without the help of *ab-initio* calculations.

Resonant Raman scattering has brought information on the electronic modifications induced by intercalants by monitoring relative intensity for p-type doping. [39] The situation is more complicated for n-type doping. From the work of Lazzeri and Mauri, [40] the Fermi level shift ε_F is linked to the charge transfer f_C (without unit) by:

$$\varepsilon_F\,(eV) = -sign(f_C) \times 6.04 \times \sqrt{|f_c|}$$

This value obtained from first principle calculations is more accurate than the expression used in the past derived from tight binding: [41]

$$\varepsilon_F(eV) = -sgin(f_C) \times \sqrt{\gamma_0^2 \pi \sqrt{3|f_c|}} = -sgin(f_C) \times 6.76 \times \sqrt{|f_c|}$$

where γ_0=2.90 eV is the next-neighbor C-C overlap integral. The charge transfer from the potassium atom is nearly complete. [42]

2.1 Raman scattering

For Raman analysis, the samples were placed in sealed cuvettes and performed in CEMES Toulouse with Dr. Pascal Puech. The color of the flake under study, indication of the stage, was visually verified before the measurements. An objective with long working distance was used (NA = 0.5). The laser power was always kept below the value leading to deintercalation, typically selecting a value of 2 mW with a magnification objective of 40x. Raman spectra were acquired with various spectrometers (UV Dilor, T64000 Jobin-Yvon Horiba, visible Dilor, XPlora) depending on the available laser sources.

For stage 1, a Fano shape is well marked, with a small q value (-1.2) at 2.33 eV, whereas in the UV range, the Fano shape is less well marked (q tending to large value). For stage 2 at 2.33 eV, the background is higher for longer wavenumbers after the coupled mode, characteristic of a Fano shape with a positive coupling factor. In the UV, the Fano shape tends to a simple lorentzian. The wavenumber fluctuations in the fitted Raman spectra are due to the intercalation process. The stoichiometry of each stage can vary a little and is easily observed with liquid p-type doping. [43] If a coupled mode has a large half width at half maximum (HWHM), its wavenumber cannot be accurate. In order to have an idea of the dispersion, we have acquired 80 Raman spectra on KC_{36} at different locations. We have selected nice surfaces with dark blue color and rejected spectra too far from our average spectrum. The deduced histograms are reported in Figure 3.12.

The standard deviation for the G band of the interior layer is 0.4 cm^{-1} and for the bounding layer 0.8 cm^{-1}. As expected, the larger the HWHM, the larger the standard deviation. We are in the optimal conditions with visual checks, and even in that case, some fluctuations appear. The laser power was really low, and de-intercalation is nearly impossible. This strategy is not possible with all samples as all our spectrometers are not equipped with binocular.

Fluctuations in the G band positions are consequently due to statistics as we probe at each time a different location of the sample. At the micrometric scale, a small fraction of the sample that could be estimated to 1% is not intercalated at the same stage.

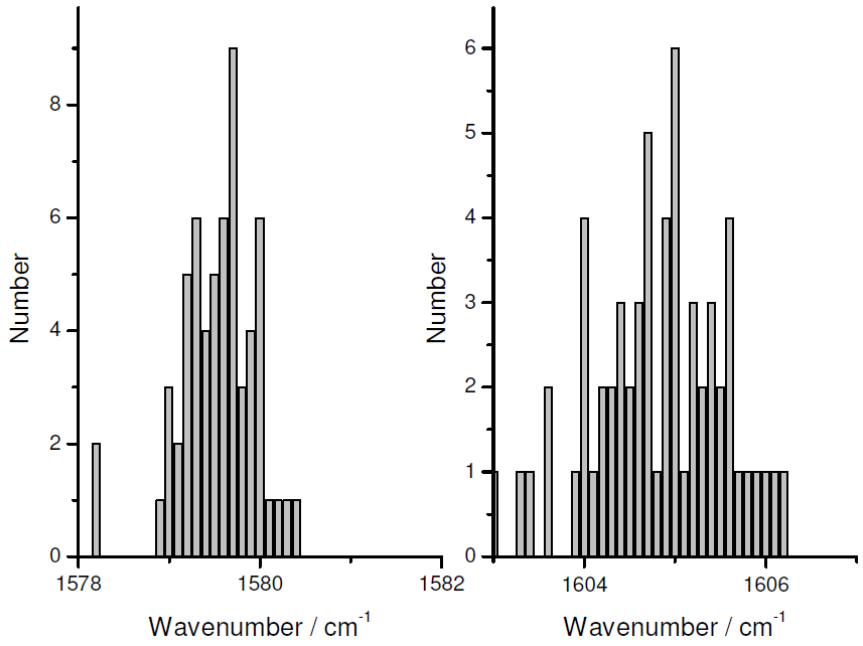

Figure 3.12: Histogram for G band position associated to Raman spectra of KC_{36} at 638 nm (1.94 eV)

Typical Raman spectra of KC_{36} using several excitation wavelengths available in our laboratory are reported in Figure 3.13. The highest available energy was 4.13 eV (300 nm). For stage-3 GICs, the interior layer is not equivalent to the boundary layers; hence, two G lines are expected, as observed. Their relative intensities change as a function of the laser energy. They can be fitted with two Lorentzians (corresponding to Fano shape with large q coupling factor $\boldsymbol{q} = 10^5$). An average value of 1580 cm^{-1} for the G mode of the interior layer is obtained with an HWHM of 4 cm^{-1}. This small value of the HWHM proves that a residual doping is present. [44] A intermediate charge transfer and lattice expansion due to the neighboring expanded boundary layers are present as recently reported. [29] For the boundary layers, a wavenumber value of 1605 cm^{-1} with an HWHM of 10 cm^{-1} is observed. The

boundary layers have a wavenumber higher than the value obtained for KC_{24}: 1595 cm^{-1} and the HWHM is weaker at 10 cm^{-1} to be compared with 14 cm^{-1} for KC_{24}.

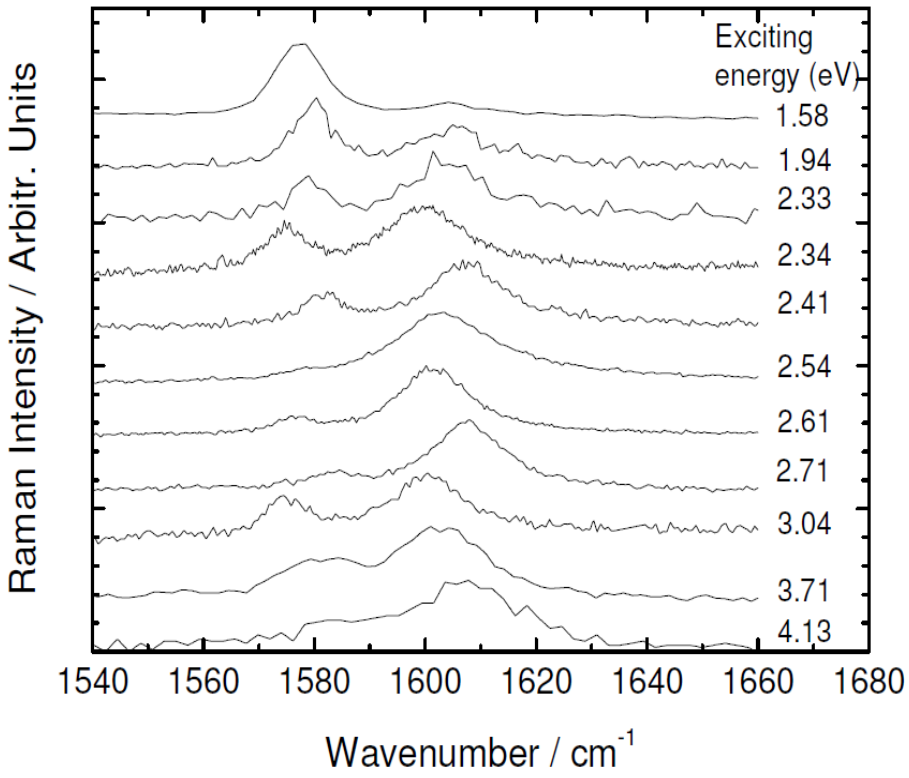

Figure 3.3: Typical Raman spectra of KC_{36} at various excitation energies. For sake of clarity, intensity of spectrum has been normalized to the highest mode. Only the relative intensities of the two G lines are meaningful.

The differences in the broadening and position between KC_{24} and the outer layers of KC_{36} could be attributed to doping. The fractional layer charge for the bounding layer is a little lower for KC_{36} than for KC_{24} as the interior layer bears some fractional charge. The first-principle calculations for stage-3 were performed by using a trilayer ABA surrounded by potassium. Charge transfer of 0.83 e^- for the potassium atom, with a fractional charge of 0.37 e^- for the A layers and 0.08 e^- for the B layer were obtained. These values are close to previous first-principle calculations. [45] As the rigidity of the assembly of n layers varies as n^3, one can suppose that KC_{36} is more rigid than KC_{24} and that the graphene layers in KC_{36} are

less distorted (corrugated) than in KC_{24}. As a consequence, the electron–phonon coupling could be larger for KC_{36} corresponding to an increased wavenumber upshift in comparison with KC_{24} at the similar doping level and also to a reduction of the HWHM between KC_{24} and KC_{36} as observed. [46]

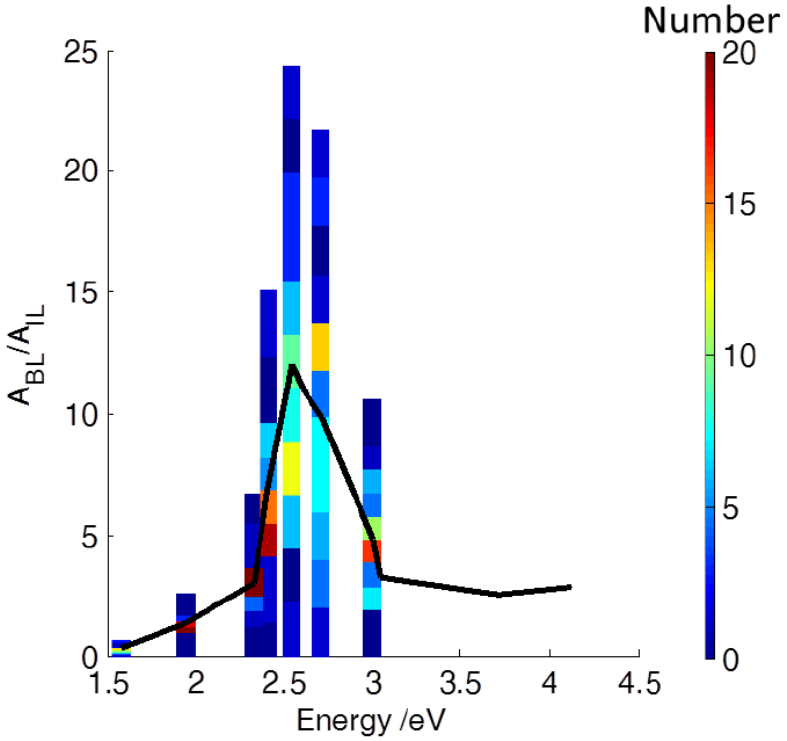

Figure 3.14: Ratio of the integrated intensity of the G band for boundary over interior layer (40 to 50 spectra depending on the excitation energy). Color codes for statistics: the number of times the experiment yields the corresponding ratio. The black line corresponds to the average value. It is clearly seen that measurements give very narrow distribution away from the resonance and highly dispersed data near and on the resonance.

In Figure 3.14, the ratio of Raman G band intensities of the bounding *versus* interior layers for KC_{36} is reported. In order to better ascertain the trend around the maximum value, some statistics have been obtained considering a sampling of 40–50 different crystals. A strong increase of the bounding versus interior G band intensity ratio is observed around 2.5 ± 0.1

eV. Away from 2.5 eV, statistics show a narrow distribution, while data around 2.5 eV are highly dispersed, as is expected close to a resonance. Above 2.5 eV, the ratio of intensity bounding/ interior is between 2 and 3, which is roughly close to the weight of 2 expected considering the number of layers. For exciting energies below 2.5 eV, the ratio of intensity bounding/interior increase with increasing exciting energy, and the fluctuations are very small. Around 2.5 eV, Yang and Eklund have reported strong vertical transitions associated with the interband structure in the optical dielectric function for the bounding layer. [47] Other weaker transitions (1.1 eV for interior layer and1.7 eV for interlayer) are also mentioned.

2.2 *ab*-initio simulation of Electronic band structure of KC_{36}

In order to check the origin of this maximum value at 2.5 eV, total-energy density functional theory calculations were performed by Dr. Iann Gerber in INSA with the *Vienna ab initio simulation package*, [47-50] All atoms have been fully relaxed until the forces on individual atoms were smaller than 0.01 eV/$Å^{-1}$. Cell shape and cell volume were also allowed to relax. The calculation cell used contained three layers of 24C atoms and 2K atoms [electronic configuration (Ne) $3s^2 3p^6 4s^0 3d^1$].

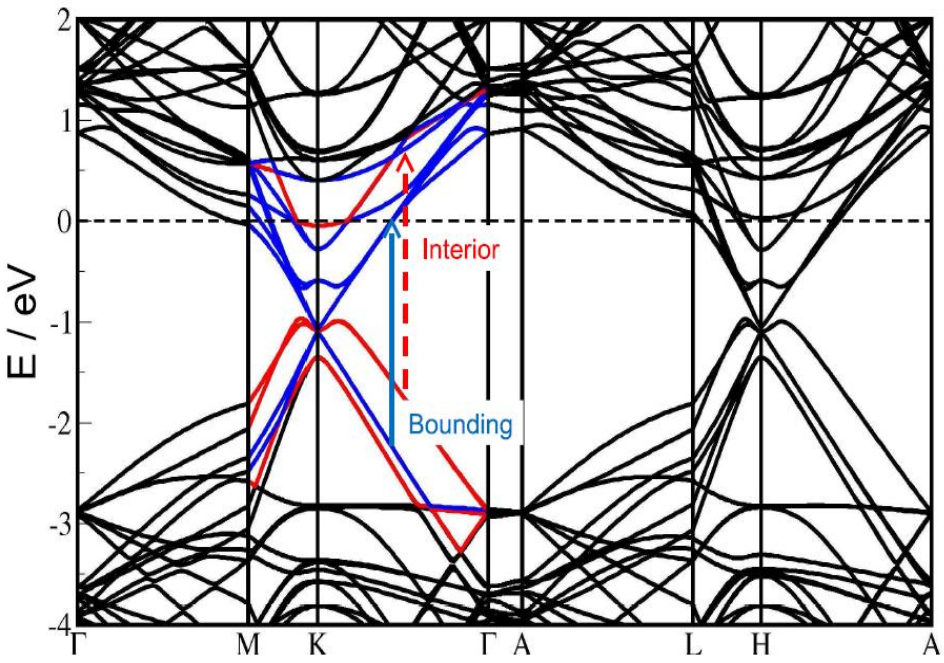

Figure 3.13: Electronic band structure of KC_{36}. The solid blue (dashed red) arrow corresponds to the bounding (interior) $\pi \rightarrow \pi^*$ transition. The Fermi level position is indicated.

A trilayer of graphene with ABA stacking is surrounded by potassium. Because of the presence of a symmetry center, there is no band gap in the structure reported in Figure 3.13. The electronic band structure is similar but more accurate than in the case of Yang and Eklund. Moreover, we obtain directly the whole structure in the three-dimensional Brillouin zone. [47] With this full electronic band structure, one can observe that at 2.5 eV, the transition $\pi \rightarrow \pi^*$ for the bounding layer is near the Fermi level. The inspection of the electronic band structure has not allowed to find another consistent explanation. Hence, we reason that resonance effects originating from the $\pi \rightarrow \pi^*$ transition account for the strong changes in the G band intensities ratio observed around 2.5 eV. [26]

3. Graphenide solutions

Carbon macromolecular materials, like carbon nanotubes, carbon nanocorn and graphene, are difficult to dissolve because of their high surface energy. The ordinarily used dispersion ways with aide of surfactant and/or sonication do reduce surface energy, but these kinds of dispersion are always unstable. In 2005, Pénicaud and coworkers succeeded for the first time in obtaining a thermodynamically stable carbon nanotube solution in a polar solvent Dimethyl sulfoxide (DMSO), [51] which originated from the spontaneous dissolution of Na reduced carbon nanotubes. By varying potassium/carbon ratios, later work on these solutions established a thermal model of the Gibbs free energy of dissolution revealing that counterions entropy gain drives this spontaneous dissolution. [52] Those reduced carbon naotubes show similar behavious of stiff polyelectrolytes. The solubility depends strongly on the charge density.

The intercalation of graphite with different quantities of potassium makes the basal graphene planes to be reduced with different charge densities, which provide us with a system similar to reduced carbon nanotubes. Previous works concerning graphenide solutions performed by Dr. Amélie Catheline and Dr. Cristina Vallés showed that potassium intercalated compounds, such as stage-1KC_8 and K(THF)C_{24}, can be dissolved in various organic solvents, N-methyl-2-pyrrolidone (NMP), Dimethylformamide (DMF), Tetrahydrofuran (THF), 2-Methyltetrahydrofuran(Me-THE), Cyclopentyl methyl ether (CPME), Dimethyl sulfoxide (DMSO), Acetone etc.[1,2,53] In this work, we used the K-GICs presented in previous part to synthesize the graphenide solutions in two polar organic solvent, one high boiling point solvent NMP with boiling point of 202 – 204 °C and one low boiling point solvent THF with boiling point of 66 °C.

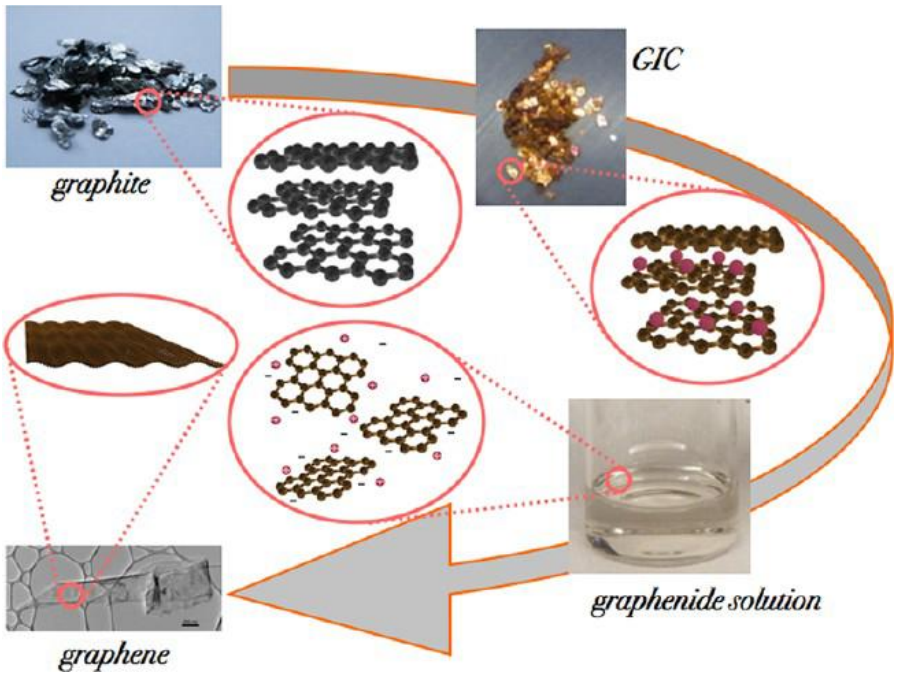

Figure 3.16: production process of graphenide solution [33] a

3.1 Synthesis of graphenide solutions

As illustrated in figure 3.16, the production method of graphenide solution consists of two steps under inert atmosphere without applying surfactants and sonication. The first step is synthesis of K-GICs; in our work, we have made three kinds of K-GICs from stage-1 KC_8 to stage-3 KC_{36}. Then these compounds were dissolved in organic solvents with a magnetic stirrer bar to accelerate the dissolving process. The dissolutions of K-GICs in solvents were performed by 2mg of GICs in 1mL solvents. NMP used in this work was purified with reflux method in order to eliminate impurities and water before dissolving the GICs in the solvents. After stirring 5 days, a mild centrifugation process was used to remove insoluble material. The GICs+NMP solutions were centrifuged at 2870 g for 1 hour. The centrifugations of GICs+THF solutions were generally performed at 785 g for 15-20 mins. The produced solutions were stable and stored under inert atmosphere for further characterizations. At first,

we practiced dry extract of the solutions to determine the concentration of each graphenide solution.

	NMP	THF
Stage 1 KC_8	0.43 mg/ml	1.78 mg/ml
Stage 2 KC_{24}	0.24 mg/ml	0.2 mg/ml
Stage 3 KC_{36}	0.21 mg/ml	0.12 mg/ml

Table 3.7: Concentrations of GICs in NMP and THF.

The concentrations obtained from dry extracts are listed in table 3.7. All dry extracts were performed in a homemade vacuum heater for more than 10 hours in glove box. The temperatures of practicing dry extracts are 60 °C and 160 °C respectively for THF and NMP solution. From table 3.7, we can see that graphenide solution KC_8+THF has the highest concentration, and stage 2 and stage 3 in THF show lower concentration compared with these compounds in NMP.

3.2 Absorption UV-Visible of graphenide solutions

In Dr. Amélie Catheline's work, the graphenide solution, KC_8+NMP, was characterized by UV-Visible absorption. The as-produced soltution, KC_8+NMP, is characterized by a band in the UV range at 300 nm (4.14 eV) with no tailing into higher wavelength region (FWHM = 50 nm). [2]

We also characterized graphenide solutions K-GICs+NMP and K-GICs+THF with UV-visible absorption. The air-sensitive graphenide solutions were loaded into a quartz cuvette under argon atmosphere inside glove box and then sealed with paraffin. The absorption spectra of dilute K- GICs+NMP and K- GICs+THF are illustrated in figure 3.17. We can see

that for GICs+NMP system there is always absorption at 300 nm (4.14 eV) despite the charge density. With Beer-Lambert law:

$$A_\lambda = c \cdot l \cdot \varepsilon$$

where A_λ is absorbance, l is optical path (2 mm), ε represents extinction coefficient, we can calculate extinction coefficient for three K-GICs+NMP solutions: KC_8 + NMP (ε_{300}= 26.5 $L \cdot g^{-1} \cdot cm^{-1}$), KC_{24}+NMP (ε_{300}= 25.5 $L \cdot g^{-1} \cdot cm^{-1}$), KC_{36}+NMP (ε_{300}= 27.1 $L \cdot g^{-1} \cdot cm^{-1}$).

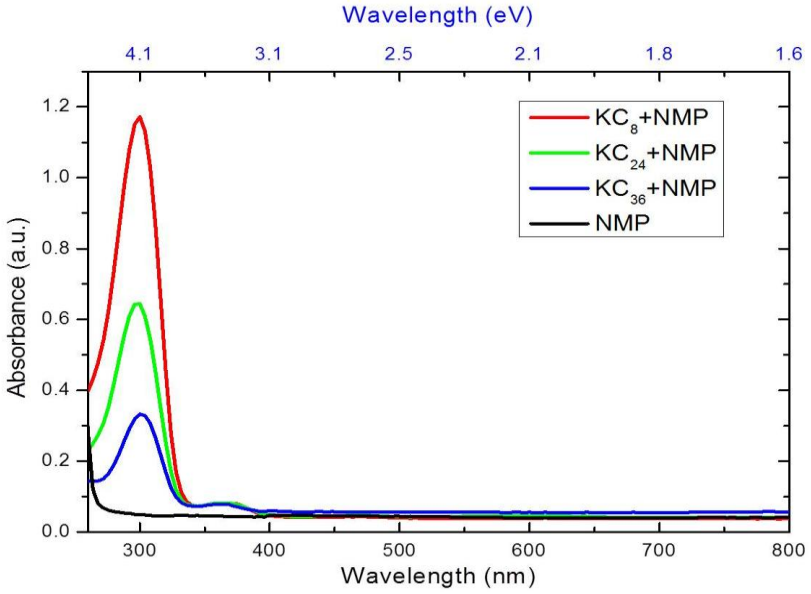

(a)

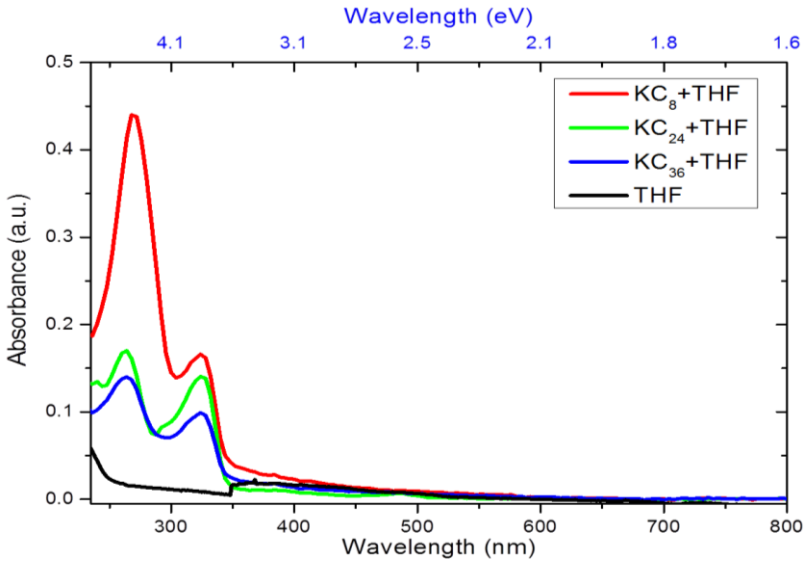

(b)

Figure 3.17: (a).UV-Visible absorption spectrum of dillute K-GICs+NMP; (b). UV-Visible absorption spectrum of dilute K-GICs+THF.

To explain the absorption band at 300 nm in GICs+NMP solutions despite the charge density, we can make a hypothesis that the dissolution of stage 1 KC_8, stage 2 KC_{24} and stage 3 KC_{36} in NMP produced some materials. We suppose that the absorption band at 300 nm was originated from dissolution of KC_8. Thus in solution KC_{24}+NMP and KC_{36}+NMP, there exit respectively disproportionation in these solutions:

$$KC_{24} \rightarrow KC_8 + C_{16}$$

$$KC_{36} \rightarrow KC_8 + C_{28}$$

Both KC_{24} and KC_{36} could be dissolved into KC_8 and neutral carbon. These hypotheses need to be proven by further characterization of solutions.

On the other hand, for GICs+THF, we can find two absorption bands in the ultraviolet. One located around 280 nm, the intensity of which varies according to charge density, the other at 328nm one doesn't change. The oxidation of graphenide solutions in air results in oxidation of negatively charged graphene flakes in solvents, thus aggregation of graphene flakes appears. The insert in figure 3.16 shows that initial graphenide solution KC_8 + THF is transparent under inert atmosphere inside the glove box. After opening the cap outside the glove box, the solution is oxidized, and aggregates precipitate at the bottom of the vial, accompanied by a change of the UV-Visible spectrum. The evolution of this oxidation is reflected in figure 3.18.

We can see that once the solution was exposed to air, the absorbance decrease with time of oxidation. From UV-visible absorption of KC_8+THF, we didn't observe the absorption band around 328 nm which is observed at dilute KC_8+THF illustrate in figure 3.17 (b). The absorption band at 328 nm was also observed by Dr Amélie Catheline in KC_8 + THF

protected under inert atmosphere. [53] In figure 3.18, a great absorbance decrease was observed between 25 minutes and 45 minutes due to man-made agitation for accelerating oxidation process. The concentration obtained from dry extract shows that concentration of charged graphene in solvent NMP is in general higher than in solvent THF, but for analyzing the deposits of graphenide solution with other techniques, such as AFM and Raman, we prefer the K-GICs + THF system because of low boiling point of THF which makes sample easier to prepare.

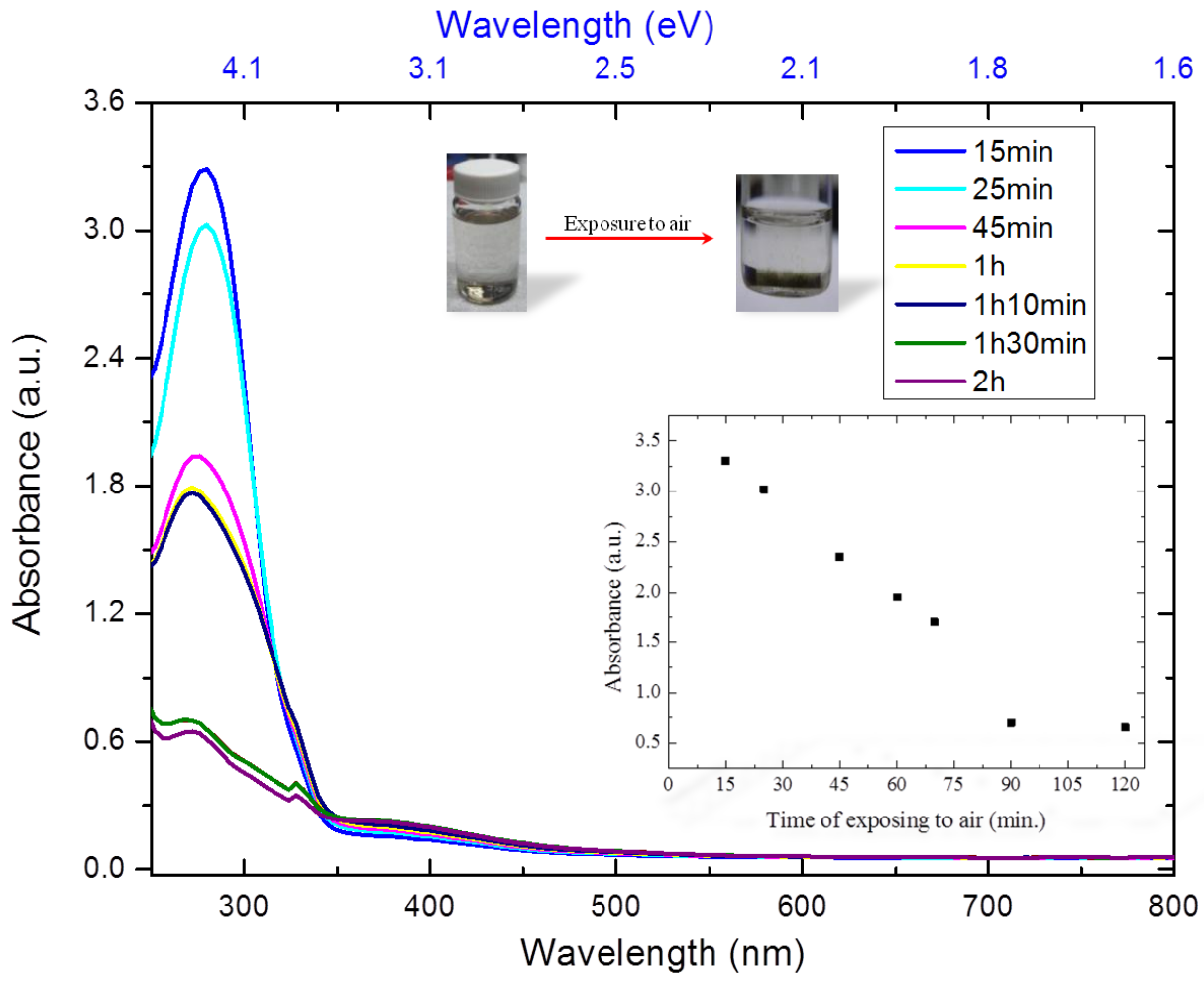

Figure 3.18: Evolution of UV-Visible spectra of one graphenide solution KC_8+THF once the solution was exposed to air. Insert: photos of exposing graphenide solution KC_8+THF to air (top); absorbance vs. time of oxidation of solution KC_8+THF (below).

3.3 Observation with Transmission electron microscopy

Transmission electron microscopy (TEM) was used to observe produced graphene flakes. This technique can provide us information about morphology, defect and size. With high-resolution transmission electron microscopy (HRTEM) image, an unambiguous identification of the layer number can be carried out by counting the number of dark lines along the folding at the rim of a given graphene flake. The selected area electron diffraction can also be used to identify the number of layers and crystal structure. The HRTEM characterizations were performed in CEMES Toulouse by Dr. Célia Castro and Dr. Marc Monthioux. Some samples were also characterized with TEM in CRPP.

An unambiguous sample characterization via TEM requires clean specimen without surface contamination. And most samples for TEM characterization must be supported on some kind of a thin electron transparent film which can hold the specimen in place while in the objective lens of the TEM. In our case, the grids used for TEM characterization are coated by holey or lacey carbon film. With those kinds of TEM grids, graphene flakes in solutions can be rather easily deposited in the grids while solvent can be easily eliminated in the following washing and drying treatment. The preparations of TEM grid with graphenide solution have to be performed in the glove box. At first, several drops of graphenide solutions (~ 60 µl) were deposited on grid with micro-pipette. The solvent in solution flows away from holes in carbon films, and graphene flakes remain on the carbon film. The grids were then taken out of glove box in order to oxidize the graphene flakes. After oxidation, these grids have to be washed in order to eliminate the particles composed of potassium which were formed by reaction between counterion K^+ and oxygen. A simple washing process with distilled H_2O, acetone and isopropanol can efficiently eliminate these particles. The TEM images of graphene flakes produced from K-GICs + THF are illustrated in figure 3.19.

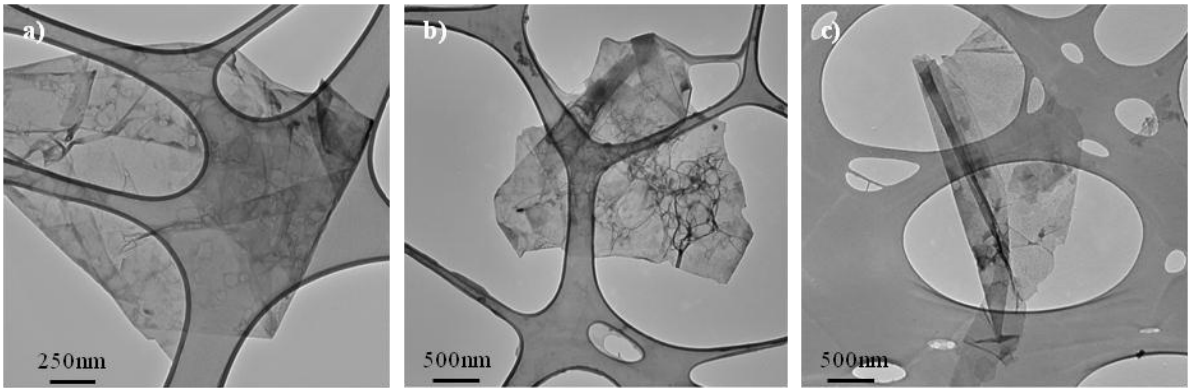

Figure 3.19: TEM images of graphene flake produced from (a) KC_8+THF solution; (b) KC_{24}+THF solution; (c) KC_{36}+THF solution.

The TEM images show that the flakes fold and overlap with themselves. The lateral size of the graphene can be up to several micrometers. Since KC_8+THF solution has the highest concentration compare to KC_{24}+THF and KC_{36}+THF solution, we then focused our attention on this solution. In order to identify the number of layer with TEM, one grid prepared with KC_8+THF was characterized with HRTEM in CEMES Toulouse. The number of graphene layers is simply and reliably characterized by counting lines of contrast along a backfolded edge of a graphene flake illustrated in figure 3.20 (b), similar to determining the number of walls of carbon nanotube.

As shown in figure 3.20, a large graphene flake with size of ~ 8.6 x 6.4 μm^2 was observed by HRTEM. Like graphene flakes presented in figure 3.19, this large graphene flake is also folded. The image in figure 3.18 (f) illustrates that this graphene is pocked with holes. We then observed the number of layer varies from 2 layers to 10 layers in different location according to lines of contrast accounted along a self-backfolded edge of the graphene flake, which could probably mean that the observed graphene flake was a bilayer graphene.

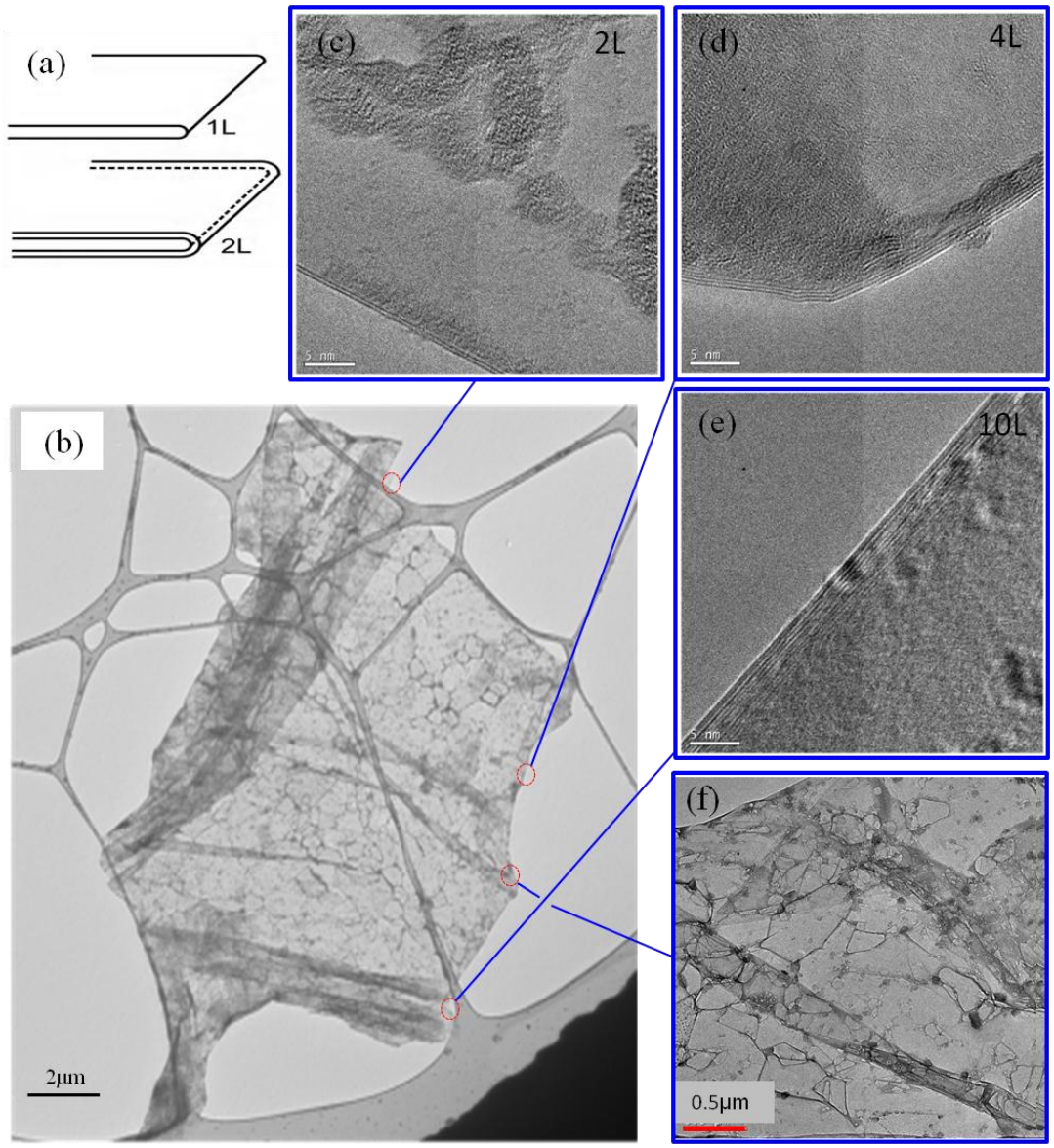

Figure 3.20: Determination of the number of graphene layers via HRTEM images: (a) schematic of backfolded edges of monolayer (1L) and bilayer (2L) graphene. (b) TEM image of a large graphene flake. The HRTEM images on right side from top to down correspond respectively to 2 layer, 4 layers and 10 layers. The scale in HRTEM is 5nm.

3.4 Characterization of deposit of KC_8+THF solution with AFM

Atomic force microscopy (AFM) is also considered as a very useful tool for characterizing the number of layers of graphene on a support, the shape of deposited graphene etc. Since the previous TEM images demonstrate that the graphene flakes on TEM grid feature a self-folded

morphology, determination of number of layers with AFM in our case could not give promising information about number of layers. However, AFM can provide a direct-viewing topology of graphene on a continuous substrate, which could be helpful for the future application of graphene. The topology of graphene is sensitive to the surface on which it is deposited. Indeed, graphene tends to follow the underlying topology of substrate; this can make identification of the number of layers by height measurements somehow tricky. [54] For the moment, the most used substrates for AMF study of graphene are SiO_2 and mica. We also tested SiO_2 and mica as substrate. Mica exhibits a smoother landscape than pristine SiO_2 support. For our AFM measurement, mica was used as substrate.

Beside substrate, the preparation of specimen is a critical factor for AFM characterization of graphene produced by liquid-phase route, especially when organic solvents are applied during the production process. The trace of organic solvents can easily "submerge" graphene flakes, which lead to difficulty of characterization of graphene flake. In addition, the surface contamination induced by improper preparation method can also ruin the specimen. We have developed one simple process which helps us to prepare a suitable sample for AFM characterization. The deposit of graphenide solution KC_8 + THF was performed in glove box on freshly cleaved mica surface by successive drop-casting of KC_8 +THF solution with micro-pipette. The as-prepared sample was dried in anti-chamber under vacuum for more than 30mins, and oxidized out of the glove box. The sample was then washed with fresh MillQ H_2O, acetone (ReactPur) and Isopropanol (RectPur). Finally, the washed sample was dried in an oven for overnight at 60 °C. We employed amplitude AFM with tapping mode to characterize the topography of graphene samples.

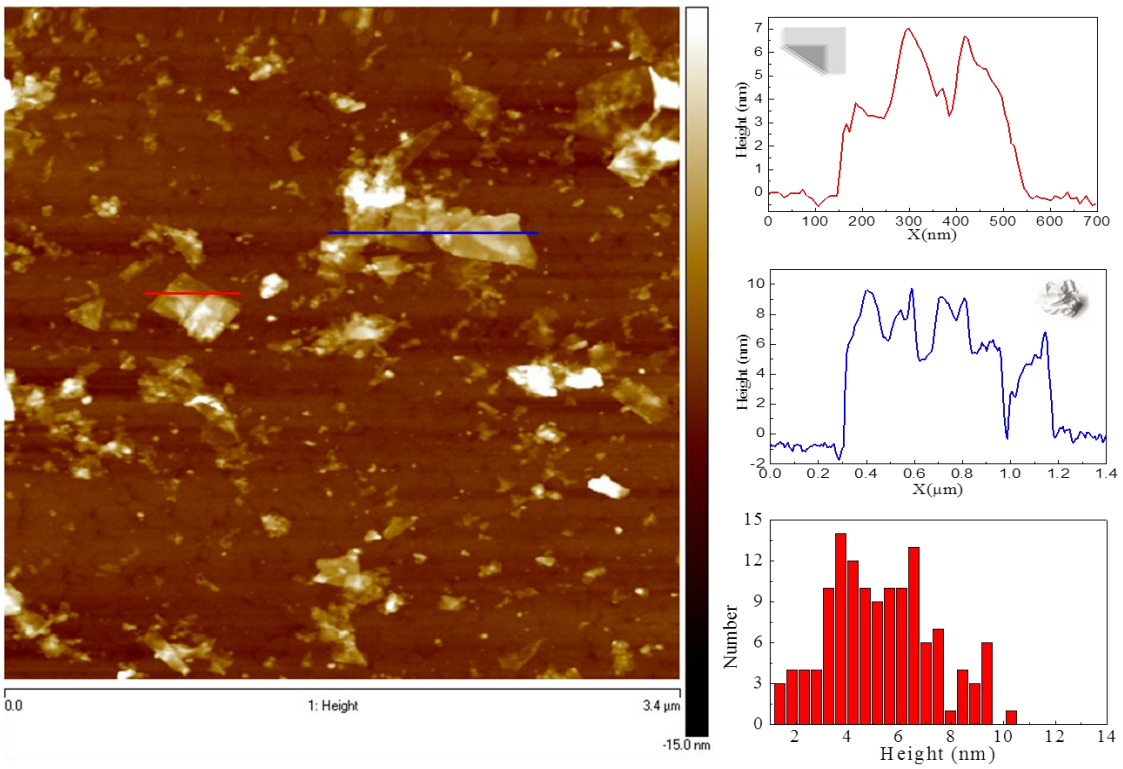

Figure 3.21: AFM image showing a deposit of graphenide solution on Mica surface (left). The height profiles of folded (red), crumpled (blue) graphene flake and histograme of height are shown on the right side.

AFM in figure 3.21 shows that the graphene flakes are either folded or crumpled on mica surface. Those morphologies are in accordance with TEM images shown in figure 3.18 and 3.19. From height profiles of two graphene flakes illustrated in right side, it seems that the folded graphene flake, which shows height profile varying from 4 nm to 7 nm, is less high than the crumpled one. The histogram of height shows that average height of graphene flake is around 4 nm. In 2009, Petr Kral et al. demonstrated by molecular dynamics simulations that water nanodroplets can activate and guide folding of graphene nanostructures. The folding can be realized by different types of motions, such as bending, sliding, rolling, or zipping that lead to stable or metastable structures. [55] Moreover, the previous works from Dr. Amelia Catheline had modeled that graphene folding can be triggered by the presence of nanodroplets

of solvent. [32] During our sample preparation step, we had applied washing process involving water and solvents, which might be another cause for changing morphologies of graphene.

3.5 Raman study of deposit from KC_8+THF solution

Raman spectroscopy is a powerful tool to characterize sp^2 carbon allotropes. Raman has been widely used in graphite and carbon nanotubes to study the defects, diameters, optical transition energies etc. [14, 56] In 2006, the first Raman spectroscopy experiments of graphene showed that Raman spectroscopy can be used to determine the number of graphene layers for graphene stacked in the Bernal (AB) configuration. [57] Raman can also be used to probe electron and phononon properties, strain effects, [58] doping [59] in graphene materials. Recent Raman scattering studies in graphene have made this technique to be an integral part of graphene research. We also applied this technique to characterize our specimen. The most used substrate is Si/SiO_2 for Raman study. During our work, we used both Si/SiO_2 substrate and Mica substrate for Raman study. Here we will present one spatial Raman mapping study performed on deposits of graphene on Si/SiO_2. For graphene Raman study, extreme care has to be taken to avoid sample damage induced by laser irradiation. In reference [57], Ferrari et al. performed Raman measurements on graphene prepared by micromechanical cleavage. They varied incident laser power from ~ 4 to ~ 0.04 mW, and no significant spectral change was observed in this range. [62] But one should notice that graphene prepared by micromechanical cleavage present almost perfect graphene crystal microstructure which make them to be more resistant to laser damage. For our Raman mapping, we used a laser power of 1.66 mW, low enough but with which we can obtain relatively strong intensity. The Raman measurements were performed with JOBIN YVON Xplora at room temperature using laser of 532 nm (2.33 eV). The spectra were collected under a microscope (× 50objective). The

Raman-scattered light was dispersed by a holographic grating with 2400 lines/mm for high spectral resolution and detected by a charge-coupled device (CCD) camera.

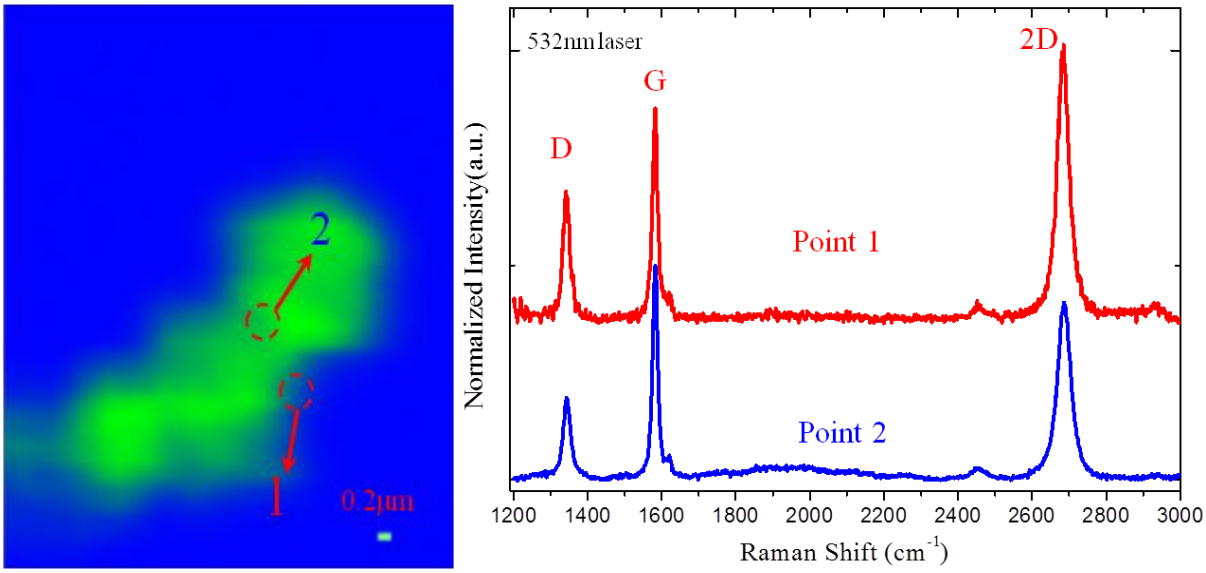

Figure 3.22: Raman mapping of graphenide solution KC_8+THF deposited on Si/SiO_2 substrate. The Raman mapping is reconstructed by intensity of G peak. Two Raman spectra on the right correspond to two points indicated in Raman mapping.

From two Raman spectra presented on the top right in figure 3.22, we can find three characteristic bands of graphitic materials: D band around 1346 cm^{-1}, G band (1589 cm^{-1}) and 2D band (2685 cm^{-1}). The details of Raman spectra line-shape analysis are displayed in figure 3.23.

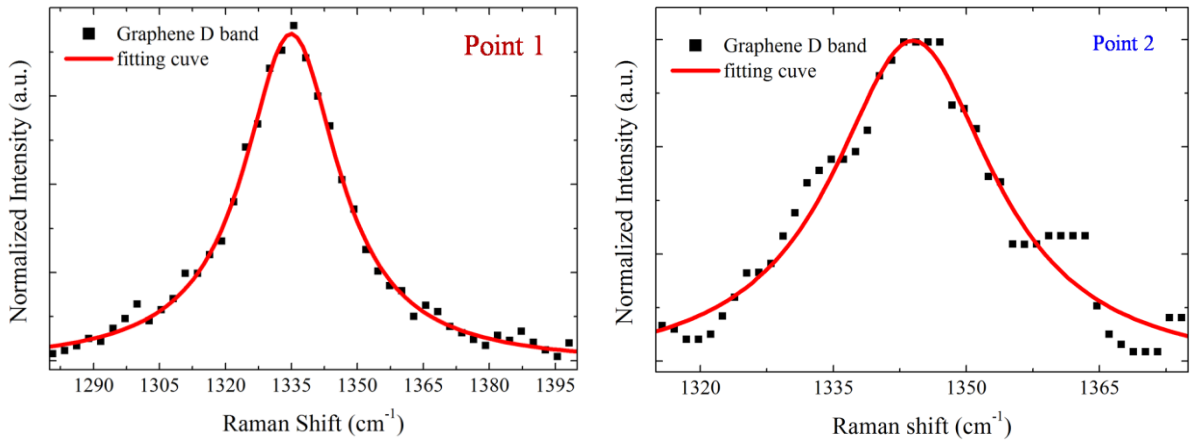

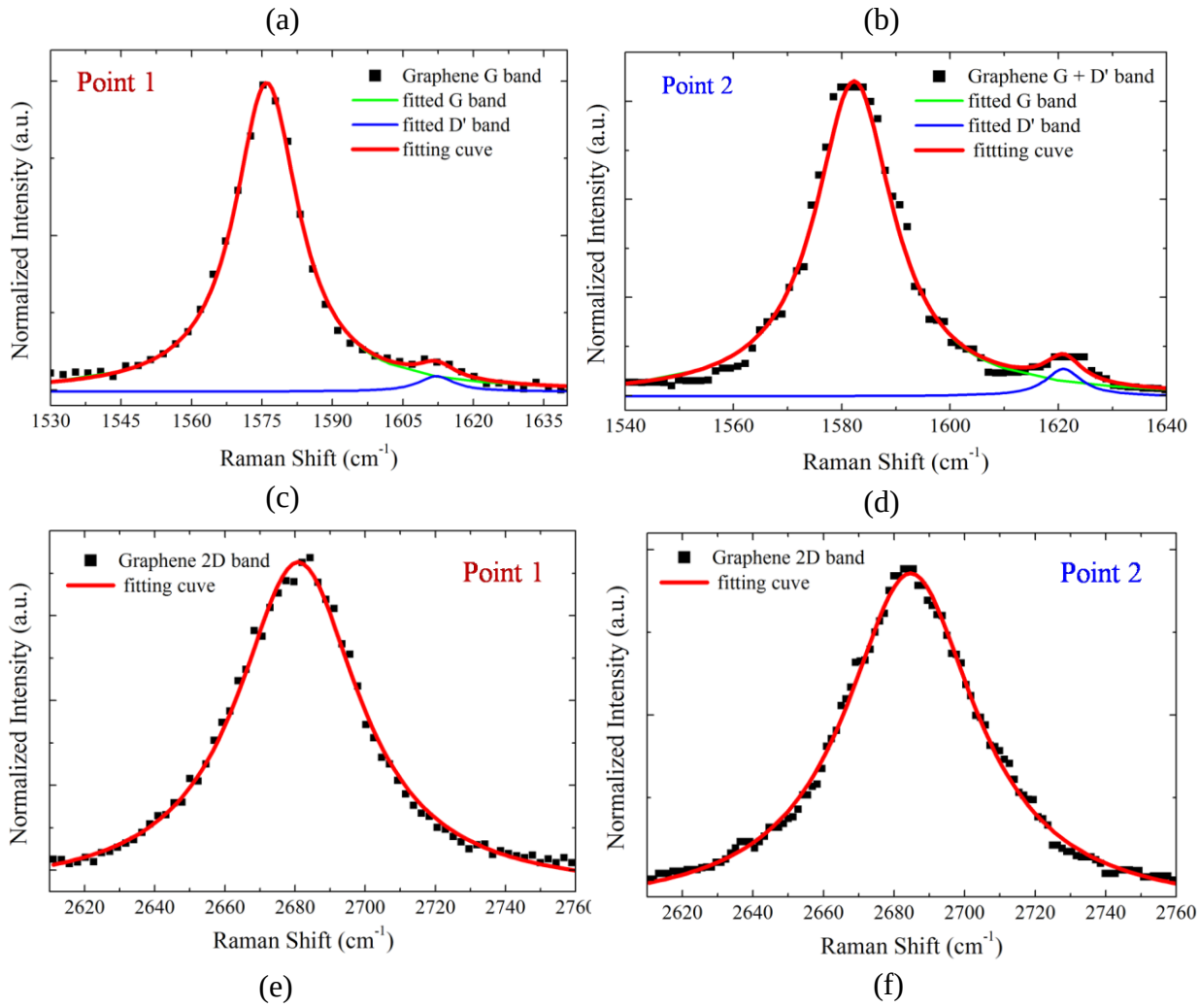

Figure 3.23: Raman mapping of graphenide solution KC_8+THF deposited on Si/SiO_2 substrate. The Raman mapping is reconstructed by intensity of G peak. Two Raman spectra on the right correspond to two points indicated in Raman mapping. Raman shape-line analysis of graphene deposition: (a) and (b) D band analysis for point 2 and point1; (c) and (d) G band analysis for point 2 and point 1; (e) and (f) 2D band analysis for point 2 and point 1.

Unlike D band of graphite, which is fitted by two Lorentzian functions shown in figure 3.5, for graphene, D band can be fitted by one single Lorentzian function. The analysis of the G band shows that there is another small band on the shoulder of G band, called D' band located around 1620 cm^{-1}. G band is fitted with a single Lorentzian function, but D' band is fitted by a

Fano function. The analysis of the 2D band illustrated in figure 3.20 (c) and (f) show a simple and monolayer-like 2D band which can be fitted by a single Lorentzian function. Ferrari et al. demonstrated that monolayer graphene produced from micromechanical cleavage method display also a single 2D band which can be fitted by one single Lorentzian function, and for AB stacked bilayer graphene 4 Lorentzian functions were used to fit its 2D band. [57] Since our method is liquid-route exfoliation, care should be taken in asserting that a single Lorentzian 2D peak is proof of monolayer graphene. Once graphene solution was deposited on substrate, any relative orientation and stacking of graphene layers could be possible, and this would be reflected in a significant change of the band structure. [60] This twisted and/or disorientated stacking order can result in a monoylayer-like 2D peak. [61] We studied then the Raman mapping in more detail.

By analyzing the intensity, frequency and line width of the characteristic D, G and 2D Raman band for the whole scanned area, we are able to deduce some valuable information about graphene produced. From the observation of whole graphene, G band is from 1580 cm^{-1} to 1585 cm^{-1}. The frequency of the G band is often used as a measure of the doping level. [38] Compare to reported G band frequency (~ 1580 cm^{-1}) of graphene produced by micromechanical cleavage method and deposited on Si/SiO_2 substrate, [57, 62] there is no significant G band shift for this observed graphene, which means that most part of the observed graphene doesn't get too much doping from production and deposition process. In addition, ω_G can be up to 1590 cm^{-1} in certain zone, which implies the inbomogeneity of the doping level. These doping may be caused by production method or by the substrate. From figure 3.24 (b), we can clearly see that the linewidth of G band is ~ 7.5 cm^{-1} for edge and ~ 10 cm^{-1} for centre. For 2D band, we observe the average of frequency of 2D is around 2685 cm^{-1}, in the bottom left part, the frequency of 2D is even shifted to 2700 cm^{-1}. Compare with

reported ω_{2D} of monolayer graphene, located around 2670 cm^{-1}, [57, 62] the 2D bands are largely blue-shifted. For linewidth of 2D band, the average Γ_{2D} is ~ 20 cm^{-1}; thus the FHWM of 2D is ~ 40 cm^{-1}, which is twice larger than the reported monolayer graphene FHWM (2D) (~ 23 cm^{-1}). Both frequency ω_{2D} and width Γ_{2D} imply that the observed graphene are not monolayer. The I_D/I_G image figure 3.24 (e) shows us that the maximum is not at edge. And the ratio of I_{2D}/I_G varies from 1.5 to 4. These results support that the observed graphene is not monolayer. It is more like a randomly stacked few layer graphene or self-folded graphene.

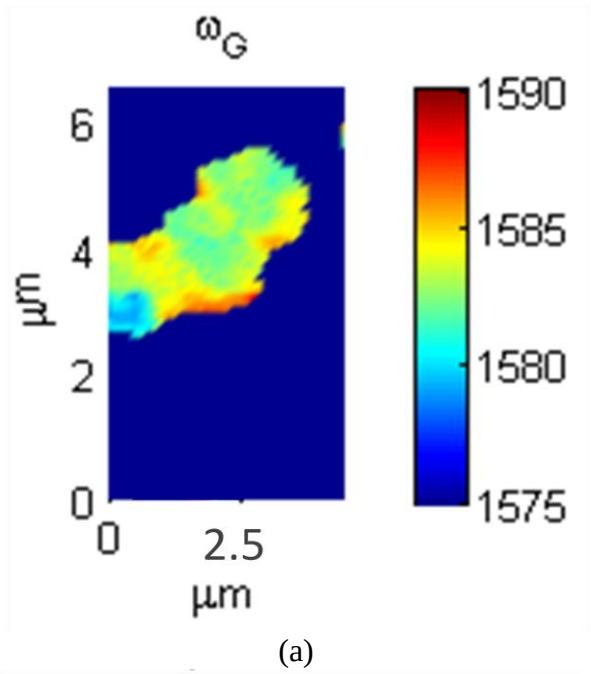

(a)

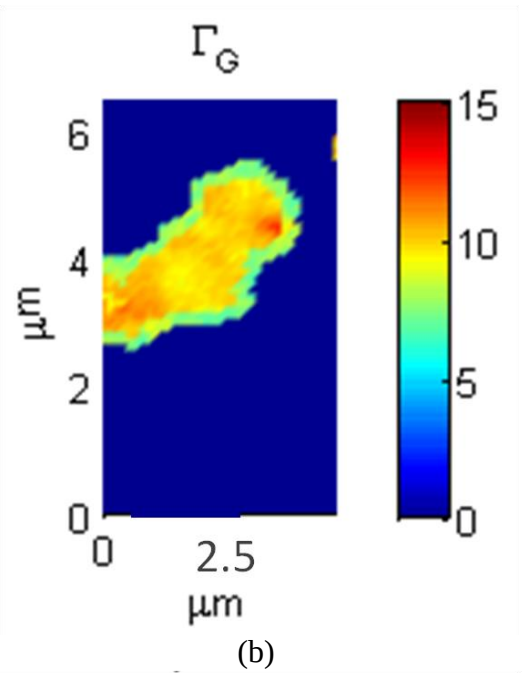

(b)

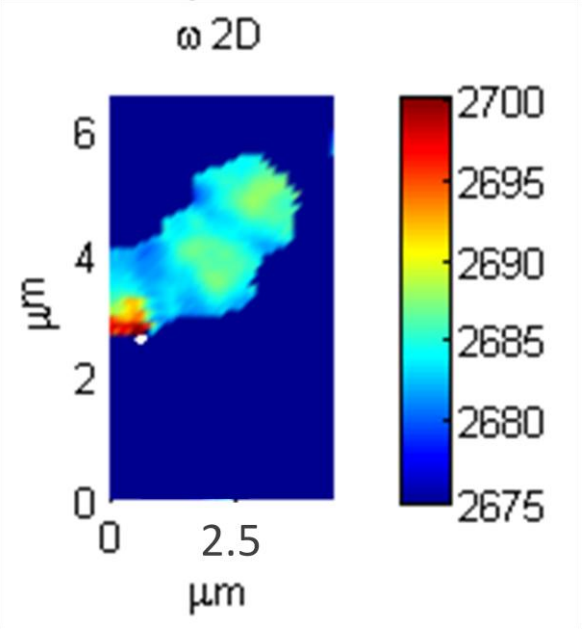

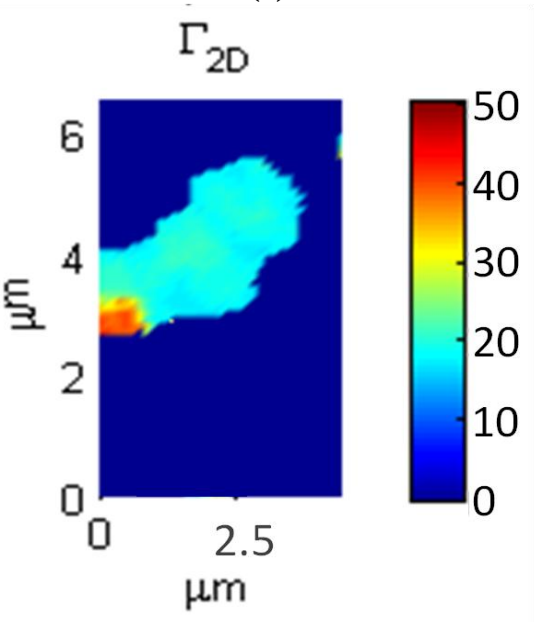

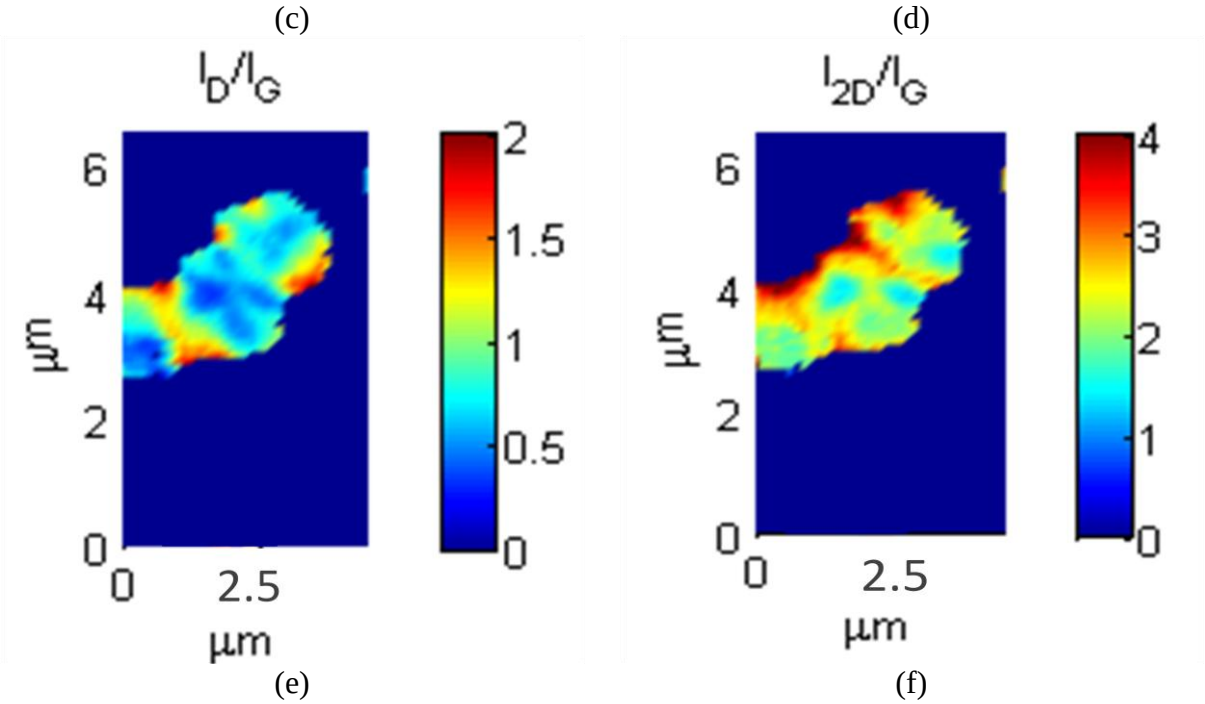

Figure 3.24: Spatial maps of the Raman features of a graphene sample: (a) and (c) are respectively the G band and 2D band frequency, ω_G and ω_{2D}; (b) and (d) the G mode and 2D band line width, Γ_G and Γ_{2D}; (e) the ratio of integrated intensity of D mode to that of the G mode, I_D/I_G; (f) the ratio of the integrated intensity of the 2D mode to that of the G mode, I_{2D}/I_G. Data in (a) and (f) are based on fits of line shape to the experimental data.

Starting from graphite (Bernal stacking), Raman analyses demonstrate that there is no fingerprints from multilayer of AB stacked multilayer graphene, but rather uncorrelated, stacked or self-folded graphene,graphenide solutions allow us to exfoliate completely the starting graphite.

We also noticed that D and D' band are presented both in centre and edge, which indicates that the observed graphene samples are defective. From HRTEM observation, we have noticed that there are holes in the graphene flakes. This is one reason for explaining the presence of D band. At the same time, both HRTEM and AFM reveal that graphene flake are folded and crumpled on substrate. When one monolayer graphene flakes folds into these

morphologies, the graphene flakes can be considered as multilayer graphene stacked with random stacking order, as illustrated in figure 3.25. Gupta et al. observed two peaks in the D-band region on a sample in which monolayer graphene was folded back upon itself into skewed bilayer, although the parent monolayer does not exhibit a D band. [63] Thus not only the structure defects, like vacancies and pentagon-heptagon pair, contribute to the D band, but rotationally stacked structure can also produce a D band.

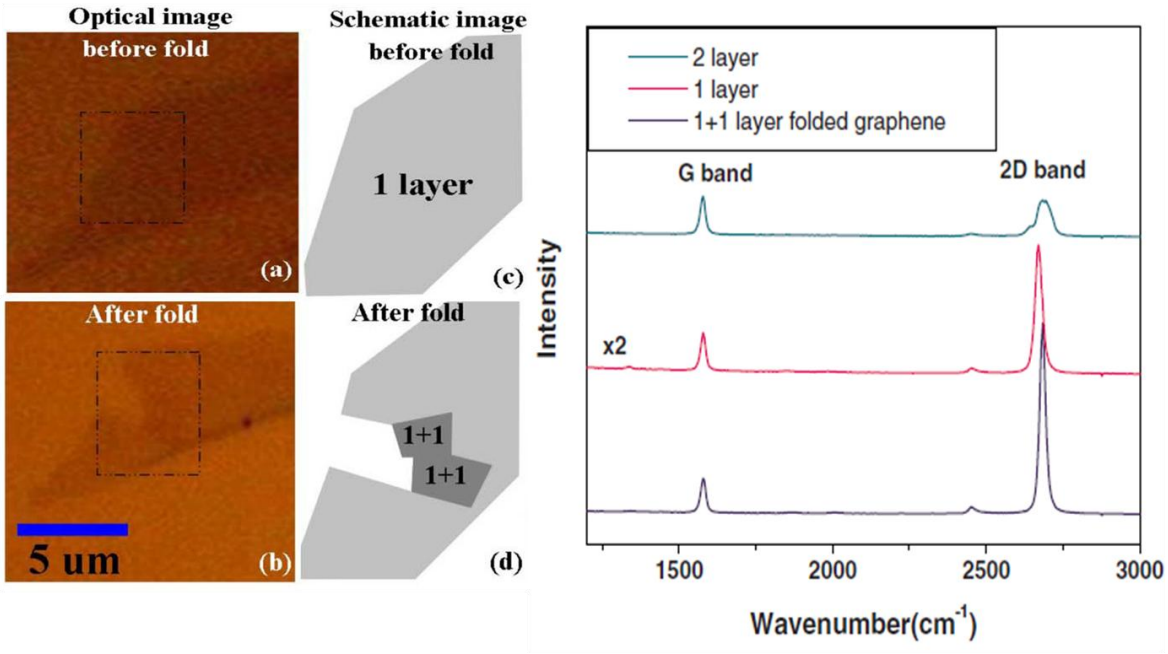

Figure 3.25: (a) and (b) show the optical image of single layer graphene (SLG) before and after folding. (c) and (d) give the schematic image of SLG before and after fold. (On right side)The Raman spectrum of bilayer graphene, monolayer graphene, and 1+1 layer folded graphene. [66]

We also noticed that the D band is intense both on centre area (point 2) and on edge (point 1). In general, one can find a more intense D band on edge than in centre of a given graphene because more defects are presented in edge. Beside the reasons described above for the presence of D band, we rechecked the Raman measurement, for example laser energy. Indeed, laser-induced degradation had been observed previously for a weak laser power (1mW) over a

long time scale (~18 h) on the monolayer graphene deposited on SiO_2 substrate. [64] For the Raman mapping where graphene sample is scanned by laser spot under fixed exposure time, not only the laser energy have to be considered, but one must also take laser exposure time into account for Raman measurements. For our Raman mapping measurement, it took almost one days to finish whole Raman mapping because of applying small increment, exposure time of 1 second and large scanning area. This could also cause slight sample degradation.

Raman mapping is a powerful tool for characterizing sample in spatial scale, but one should not only pay attention to laser energy, the acquisition time should also be taken into account in order to avoid laser-induced sample damage. In the following part, all the Raman mapping measurements were performed by taking both laser energy and acquisition time into account. For ending this Raman characterization part, a summary concerning the quality of graphene will be made in order to comparing quality of graphene produced by different liquid-route exfoliation method, like reduced graphene oxide, graphene suspension in organic solvent by sonication and graphene produced by our method. Raman has been widely accepted as tool to investigate quality of produced graphene, since the D band is a defect-active mode.

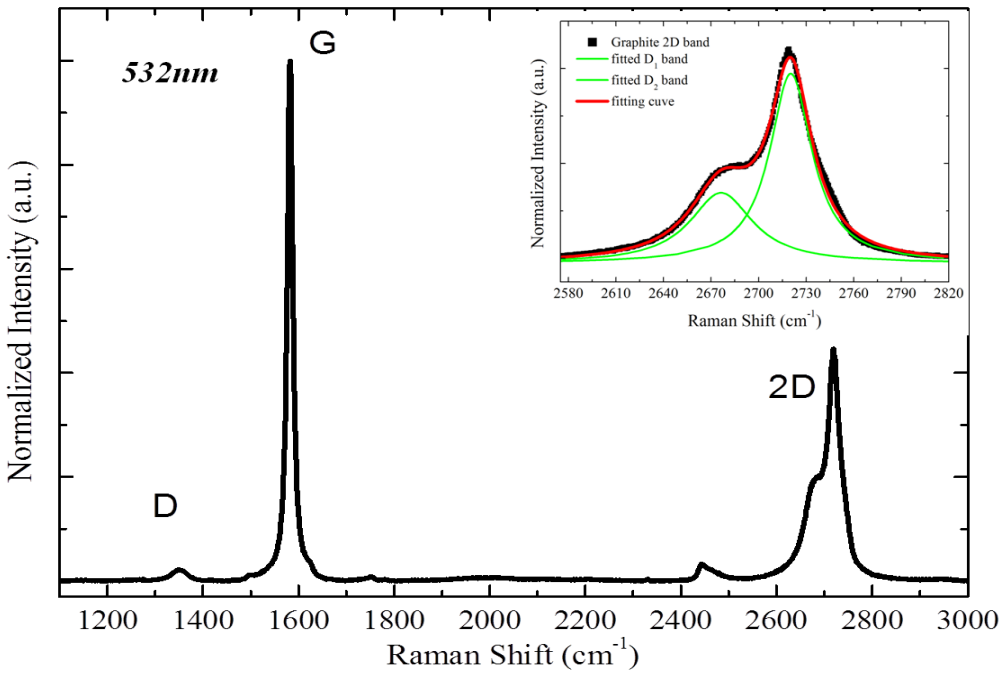

(a)

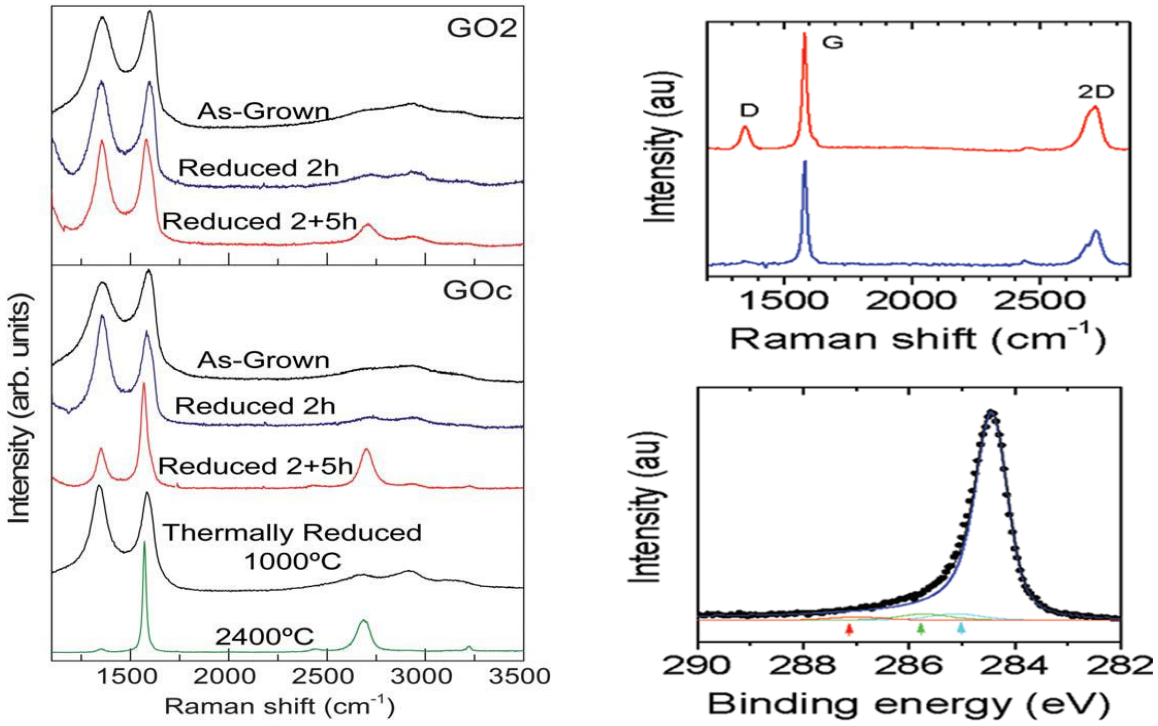

Figure 3.26: (a) Raman spectrum of graphite (Nature 4) with laser excitation energy 2.33 eV (523 nm); insert: line-shape analysis of graphite 2D band; (b) Raman spectra of as-grown (black) and chemically reduced (2 h, blue, and 2 h + 5 h, red, in hydrazine) GO2 and GOc thin films and thermally reduced (1000 °C and 2400 °C) GOc powder. [65] (c) Raman spectra of graphene produced by suspension of graphene in organic solvent Top: Raman spectra of (red) a small flake and (blue) a larger flake. Bottom: C1s XPS spectrum of a thin film of graphene flakes. The contributions marked by arrows are due to the solvent. [70]

In all the liquid-route exfoliation methods, the starting material is graphite. One typical Raman spectrum of Bernal stacked graphite (Natural graphite) is presented in figure 3.26 (a). The 2D band can be fitted by two Lorentzian functions illustrated in the insert image of figure 3.26 (a). In figure 3.5, the line-shape analysis of D band shows that the D band can be fitted by two Lorentzian functions located respectively at 1348 cm^{-1} and 1360 cm^{-1}. The results are in accordance with previously reported analysis in reference 57. In graphene oxide, the basal

graphene sp^2 structure is converted into sp^3 structure, which results in insulating GO. In figure 3.26 (b), the Raman spectra of graphene oxide and reduced graphene oxide are shown. Due to oxidation effects, a huge D band is apparent in GO Raman spectra and 2D band has almost disappeared. Reduction can repair sp^2 structure and restore the 2D band, but it seems only high temperature treatment (2400 °C) and chemical reduction for long time (7h in hydrazine) that can decrease significantly the D band and restore the 2D band. For graphene suspended in organic solvent, Coleman claimed that this method can produce a defect-free graphene. [66] But in figure 3.26 (c), we can still observe a visible D band which is attributed to edge effect by the authors. It also displays a broad 2D band which is characteristic of few layer flakes. For the Raman spectrum below, which doesn't display a D band, but the 2D band more or less demonstrate a line-shape of graphitic 2D band, there is a small band on the low frequency side of the 2D band. These two Raman spectra demonstrate that with graphene suspension in organic solvent one can hardly exfoliate completely the graphite into monolayer graphene. On the other hand, from the Raman spectra obtained from graphene produced by our method, even though a D band due to structure defects and self-folding is visible, the monolayer-like 2D band has a characteristic of uncorrelated graphene layers, shows that the graphite has been thoroughly exfoliated by the dissolution procedure.

4. Conclusion

Our group has developed an alternative method to produce graphene from graphite by dissolving graphite intercalation compounds (GICs) in organic solvents. The dissolution of GICs allows to produce thermodynamically stable graphenide solutions under inter atmosphere. Compared to previous studies concerning graphenide solutions, we have performed a systematic study from starting materials graphite to graphenide solutions.

In order to produce graphenide solutions with best quality, different techniques were used to characterize their crystal structure and elemental composition. The best graphite sample was used to synthesize potassium intercalated compounds (K-GICs) by using one-zone and two-zone vapour transport techniques. Stage-1 KC_8, stage-2 KC_{24} and stage-3 KC_{36} were synthesized and studied during this work. X-ray diffraction and Raman scattering were mainly applied to verify the phase purity and electronic properties changes due to charge transfer between layers of graphite and intercalated potassium layers, which can lead to a strong shift of the Fermi level. By performing a Raman resonance study for three K-GICs, we observed a Raman resonance effect for stage-3 KC_{36} at room temperature. In stage-3 KC_{36}, the intensity of the boundary layers G band versus that of the interior layer is maximum at 2.5 eV. Using first-principle calculation, we associate this transition to $\pi \rightarrow \pi^*$ of the bounding layers of graphene.

The three K-GICs were then used to dissolve in two organic solvents, NMP with high boiling point and THF with low boiling point. With the highest charge density in stage-1 KC_8, this K-GIC can allow us to obtain the most concentrated graphenide solutions. Because of low boiling point of THF, graphene produced from KC_8+THF solution was then characterized with HRTEM, AFM and Raman. Characterizations from these techniques show that graphene

can be produced with a good quality without using surfactants and sonication. These graphenide solutions can be applied to produce graphene based materials. This will be described in the following chapter.

References

[1] C. Vallés, C. Drummond, H. Saadaoui, C. A. Furtado, M. He, O. Roubeau, L. Ortolani, M. Monthioux, A. Pénicaud, J. Am. Chem. Soc., 2008, 130, 15802.

[2] A. Catheline, C. Vallés, C. Drummond, L. Ortolani, V. Morandi, M. Marcaccio, M. Iurlo, F. Paolucci, A. Pénicaud, Chem. Commun., 2011, 47, 5470.

[3] V. A. Nalimova, S. N. Chepurko, V. V. Avdeev, and K. N. Semenenko, Synth. Met. 1991, 40, 267.

[4] C. Hérold, E.G. Mohammed, J.F Marêché, P. Lagrange. KC4, a new graphite intercalation compound. Molecular Crystals and Liquid Crystals Science and Technology. 1994, 244, 41.

[5] H. Shioyama, R. Fujii. Electrochemical reactions of stage 1 sulfuric acid-Graphite intercalation compound. Carbon 1987,25,771-774.

[6] P. Setasuwon, N. Vaneesorn, S. Kijamnajsuk, A. Thanaboonsombut. Science and Technology of Advanced Materials, 2005, 6, 278.

[7] J. Zhao, L. Yang, F. Li, R. Yu, C. Jin. Structural evolution in the graphitization process of activated carbon by high-pressure sintering. Carbon, 2009, 47, 744.

[8] P. Scherrer, "Bestimmung der Grösse und der inneren Struktur von Kolloidteilchen mittels Röntgenstrahlen," *Nachr. Ges. Wiss. Göttingen*, 1918, 26, 98.

[9] J.I. Langford, A.J.C. Wilson, "Scherrer after Sixty Years: A Survey and Some New Results in the Determination of Crystallite Size," J. Appl. Cryst. 1978, 11, 102.

[10] M.S. Paterson. Calculation of the Correction for Instrumental Broadening in X-ray Diffraction Line. Proceeding of the Physical Society, 1950, 63, 477.

[11] F. Tuinstra, J. L. Koenig, Raman spectrum of graphite. J. Chem. Phys. 1970, 53, 1126.

[12] D. S. Knight, W. B. White, Characteriation of diamond films by Raman spectroscopy. J. Mater. Res. 1989, 4, 385.

[13] T. P. Mernagh, R.P. Cooney, R.A. Johnson, Raman spectra of graphon carbon black. Carbon, 1984, 22, 39

[14] L. G. Cançado, K. Takai, T. Enoki, M. Endo, Y. A. Kim, H. Mizusaki, A. Jorio, L. N. Coelho, R. Magalhães-Paniago, M. A. Pimenta. General equation for the determination of the crystallite size L_a of nanographite by Raman spectroscopy. Appl. Phys. Lett. 2006, 88, 163106

[15] N. J. Everall, J. Lumsdon, D. J. Christopher, The effect of laser-induced heating upon the vibrational raman spectra of graphites and carbon fibres. Carbon. 1991, 29, 133.

[16] M. S. Dresselhaus and G. Dresselhaus. Adv. Phys. 2002, 51, 1-186.

[17] U. Fano, Phys. Rev. 1961, 124, 1866.

[18] M. S. Dresselhaus and G. Dresselhaus, Adv. Phys. 1981, 30, 139.

[19] S. A. Solin, N. Caswell, J. Raman Spectrosc. 1981, 10, 129.

[20] J. C. Chacon-Torres, T. Pichler, Phys. Status. Solidi. B. 2011, 248, 2744.

[21] C. A. Howard, M. P. M. Dean, F. Withers, Phys. Rev. B. 2011, 84(24), 241404.

[22] M. P. Dean, C. A. Howard, S. S. Saxena, M. Ellerby, Phys. Rev. B. 2010, 81(4), 045405.

[23] A. C. Ferrari and J. Robertson, Phys. Rev. B 61(20), 14095–14107 (2000).

[24] J. C. Chacon-Torres, A. Y. Ganin, M. J. Rosseinsky, T. Pichler, Phys. Rev. 2012, 86, 075406.

[25] A. M. Saitta, M. Lazzeri, M. Calandra, F. Mauri, Phys. Rev. Lett. 2008, 100(22), 226401.

[26] Y.Wang, P. Puech, I. Gerber, A. Pénicaud. Resonant Raman scattering of graphite intercalation compounds KC_8, KC_{24}, KC_{36}. J. Raman Spectrosc. 2014, 45, 219-223.

[27] A. M. Rao, P. C. Eklund, Shunji Bandow, A. Thess, R. E. Smalley. Evidence for charge transfer in doped carbon nanotube bundles from Raman scattering. Nature. 1997, 388,257-260.

[28] S. Reich, C. Thomsen, Phil. Trans. R. Soc. Lond. A 2004, 362, 2271–2288.

[29] J. C. Chacon-Torres, L. Wirtz, T. Pichler, ACS Nano, 2012, 7(10), 9249-9259.

[30] A. Grüneis, C. Attaccalite, A. Rubio, D. V. Vyalikh, S. L. Molodtsov, J. Fink, R. Follath, W. Eberhardt, B. Buchner, T. Pichler, Phys. Rev. B. 2009, 80, 075431.

[31] A. Grüneis, C. Attaccalite, A. Rubio, D. V. Vyalikh, S. L. Molodtsov, J. Fink, R. Follath, W. Eberhardt, B. Buchner, T. Pichler, Phys. Rev. B. 2009, 79, 205106.

[32] A. Catheline, L. Ortolani, V. Morandi, M. Melle-Franco, C. Drummond, C. Zakri, A. Pénicaud, Soft Matter 2012, 8, 7882–7887.

[33] A. Pénicaud, C. Drummond. Deconstructing Graphite: Graphenide solutions. Acc. Chem. Res., 2013, 46, 129.

[34] E. M. Milner, N. T. Skipper, C. A. Howard, M. S. P. Shaffer, D. J. Buckley, K. A. Rahnejat, P. L. Cullen, R. K. Heenan, P. Lindner, R. Schweins, J. Am. Chem. Soc., 2012, 134, 8302–8305.

[35] S. Pisana, M. Lazzeri, C. Casiraghi, K. S. Novoselov, A. K. Geim, A. C. Ferrari, F. Mauri, Nature Mater. 2007, 6, 198.

[36] G. U. Sumanasekera, J. L. Allen, S. L. Fang, A. L. Loper, A. M. Rao, P. C. Eklund, J. Phys. Chem. B 1999, 103, 4292.

[37] P. Puech, T. Hu, A. Sapelkin, I. Gerber, V. Tishkova, E. Pavlenko, B. Levine, E. Flahaut, W. Bacsa, Phys. Rev. B 2012, 85, 205412.

[38] C. Casiraghi, S. Pisana, K. S. Novoselov, A. K. Geim, A. C. Ferrari, Appl. Phys. Lett. 2007, 91, 233108.

[39] P. C. Eklund, G. D. Mahan, J. G. Spolar, J. M. Zhang, E. T. Arakawa, D. M. Hoffman, Phys. Rev B. 1988, 37, 691.

[40] M. Lazzeri, F. Mauri, Phys. Rev. Lett. 2006, 97, 266407.

[41] J. Blinowski, N. Hy Hau, C. Rigaux, J. P. Vieren, R. Toullec, G. Furdin, A. Herold, J. Melin, J. Phys. (Paris) 1980, 41, 47.

[42] K. Kume, K. Nomura, Y. Hioryama, Synth. Met. 1985, 12, 307.

[43] P. C. Eklund, C. H. Olk, F. J. Holler, J. G. Spolar, E. G. Arakawa, J. Mat. Res. 1986, 1, 361–367.

[44] A. C. Ferrari, Solid Stat Commun. bf 2007, 143, 47–57.

[45] C. Hartwigsen, W. Witschel, E. Spohr, Phys. Rev. B. 1997, 55, 4953.

[46] J. Nicolle, D. Machon, P. Poncharal, O. Pierre-Louis, A. San-Miguel, Nano Lett. 2011, 11, 3564–3568.

[47] M. H. Yang and P. C. Eklund, Phys. Rev. B 1988, 38, 3505.

[48] G. Kresse, J. Hafner, Phys. Rev. B 1994, 49, 14251.

[49] G. Kresse, J. Furthmüller, Comput. Mat. Sci. 1996, 6, 15.

[50] G. Kresse, J. Furthmüller, Phys. Rev. B 1996, 54, 11169.

[51] A. Pénicaud, P. Poulin, A. Derré, E. Anglaret, P. Petit, Spontaneous dissolution of a single-wall carbon nanotube salt. J. Am. Chem. Soc. 2005, 127, 8–9.

[52] D. Voiry, C. Drummond, A. Pénicaud. Portrait of carbon nanotube salts as soluble polyelectrolytes. Soft Matter, 2011, 7, 7998.

[53] A. Catheline. Film de nanotubes de carbone et solutions de grapheme. Thèse de doctorant de Université Bordeaux I, 2011.

[54] C. Lui, L. Liu, K.F. Mak, G. W. Flynn, T.F. Heinz. Ultraflat graphene. Nature, 2009 462, 339.

[55] N. Patra, B. Wang, P. Kral. Nanodroplet activated and guided folding of graphene nanostructures. Nano. Letters. 2009, 9, 3766-3771.

[56] M. S. Dresselhaus, G. Dresselhaus, R. Saito, A. Jorio. Raman spectroscopy of carbon nanotubes. Physics Reports, 2005, 409, 47-99.

[57] A. C. Ferrari, J. C. Meyer, V. Scardaci, C. Casiraghi, M. Lazzeri, F. Mauri, S. Piscanec, D. Jiang, K. S. Novoselov, S. Roth, A. K. Geim. Raman spectrum of graphene and graphene layers. Phys. Rev. Lett. 2006, 97, 187401.

[58] T. M. G. Mohiuddin, A. Lombardo, R. R. Nair, A. Bonetti, G. Savini, R. Jalil, N. Bonini, D. M. Basko, C. Galiotis, N. Marzari, K. S. Novoselov, A. K. Geim, A. C. Ferrari. Uniaxial strain in graphene by Raman spectroscopy: G peak splitting, Grüneisen parameters, and sample orientation. Phys. Rev. B, 2009, 79, 205433.

[59] A. Das, B. Chakraborty, S. Piscanec, S. Pisana, A. K. Sood, A. C. Ferrari. Phonon renormalization in doped bilayer graphene. Phys. Rev. B, 2009, 79, 155417.

[60] S. Latil, V. Meunier, L. Henrard. Massless fermions in multilayer raphitic systems with misoriented layers: Ab initio calculations and experimental fingerprints. Phys. Rev. B, 2007, 76, 201402(R).

[61] Z, Ni, Y.Wang, T.Yu, Y.You, Z. Shen. Reduction of Fermi velocity in folded graphene observed by resonance Raman spectroscopy. Phys. Rev. B, 2008, 77, 235403.

[62] S. Berciaud, S. Ryu, L. E. Brus, T. F. Heinz. Probing the intrinsic properties of exfoliated graphene : Raman spectroscopy of free-standing monolayers. Nano Lettres, 2009, 9(1), 346-352.

[63] A.K.Gupta, Y. Tang, V. H. Crespi, P. C. Eklund. Nondispersive Raman D band activated by well-ordered interlayer interactions in rotationally stacked bilayer graphene. Phys. Rev. B, 2010, 82, 241406.

[64] B. Krauss, T. Lohmann, D.-H. Chae, M. Haluska, K. von Klitzing, J. H. Smet. Laser-induced disassembly of a graphene single crystal into a nanocrystalline network. Phy.Rev. B. 2009, 79, 165428.

[65] X. Diez-Betriu, S. Alvarez-Garcia, C. Botas, P. Alvarez, J. Sanchez-Marcos, C. Prieto, R. Menendez, Alicia de Andres. J. Mater. Chem. C, 2013, 1, 6905

[66] J. Coleman. Liquid Exfoliation of Defect-Free Graphene. Acc. Chem. Res., 2013, 46, 14.

Chapter IV: Transparent Conductive Graphene Films

In the previous chapter, with several analysis techniques we demonstrated that thermodynamically stable graphenide solutions can allow us to produce graphene materials with relative good quality compared to graphene produced by reduced graphene oxide or suspension of graphene in organic solvents. These graphenide solutions can be produced in large scale under inert atmosphere. These advantages render the produced graphene a promising material for further application. It is largely reported that graphene production via liquid-phase exfoliation can be used for the scalable production of functional films and composites.

In fact, for application of graphene produced from liquid-phase exfoliation, one is always faced with several common challenges. For example, one challenge is that liquid-phase exfoliation methods offer limited control over the number of layers in the dispersed graphene sheets, which makes the produced graphene and rGO solutions or suspensions to suffer from polydispersity. As a matter of fact, for this challenge, Hersam et al. reported a density gradient ultracentrifugation (DGU) to isolate graphene sheets with controlled thickness. [1] For some applications, this polydispersity is not a problem. Another challenge is that by whatever exfoliation methods one applies, the produced graphene possesses relative small lateral size. Among the published articles concerning liquid-phase production, Pénicaud et al. reported the observation of a monolayer graphene flake with lateral size up to 50 μm. [2] This observed graphene sheet was produced from graphenide solution. For reduced graphene oxide, Dong et al. demonstrated monolayer reduced graphene oxide flake (up to 50 μm in lateral size). [3] These are the largest monolayer graphene flakes reported for liquid-phase produced graphene. Indeed, the average size of the graphene flakes typically ranges from tens of nanometers to several microns. [2, 4, 5] They are often too small for some kinds of applications. The question

one might ask here is how can we apply these liquid-phase exfoliated graphene? Actually, scientists and engineers have worked with different techniques to apply graphene produced from liquid-route methods to make device and materials. As introduced in chapter I, rGO and graphene suspension have been largely reported to produce transparent conductive films (TCFs).

In this chapter, we will present a method to produce graphene TCFs by using as-produced graphenide solutions. The optical and electrical properties of produced graphene films were then characterized. In second place, one simple and effective thermal treatment will be presented. With this treatment, the properties of films can be significantly improved. Several characterization techniques were employed to support the efficiency of this treatment. Based on results obtained from thermal treatment, laser treatment was also applied to improve electrical and optical properties of graphene films. Finally, some primary results concerning graphene/carbon nanotube hybrid films will be also introduced in this chapter.

1. Elaboration of transparent conductive graphene films

In chapter I, we made a summary about graphene films, which can be prepared by several methods, such as vacuum filtering, spray-coating, dip-coating and Langmuir–Blodgett (LB) techniques. All these reported graphene films were made either from reduced graphene oxide or from graphene suspension. We can also adopt these introduced methods to elaborate TCFs with graphenide solutions. Since graphenide solutions are sensitive to air and moisture, in our case the elaboration method for producing film should be applicable under inert atmosphere. Dr Amélie Catheline had developed an effective vacuum filtering method to produce CNTs films from reduced carbon nanotube solutions. [6] The produced CNTs films exhibit very good electrical and optical properties. By adapting this developed production method, we used filtration method under inert atmosphere to produce graphene TCFs.

1.1 Films production method

The filtration method possesses several advantages: (i) the homogeneity of the film can be control by the process itself. When graphene flakes accumulate on the membrane, they generate a self-controlled network. When a region becomes thicker, the local permeation of solvent becomes slow, this can allow thinner part to accumulate more graphene flakes and become thicker. (ii) By controlling concentration and/or volume of graphenide solution used for film production, the thickness of film can also be controlled.

Graphene film production process is shown in figure 4.1. The filtration of graphenide solutions was performed under inert atmosphere in a glove box. At first, the graphenide solutions, KC_8+THF, were filtered onto Al_2O_3 membrane (Anodisc 47, 0.02μm, Whatman) with a vacuum filtration apparatus (figure 4.1 (1)). In Dr Amélie Catheline's work concerning CNT films, before filtration the CNTs solution was diluted several times because as-produced

CNT solutions are concentrated. In case of KC_8 +THF, the solution doesn't need to be diluted because of their relatively low concentration. Care is taken in pouring the graphenide solution into the filter funnel to avoid bubbles on the solution surface. Bursting bubbles disrupt the film uniformity when it is still wet and fragile. As the solutions are filtered down, vacuum is kept on filtration apparatus until the film is mostly dried (~ 20 min). The filtrated film on Al_2O_3 membrane is further dried in the glove box overnight, and then oxidized with dry air outside of the glove box (figure 4.1(2)). The film can be then transferred onto any desired substrate.

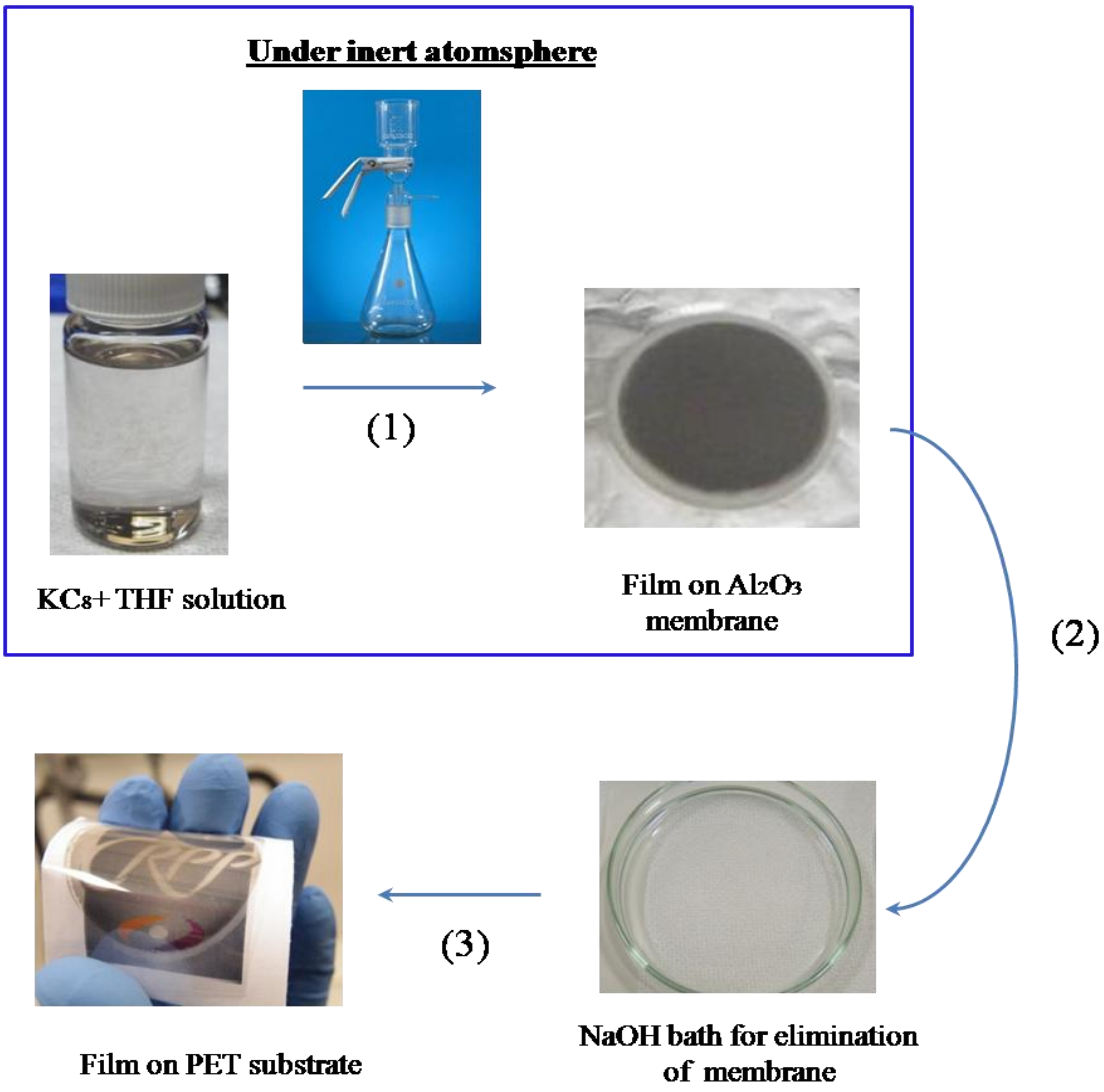

Figure 4.1: Filtration method for preparing graphene film

The transfer process is done in 1.5 M NaOH bath illustrated in figure 4.1 (2-3). The Al_2O_3 membrane is dissolved in the NaOH bath. After complete dissolution of the membrane, a transparent homogeneous film is floating on the liquid surface. Then, several washing process with MillQ H_2O are done until the pH value of the washing bath is 7. Free-standing films can then be transferred to a desired substrate, such as pre-washed PET film, glass, Si/SiO_2 wafer etc. We first transferred the film onto polyethylene terephthalate (PET) substrate (PET, GoodFellow, biaxially oriented PET film). For PET film, one has to use biaxially oriented film. PET substrate suffers several organic solvents (acetone and isopropanol) involved in the washing process before transferring the graphene film onto it. These organic solvents can damage PET which hasn't had biaxially oriented treatment; especially optical properties of the PET substrate will be degraded after washing with organic solvents. The transferred film is dried in oven at 50 °C overnight. Several films were prepared with this method by varying volume of graphenide solutions.

1.2 Characterizations of graphene films

The electrical-optical properties of as-transferred films were tested. Several common techniques were also applied to study these films. During these studies, we made some detailed comparison between our film and graphene films produced by other solutions routes. This can help us understand better our films, thus we can find efficient way to improve their properties.

1.2.1 Surface resistivity and transmittance

An image of a transferred film on PET is shown in figure 4.1. The film is transparent, continuous and flexible. The surface resistivity of films was measured by four-point probe

method presented in chapter 2. After the transfer of graphene film onto the substrate, the film is patterned by four gold contacts through a mask to ensure electrical contact between film and measuring instrument. The current−voltage was measured by Keithley 6220 and 2000 Multimeter. The optical transmittance of films is characterized by UV-Visible-NIR Microspectrophotometer (CRAIC 20/20 PV^{TM} Dual Microscopectrophotometer).

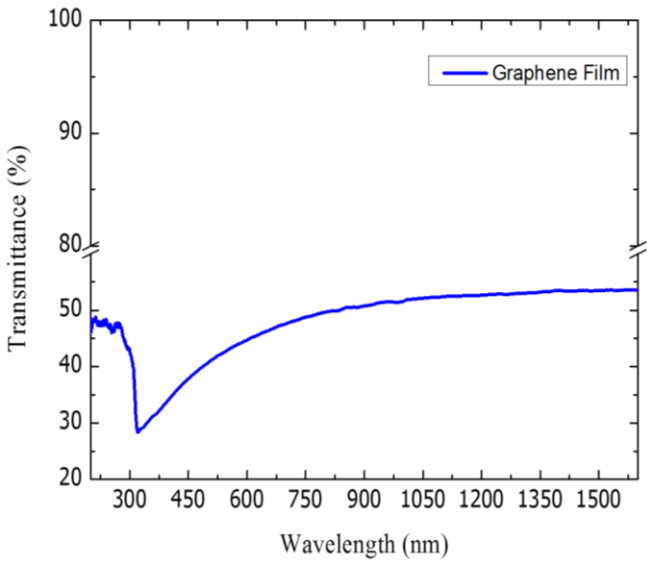

(a)

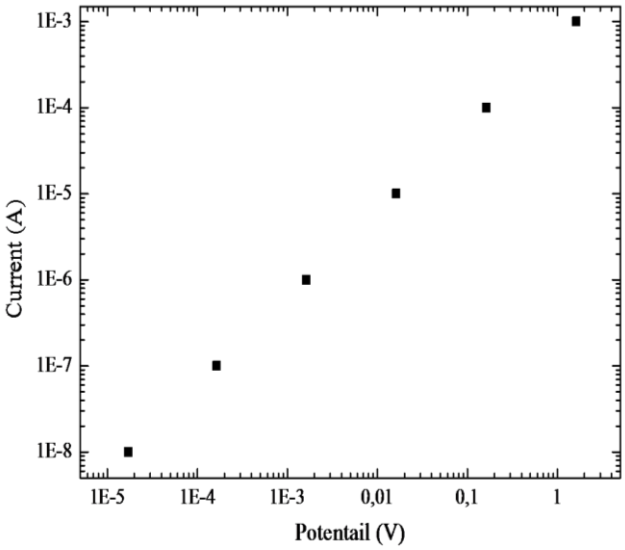

(b)

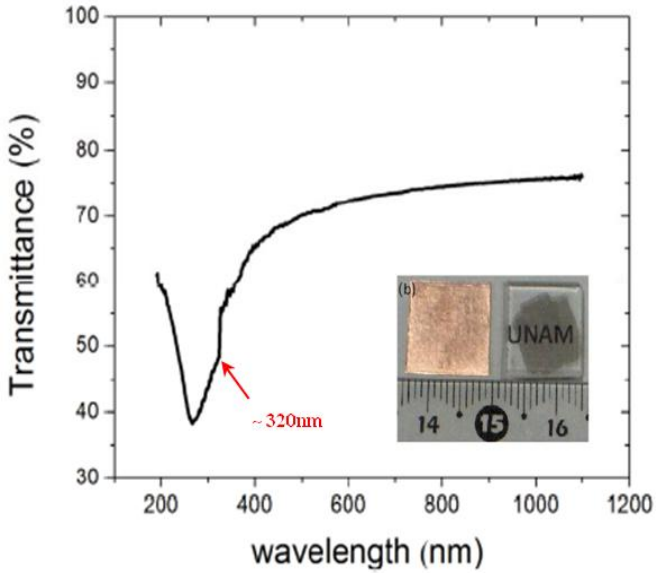

(c)

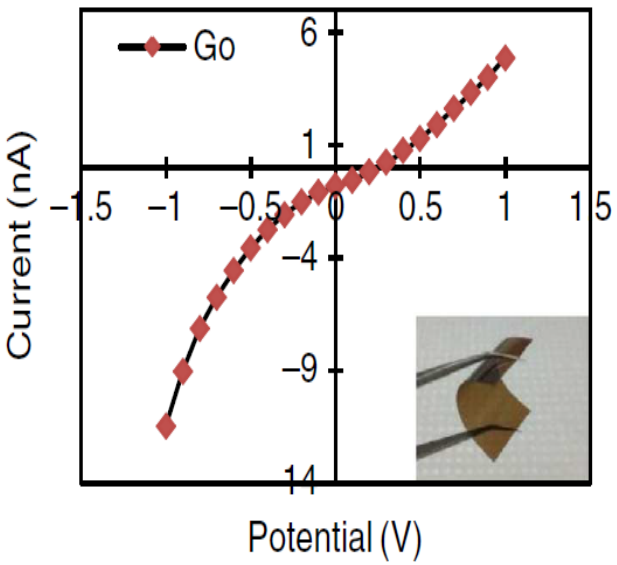

(d)

Figure 4.2: (a) UV-Visible transmittance spectrum of graphene film on PET substrate; (b) I -V curve of the graphene film; the current and potential scale are in logarithmic scale; (c) UV-Vis transmittance spectrum of multilayer graphene (11 layers) synthesized by CVD method; insert: graphene samples on Cu and fused quartz (right); [7] (d) I–V curves of GO; [8] insert: graphene oxide paper/film.

From a typical transmittance spectrum of graphene film on PET substrate illustrated in figure 4.2 (a), we can see that there is an absorbance peak around 310 nm in our film. The graphene film synthesis by CVD method displays an absorbance peak around ~ 268 nm. [9] Yang et al. attributed this peak to resonant excitonic effects. [10] The reported transmittance spectra of reduced GO films were shown only in visible region (400 - 800 nm). [11] But from their UV-visible absorption spectra which have been largely studied, one can also obtain information concerning their optical properties. The GO film showed a dominant absorbance peak around 233 nm, which is ascribed to $\pi \rightarrow \pi^*$ transition of aromatic C-C bonds, and a shoulder at 300 nm, associated with $n \rightarrow \pi^*$ transition of C=O bonds. [10, 12] The shoulder around 300 nm disappeared after chemical reduction treatment, most likely due to the decrease in the concentration of carboxyl groups. [10] For rGO film the main peak was red-shifted to 270nm as the electronic conjugation was restored. [12, 13]

From the comparisons of optical properties in UV to visible wavelength region with CVD graphene film and rGO film, we can see that our films show similar transmittance profiles as CVD graphene and reduced rGO film. This shifted peak may indicate that the observed film contain some sp^3-like characters and/or contamination. But one should also notice that optical properties of multilayer graphene film depend on its electronic band structure which can also be dramatically changed by their stacking order.[14] Indeed, in some multilayer graphene films synthesized by CVD, as shown in figure 4.2 (c) one can observed a small peak around ~ 320

nm in the corresponding transmittance spectrum. [7] The red-shifted peak observed in our film could possibly be due to stacking order of graphene planes.

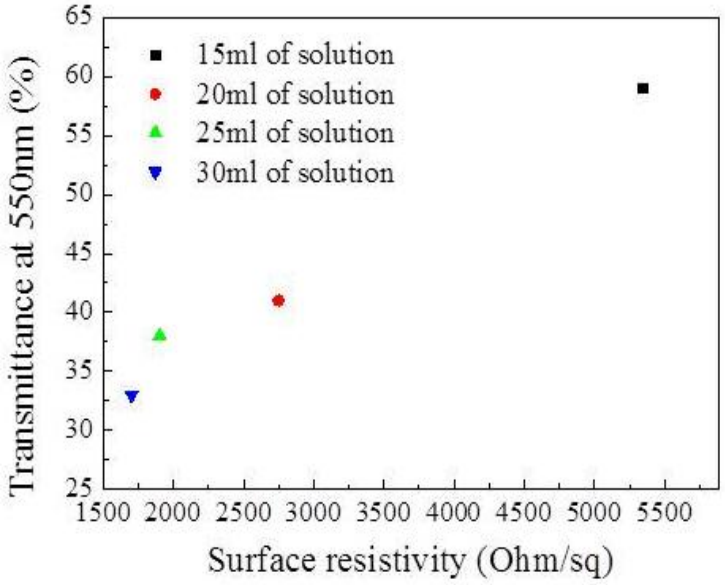

Figure 4.3: Surface resistivity and optical transmittance at 550nm for 4 films produced

The I-V curve illustrated in figures 4.2 (b) shows a linear behavior which is observed in a large tested range (from 10nA to 1mA). Graphene films synthesized by CVD method also show this linear behavior in I-V curve. [9] This linear behavior indicates that the film has good electrical properties. Indeed, the calculated surface resistivity from this film is around 2700 Ω/sq. On the other hand, the GO film exhibits nonlinear and slightly asymmetric behavior illustrated in figure 4.2 (d). The GO films show a different conductivity value ranging from 8.07×10^{-4} to 5.42×10^{-3} S/m. [15,16] Figure 4.3 shows transmittance and surface resistivity for the films prepared with 15-30 ml of graphenide solution. The surface resistivity varies from 1700 to 5500 Ω/sq, while transmittances increase from 33 % to 60%. Like all kinds of graphene film, the surface resistivity obviously decreases with decrease of transmittance because of increase of thickness. But compared to graphene films produced by other liquid-

phase routes (table 2 in chapter I), films from graphenide solutions show better electrical properties.

1.2.2 Characterization of SEM, AFM and HRTEM

AFM, SEM and TEM were used to probe film morphology. For AFM characterization, one graphene film was transferred onto PET substrate. Figure 4.4 displays characteristic AFM images of transferred film. The atomic force microscopy (AFM) image was measured by a tapping mode (Digital Instruments NanoScope MultiMode Scanning Probe Microscope). We observed that graphene sheets stack together to form continuous film and large graphene sheets are folded. It is also possible to distinguish edges of individual sheets from AFM image. In chapter 3, from observation of individual graphene sheet by HRTEM and AFM, individual graphene sheet show similar morphology. The thickness of such film was characterized also by AFM. Figure 4.4 (b) show thickness measurement performed on a film prepared with 30 ml KC_8 + THF solution. The white parts are contamination particles adsorbed on the film. The height profiles (c) and (d) demonstrate that average thickness of the film is around 25 nm.

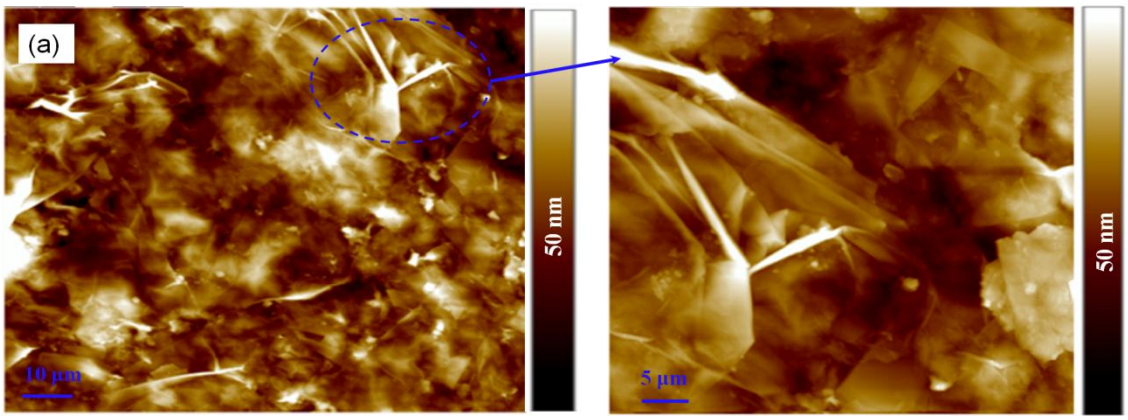

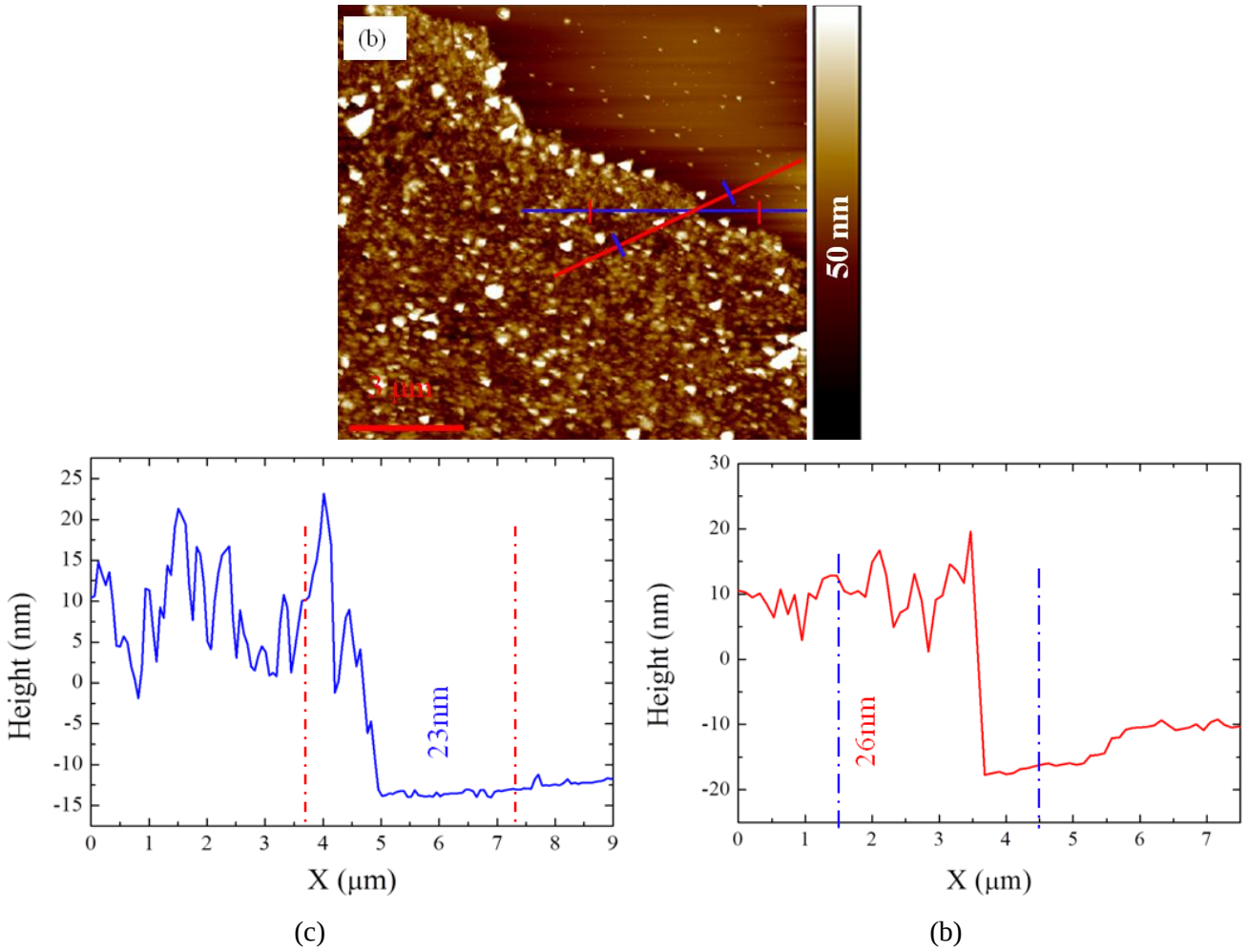

Figure 4.4: (a) and (b) AFM image of graphene film on PET substrate; (b) Thickness measurement of graphene film with AFM; Height profile of blue section (c) and red section (d).

Scanning electron microscopy (SEM) image were obtained by JEOL 6700F high resolution instrument. Figure 4.5 (a) shows a morphology similar to that of AFM image (figure 4.4). The insert in figure 4.5 (a) shows also a folded graphene sheet deposited on another graphene sheet. The SEM image of edge of film shown in figure 4.5 (b) demonstrates that the film consists of a disordered array of graphene/graphitic sheets lying approximately in the plane of the film.

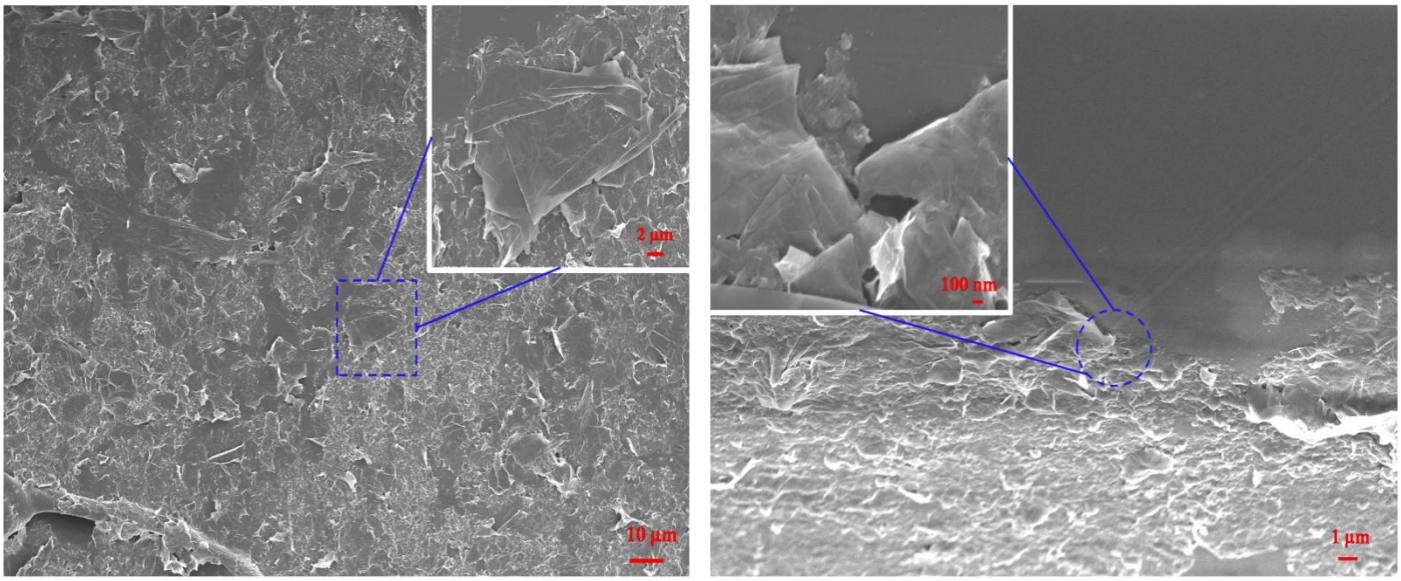

(a) (b)

Figure 4.5: SEM of graphene film on Al_2O_3 substrate. (a) centre of film; (b) edge of film.

Compared to AFM and SEM studies performed on other graphene films produced by other solution routes, graphenide film displays a similar morphology. But some self-folded graphene sheets were observed in our film, which is not reported neither for rGO films nor for films produced from graphene dispersion. [17, 18] Especially, self-folded graphene sheets were seldom observed in graphene films produced from surfactant stabilized graphene dispersions, which can prevent graphene sheets from forming self-folded configuration. But surfactant decrease electrical performance of produced thin film.

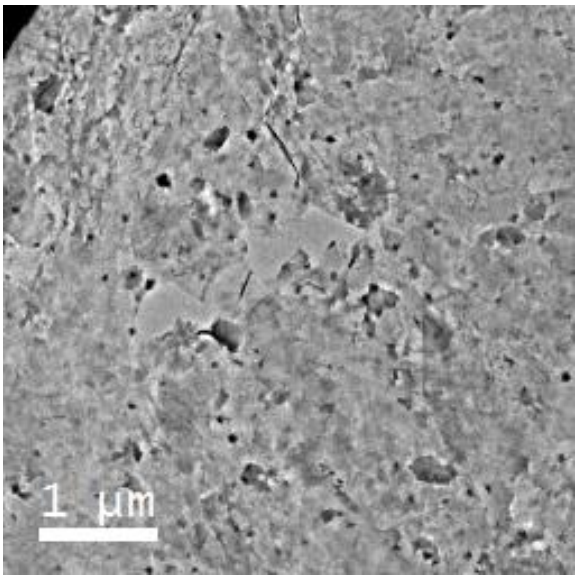

(a)

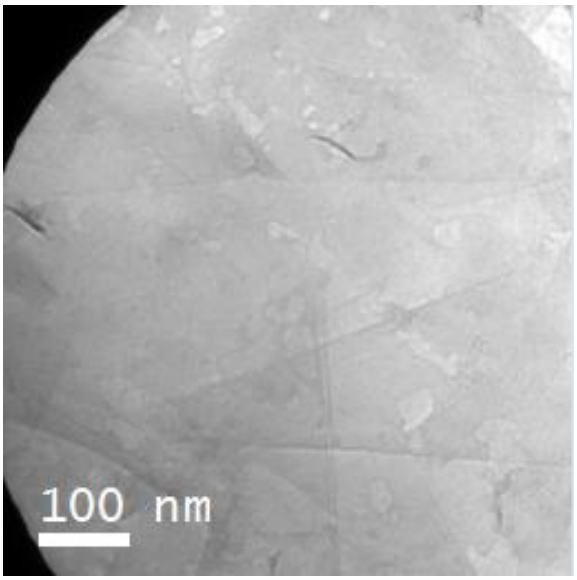

(b)

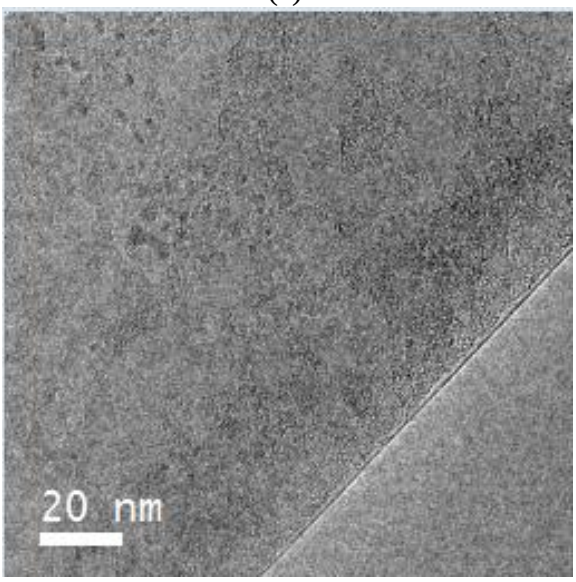

(c)

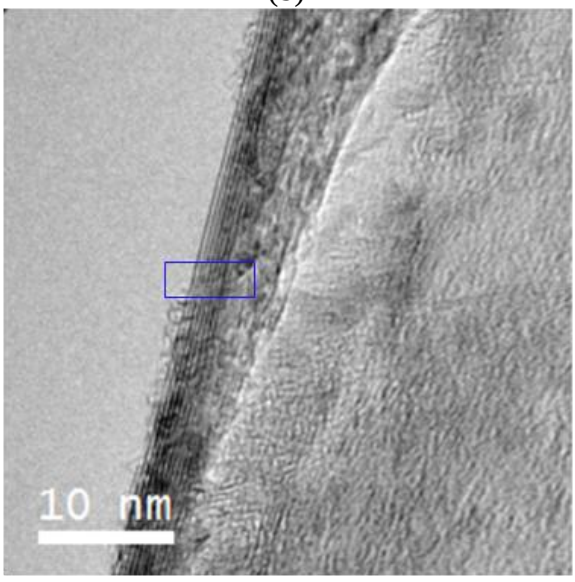

(d)

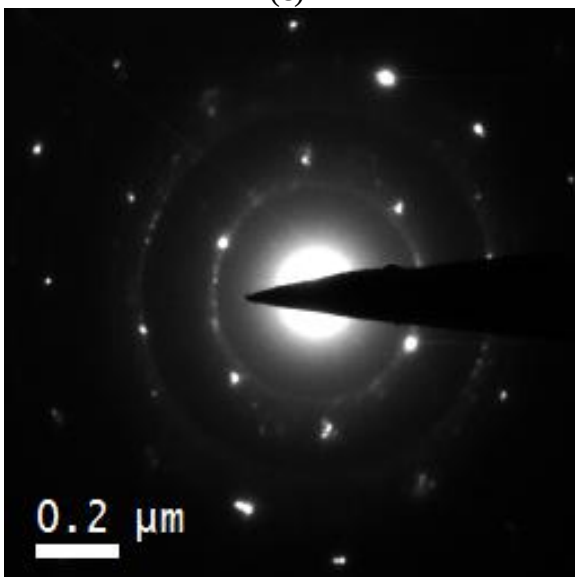

(e)

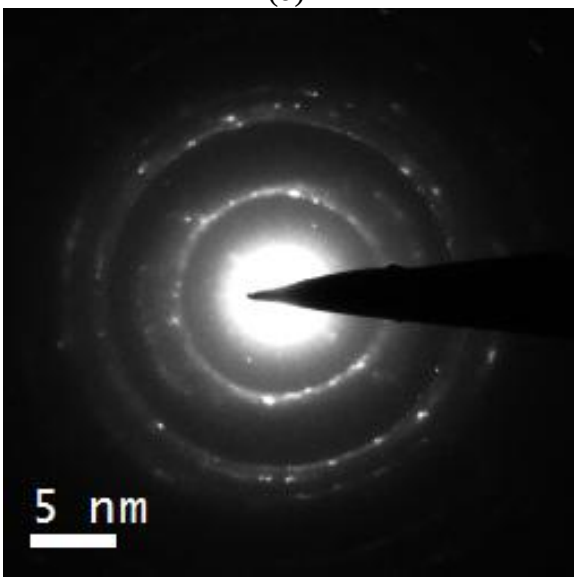

(f)

Figure 4.6: (a, b) TEM images of graphene film transferred onto Cu grid. (c) High-resolution TEM image of monolayer graphene sheet. (d) High-resolution TEM image of multilayer graphene sheet. (e,f) Selected area electron diffraction pattern (SAED) of graphene film.

For characterization by HRTEM, a graphene film was transferred onto one special TEM grid, Cu grid having 2000 mesh. Then the Cu grid was dried in oven at 50 °C overnight. The observations of HRTEM specimen was performed by Dr. Célia Castro in CEMES Toulouse. The TEM images also demonstrate (figure 4.6 (a) and (b)) similar morphology as illustrated by AFM and SEM. A HRTEM image of one individual graphene sheet shown in figure 4.6 (c) illustrates one monolayer graphene. In figure 4.6 (d), The number of layer shown in the blue rectangle is ~ 7. Selected area electron diffraction (SAED), figure 4.6 (e) and (f), indicate a graphene-like disordered nature with turbostatic arrangement of hexagonal layers in film. Especially, in diffraction pattern shown in figure 4.6 (f), individual spots are barely visible as the contributing patterns merge into a ring pattern characteristic of a polycrystalline sample. This suggests that there are no preferred stacking orientations between graphene sheets when the thin film is formed in this way. Starting from graphite, we got uncorrelated stacked graphene films.

1.2.3 Characterization of as-produced film with XPS

The objective of this study is to evaluate chemical changes of very thin films composed of graphene sheets by using X-ray photoelectron spectroscopy (XPS). XPS measurements were performed with a VG 200i XL ESCALAB spectrometer. All spectra were taken using an Mg non-monochromatized source (1253.6 eV) at 200 W. The typical operating pressure was $2x10^{-7}$ Pa. Both the starting graphite and graphene films were stamped on a XPS sample holder by using conductive copper adhesive tape. The measurement of chemical composition

from XPS shows that in the starting graphite the atomic concentration of oxygen is 1.71 %, whereas in graphene films it has increased to 5.24 %, which leads to a C/O atomic ratio of 21.3.

In order to understand whether this important increase of oxygen content is due to oxidation provoked during production process and other cause, we studied C1s and O1s XPS spectra for starting graphite and as-prepared graphene film.

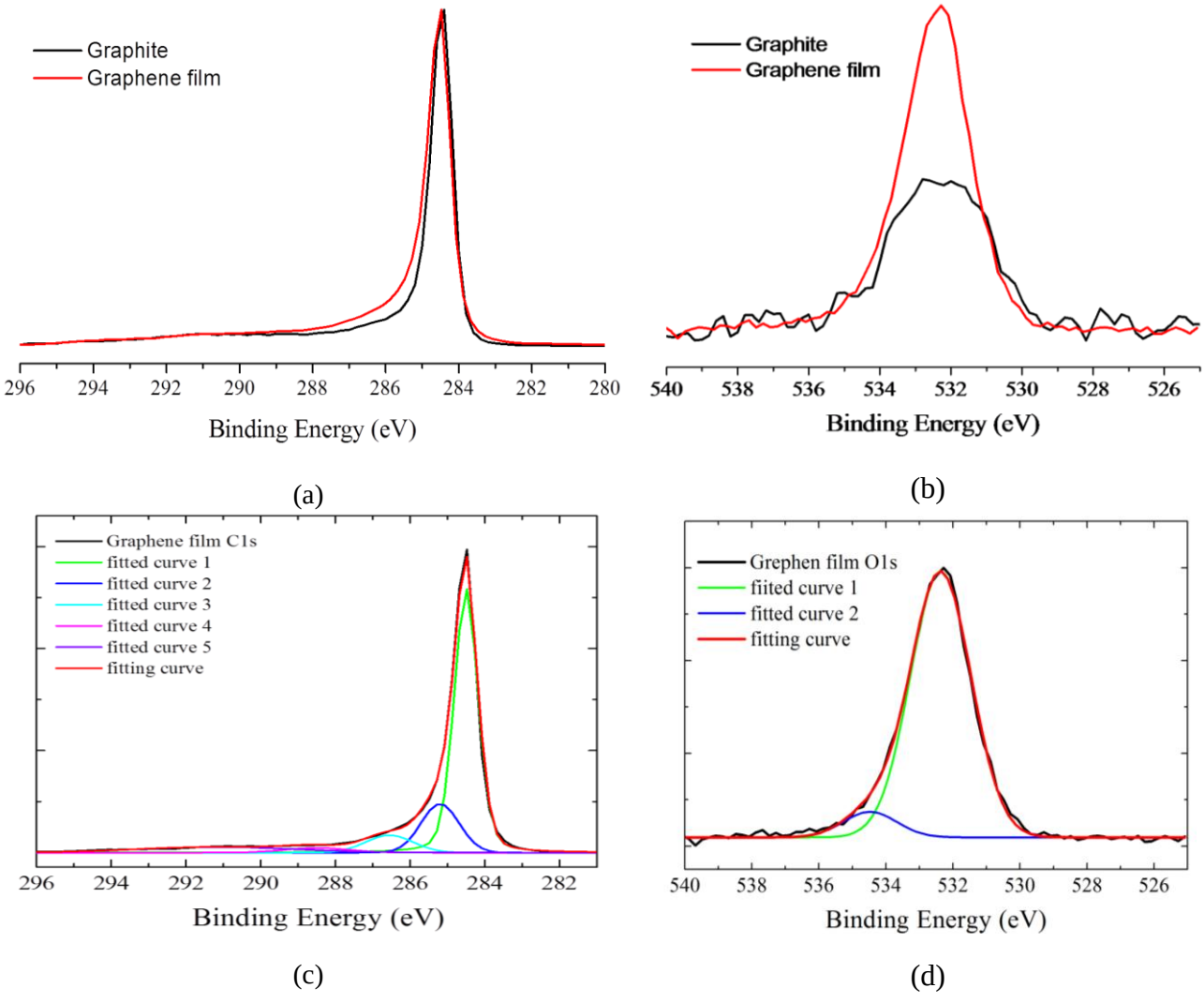

Figure 4.7: XPS spectra for graphene film and graphite: (a) C1s peaks; (b) O1s peaks; De-convolution of graphene film C1s and O1s peaks: (c) de-convolution of C1s peak into four components centered at

284.5 eV (green), 285.3 eV (blue), 286.6 eV (cyan), 288.5 eV (oliver) and 290.8 eV (violet); (d) deconvolution of O1s peak into two components centered at 532.4 eV (green) and 534.5 eV (blue)

The XPS spectra shown in figure 4.7 (a) and (b) are respectively C1s and O1s spectra of graphite and graphene film transferred on glass substrate. From C1s peaks, we can see that C1s peak of graphene film are broaden at relatively high binding energy (BE) (from ~ 285 eV). In general, the binding energy of C - C and C - H bonding are assigned around 285 eV. And their chemical shifts of + 1.5, + 2.5 and + 4.0 eV are typically attributed to C - OH, C = O and O = C - OH functional groups, [19, 20] which are observed in GO film.

A detail studies for C1s and O1s of graphene peaks were performed by XPS peaks de-convolution analysis. The XPS peaks were fitted with Voigt function having 80% Gaussian and 20% Lorentzian character, after performing a Shirley background subtraction. From figure 4.7 (c), we can see that the C1s peak of graphene film can be mathematically fitted with four components, which are located at BE of 284.5 eV (FWHM ~ 0.75 eV) assigned to graphitic sp^2 peak, 285.3 eV (FWHM ~ 1.20 eV), 286.6 eV (FWHM ~ 1.50 eV), 288.5 eV (FWHM ~ 2 eV) and 290.8 eV (FWHM ~ 5.00 eV) assigned to $\pi \rightarrow \pi^*$ shake-up satellite peak of graphitic carbon band. The $\pi \rightarrow \pi^*$ shake-up satellite peak located at ~ 290.8 eV (FWHM ~ 5.00 eV) indicates that a delocalized π conjugation, characteristic of aromatic C structures. It is significant to note that for GO materials there is no $\pi \rightarrow \pi^*$ shake-up satellite peak and this peak won't appear until 400 °C for thermally reduced graphene oxide materials. [21-23] Thus, there is a fundamental different between our film and oxidized graphene material.

It was found that the bands appearing at higher energy tended to be broader (FWHM > 1 eV) than the sp^2 component (FWHM ~ 0.75 eV). The larger FWHM and broad tail towards higher binding energy imply that contributions of a variety of different carbon bonding

configurations are superimposed. This makes precise assignment difficult. For GO materials, one can find a component at 285.6 eV which is generally attributed to C atoms directly bonded to oxygen in hydroxyle configurations (shifts of 1 - 1.5 eV to higher BE), and de-convolution analyses show that their FWHM are always around 1 eV.[21,24-30] In our film, the assignement of component located at 286.6 eV (FWHM ~ 2.85 eV) is a little tricky, some author assign the peak around 286.5 eV to epoxy/ether C-O groups, [31, 32] while others assign them to defective graphite structure and C sp^3. [33] It is a little subjective to assign this component to special functional groups, because almost all of these de-convolution studies were based on graphite oxide for which FWHM of functional peak is around 1 eV. For high temperature (~ 1000 °C) reduced graphene oxide materials, Yang et al. attributed one peak around 286.4 eV to C-OH species. Based on high resolution XPS study performed on graphene oxide, the small peak ~ 288.5 eV can be associated to carboxyl groups (COOH or HO-C=O). [32] Regardless of peaks assignment, the C1s peaks shows that the graphitic C = C species are dominant, which has huge difference with C1s of GO film. [32, 34]

The shape of the O1s peak obtained from graphene film suggests a de-convolution into two components at 532.4 eV (FWHM ~ 2.1 eV) and 534.5 eV (FWHM ~ 1.9 eV). The assignment of peaks for O1s spectra is of interest, as there are some conflicting assignments of the "carbon-oxygen" functional groups in the literature. [35-37] Researchers suggest using analysis results of O1s spectra to provide complementary information for C1s spectra. The generally accepted de-convolution for O1s peaks consists of components at the lowest BE corresponding to doubly-bonded oxygen groups, such as C = O or carboxyl groups O = C – OH, and another component at higher BE corresponding to singly-bonded oxygen C – O. [37] In published articles, researchers have assigned O1s peak around 531 eV to C = O and O = C – OH groups and assigned peak at 533 eV to C – OH groups. [26, 37, 38] The photoelectron

kinetic energies of O1s are lower than those of C1s; therefore the O1s spectra are more surface specific compare to C1s. This means increased O1s intensity could also be due to oxygen-containing elements absorbed on surface of materials.

1.2.4 Characterization of film with Raman spectroscopy

The Raman spectra were acquired by Raman spectroscopy HORIBA Xplora with 532, 638 and 785 nm wavelength incident laser light at room temperature. We used 1 % laser power filter which can decrease the laser power to < 0.2 mW to avoid laser induced defects discussed in chapter 3. The spectra were collected under a microscope (× 50 objectives). The Raman-scattered signal was dispersed by a holographic grating with 1800 lines/mm for high spectral resolution and detected by a charge-coupled device (CCD) camera.

Raman spectra of graphene film transferred on glass substrate are shown in figure 4.8. The Raman spectra of as-produced graphene film display a D band located ~ 1340 cm^{-1}, a G band at 1580 cm^{-1} corresponding to an ideal graphitic lattice vibration mode with E_{2g} symmetry and a 2D band located ~ 2650 cm^{-1}. The line-shape analysis of D band shown in figure 4.7 (b) exhibits a single Lorentzian curve, which is different from D band of starting graphite illustrated in chapter 3. In graphite, D band is fitted by two Lorentzian curves (see figure 3.26(a)). While for G band, one Lorentzian curve was applied to fit G band and the small band at the shoulder of G band was fitted by one Fano function. 2D band can also be fitted by one single Lorentzian curve, which demonstrates that uncorrelated graphene sheets stacked randomly in the film without reforming graphitic AB stacking order. Meanwhile, D band and D' band were observed under three laser excitation energy. The presence of D and D' band is commonly attributed to the defects. [39-42] Since the intensity of G band $I(G) \propto E^4$ laser, while the I(D) is independent of the laser energy for the 1.9 eV (652 nm) – 2.7 eV (459 nm) laser

excitation, [43] we can see from figure 4.8 (a) and table 1 the relative intensity of D band I(D) decreases with laser excitation energies compare to I(G).

We discuss in following part about defect-active band, D band. It is known that the D band results from symmetry breaking occurring at the edges of graphite planes in sp^2 carbon materials. [44] Indeed, Raman spectrum of turbostratic graphite also exhibits an additional first-order defect D band known to be a characteristic of disordered graphite lattice. [45, 46] Theoretical calculations have shown that each of first-order Raman bands in spectra of highly ordered and disordered graphitic materials can be attributed to the vibrational modes the ideal graphitic lattice. Charlier et al. performed in 1992 a simulation results for pregraphitic (disordered) carbon by using tight-binding calculation. [46] They reported that the density of states of π-electrons in turbostratic graphite present a 2D behavior.[46] This is also the reason that in turbostatic graphite 2D band displays a simple peak configuration so that turbostratic graphite can be considered to be 2-D graphite, like monolayer graphene. In this structure, the graphitic layers are shifted and rotated at random and interlayer spacing varies from plane to plane. The irregularities of such a stacking sequence can lead to a "fuzziness" of bottoms and tops of the electronic band edges, like amorphous carbon. [46-48] It is well known that in a Raman spectrum of amorphous carbon film there is a huge D peak. [49] These D bands correspond to a graphitic lattice vibration mode with A_{1g} symmetry. In addition to D band, in disordered graphite there is another first-order band called D' band located around 1620 cm^{-1}. The D' band feature is associated with the presence of defects in the lattice and originates from a double resonance process close to the Brillouin zone centre. [44, 45] Similar to the G band, the D' band corresponds to a graphitic lattice mode with E_{2g} symmetry. [50, 51] The relative intensity of D' bands increases with increasing incident laser wavelength which is

also attributed to resonance effects.[52] The intensity of D' band is in function with density of disorder.

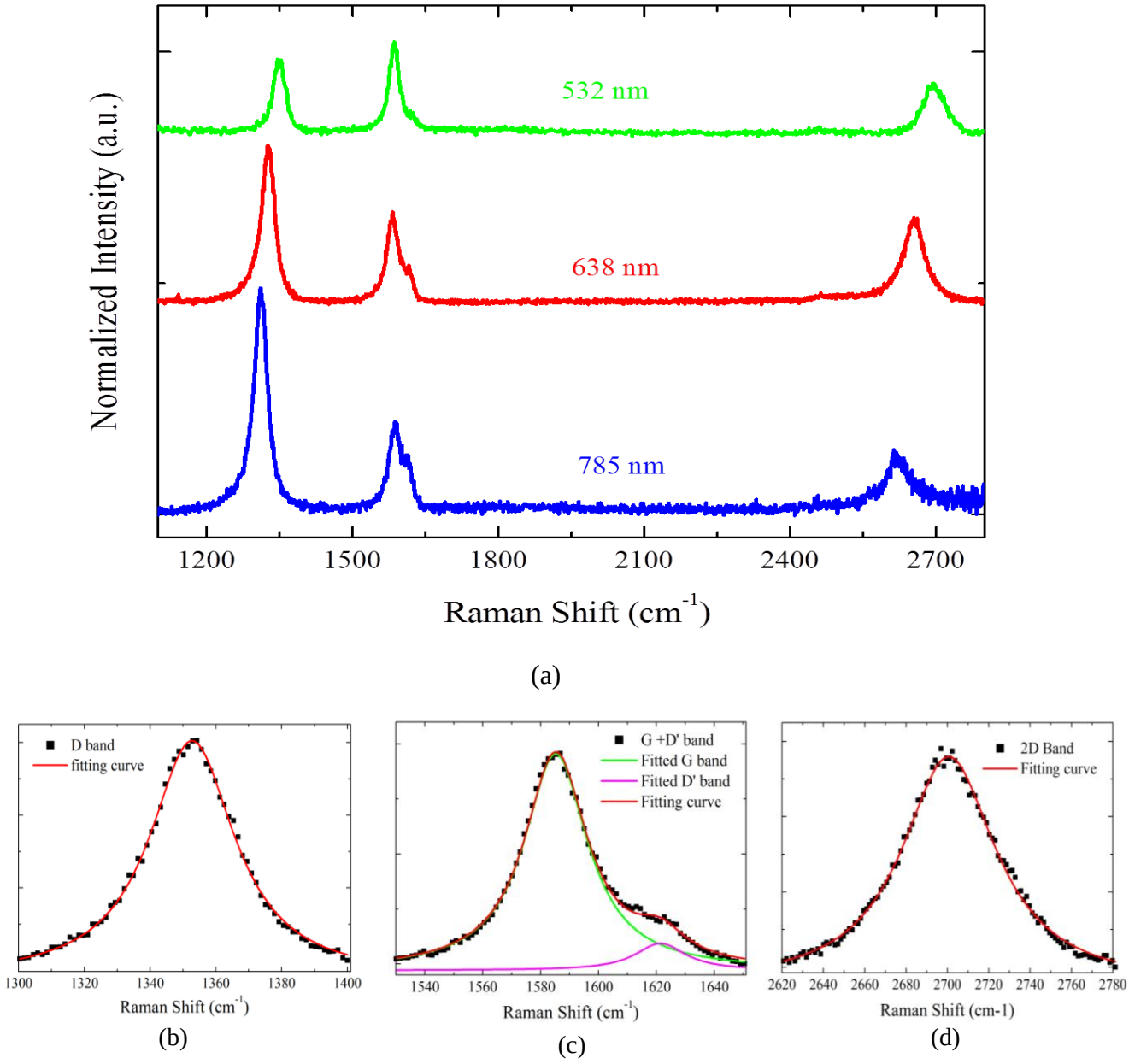

Figure 4.8: (a) Raman spectra of graphene film with 532nm, 638nm and 785nm laser excitation. Line-shape analysis for Raman spectra acquired with 532 nm laser excitation: (b) D band; (c) G band; (d) 2D band.

Like Raman spectrum acquired by 532 nm laser excitation, the Raman spectra for laser wavelength excitations of 638 nm and 785 nm shown in figure 4.8 (a) can also be fitted by

Lorentizan and BWF functions. The Raman shift and FWHM (2 Γ) of D band, G band, D' band and 2D band deduced from line-shape analyses are summarized in table 1. The Raman shift of G band is independent of laser energy, so ω (G) are located ~ 1585 cm^{-1} for three lasers wavelength, while FWHM of G band increase with decrease of laser excitation energy. The bleu-shifted ω (G) implies that graphene film is slightly dopped. We can see the frequencies of D band and 2D band display a red-shift when laser excitation energy change from 532 nm to 785 nm.

	D band		G band		D' band		2D band	
	ω (cm^{-1})	Γ (cm^{-1})	ω (cm^{-1})	Γ (cm^{-1})	ω (cm^{-1})	Γ (cm^{-1})	ω (cm^{-1})	Γ (cm^{-1})
532 nm	1349	15	1585	12	1620	5.5	2695	29.5
638 nm	1326	16	1586	15.5	1616	7	2654	28
785 nm	1310	16	1587	16.5	1613	7.5	2621	25.5

	I(D)/I(G)	A(D)/A(G)	I(D')/I(G)	A(D')/A(G)	I(2D)/I(G)	A(2D)/A(G)
532 nm	1.05	0.85	0.10	0.05	1.35	0.60
638 nm	1.92	1.83	0.28	0.15	0.61	0.97
785 nm	2.54	2.57	0.39	0.19	0.77	0.52

Table 1: Raman spectra parameters of graphene for 3 laser energy excitation.

The ratio of I(D)/I(G) is often used to study the defects in graphitic materials. Note that in some cases the integrated area (A) is also used as intensity to evaluate disorder in graphitic materials.[53] Thus, for disorder study we can use peak intensity (the height of the peaks) ratio denoted as I(D)/I(G) or integrated intensity (the integrated area) ratio A(D)/A(G). It is then interesting to compare the evolution of I and A to investigate disorders. From table 1, we can see that I(D)/I(G) ratios are similar to that of A(D)/A(G) for three laser energy and both of ratios increase as laser excitation decrease. For large disorder the intensity ratio I(D)/I(G) can provide enough informations about disorders.[39,54] In general, groups using BWF + Lorentzian functions report peak height ratio, while groups using two Gaussains report the

area ratio. [45] This difference is not so important for in our graphene film, since BWF and Lorentzian functions were used to practice shape analyses. Taking into account that I(G) is constant, I(D') is simply proportional to I(D). Thus I(D')/I(G) exhibits similar behaviors. In the following part of this chapter, I(D)/I(G) will be used to study the defects.

In the previous part, we compared C1s peak of our graphene film with that of thermal reduced GO film, as high temperature thermal reduction (~ 1000 °C) is considered as the most effective reduction method. Both C1s peaks have a very similar profile and they have an almost equal C/O ratio. With Raman spectra, we can also make a comparison between our film and high temperature reduced GO films (see figure 3.26(b)). We can see there is great difference between our film and rGO films. In Raman spectrum of rGO films, there is one intensive D band and 2D band is almost invisible. Thus, we have reason to believe that in our film the increase of oxygen content raised from different cause than rGO films. Thus a series of thermal treatments were performed onto our film to reveal the reason and improve properties of films.

2. Evaluation of graphene films

Before performing a thermal treatment, thermogravimetric experiments were performed on graphene films in order to understand the thermal properties of as-produced graphene films. In order to obtain sufficient material for thermogravimetric experiments, more than six graphene films (for the 6 films m ≈ 1.37 mg) were prepared and transferred onto an alumina sample holder. To better control and understand the thermal treatment process, films were placed into thermogravimetry (TG, SETARAM Setsys) and heated at 900 °C for 1 hour under constant Ar flow. The ramp up time from room temperature is 5 °C/min, so is cooling rate. Figure 4.8 (a) show TG results of graphene materials under Argon. Once these graphene materials were treated and/or deoxygenated under argon, they were then submitted to calcination under air at 900 °C for 1 hour. Figure 4.9 (b) shows that the treated film are highly stable up to 500 °C.

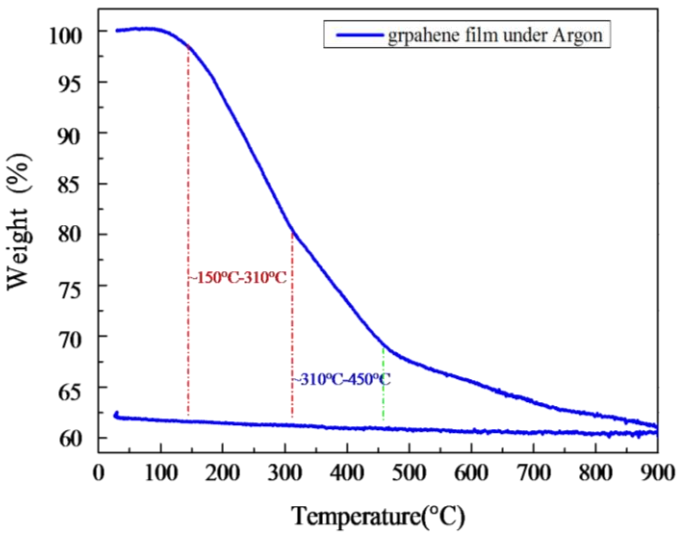

(a)

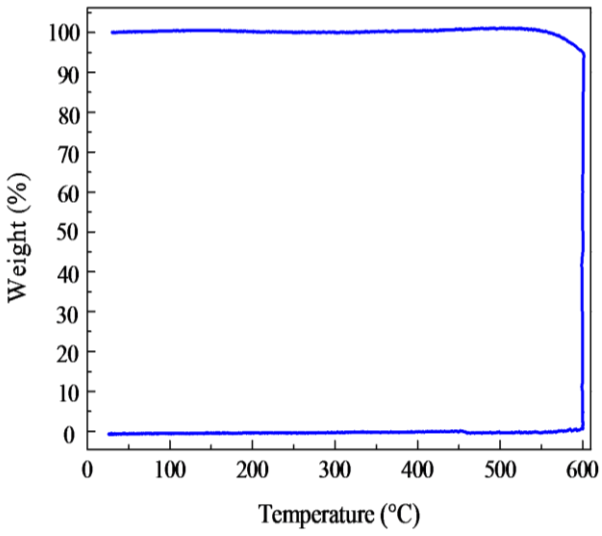

(b)

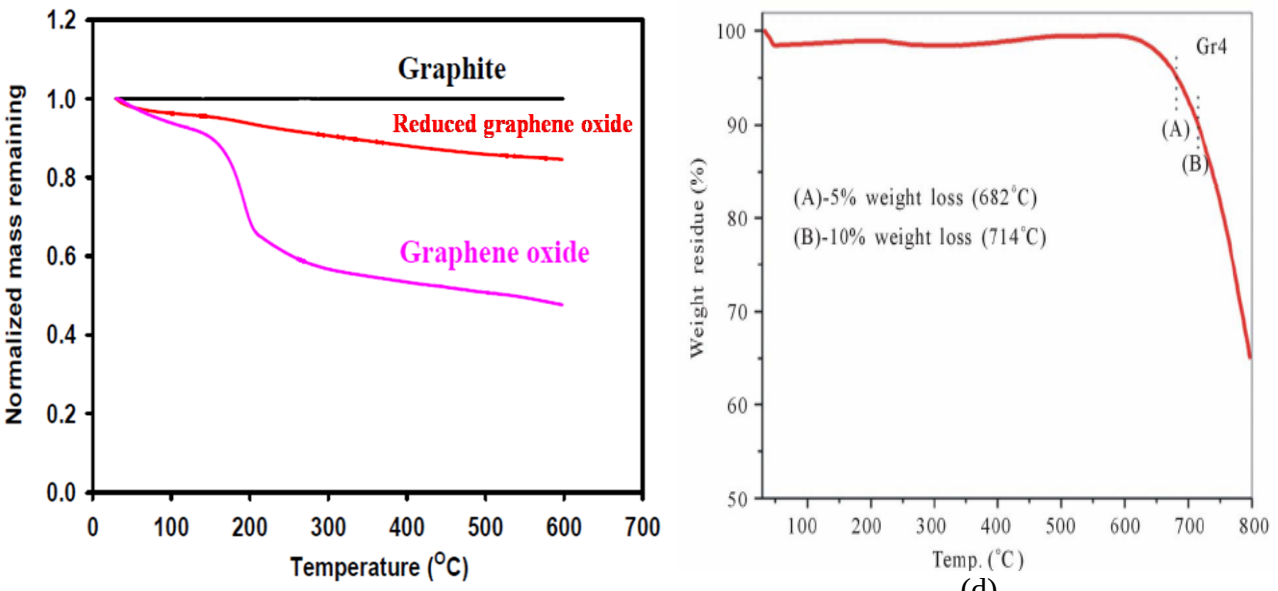

Figure 4.9: (a) TG results of graphene films under Ar. (b) TG results of calcination of deoxygenated graphene films under air. (c) Normalized TGA plots for graphite, graphene oxide and reduced graphene. [55] (d) TGA curve of graphene materials produced from dispersion method in ortho-dichloro benzene (ODCB) with aide of sonication. [56]

Figure 4.9 (a) shows under argon atmosphere a slight mass decrease around 100 °C, which can be ascribed to the removal of adsorbed water. The main mass loss (~ 38 %) occurs from 150 °C to 900 °C. By considering weight-loss rate / slope of TG curve, we can divide the main mass loss region into three zones. From 150 °C to 310 °C, there is a steady mass loss (~ 20 %). TG curve displays another steady mass loss (~ 13 %) from 310 °C to 450 °C. The mass loss for temperatures above 450 °C is only ~ 5 %. This implies that the film contains some substances which can be easily removed by mild thermal treatment. This could be some residual THF solvent trapped in film, functional groups ions like OH^- and H_3O^+ originating from water and solvent molecules attached on film.

Compared to TG plots shown in figure 4.9 (a), GO, rGO (figure 4.9 (c)) and graphene produced from dispersion of graphite (figure 4.9 (d)) exhibit different TG curves. For

graphene oxide, the main mass loss (~ 30 %) occurs around 200 °C, and this mass loss is attributed to the decomposition of labile oxygen functional group. [34, 57, 58] The steady loss observed for temperatures above 300 °C and up to 1000 °C, which amounts to ~ 20%, is assigned to the release of more stable oxygen functionalities. [59] On the other hand, as illustrated in figure 4.9 (c), the chemically reduced graphene oxide film also shows a steady mass loss for temperature above 100 °C. Paredes et al. interpret such a result by assigning this mass loss to decomposition of more stable oxygen functional groups which cannot be eliminated by chemical reduction. [34, 57] For graphene materials produced from dispersion of graphite in solvent with sonication, the TG curve shown in figure 4.9 (d) manifests that the major mass loss (~ 5 %) occurred at around 680 °C.

Returning to our films, once the graphene materials were treated under argon, a second cycle was performed under dry air. The heating-rate and cooling-rate are both set for 5 °C/min. Figure 4.9 (b) shows that thermal treated graphene materials didn't exhibit any moss loss until 530°C, and that around 600 °C the graphene material was all burnt away. Although the comparison of TG curves among different graphene materials cannot provide us decisive conclusion concerning the oxidation of our film, together with XPS and Raman results we believe that there are others reason to explain the increase of oxygen content and that some impurities might be removed from our film by simple thermal treatment. Based on these TG results, we decided to perform a thermal treatment for our graphene film at 450°C under argon.

2.1Thermal treatment of graphene films

For thermal treatment, one film was prepared with 30ml KC_8 + THF solution, and transferred on glass substrates which had been washed with MillQ H_2O, acetone and isopropanol prior to

transfer. One film was preserved as reference film. The other films were submitted to a series of annealing treatment. The samples were then air dried under ambient lab conditions. As illustrated in figure 4.10, the films were treated by thermogravimetry (TG, SETARAM Setsys) at 900 °C for 1 hour (TF1) and 2 hours (TF2) under constant Ar flow. Both heating rate and cooling rate were set at 5 °C/min. The surface resistivity and transmittance at 550 nm were measured for reference film and treated films. In order to study the thermal treatment, XPS, Raman and XRD measurements were performed. The flow diagram of processing steps and measurement with different characterization techniques is shown in figure 4. 10.

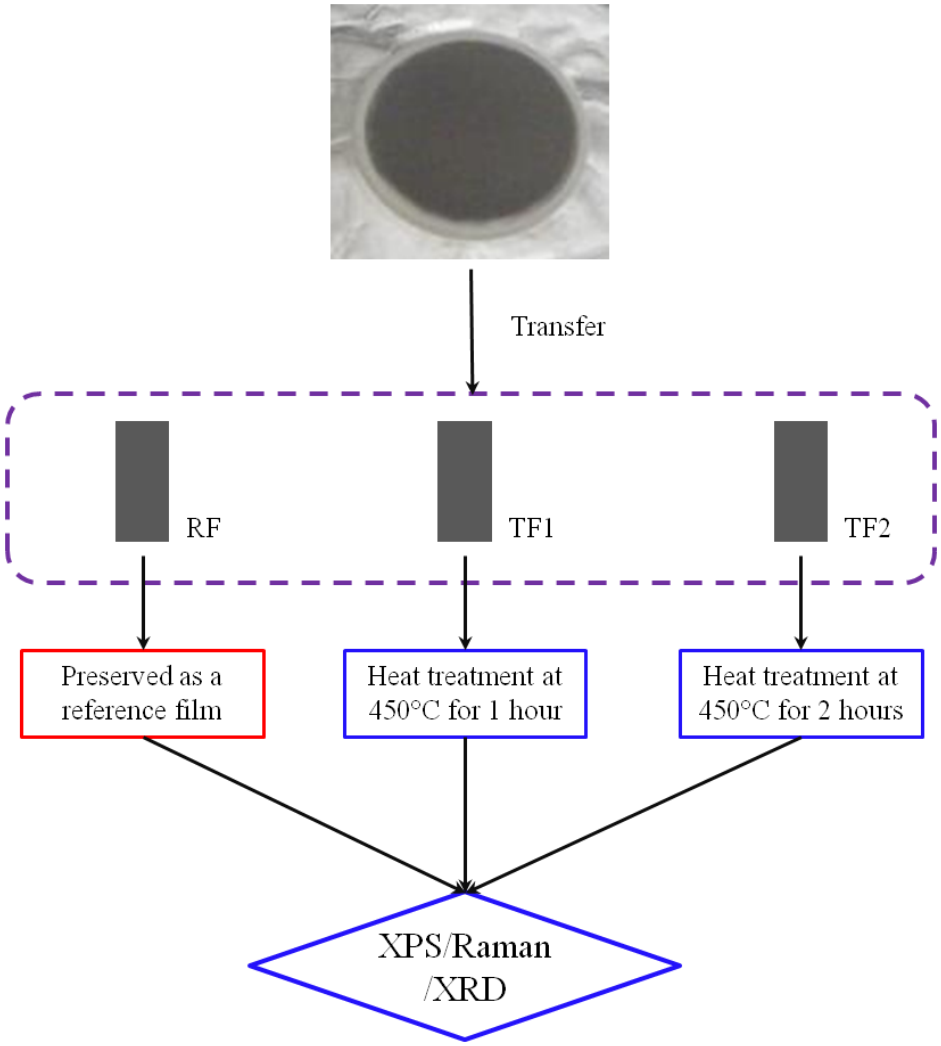

Figure 4.10: Flow chart of the experimental procedure. RF: reference film; TF1: treated film 1 (annealed at 450 °C for 1 hour); TF2: treated film 2 (annealed at 450 °C for 2 hours)

As shown in figure 4.11, a steady mass loss was observed in TG curves for both treatments. Like TG curves in figure 4.9 (a), the mass loss began around 100 °C. Almost all the removable substances were eliminated during heating stage. When temperature arrived at 450 °C, the mass became stable. During isothermal stage, the films did not demonstrate mass loss. TG curves show there were ~ 35 % of mass losses for both films.

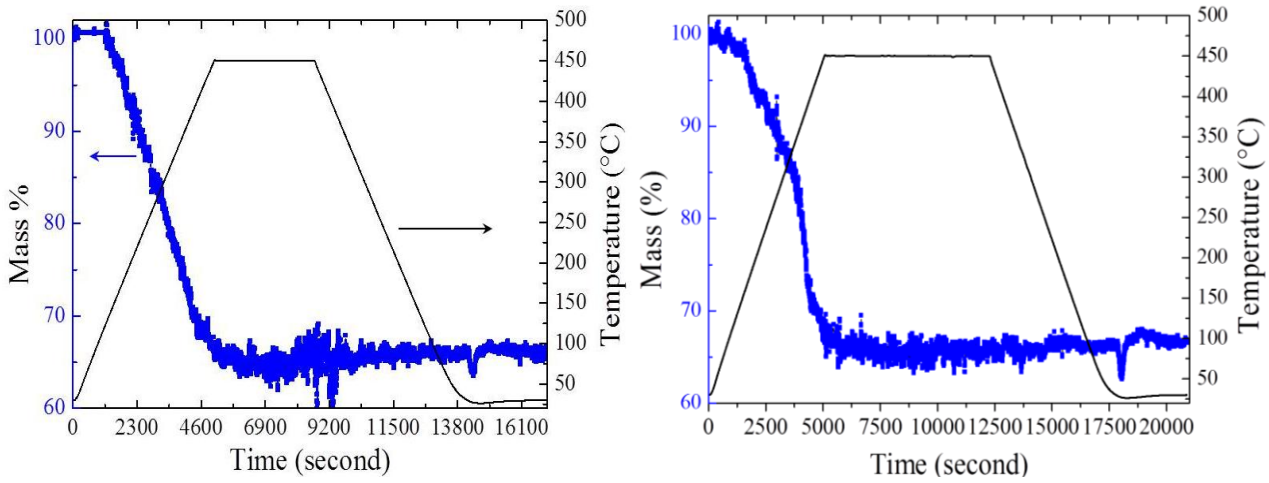

(a) (b)

Figure 4.11: Thermal treatment of graphene films treated at 450 °C for 1 hour (a) and 2 hours (b).

After treatment, we firstly tested the surface resistivity and transmittance at 550 nm of treated films. The characterized results are presented in figure 4.12. From I-V curve shown in figure 4.12 (a), we can see that after treatment for both films the I-v curve still demonstrate a linear behavior. The fitted curve of I-V show that the resistivity of the films decreased. From I-V curve, we calculated the surface resistivity of films, which decreased significantly from 1900 Ω/sq to 446 Ω/sq and 443 Ω/sq respectively for TF1 and TF2. As shown in figure 4.12 (b), the transmittance at 550nm is constant at ca.30 % before and after annealing treatment. The annealing treatment doesn't change the position of the absorption peak which is located at 310nm. By analogy with GO and rGO film in which the absorption peak are drastically

changed before and after reduction treatment duo to elimination of oxygen containing groups, we can hypothesize that the functional groups is not the main reason for explaining the dramatically decreased surface resistivity. In the following sections, the different characterizations will give a strong support to this assertion.

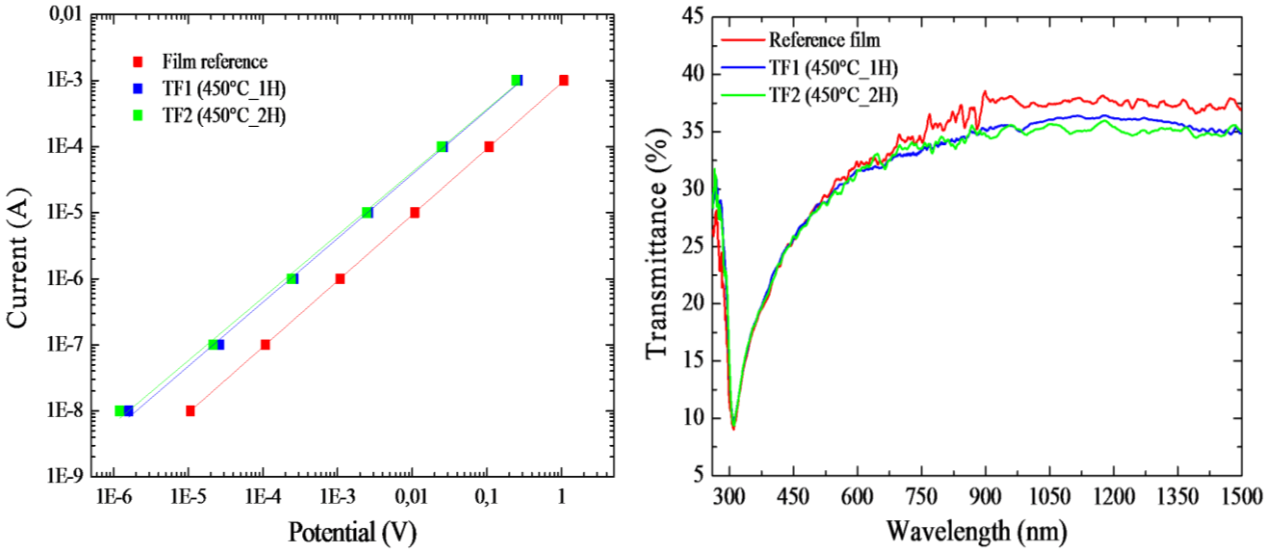

(a) (b)

	RF	TF1	TF2
Surface resistivity (Ω/sq)	1937	446	443

Figure 4.12**:** (a) I -V curve of films; the current and potential scale are in logarithmic scale; (b) UV-Visible absorption spectra of graphene films before and after treatment; Table: calculated surface resistivity and transmittance at 500nm for film before and after treatment.

2.2 Characterization of graphene films

With these annealing treatments, we can improve significantly the electrical properties of graphene films due to elimination of impurities. In next section, we will present the characterization results obtained by different techniques.

2.2.1 XPS characterizations

Evaluations of chemical changes before and after treatment were performed by XPS. The XPS measurements for films before and after treatment were performed by a VG 200i XL ESCALAB spectrometer with an Mg non-monochromatized source (1253.6eV) at 200W under pressure of $2x10^{-7}$ Pa. The atomic percentage of each detected elements are summarized in table 2.

	C1s	O1s	K2s	Si2p	Na1s
Graphite	98.29	1.71	-	-	-
Reference film	93.5	5.24	~ 0.16	1.05	~ 0.05
TF1 (450 °C_1H)	95.4	3.12	~ 0.14	1.31	~ 0.03
TF2 (450 °C_2H)	95.94	2.62	~ 0.25	1.17	~ 0.01

Table 2: XPS analyses: atomic percentage of carbon, oxygen, potassium, silicium, sodium, estimated from their corresponding peak.

As seen in table 2, after annealing treatment, the oxygen content decreased. We also noticed that there was a small amount of potassium which can be attributed to residual potassium oxide. And sodium was also found in graphene film. During film transfer step, we used NaOH to dissolve Al_2O_3 membrane. This is probably the reason why sodium was also observed in minute quantities in graphene films. Potassium and sodium content are very low, so oxygen associated with these elements can be ignored. Silicium was also detected in reference and annealed films due to contamination for reasons unknown to us.

A depth profile of the sample in terms of XPS quantities can be obtained by combining a sequence of ion gun etch cycles interleaved with XPS measurements from the current surface. The objective of these experiments is to plot the trend in the quantification values as a function of depth. We also applied this experiment to study our films to understand the evolution of each detected element in the films.

The etchings of film were realized with Ar^+ ion gun. Since the films were very thin, for etching procedure we used soft conditions: 500 eV energy, low mode, 1 mm of diameter of Ar^+ ion spot. Depending on the Ar^+ spot diameter, the estimated sputtering rate is 0.2 nm/s. The XPS measurements were acquired with VG 200i XL ESCALAB spectrometer with an Mg non-monochromatized source (1253.6eV) at 200W. The contents of detected elements in function of etching-depth are displayed in figure 4.13.

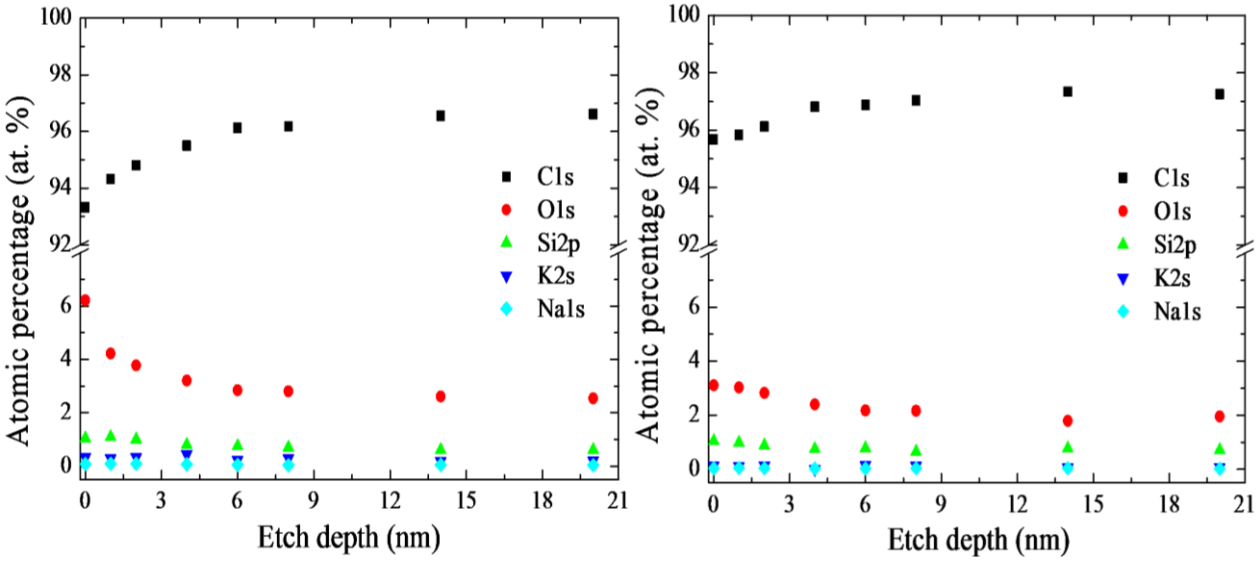

Figure 4.13: XPS Depth Profile of C1s, O1s, K2s, Si2p, Na1s for (a) reference film and (b) TF1 (450°C_1H) film.

The atomic percentage of carbon and oxygen in reference film and TF1 change in opposite directions in function of the depth analyzed. As oxygen decrease in function of depth, atomic percentage of carbon increase, as shown in figure 4.13. In the reference film, the atomic content of oxygen is around 6% at surface of film. The at.% of oxygen quickly decreases to 3 % at depth of ~ 6 nm and then becomes constant. After annealing treatment, the at.% of oxygen at surface decreased to 3 %, and the oxygen content further decreased to 2 % at depth of ~ 6 nm. These depth-depending changes of oxygen content could be explained by two ways: (i)

on the surface of the films there were absorbed oxygen-containing substances; (ii) there were also oxygen-containing functional groups on the surface of film. Even though treatment under inert atmosphere can eliminate some of these substances, there are still some oxygen-containing substances remaining on the surface. In both film, atomic percentage of silicium is constant in films before and after treatment, always around 0.9 %. We could attribute the presence of silicum to contaminations in XPS. Potassium and sodium are also constant along the thickness of film.

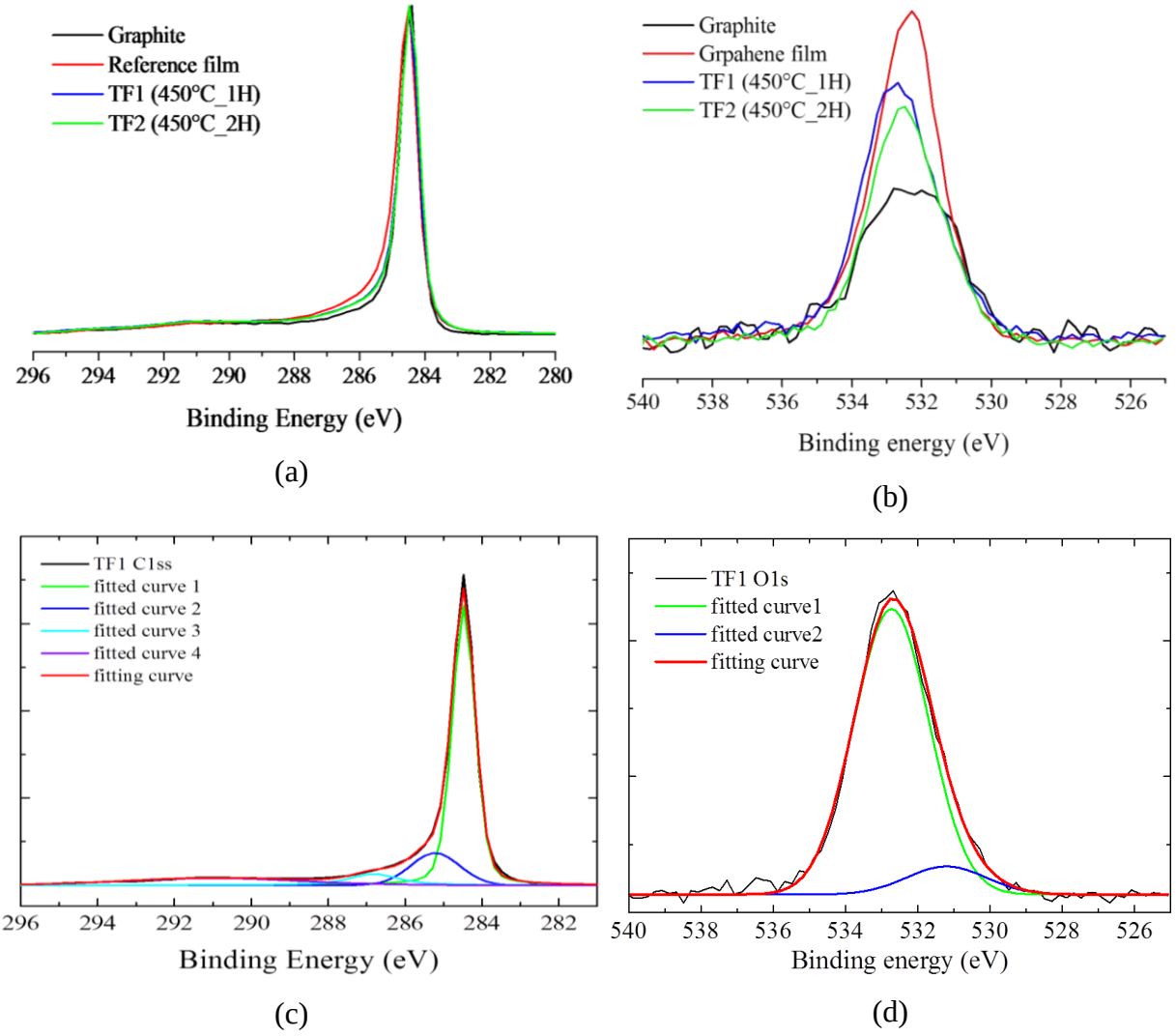

Figure 4.14**:** (a,b) C1s and O1s of starting material graphite (black), reference film (red), two films after thermal treatment TF1 (blue) and TF2(green). Deconvolution of TF1 film C1s and O1s peaks: (c)

deconvolution of C1s peak into three components centered at 284.5 eV (green), 285.3 eV (blue), 286.8 eV (cyan) and 290.8 eV (violet); (d) deconvolution of O1s peak into two components centered at 531.2 eV (green) and 532.7 eV (blue)

The comparison of C1s and O1s peaks between the graphene film before and after treatment is shown in figure 4.14. From C1s peak, we can see that after annealing treatment C1s profiles of graphene film are close to that of graphite compare to C1s peak before the treatment. Especially, the C1s intensity at binding energy around 285eV is slightly decreased, which could be assigned to the decomposition of functional groups and/or elimination of impurities during the annealing treatment. C1s peak for TF1 and TF2 films are undistinguishable. After annealing treatment, O1s peak intensity is also decreased, that of TF2 being a little smaller than TF1. The center of the O1s peak is slightly shifted after treatment. The duration of treatment doesn't change C1s peak, thus we only analyzed C1s peak for TF1.

Since the C1s and O1s peaks of TF1 and TF2 films are similar, we present here only a XPS peak de-convolution analysis for TF1. The C1s and O1s peaks were fitted with Voight functions. From figure 4.14 (c), we can see that for C1s peak of TF1 there are four components which are located at 284.5 eV (FWHM ~ 0.70 eV), 285.3 eV (FWHM ~ 1.50 eV) 286.8 eV (FWHM ~ 1.50 eV) and 290.8 eV (FWHM ~ 5.30 eV). The peak at 284.5 eV is assigned to graphitic sp^2 species. FWHM of this sp^2 peak is equal to that of starting graphite and reference film presented in section 1.2.3. It was found that the bands appearing at the higher energy region tended to be much broader than the sp^2 component. The $\pi \rightarrow \pi^*$ shake-up satellite peak located around 290.8 eV was also found in C1s peak after annealing treatment.

In addition to the sp^2 graphitic component at 284.5 eV and $\pi \rightarrow \pi^*$ shake-up satellite peak at 290.8 eV, we found only one component around 285.9 eV which is broader than two peak

(285.5 eV and 286.9 eV) found in reference film shown in figure 4.6. Hontora-Lucas et al. reported the presence of a weak C – O peak centered at ~ 285.5 eV in graphite. They claimed that this C – O peak in graphite can be explained by assuming an atmospheric oxidation. [29] Meanwhile, Barinov et al. assigned a peak at ~ 285.6 eV to epoxy and ether configurations by studying oxidation of multiwalled carbon nanotubes. [30] They claimed its close BE is shifted ~ 1 – 1.5 eV to higher BE relative to sp^2 peak. Thus, we similarly assign the peak at ~ 285.3 eV to C – O single bond coming from atmospheric oxidation.

The shape of the experimental O1s peak obtained for graphene film suggests a de-convolution into two components at 532.7 eV (FWHM ~ 2.6 eV) and 531.2 eV (FWHM ~ 2.5 eV). As discussed previously in 1.2.3, these two peaks can be assigned to singly-bonded oxygen and doubly-bonded oxygen groups. The important point is that after annealing treatment, oxygen content in film decreases.

2.2.2 Raman spectroscopy

Raman spectroscopy was also applied to study the films after annealing treatment. The Raman spectra were acquired by Raman spectrometer HORIBA Xplora with 532, 638 and 785 nm incident laser wavelength at room temperature. In order to avoid any laser induced defects, the laser power on the film were decreased to 0.166 mW by using one 1% and exposition time of laser light were limited to 2 second. The spectra were collected under a microscope (× 50 objectives). The Raman-scattered light was dispersed by a holographic grating with 1800 lines/mm for high spectral resolution and detected by a charge-coupled device (CCD) camera.

The Raman spectra of films before and after treatment under three lasers excitation are shown in figure 4.15. We can see that they display three bands: D band, G band (~ 1580 cm^{-1}) and

2D band. The D' band can also be found at shoulder of G band. As explained in previous section, the relative intensity of D band increase when laser excitation energy decrease.

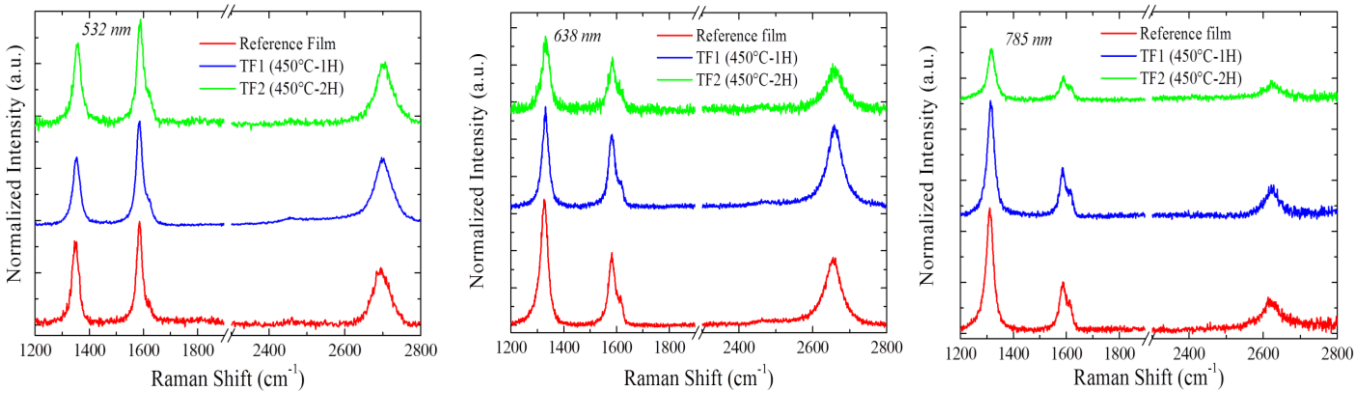

(a)

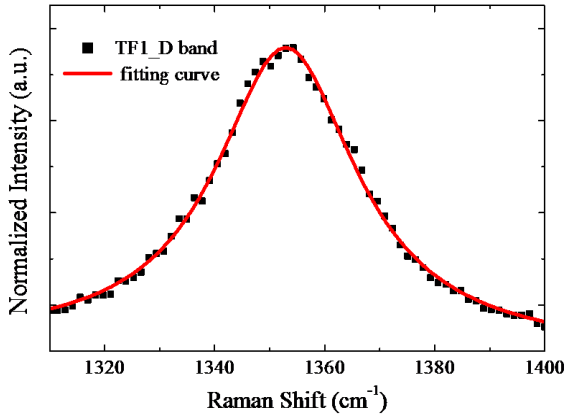

(b)

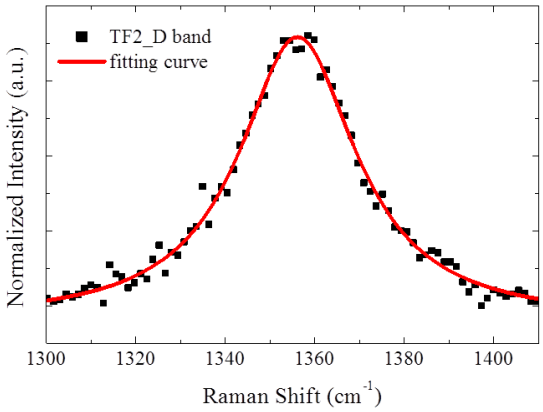

(c)

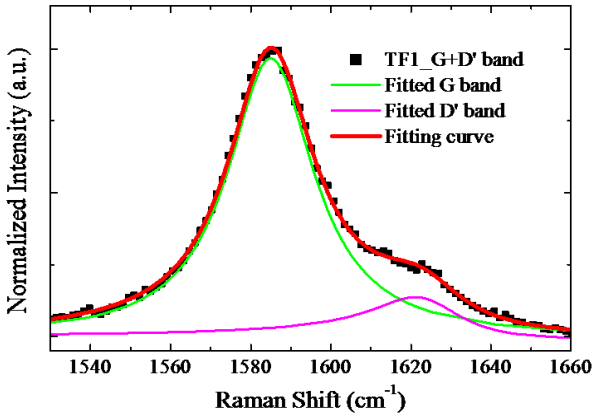

(d)

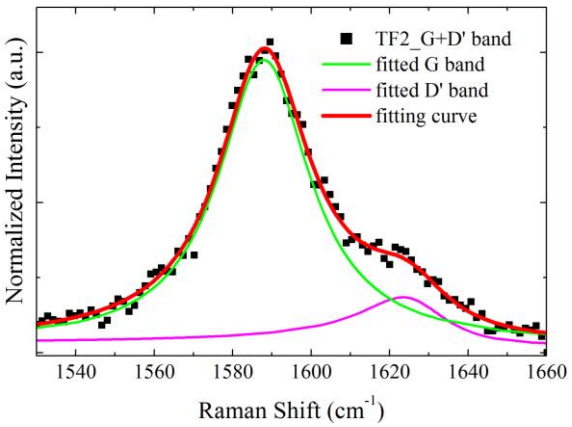

(e)

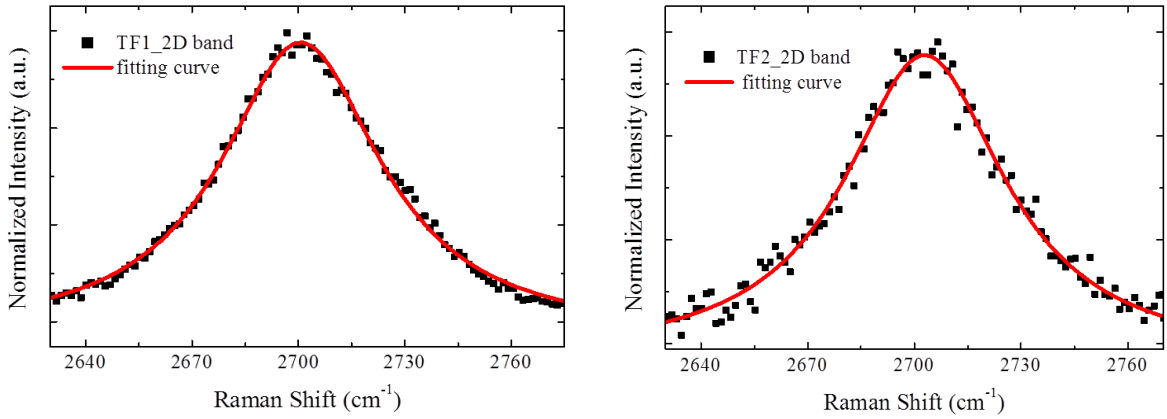

Figure 4.15: (a) Raman spectra of graphene film before and after treatment with 532nm, 638nm and 785nm laser excitation wavelength. (b-g) Peak analysis of D, G, and D' band and 2D band for TF1 and TF2 film; Raman spectra were acquired with 532nm laser wavelength. D and 2D bands can be fitted with one Lorentzian function. The G and D' bands can be fitted by one Lorentzian function and one Breit-Wigner-Fano (BWF) function.

The line-shape analyses of film were performed for reference film, TF1 and TF2 film. In figure 4.8, we demonstrated analyses results for one film before treatment. We here concentrate on analyzing TF1 and TF2. The analyses of their Raman spectra obtain under 532 nm laser wavelength are illustrated in figure 4.15 (b-g). Like reference film, their D bands contain one single Lorentzian form. G bands around 1585 cm^{-1} can be fitted by one single Lorentzian function. And it is clearly shown that around 1620 cm^{-1} one D' band is fitted by BWF function with *q* around -5. The 2D bands around 2700 cm^{-1} can also be fitted by one Lorentzain function. This is typical profile of 2D band in Raman spectra of graphene film formed by randomly stacked graphene sheets. However, for a thermal reduced GO film, only in high temperature (≥ 1500 °C) reduced GO film in which O/C atomic ratio is inferior to 0.001, one can also observe one similar 2D band. [37]

	D band						G band					
	ω (cm^{-1})			Γ (cm^{-1})			ω (cm^{-1})			Γ (cm^{-1})		
	RF	TF1	TF2	RF	TF1	TF2	RF	TF1	TF2	RF	TF1	TF2
532nm	1349	1352	1355	15	15.5	16	1585	1581	1583	12	13.5	14

638nm	1326	1330	1332	16	16	16	1584	1580	1581	15.5	14.5	13.5
785nm	1311	1315	1320	16	16	16.5	1587	1582	1580	16.5	13.5	13.5
	D' band						2D band					
	ω (cm^{-1})			Γ (cm^{-1})			ω (cm^{-1})			Γ (cm^{-1})		
	RF	TF1	TF2	RF	TF1	TF2	RF	TF1	TF2	RF	TF1	TF2
532nm	1621	1621	1623	5.5	5.5	6	2696	2698	2700	29.5	28	27.5
638nm	1621	1620	1622	7	5.5	7.5	2654	2659	2661	28	25	27.5
785nm	1614	1617	1620	7.5	6	8	2621	2623	2621	25.5	26.5	26.5

Table 3: Raman spectra parameters of graphene films under 3 laser energy excitations.

The Raman shift and FWHM (2Γ) of D band, G band, D' band and 2D band for reference film, TF1 and TF2 film are summarized in table 3. The Raman shift of D band display a small blue-shift after annealing treatment, but FWHM are always remain the same. For G band, ω (G) are close to neutral graphene, ~ 1581 cm^{-1}, which implies the treatments can remove residual doping, like OH^- and H_3O^+ originating from water or organic solvent molecules which could be attached to the surface. These ions and absorbed molecules can make graphene film to be slightly charged. The D' band exhibit a similar behavior as D band before and after treatment. Before and after treatment, 2D band didn't exhibit a change in terms of Raman shift and FWHM. Thus, low temperature annealing treatment didn't change stacking order of graphene film.

	I(D)/I(G)			I(D')/I(G)			I(2D)/I(G)		
	RF	TF1	TF2	RF	TF1	TF2	RF	TF1	TF2
532nm	1.05	0.66	0.68	0.10	0.12	0.12	1.35	0.62	0.65
638nm	1.92	1.36	1.35	0.28	0.217	0.21	0.61	1.11	1.09
785nm	2.54	2.75	2.63	0.39	0.487	0.46	0.77	0.64	0.65

Table 4: Raman analysis of graphene film under 3 laser energy excitations.

From the table 4, we can see that the intensity ratio I(D)/(G) and I(D')/I(G) slightly decrease for the film after treatment for laser excitation wavelength of 532 nm and 638 nm, which

indicate that the thermal treatment can decrease the disorder. But at 785 nm, these two ratio increase, which remain incomprehensible for us.

Since the thermal treatment can eliminate some “impurity” from the film without damage graphitic structure, this effect results in a remarkable decrease of surface resistivity. One can expect that this effect can be reflected by decrease of D band in Raman spectra over whole graphene film. With 532nm wavelength incident laser light, Raman mapping analyses were employed to observe global structural information for the reference film and two thermally treated films within 12 x 16μm area. During Raman mapping analyses, the incident laser power were carefully tuned to be 0.16 mW to avoid any damaged caused by laser. Meanwhile, the acquisition time were strictly limited to be inferior to 8 hours which implies acquisition time of each scanning spot is 1 second. The study of intensity ratio of D band to G band shows efficiency of treatment. As can be seen in Raman mapping shown in figure 4.16, the Raman mapping and frequency histogram show a slight decrease of average ratio I(D)/I(G) after thermal treatment.

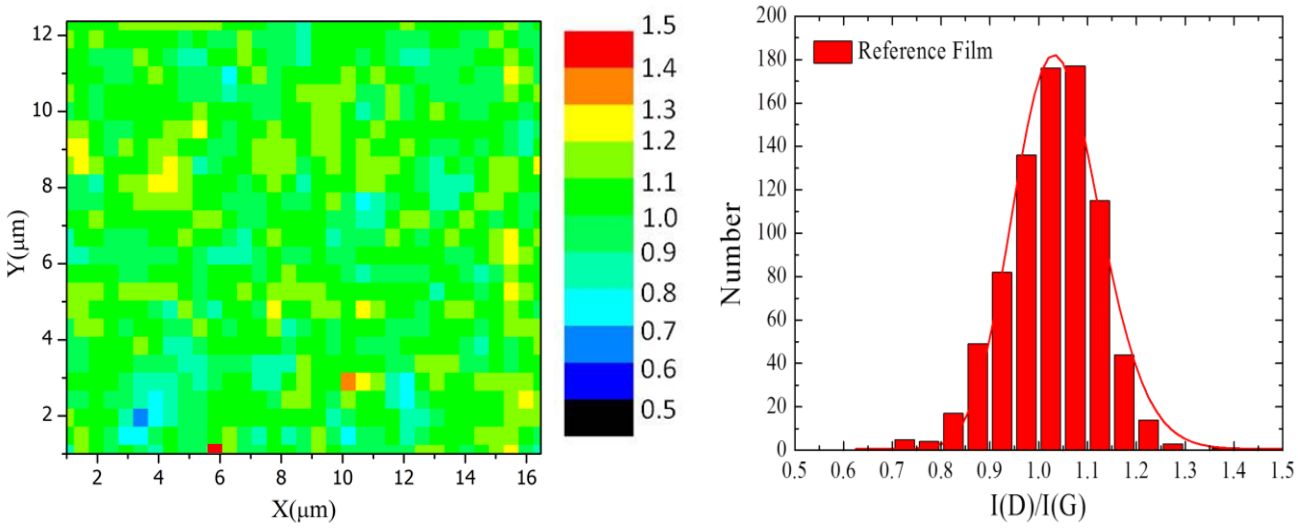

(a) (b)

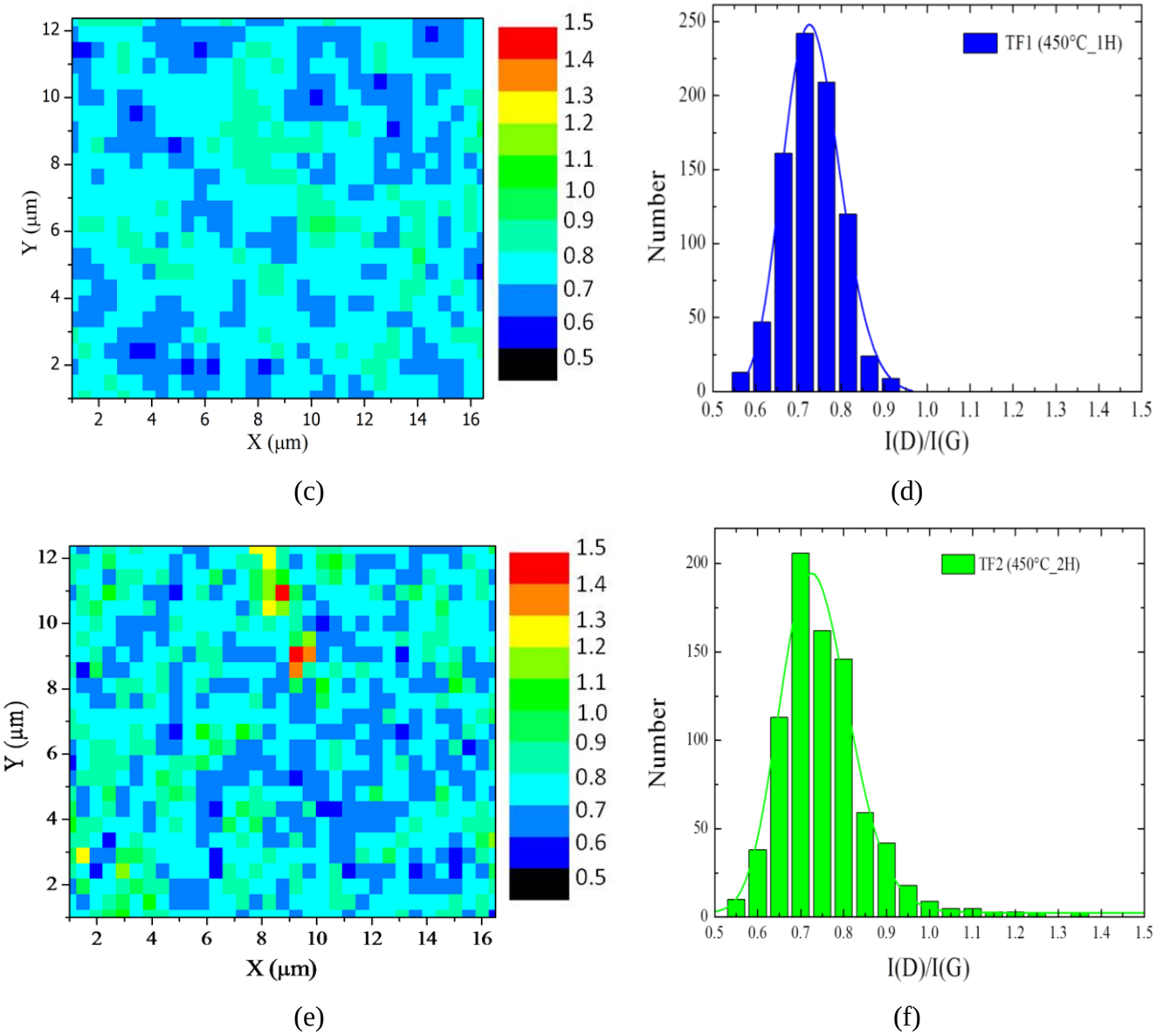

Figure 4.16: Raman analysis for the film before and after thermal treatment. (a,b) mapping and histograms of I(D)/I(G) for reference film; (c,d) mapping and histograms of I(D)/I(G) for reference TF1 film; (e,f) mapping and histograms of I(D)/I(G) for reference TF1 film.

For the film before treatment, as shown in figure 4.16(a), the ratio I(D)/I(G) of whole analyzed area is located in green zone (0.9 - 1.2). The histograms of I(D)/I(G) in figure 4.16 (b) demonstrate that mean ratio is ~ 1.03. After treatment, Raman mapping I(D)/I(G) of TF1 and TF2 film are down-shifted to light-blue zone (0.5 - 1.0). The mean I(D)/I(G) are decreased to 0.73 and 0.71 respectively for TF1 and TF2 film. We can conclude from these

mapping analyses that after annealing treatment intensity of D band decrease over whole film area, which indicates that the treatment decreases the disorder of films. Together with TG results and XPS analyses, we think that it could be residual solvent confined in graphen film and ions/moleculs attaching on graphene film, which results in a higher surface resistivity and oxygen concentration. If our hypothesis was correct, structure of the film would be different before and after the treatment.

2.2.3 X-Ray scattering

To test this idea, X-Ray scattering was peformed. X-Ray scattering measurements were performed on a rotating anode and under vacuum, to optimize the signal over background ratio, using monochromated MoK_α radiation ($\lambda = 0.711$ Å). For X-ray scattering experiments, the graphene film was deposited onto an ultra thin silicon wafer (~10 µm thick), to minimize scattering from the substrate. As shown in figure 4.17, the incident X-ray beam is parallel to film.

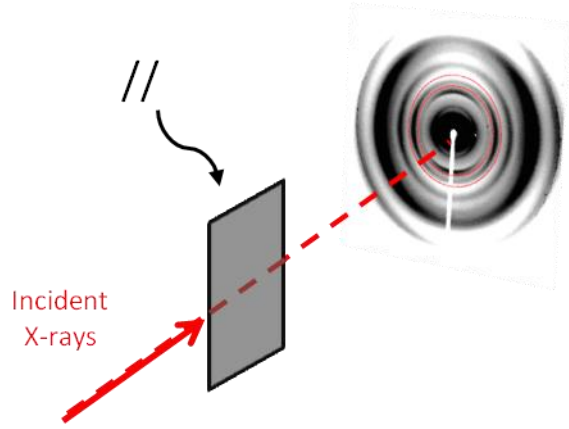

Figure 4.17: Schematic diagram of X-ray scattering with ultrawafer.

As-deposited film and heated film were studied at room temperature. Scattering patterns were recorded on imaging plates, in transmission, with the wafer plane containing the direction of the incident X-ray beam. On the diffraction pattern of figure 4.18, two diffraction peaks from

the graphene film, located at Q ≈ 1.85 $Å^{-1}$, are clearly visible, along with Bragg peaks and thermal diffuse scattering of silicon. [59] The peaks at Q ≈ 1.85 $Å^{-1}$ reveal the staking of the graphene planes forming the film. With Bragg's law and scattering vector:

$$Q = \frac{4\pi}{\lambda}\sin(\theta)$$

mean interlayer distance, d = 3.40 (+/-0.05)Å, can be calculated. Moreover, these peaks display an asymmetric feature with higher intensity at low Q values for the as-deposited film, which indicates a distribution of interlayer distances towards larger distances (see figure 4.19). The same peaks become symmetrical and narrower after thermal treatment which corresponds to a smaller distribution of interlayer distances centered around the mean value d. Azimuthal integration curves at Q =1.85$Å^{-1}$ are shown in figure 4.20. The width of the curve is related to the angular disorientation between the stacked graphene planes. Both curves are fitted with a Lorentzian lineshape and are characterized by their Full Width at Half Maximum (FWHM). After thermal treatment, the angular extent of the graphene stacking peaks becomes narrower (FWHM = 8.4° after thermal treatment, compared to 12° before treatment). Therefore, it follows that thermal treatment improved both the stacking of the graphene planes and the relative orientation of the assemblies of stacked planes.

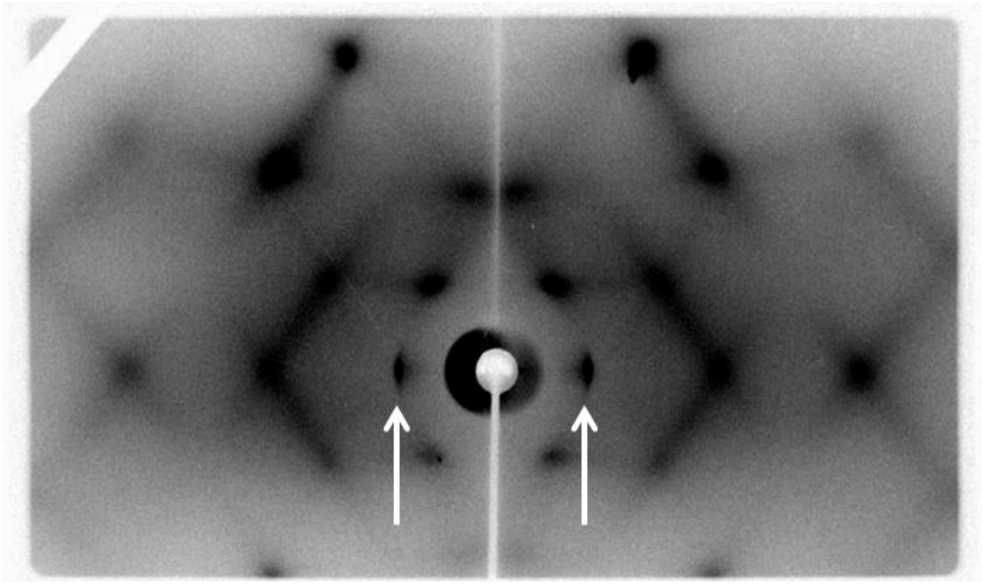

Figure 4.18: Diffraction pattern obtained from the graphene film on silicon wafer before the thermal treatment. White arrows point to the scattering peaks at Q ~1.85Å^{-1} of graphene using X-ray radiation (λ= 0.711 Å).

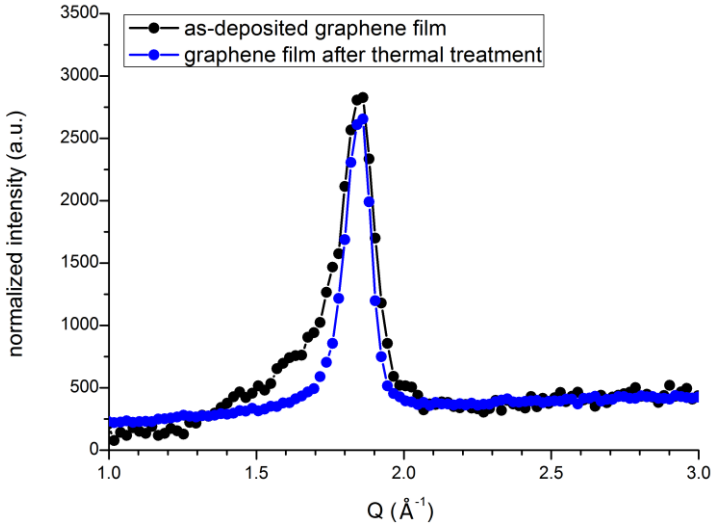

Figure 4.19: X-ray scattered intensity along the horizontal direction in figure 1, through the scattering peak of graphene before and after thermal treatment.

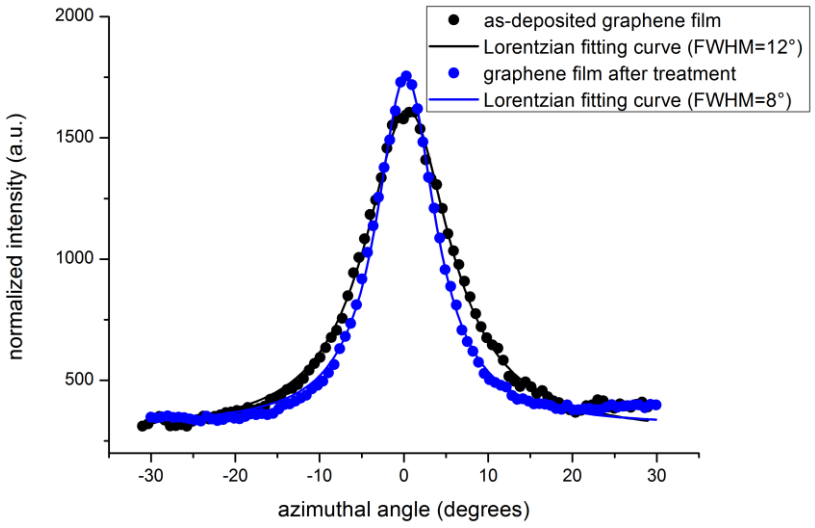

Figure 4.20: Azimuthal integration of the scattered intensity at Q=1.85 Å^{-1} (from 1.80 to 1.90 Å^{-1}), before and after thermal treatment. Circles: experimental data, lines: fits with a Lorentzian function.

XRD, Raman and XPS results support the "impurities" in the film are not the oxygen-containing functional groups. During filtration process, some residual solvent THF can be trapped in graphene sheets. These residual solvent are rather stable under atmosphere and act like scattering sources which increase the surface resistivity. But with annealing temperature, they can be evaporated, thus surface resistivity can be decreased. Back to figure 4.9 (a), it was noticed that the film begun to lose the weight at ca. 100 °C, so thermal treatments at low temperature may also improve the film performances. Thus, another thermal treatment, under Argon at 120°C for 2 hours, was also tried. After this treatment, the surface resistivity was decreased to 680 Ω/sq. The XPS and Raman analysis performed for this treated film were summarized in annex. Considering that the temperature range of PET film is from -70 °C to 150 °C (Ampef^{TM}), this low temperature opens a route to improve the electrical properties of the graphene film deposited on a flexible polymer substrate.

Graphene production methode	**Film production methode**	**ρ_s(surface resistivity)**	**Transmittance**	**Ref**
Thermal reduction of GO	Dip-Coating	1,8+/- 0,08KΩ/sq	~ 60%	[60]
Graphene dispersion in DMF	spray-coating	5KΩ/sq	90%	[61]
polycyclic aromatic hydrocarbons (PAHs)	Spin-coating	~1,6KΩ/sq	~50%	[62]
GO → rGO(Chemical reduction of GO)	Spin-coating	~800Ω/sq	~82%	[63]
Chemical reduction of GO	spin-coating, drop-casting	>1KΩ/sq - ~100KΩ/sq	~30% - ~90%	[64]
thermal reduction of GO		~100Ω/sq - ~100KΩ/sq	~5% - ~90%	
chemical and thermal reduction of GO	vacuum-filtration	~43kΩ/sq	~ 75%	[65]
graphene dispersion in DMF	vacuum-filtration	~22KΩ/sq	~60%	[66]
TBA and oleum intercalated graphite dispersed in DMF	langmuir blodgett	~150, 20 and 8KΩ	~93, 88 and 83%	[67]
chemical reduction of GO	vacuum-filtration	2000KΩ/sq	96%	[13]

chemcial and thermal reduction of GO	spray-coating, drop-casting		188KΩ/sq	~98%	[68]
GO → rGO(chemical or thermal reduction)	spin-coating		100kΩ/sq	85%	[69]
			5KΩ/sq	~50%	
GO → rGO (chemicalor thermal reduction)	langmuir blodgett		19MΩ	95%	[70]
GO → rGO(chemical or thermal reduction)	vacuum-filtration		70KΩ/sq	65%	[71]
GO → rGO (chemical reduction)	Self-Assembled GO hydrosol		1,6KΩ/sq	85%	[72]
GO → reparative reduction of GO	Spin-coating		2,85KΩ/sq	95%	[73]
graphene dispersion	Vacuum Filtration		1KΩ/sq	54%	[3]
			2KΩ/sq	75%	
graphite exfoliated in organic solvants	vacuum filtration		6KΩ/sq	70%	[74]
			200KΩ/sq	90%	
Graphenide solution	Vacuum Filtration	(before treatment)	1900Ω/sq	30%	Our film
		(after treatment)	450Ω/sq	30%	Our film

Table 5: Resistivity and transmittance for graphene film produced from solution routes

As presented in chapter 1, researchers and engineers has already made graphene film from graphene produced by liquid-phase route, such as reduced graphene oxide, dispersion of graphene in organic solvent etc. In table 5, we made a relatively exhaustive list concerning surface resistivity and transmittance of reported graphene transparent conductive electrodes. From this table, we can see that electrical property of our films after annealing treatment show very promising properties compared to other films. This is probably due to the relatively good quality of graphene produced by graphenide solution. For reduced graphene oxide material, in addition to vacuum filtration, spin-coating and spray-coating were also used to produce graphene film. These techniques were also employed for our graphenide solution to produced graphene film from graphenide solutions. Unfortunately, films prepared by these techniques do not demonstrate very good electrical properties. Results concerning these films are presented in annex.

Besides thermal treatment, we also noticed an interesting phenomenon in our film. As presented in chapter I, graphene possess a very unique electronic structure. In pristine graphene shown in figure 4.21(c), the valence and conduction bands touch at the Brillouin zone corners thus forming a zero-band-gap at the Dirac point. Graphene can be doped by electric field, by adsorption of atoms and by substrate. Here, we will focus on chemical doping. In chemical doping, charge transfer is often involved. In this case, doping is achieved by electron exchange between graphene and a dopant. In general, charge transfer involved doping does not disrupt the structure of graphene and most cases of these doping can be reversible. This is a fundamental difference from another type of chemical doping, substitutional doping. For substitutional doping, carbon atoms in the honeycomb lattice are substituted by other atoms, such as nitrogen and boron. [75, 76] Figure 4.20 (c) shows the shift of the Fermi level induced by charge transfer. Graphene can be p-type or n-type doped via charge transfer. p-type doping drives the Fermi level of graphene below the Dirac points. On the contrary, in n-type doping, the Fermi level is above the Dirac points.

In some articles, researchers announced that the sheet resistance of graphene film decreases by p-doped with acid, Br_2 and I_2. [77, 78] In these systems, the p-doping creates a high density of holes around the Fermi energy, thus the carrier concentration increase and the resistance is reduced. Since our film is prepared from negatively charged graphene flakes, the electrons transferred from potassium atom to graphene will partly fill the anti-bonding π^*-band which is initially empty in neutral graphene. The electrons added to the anti-bonding band behaving as carriers, they increase the electrical properties of the film.

(a) (b)

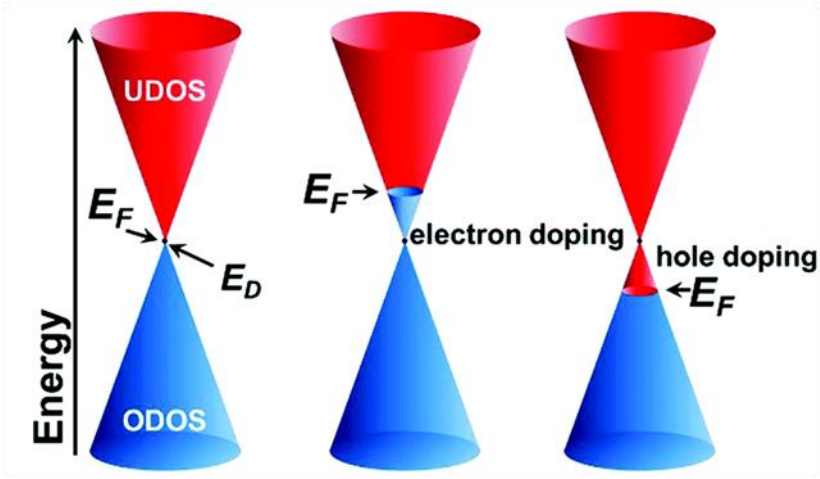

(c)

Figure 4.21: (a). One freshly filtrated graphene film with Al_2O_3 membrane in glovebox. (b). Graphene film after 30 mins of drying in glove box; (c) Representation of the Dirac cone (E_D) at the K point in (B) depicting the linear dispersion of conduction and valence bands that meet at the Dirac point. Rigid band shifts due to charge transfer to and from graphene are depicted as electron or hole doping, respectively, wherein the Fermi level (E_F) is displaced to higher or lower energy with respect to the Dirac point. [79] (UDOS: unoccupied density of states; ODOS: occupied density of states)

We prepared one film and measured its surface resistivity in glove box. As shown in figure 4.21 (a), the freshly filtrated graphene film on Al_2O_3 membrane exhibits a yellow-brown color which is similar to that of stage-I KC_8. It's interesting that the color of this film turn rapidly into black in less than 10 mins. The image shown in figure 4.21 (b) demonstrate that the film is in black color after 30 mins of drying in glove box. The surface resistivity was determined from the measured four-probe sample resistance R. The surface resistivity of freshly filtrated (still in yellow-brown color) is 645 Ω/square. However, the surface resistivity of dried film (30min drying in glove-box, black color) decreased to the remarkable value of 155 Ω/square. When the film was dried, there were less residual THF in the film, which means there were less scattering sources in the film. As discussed previously, the elimination of impurity will significantly increase the electrical performance of film. Unfortunately, it has not been possible to measure the transmittance of the film inside the glove box.

3. Film treatment with laser

The annealing treatment can largely improve electrical properties of graphene film. But the transmittances at 550 nm are always ~ 30%. The increase of transmittance can be achieved by making film thinner. If we could manage to eliminate the impurity and make the film thinner, both electrical and transmittance of film will be improved. Lee et al. reported that conductivity and transparency of carbon nanotube film produced from surfactant dispersed solution were improved by laser treatment. [80] They claimed that individual nanotubes absorb the laser energy and generate heat to vaporize the surrounding surfactant. As a result, the conductivity was increased. To improve conductivity and transmittance of our film, laser induced thermal treatments were also tested with Mr. Anthony KIRSCH in Centre Technologique Optique et Lasers (ALPhANOV).

One film was prepared and transferred on PET substrate. The transferred film was then divided into 4 small bands (5 mm x 28 mm) for laser treatment. The band 1 was conserved as reference. Band 2, 3 and 4 were treated with laser beam under different conditions. The treatments were performed by using a laser with cadence of 50 KHz. The power of this laser is 0.05 W. The laser beam having a diameter of ~ 30 μm scanned the bands with scanning rate of 750 mm/s. The flux of energy is around 1.32×10^{-2} J/mm^2. The laser beam scanned band 2 one time in crosshatch scanning fashion. The band 3 and band 4 were scanned respectively 50 and 100 times over. The sheet resistance and transmittance of the reference film and treated bands were measured to analyze treatment. The sheet resistances were measured by using a 4-probe and the transmission spectra were obtained with a UV-Visible-NIR microspectrophotometer.

	Surface resistivity (Ω/sq)	Transmittance at 550 nm (%)

Band 1	1700	32
Band 2	920	36
Band 3	613	45
Band 4	770	47

Table 5: surface resistivity and transmittance at 550 nm for reference band and laser treated bands.

From table 5, we can see that laser treatment can improve the surface resistivity and transmittance. As scan number increase, the surface resistivity of bands decrease. The graphene film can absorb laser energy which can remove oxygen-containing functional groups and impurities. As a result, the surface resistivities decrease with increasing of irradiation time. Band 4 exhibits an increased surface resistivity compare to band 2 and band 3. This can be explained that laser irradiation of laser create too much defect in band 4. The laser treatment study of CVD graphene film performed by Kiisk et al. shown laser irradiation (~ 200 mJ/cm$^{2)}$ can produce visible damage. [81] In our laser treatment, the laser irradiation can remove the graphitic materials. Thus, the transmittance at 550 nm of films increases as irradiation time increase.

The reference film and treated films were characterized by Raman to understand laser treatment. The Raman spectra of films and PET substrate were obtained by Raman spectrometer HORIBA Xplora with 532 nm wavelength incident laser light at room temperature. 1% laser power filter was used to decrease the laser power to 0.166 mW in order to avoid any damage produced by laser irradiation. The acquisition time was always inferior to 2 seconds. The spectra were collected under a microscope (× 50 objective). The Raman-scattered light was dispersed by a holographic grating with 1800 lines/mm for high spectral resolution and detected by a charge-coupled device (CCD) camera.

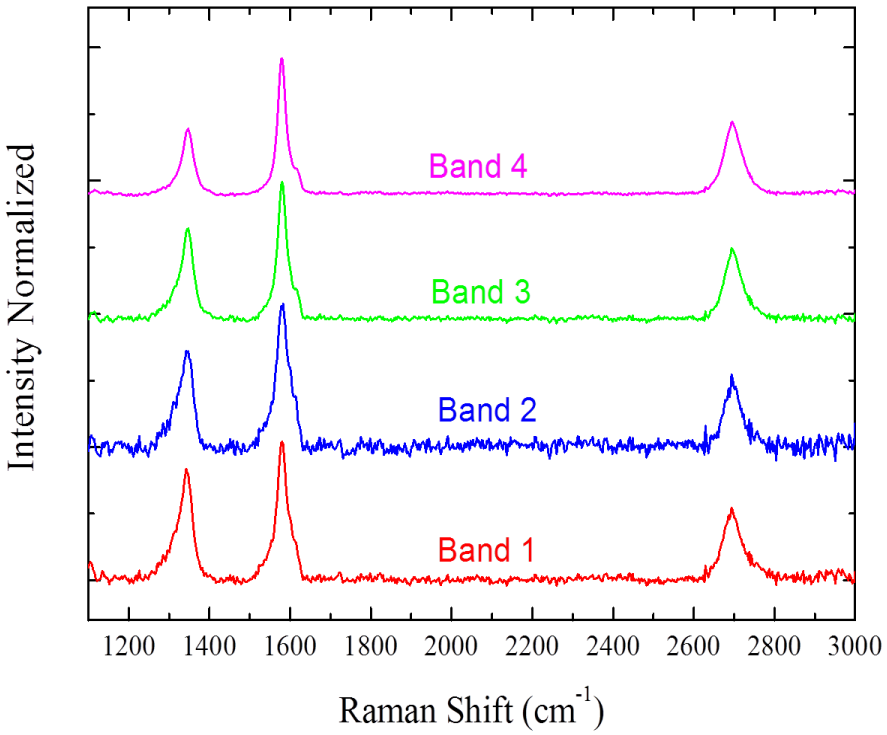

Figure 4.23: Raman spectra of graphene film treated by laser irradiation and PET substrate at 532 nm wavelength excitation laser.

Before and after treatment, we found three intensive bands located at 1348 cm^{-1}, 1582 cm^{-1} and 2696 cm^{-1} which correspond to D band, G band and 2D band. These bands show no significant difference compare to spectra of graphene films deposited on glass/wafer substrate shown in previous sections. For graphene film, there is peak at shoulder of G band around 1620 cm^{-1}which is assigned to defect-active D' band. We focused on analysis of D band and G band.

With 532nm wavelength incident laser excitation, Raman mapping analyses were performed within 14 x 14μm areas for films before and after treatment. During Raman mapping analyses, the incident laser power was carefully tuned to be 0.16 mW. Meanwhile, the acquisition time of whole Raman mapping were strictly limited to be inferior to 8 hours; in other word, for each scanning spot, the acquisition time is 1 second. We studied the intensity ratio of D band to G band intensity for further understanding the efficiency of treatment over large area. The

Raman mappings presented below were constructed strictly by the intensity height of D band (~ 1344 cm^{-1}) and G band (~ 1580 cm^{-1}).

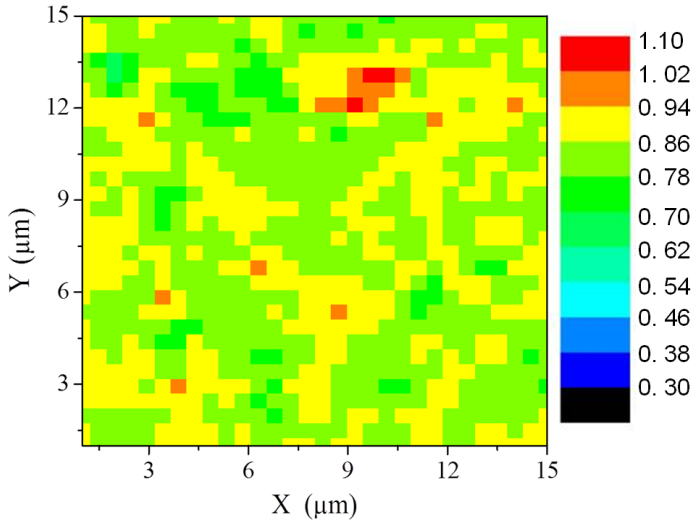

(a)

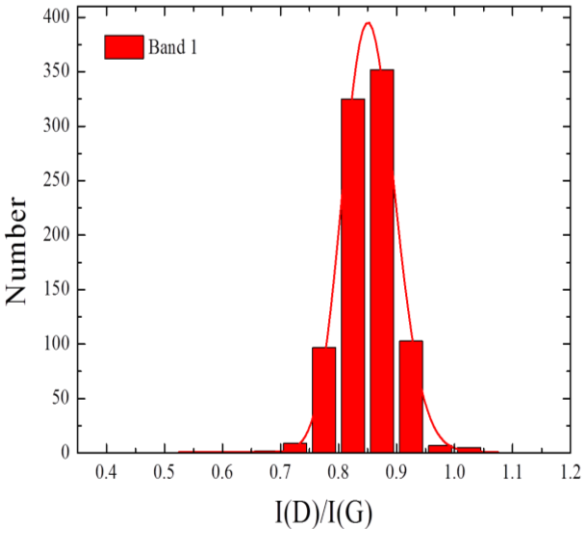

(b)

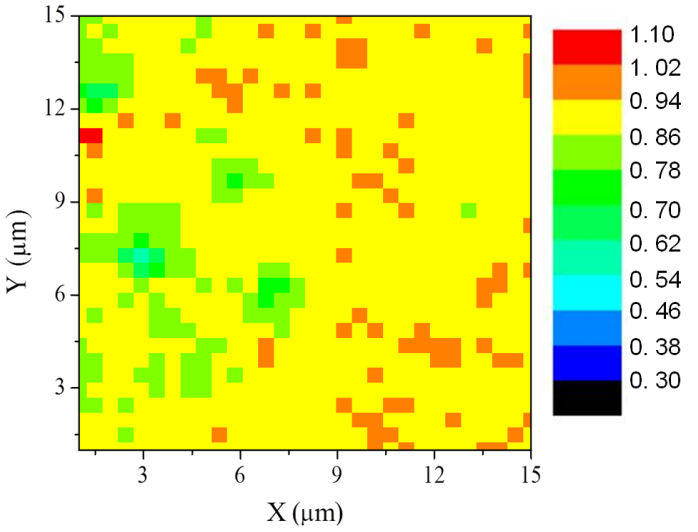

(c)

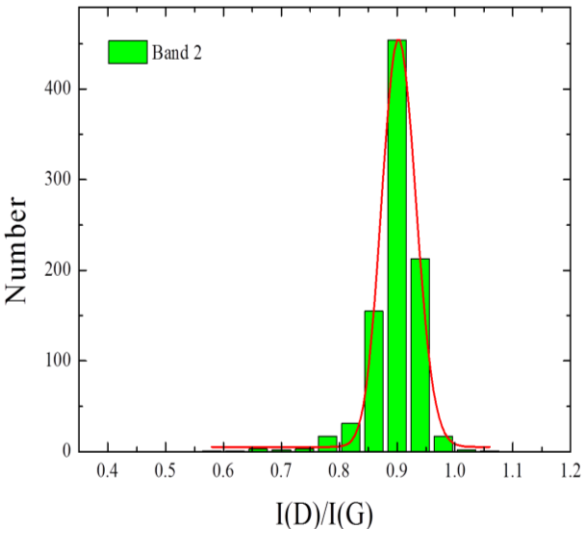

(d)

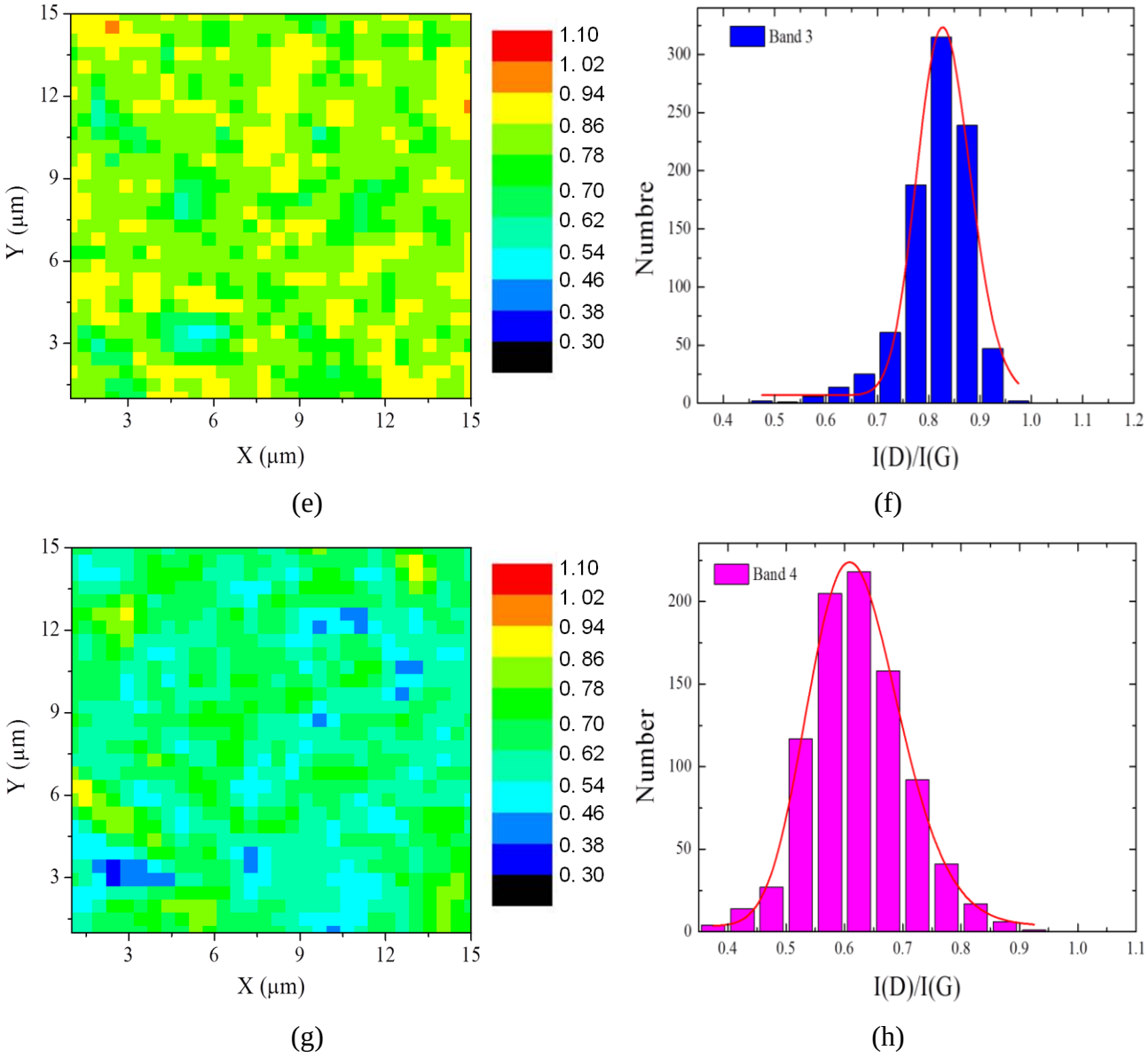

Figure 4.24: Raman analysis for films before and after laser treatment. (a, b) I(D)/I(G) mapping and histograms for Band 1(reference film); (c, d) I(D)/I(G) mapping and histograms for Band 2; (e, f) I(D)/I(G) mapping and histograms for Band 3; (g, h) I(D)/I(G) mapping and histograms for Band 4.

The I(D)/I(G) mapping and histograms of reference film and laser treated films are shown in figure 4.24. The mean ratio I(D)/I(G) of reference film is ~ 0.87. After laser treatment, mean I(D)/I(G) of band 2 increases to ~ 0.9. But mean I(D)/I(G) of band 3 and I(D)/I(G) of band 4 decrease respectively to ~ 0.83 and ~ 0.61. For band 2, after laser treatment, surface resistivity

decreases. But why mean I(D)/I(G) of band 2 shows a contradict result? We think that during laser irradiation, the laser power was so powerful that graphitic materials can be removed by laser beam scanning, which means the laser treatment process itself can cause defects on this graphitic material. Compare to annealing treatment which removed only residual THF and improved stacking structure of film without creating defects, mean I(D)/I(G) of laser treated film could be increased. In essence it is important to understand that an increase or decrease of I(D)/I(G) is not necessarily correlated with increase or decrease of defects in graphitic materials. For example, chemically reduced graphene oxide materials show an increased I(D)/I(G).[24] Stankovich et al. interpret such a result by assuming that reduction increases the number of aromatic domains of smaller overall size in graphene, which would lead to an enhancement of the I(D)/I(G) ratio.[24] Thus we suggest that care should be taken when one use only I(D)/I(G) to evaluate the defects of graphitic materials. To better understand evaluation of defects of graphitic materials, one should understand treatments that the materials suffered and several techniques should be used in order to have reasonable interpretations.

4. Production of mixed graphene-nanotube films

Graphenide solutions can be used to produce large area and continuous graphene films which exhibit good electrical and optical properties. The electrical properties can be largely improved by annealing treatment. The laser treatment can both improve electrical and optical properties of produced graphene film. Even though these properties are promising compared to other graphene films produced from solution routes, the surface resistivity and transmittance are still far from industry requirements for application as transparent conductive electrodes. In chapter I, from review of transparent conductive electrodes, it appears that transparent conductive electrodes made from carbon nanotubes demonstrate very promising electrical and optical properties, better than that of reported graphene films. We then performed some experiments to make transparent conductive films by using graphenide solutions and carbon nanotube solutions together.

Several groups have reported graphene-Carbon nanotube hybride materials for transparent conductors. [82-86] The idea consists to produce nanocomposite comprised of graphene and carbon nanotubes. Figure 4.25 shows schematically the carrier transport in graphene-carbon nanotube film. Carbon nanotubes act as a link between graphene flakes, which can enhance carrier transport and improve the conductivity of this hybrid material. Most of reported graphene-carbon nanotube hybrid films were synthesized by mixing reduced GO solution and aqueous dispersion of carbon nanotube. Yang et al. reported one graphene-carbon nanotube film produced from solution-based method that exhibits 240 Ω/sq and 86 % transmittance. [64] They demonstrated that electrical properties of produced hybrid film are improved compared to both CNT films and reduced GO films.

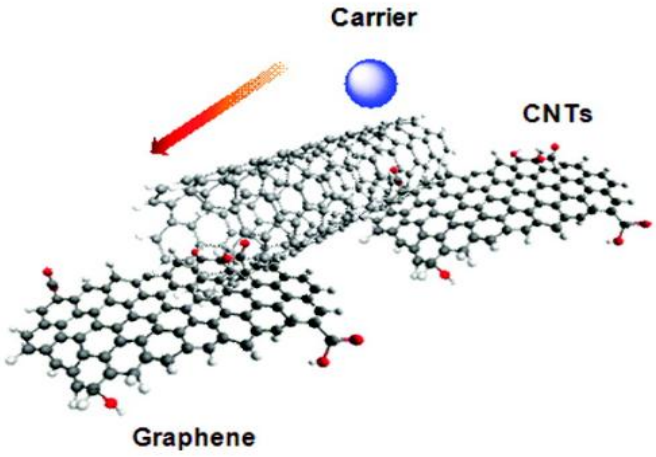

Figure 4.25: Carrier transport in graphene-carbon nanotube hybrid materials [80]

Unlike those reported hybrid film, we have used negatively charged CNT solution and graphenide solution to make hybrid films. Negatively charged carbon nanotubes HiPco (High Pressure Carbon Monoxide Process) were prepared by Dr Fabienne Dragin in glove box as a CNTs salt. Then the CNT salt was dissolved in DMSO. After centrifugation at 4000 RPM (~ 3000 g) for 2 hours, the supernatant was removed from undissolved carbon nanotubes. The concentration of this solution is ~ 3.851mg/ml, which is calculated from dry-extract. The prepared carbon nanotube solution is viscous, thus to prepare a film, the solution needs to be diluted. In previous work concerning CNT films performed by Dr. Amélie Catheline, carbon nanotube solutions were always diluted more than 100 times in DMSO solvent in order to make CNT films. In this experiment, the CNT solution was diluted 1000 times, which lead to a concentration of 0.00385 mg/ml. Graphenide solution (KC_8 in THF) was prepared by the method presented in chapter III. The concentration of KC_8 in THF is ~ 0.15 mg/ml. The prepared graphenide solution was diluted in THF for 10 times. In order to compare to electrical and optical properties of films, one reference film was prepared by using only 15 ml of diluted CNTs solution. The mass of CNTs film is around 57.75 µg. This mass is used as reference mass. During hybride films preparation, quantity of CNTs solution and graphenide

solution were determined by keeping total mass of hybrid materials equal to this reference mass. In this way, we can compare the properties of films.

Two ways were employed to prepare graphene-CNT films. Route (I): CNT solution was first filtrated and then graphenide solution was filtrated, which can lead to a layered structure. Route (II): CNTs solution and graphenide solution were mixed, and then this mixed solution was used to make films. As for the production of graphene films, the solutions were filtrated onto Al_2O_3 membrane with a vacuum filtration apparatus. In first way in which CNTs solution and graphenide solution are filtrated successivley, care was taken when pouring the graphenide solution onto filtered CNTs film to avoid damage of CNTs. For both production way, the quantity of CNTs were varied from 80 wt % , 50 wt % and 20 wt %, thus the corresponding quantity of graphene were 20 wt %, 50 wt% and 80 wt%. The sheet resistances were measured by using a 4-probe and the transmission spectra were obtained with a UV-Visible-NIR Microspectrophotometer.

Reference film	Surface resistivity (Ω/sq)	Transmittance at 550 nm (%)	FOM
CNTs film	1460	55	872
route (I)	Surface resistivity	Transmittance at 550 nm (%)	FOM
CNTs (20 Wt.%); Graphenide (80 wt.%)	11531	85	1874
CNTs (50 Wt.%); Graphenide (50 wt.%)	2395	70	854
CNTs (80 Wt.%); Graphenide (20 wt.%)	1389	60	709
route (II)	Surface resistivity	Transmittance at 550 nm (%)	FOM
CNTs (20 Wt.%); Graphenide (80 wt.%)	28035	95	1438
CNTs (50 Wt.%); Graphenide (50 wt.%)	8837	82	1753
CNTs (80 Wt.%); Graphenide (20 wt.%)	2367	57	1330

Table 6: Surface resistivity and transmittance of graphene-carbon nanotube hybrid films

A surface resistivity around 1460 Ω/sq and 55 % transmittance was obtained for reference CNT film. The surface resistivity of most hybrid films is larger than CNT film. With FOM, we compare films by considering both surface resistivity and transmittance.

$$FOM = -R \cdot \ln \frac{T}{100}$$

where *R* is surface resistivity, *T* is transmittace.

In both routes, the surface resistivity of hybrid film decrease as quantity of CNTs increase, which implies that the conductivity of the film is dominated by carbon nanotubes. The transmittance displays an opposite tendency. By comparing surface resistivity and transmittance of produced hybrid films, we can clearly see that hybrid films produced by route (I) show a lower surface resistivity than those produced by route (II). It should be noticed that charged carbon nanotubes and charged graphenes were dissolved in different solvents. The mixture of these two solutions could not form a homogeneous solution, thus the idea of using carbon nanotube as link is hard to achieve. Except the third film in route I, the electrical and optical properties didn't get improve when we employed two solutions to make hybrid film. Maybe, in our methods, graphene and carbon nanotube didn't well connect together to form an ideal network shown in figure 4.25. Further characterization and procedure optimization should be performed to improve performances of hybrid film.

5. Conclusion

Graphenide solutions, KC_8 in THF, were explored to produce transparent conductive electrodes by using vacuum filtration method. The filtrated films can be transferred onto any desired substrate. As-filtrated films were transferred at first onto flexible substrate PET to characterize surface resistivity and optical transmittance. The as-produced film exhibits a relatively good electrical properties and reasonable transmittance. Like all other graphene films produced from solution ways, surface resistivity increases as transmittance decreases.

To characterize furthermore these graphene films, several films were produced and transferred onto glass and wafer substrate. SEM, AFM and TEM results show that these films consist of a disordered array of graphene sheets lying randomly in the plane of the film. XPS results show that oxygen content of film is increased compared to starting graphite, which led us to think that the films are either oxidized or there are other reasons to explain increased oxygen. The detail analyses of XPS spectra, C1s and O1s spectra, demonstrate that there are some oxygen-containing groups in the films. Raman spectroscopy was also used to characterize the graphene films. The detailed comparison of XPS and Raman results between our film and reduced graphene oxide film having similar oxygen content made us to believe that the oxidation is not the reason to explain the increased oxygen content. Especially, Raman spectra of film possess a relative low I(D)/I(G) ratio and an intense 2D band which can be fitted only by one Lorentzian function, which demonstrate that our films have a better sp^2 graphitic structure. This pronounced 2D band confirms the randomly stacking order of film. Under this structure, graphene films present a 2D behavior similar to monolayer graphene. After all, there are fundamental differences between our film and reported rGO film. By eliminating those oxygen-containing impurities, the properties of film can be improved.

To improve performances of graphene film, annealing treatments at 450 °C under argon atmosphere were performed for graphene films transferred onto glass substrates. After annealing treatment, the surface resistivity was decreased from 1930 Ω/sq to 450 Ω/sq while the transmittances remained the same. The XPS, Raman and XRD analysis were performed for graphene films before and after treatment. After treatment, oxygen contents had largely decreased, and XPS-etching profile of oxygen shows that there is higher oxygen content at the surface of film. C1s of treated film demonstrate a similar envelope to that of starting graphite because of de-oxygenation. The Raman ratio I(D)/I(G) were used to evaluate defects change before and after treatment. By using Raman mapping, the observation of I(D)/I(G) for a large area shows that after treatment this ratio decreased from 1.13 to 0.73 which implies that after treatment, the film are less defective. The structural changes were characterized by X-ray scattering. Scattering patterns of graphene film exhibits one clearly visible diffraction peak, located at $Q \approx 1.85$ $Å^{-1}$, which reveal the staking of the graphene planes forming the film and correspond to a mean interlayer distance of d = 3.40 (+/-0.05)Å. Before treatment, these peaks appear asymmetric with a higher intensity at low Q values, which indicates a distribution of interlayer distances towards larger distances. The same peaks become symmetrical and narrower after thermal treatment which corresponds to a smaller distribution of interlayer distances. Azimuthal integration curves at $Q = 1.85$ $Å^{-1}$ were also performed to study the angular disorientation between the stacked graphene planes. After thermal treatment, the angular extent of the graphene stacking peaks becomes narrower (FWHM=8.4° after thermal treatment, compared to 12° before treatment). The thermal treatment can eliminate scattering sources, residual solvent THF, meanwhile both the stacking of the graphene planes and the relative orientation of stacked graphene planes were improved during the annealing treatment. As a result, the surface resistivity can be largely decreased. The low temperature annealing treatment performed at 120 °C also shows that surface resistivity was decreased. This means

that the electrical properties of films transferred on PET can be improved by low temperature treatment. To improve electrical properties and optical transmittance, a series of laser treatment were performed on the films transferred on PET. After laser treatment, both conductivity and transmittance were increased. In laser treatment process, graphene films absorb the laser energy and generate thermal effect which can vaporize the residual THF solvent in films, which result in decreasing of surface resistivity. Meanwhile, the laser power is high enough to remove some graphitic materials, thus transmittances were also improved.

The graphene film produced from graphenide solution KC_8+THF demonstrate very promising electrical properties compared to other graphene film from solution routes. The thermal treatments provide very efficient way to improve performance of graphene films. These films can be further used in flexible conductive electrodes field where the requirement of transmittance is not too demanding, like supercapacitor and sensor etc.

References

[1] A. A. Green, M.C. Hersam. Solution phase production of graphene with controlled thickness via density differentiation. Nano Letters, 2009, 9(12), 4031-4036.

[2] A. Pénicaud, C. Drummond. Deconstructing Graphite: Graphenide solutions. Acc. Chem. Res., 2013, 46, 129.

[3] X. Dong, C. Su, W. Zhang, J. Zhao, Q. Ling, W. Huang, P. Chen, L. Li. Ultra-large single-layer graphene obtained from solution chemical reduction and its electrical properties. Phys. Chem. Chem. Phys., 2010, 12, 2164–2169.

[4] L.J. Cote, F. Kim, J. Huang. Langmuir-Blodgett Assembly of graphite oxide single layers. J. Am. Chem. Soc. 2009, 131, 1043.

[5] J. Coleman. Liquid Exfoliation of Defect-Free Graphene. Acc. Chem. Res., 2013, 46, 14.

[6] A. Catheline. Film de nanotubes de carbone et solutions de grapheme. Thèse de doctorant de Université Bordeaux I, 2011.

[7] C. B. Flores, D.M. López. Multilayer Graphene Synthesized by CVD Using Liquid Hexane as the Carbon Precursor. World Journal of Condensed Matter Physics, 2011, 1, 157.

[8] M.F. El-Kady, R. B. Kaner. "Scalable fabrication of high-power graphene micro-supercapacitors for flexible and on-chip energy storage" Nature Communications, 2012,

[9] S. Bae, H. Kim,Y. Lee, X. Xu, J. Park, Y. Zheng, J. Balakrishnan, T. Lei, H. Kim,Y.Song, Y. Kim, K.S. Kim, B. Özyilmaz, J. Ahn, B. Hong, S. Iijima. Roll-to-roll production of 30-inch graphene films for transparent electrodes. Nature Nanotech, 2010, 4, 574.

[10] L. Yang, J. Deslippe, C.H. Park, M. L. Cohen, S. G. Louie. Excitonic Effects on the Optical Response of Graphene and Bilayer Graphene. Phys. Rev. Lett. 2009, 103, 186802.

[11] Y. Zhu, W. Cai, R. D. Piner, A. Velamakanni, R. S. Ruoff. Transparent self-assembled films of reduced graphene oxide platelets. Appl. Phys. Lett., 2009, 95, 103104.

[12] T.V.Cuong, V.H.Pham, Q.T.Tran, S.H.Hahn, "Photoluminescence and Raman studies of graphene thin film prepared by reduction of graphene oxide", Mater. Lett. 2010, 64(3), 399-401.

[13] D.Li, M.B.Müller, S.Gilje, R.B. Kaner, G.G. Wallace, "Processable aqueous dispersions of graphene nanosheets" Nat. Nanotechnol. 2008, 3(2), 101-105.

[14] H.S. Skulason, P. E. Gaskell, T. Szkopek. Optical reflection and transmission properties of exfoliated graphite from a graphene monolayer to several hundred graphene layers. Nanotechnology 2010, 21, 295709

[15] T. Seo, K.J. Lee, A. H. Park, S. Jeon. "Enhanced light output pover of near UV light emitting diodes with graphene/indium thin oxide nanodot nodes for transparent and current spreading electrode" Opics Express, 2011, 19(23), 23111-23117.

[16] Z.Luo, Y.Lu, L.A.Somers, A.T.C. Johnson "High yield preparation of macroscopic graphen oxide membranes". J. Am. Chem. Soc. 2009, 131(3), 898-899.

[17] H.A. Becerril, J. Mao, Z. Liu, R.M. Stoltenberg, Z. Bao, Y. Chen. Evaluation of Solution-Processed Reduced Graphene Oxide Films as Transparent Conductors. ACS Nano. 2008, 2, 463.

[18] S. De, P. J. King, M. Lotya, A. O'Neill, E. M. Doherty, Y. Hernandez, G. S. Duesberg, J. N. Coleman. Flexible transparent conducting films of randomly stacked graphene from surfactant-stabilized oxide free graphene dispersions. Small. 2010, 6, 458

[19] T.C. Chiang, F. Seitz. Photoemission spectroscopy in solids. Ann Phys 2001. 10, 61.

[20] S. Yumitori Correlation of C1s chemical state intensities with the O1s intensity in the XPS analysis of anodically oxidized glass-like carbon samples. J. Mater. Sci. 2000, 35, 139.

[21] C. Mattevi, G. Eda, S. Agnoli, S. Miller, K.A. Mkhoyan, O. Celik, D. Mastrogiovanni, G. Granozzi, E. Garfunkel, M. Chhowalla. Evolution of electrical, chemical, and structural properties of transparent and conducting chemically derived graphene thin films. Adv. Funct. Mater. 2009, 19, 2577.

[22] A. Bagri, C. Mattevi, M. Acik, Y.J. Chabal, M. Chhowalla, V.B. Shenoy. Structural evolution during the reduction of chemically derived graphene oxide Nature Chem. 2010, 2, 581–587.

[23] W. Gao, L.B. Alemany, L. Ci, P.M. Ajayan. New insights into the structure and reduction of graphite oxide. Nature Chem. 2009, 1, 403.

[24] S. Stankovich, D.A. Dikin, R.D. Piner, K.A. Colas, A. Kleinhammes, Y. Jia, Y. Wu, S.T. Nguyen, R.S. Ruoff. Carbon 2007, 45, 1558.

[25] A.Bagri, C. Mattevi, M. Acik, Y.J. Chabal, M. Chhowalla, V.B. Shenoy Nature Chem. 2010, 2, 581–587.

[26] D. Yang, A. Velamakanni, G. Bozoklu, S. Park, M. Stoller, R.D. Piner, S. Stankovich, I. Jung, D.A. Field, C. A. Ventrice Jr., R.S. Ruoff . Chemical analysis of graphene oxide films after heat and chemical treatmens by X-ray photoelectron and micro-Raman spectroscopy. Carbon, 2009, 47, 145.

[27] O. Akhavan, The effect of heat treatment on formation of graphene thin films from graphene oxide nanosheets. Carbon 2010, 48, 509.

[28] H.J. Jeong, Y. P. Lee, R. J.W. Lahaye, H. H. Park, K. H. An, I.J. Kim, C.W. Yang, C. Y. Park, R. S. Ruoff, Y. H. Lee. J. Am.Chem. Soc. 2008, 130, 1362.

[29] C. Hontoria-Lucas, A.J. Lopez-Peinado, J.D. Lopez-Gonzalez, M.L. Rojas-Cervantes, R.M. Martin-Aranda. Study of oxygen-containing groups in a series of graphite oxides: Physical and chemical characterization. Carbon 1995, 33, 1585.

[30] A. Barinov, L. Gregoratti, P. Dudin, S.L. Rosa, M. Kiskinova. Imaging and Spectroscopy of Multiwalled Carbon Nanotubes during Oxidation: Defects and Oxygen Bonding Adv. Mater. 2009, 21, 1916.

[31] O. Akhava, E. Ghaderi, A. Akhavan, Size-dependent genotoxicity of graphene nanoplatelets in human stem cells. Biomaterials, 2012, 33, 8017–8025.

[32] A. Ganguly, S. Surbhi, P. Papakonstantinou, J. Hamilton. Probing the thermal deoxygenation of graphene oxide using high-resolution in situ X-ray-based spectroscopies. J. Phys. Chem. C 2011, 115, 17009–17019.

[33] D. Yang, E. Sacher, Carbon 1s X-ray photoemission line shape analysis of highly oriented pyrolytic graphite: The influence of structural damage on peak asymmetry. Langmuir 2006, 22, 860–862.

[34] J. I. Paredes, S. Villar-Rodil, P. Solis-Fernandez, A. Martinez-Alonso, J.M.D. Tason. Atomic Force and Scanning Tuneling Microscopy Imaging of graphene Nnanosheets Derived from Graphite Oxide. Langmuir 2009, 25, 5957.

[35] C. Kozlowski, P. Sherwood. X-ray photoelectron spectroscopic studies of carbon-fiber surfaces. J Chem Soc Farad T 1 Phys Chem Condensed Phases 1984, 80, 2099.

[36] G. Zhang, S. Sun, D. Yang, J.P. Dodelet , E. Sacher. The surface analytical characterization of carbon fibers functionalized by H_2SO_4/HNO_3 treatment. Carbon 2008, 46,196.

[37] R. Rozada, J.I. Paredes, S. Villar-Rodil, A. Martinez-Alonso, J.M.D. Tascon. Towards full repair of defects in reduced graphene oxide films by two-step graphitization. Nano Research 2013, 6, 216.

[38] M.I. Awad, M.M. Saleh, T. Ohsaka T. Oxygen reduction on rotating porous cylinder of modified reticulated vitreous carbon. J Solid State Electr 2008,12, 251.

[39] A. Eckmann, A. Felten, A. Mishchenko, L. Britnell, R. Krupke, K.S. Novoselov, C. Casiraghi. Nano Lett. 2012, 12(8), 3925-3930.

[40] Venezuela, P.; Lazzeri, M.; Mauri, F. Phys. Rev. B. 84, 2011, 035433.

[41] Pimenta, M. A.; Dresselhaus, G.; Dresselhaus, M.S.; Cançado, L.G.; Jorio, A.; Saito, R. Phys, Chem. Chem. Phys., 2007, 9, 1276-1290.

[42] Malard, L.M.; Pimenta, M.A.; Dresselhaus, G.; Dresselhaus, M.S. Physic Reprots 2009, 473(5), 51-87.

[43] Jorio, A. ISRN Nanotechnology, 2012, 2012, 1-16. doi:10.5402/2012/234216

[44] A.C. Ferrari, J. Robertson. Phys. Rev. B. 2001, 64, 75414.

[45] A.C. Ferrari, J. Robertson. Interpretation of Raman spectra of disordered and amorphous carbon. Phys. Rev. B. 2000, 61, 14095.

[46] J.C. Charlier, J.P. Michenaud and P.H. Lambin Phys. Rev. B. 1992,46, 4540

[47] J. Robertson, Adv. Phys. 35, 317 (1986); G. Galli, R. M. Martin, R. Car, and M. Parrinello. Phys. Rev. B, 1990, 42, 7470.

[48] A. C. Ferrari, S. E. Rodil, J. Robertson. Phys.Rev.B. 2003, 67, 155306.

[49] J.Schwan, S.Ulrich, V.Batori, H.Ehrhardt, S.R.P. Silva. J. Appl. Phys. 1996, 80 (1), 440.

[50] R. Al-Jishi, G. Dresselhaus G 1982 Phys. Rev. B. 1982, 26, 4514.

[51] A. Cuesta. P. Dhamelincourt , J. Laureyns , A. Martinez-Alonso, J.M.D. Tascon. 1994 Carbon 1994, 32, 1523.

[52] M.J. Matthews, M.A. Pimenta, G. Dresselhaus, M.S. Dresselhaus, M. Endo. Phys. Rev. B. 1999, 59, 6585.

[53] E. H. Martins Ferreira, V.O. Moutinho, F. Stavale, M.M. Lucchese, B. Capaz, Rodrigo, C.A. Achete, A. Jorio, Phys. Rev. B 82, 2010, 125429.

[54] J.M. Englert, P. Vecera, K.C. Knirsch, R. A. Schäfer, F. Hauke, A. Hirsch. ACS Nano, 2013, 7(6), 5472-5482.

[55] E.Y. Choi, T. H. Han, J. Hong, J. E. Kim, S. H. Lee, H. W. Kima, S. O. Kim. Noncovalent functionalization of graphene with end-functional polymers. J. Mater. Chem., 2010, 20, 1907–1912.

[56] S.Sahoo, G. Hatui, P. Bhattacharya, S. Dhibar, C.K. Das. One Pot Synthesis of Graphene by Exfoliation of Graphite in ODCB. Graphene, 2013, 2, 42-48.

[57] S. Stankovich, D.A. Dikin, R.D. Piner, K.A. Colas, A. Kleinhammes, Y. Jia, Y. Wu, S.T. Nguyen, R.S. Ruoff. Carbon 2007, 45, 1558.

[58] J.I. Paredes, S. Villar-Rodil, A. Martinez-Alonso, J.M.D. Tascon. Langmuir 2008, 24, 10560.

[59] Holt, M.; Wu, Z.; Hong, H.; Zschack, P.; Jemian, P.; Tischler, J.; Chen, H.; Chiang, T.-C. Phys. Rev. Lett. 1999, 83(16), 3317.

[60] P. Blake, P. D. Brimicombe, R. R. Nair, T. J. Booth, D. Jiang, F. Schedin , L. A. Ponomarenko, S. V. Morozov, H. F. Gleeson, E. W. Hill, A. K. Geim, K. S. Novoselov, Graphene-Based Liquid Crystal Device. Nano Lett. 2008, 8, 1704.

[61] X. Wang, L. Zhi, K. Mullen. Transparent, Conductive Graphene Electrodes for Dye-Sensitized Solar Cells. Nano Lett, 2008, 8, 323.

[62] X.Wang, L. Zhi, N, Zeljko, J. Li, K. Müllen. Angew. Chem. Int. Ed. 2008, 47, 2990 –2992

[63] J. Wu, M. Agrawal, H. A. Becerril, Z. Bao, Z. Liu, Y. Chen, Peter Peumans, ACS Nano, 2010, 4(1), 43.

[64] H.A. Becerril, J. Mao, Z. Liu, R.M. Stoltenberg, Z. Bao, Y. Chen. Evaluation of Solution-Processed Reduced Graphene Oxide Films as Transparent Conductors. ACS Nano. 2008, 2, 463.

[65] G. Eda, G. Fanchini, M.Chhowalla. Nature Nanotechnology. 2008, 3, 270.

[66] S. De, P. J. King, M. Lotya, A. O'Neill, E. M. Doherty, Y. Hernandez, G. S. Duesberg, J. N. Coleman. Small. 2010, 6, 458.

[67] X. L. Li, G. Y. Zhang, X. D. Bai, X. M. Sun, X. R. Wang, E. Wang, H. J. Dai, Highly conducting graphene sheets and Langmuir-Blodgett films. Nat. Nanotechnol. 2008, 3, 538.

[68] C. Su, Y. Xu,W. Zhang, J. Zhao, X. Tang,C. Tsai, L. Li. Electrical and spectroscopic characterizations of ultra-large Reduced Graphene Oxide Monolayers. Chem. Mater. 2009, 21, 5674.

[69] J.Wu, H.A. Becerril, Z.Bao, Z.Liu, Y. Chen, P. Peumans. Organic solar cells with solution-processed graphene transparent electrodes. Appl. Phys. Lett., (2008) 92, 263302.

[70] L.J.Cote, F.Kim, J.Huang. Langmuir-Blodgett Assembly of graphite oxide single layers. J. Am. Chem. Soc. 2009, 131, 1043.

[71] G.Eda, Y.Lin, S. Miller, C. Chen, W.Su, M. Chhowalla. Transparent and conducting electrodes for organic electronics from reduced graphene oxide. Appl. Phys. Lett. 2008, 92, 233305.

[72] S. Pei, J. Zhao, J. Du, W. Ren, H. Cheng. Carbon, 2010, 48, 4466.

[73] B. Dai, L.Fu, L.Liao, N. Liu, K. Yan, Y.Chen, Z. Liu. Nano Res. 2011, 4(5), 434.

[74] J. Coleman. Liquid Exfoliation of Defect-Free Graphene. Acc. Chem. Res., 2013, 46, 14.

[75] L. S. Panchokarla, K. S. Subrahmanyam, S. K. Saha, A. Govindaraj, H. R. Krishnamurthy, U. V. Waghmare, C. N. R. Rao, Adv. Mater., 2009, 21, 4726.

[76] N. Li, Z. Y. Wang, K. K. Zhao, Z. J. Shi, Z. N. Gu and S. K. Xu. Carbon, 2010, 48, 255.

[77] A. Kasry, M.A. Kuroda, G. J. Martyna, G. S. Tulevski, A. A. Bol, ACS Nano, 2010, 4(7), 3839-3844.

[78] N. Jung, N. Kim, S. Jockusch, N. J. Turro, P. Kim, L. Brus, Nano Lett., 2009, 9, 4133.

[79] J. S. Brian, V. D. Robert, L. Vincent, B.Sarbajit. An electronic structure perspective of graphene interfaces. Nanoscale, 2014, 6, 3444–3466.

[80] M. Joo, M. Lee. Nanotechnology 2011, 22, 265709.

[81] V. Kiisk, T. Kahro, J. Kozlova, L. Matisen, H. Alles. Appl. Surf. Sci. 2013, 276, 133.

[82] V.C. Tung, L.Chen, M.J. Allen, J.K. Wassei, K.Nelson, R.B.Kaner, Y. Yang, Nano Lett, 2009, 9(5), 1949.

[83] N. Imazu, T. Fujigaya, N. Nakashima. Sci. Technol. Adv. Mater. 2014,15, 025005

[84] S. Wang, Y. Geng, Q. Zheng, J. Kim, Carbon, 2010, 48, 1815.

[85] F.Tristan-Lopez, A. Morelos-Gomez, S.M. Vega-Diaz, M. Terrones, ACS Nano, 2013, 12, 10788.

[86] X. Lin, P. Liu, Y. Wei, Q. Li, J. Wang, Y. Wu, C. Feng, L. Zhang, S. Fan, K. Jiang, Nature Communications. 2013. DOI: 10.1038/ncomms3920

Conclusion and Prospective studies

The liquid-phase exfoliation of graphite is considered as one of the most promising way to produce graphene in industrial scale because of its cost-effectiveness, processability and compatibility with current techniques. The developed liquid-route exfoliation methods are always based on exfoliating graphite or graphite oxide in a solvent with sonication and/or surfactant, which can decrease the properties of graphene produced. Moreover, graphene dispersions are unstable due to the strong $\pi \rightarrow \pi$ stacking of large graphene sheets produced, and yield of these methods are relatively low.

The objective of this thesis was to produce graphenide solutions without using surfactants or sonication and exploit these solutions to produce transparent conductive graphene films. The production of graphenide solutions consist in the synthesis at first of graphite intercalation compounds with graphite and potassium, and then to dissolve these compounds in organic solvents. The production process is performed under inert atmosphere. During this work, stage-1 KC_8, stage-2 KC_{24} and stage-3 KC_{36} were synthesized by using one-zone and two-zone vapour transport techniques and studied during this work. After characterization of X-ray diffraction and Raman scattering which allow us to identify these compounds, the compounds were dissolved in NMP (high boiling point organic solvent) and THF (low boiling point organic solvent). TEM observations demonstrated that both solvent can be used to dissolve GICs. The work performed on potassium reduced carbon nanotubes reported that counterions entropy gain drives the dissolution process, thus by varying potassium/carbon ratio, the solubility of carbon nanotube salts can be changed. For graphenide solutions, the same phenomenon was found. Both dry extract and absorption UV-Visible results show that

graphenide solutions from stage 1 KC_8 show the highest concentration. And concentration of graphenide salts decreases with the increase of potassium/carbon ratio.

Graphenide solutions show particular optical properties. From UV-Visible absorption spectra, K-GICs+NMP system have an absorption peak at 300 nm (4.14 eV) independently from the charge density. Whereas, two absorption bands, one located around 280 nm and the other at 328 nm were found in K-GICs+THF system. Those charge density independent features lead us to make a hypothesis that there is a disproportionation phenomenon in graphenide solutions when graphenide salts dissolve in an aprotic solvent. To understand further those special optical properties, more experimental and theoretical studies should be performed in the future. In parallel with studies of graphenide solution, we also performed a Raman resonance study for three synthesized K-GICs by changing the laser excitation engery from UV to near infrared. In stage-3 KC_{36}, we observed a Raman resonance effect at 2.5 eV. By comparing with first principle calculations, we can find the $\pi \rightarrow \pi^*$ transition for the bounding layer at 2.5 eV. We attribute the observed resonance effect to this $\pi \rightarrow \pi^*$ transition.

As THF is a low boiling point solvent, the post-treatment of KC_8+THF solution is easier than KC_8+NMP. Therefore, deposition of KC_8+THF was studied by HRTEM, AFM and Raman. HRTEM and AFM show that deposited graphene demonstrate self-folded and crumpled morphologies which make it difficult to determine the number of layer for observed graphene. The Raman spectra obtained for graphene produced from graphenide solution show three characteristic band of sp^2 carbon: D band, G band and 2D band. The detailed band analysis shows that the produced graphene possesses relative good quality compared to graphene materials produced by other liquid-route methods. The starting material graphite has been thoroughly exfoliated by the dissolution procedure.

By using vaccum filtration method, graphenide solutions KC_8+THF were used to produce transparent conductive films on flexible substrate PET, which exhibit relatively good electrical properties and reasonable transmittance compared to other graphene films produced by solution routes. Characterization results from SEM, AFM and TEM observations show that graphene sheets are stacked randomly to form a continuous film. The analyses of as-produced graphene film Raman spectra imply that uncorrelated graphene sheets in films do not re-stack into Bernal stacking order. XPS results show the oxygen content of the as-produced films increase compared to starting graphite; and further C1s peak line-analyses demonstrate that some oxygen-containing groups are present in the films. In order to improve the performances of graphene films and decrease their oxygen content, annealing treatments at 450 °C under argon atmosphere were performed for graphene films transferred onto glass substrates. After the annealing treatment, the surface resistivity decreased from 1930 Ω/sq to 450 Ω/sq while the transmittance didn't change. XPS analyses shows that after treatment oxygen contents decreased, which result from removal of oxygen-containing groups under thermal effects. Raman spectroscopy was applied to evaluate film before and after treatment. The Raman ratio I_D/I_G was used to investigate the defects. By performing Raman mapping within a large area, a statistic study of the ratio I_D/I_G shows that after treatment this ratio decreased from 1.13 to 0.73. After annealing treatment, the film are less defective, thus its electrical properties are improved. X-ray scattering was used to characterize structural changes. From X-ray scattering pattern, one clearly visible diffraction peak (Q ≈1.85 $Å^{-1}$) was observed. The position of this peak corresponds to a mean interlayer distance of d = 3.40 (+/-0.05) Å. Azimuthal integration curves at Q =1.85 $Å^{-1}$ were also performed to study the angular disorientation between the stacked graphene planes. After thermal treatment, the angular extent of the graphene stacking peaks becomes narrower which implies that the graphene sheets have a more homogeneous orientation after treatment. These characterization results indicates that thermal treatment can

eliminate scattering sources, such as residual solvent, attached like OH^- and H_3O^+ originating from water and solvent molecules; meanwhile the stacking of graphene sheets and relative orientation can be improved. Thus, the surface resistivity of graphene film can be largely decreased. The results from annealing treatment at 120 °C show that low temperature can also improve the electrical properties of graphene films, a result of importance since it is applicable to films deposited on flexible polymer substrates such as polyethylene terephthalate (PET). To improve both conductivity and transmittance, laser-assisted treatments were also attempted. The laser power is high enough to generate thermal effect which removes scattering source and some graphite materials, thus the treated films exhibit better electrical and optical properties.

Due to the good quality of graphene produced from graphenide solutiosn, the graphene films produced from these solutions exhibit good electrical properties after mild annealing treatment compared to the most graphene film produced by solution routes. Further studies should, however, focus on improving the optical transmittance. With their promising electrical properties, these graphene films could be used in flexible conductive electrodes field.

Acronym

AFM: Atomic Force Microscopy

BE: binding energy

CVD: Chemical vapor deposition

CPME: Cyclopentyl methyl ether

DMF: Dimethylformamide

DMSO: Dimethyl sulfoxide

EBIC: Electron beam induced current

GICs: Graphite intercalation compounds

GO: Graphene oxide

HiPCO: High pressure carbon oxide (carbon nanotubes)

HOPG: Highly oriented pyrolytic graphite

ITO: Indium tin oxide

K-GICs: Potassium intercalated graphite intercalation compounds (K-GICs)

LPCVD: Low-pressure Chemical vapor deposition

NMP: N-Methyl-2-pyrrolidone

Me-THE: Methyltetrahydrofuran

PET: Polyethylene terephthalate

PMMA: Polymethyl methacraylate

rGO: Reduced graphene oxide

SEM: Scanning electron microscopy

TEM: Transmission electron microscopy

THF: Tethrahydrofurane

TG: Thermogravimetry

XPS: X-ray photoemission spectroscopy

XRD: X-ray diffraction

Annex 1

De-intercalation of GICs with laser irradiation

Potassium intercalated GICs, stage 1 KC_8, stage 2 KC_{24} and stage 3 KC_{36}, are very sensitive. Especially the highly intercalated GICs are sensitive to laser-induced deintercalation from a local heating of the sample with different laser power density. [A1] At high laser power, GICs can easily deintercalate into other stages. Thus to obtain correct Raman response of the K-GICs, laser-induced deintercalation studies were performed by changing laser power.

For Raman characterizations, the K-GICs samples were sealed into a quartz cuvette inside glove box. Raman measurements were performed on a JOBIN YVON Xplora at room temperature using 532 nm (2.33 eV) laser light. The spectra were collected under a microscope (× 50 objective). The Raman-scattered light was dispersed by a holographic grating with 2400 lines/mm for high spectral resolution and detected by a charge-coupled device (CCD) camera. The laser power can be varied by an integrated power filter which can change laser power from 16 mW (100 %) to 0.16 mW (1 %).

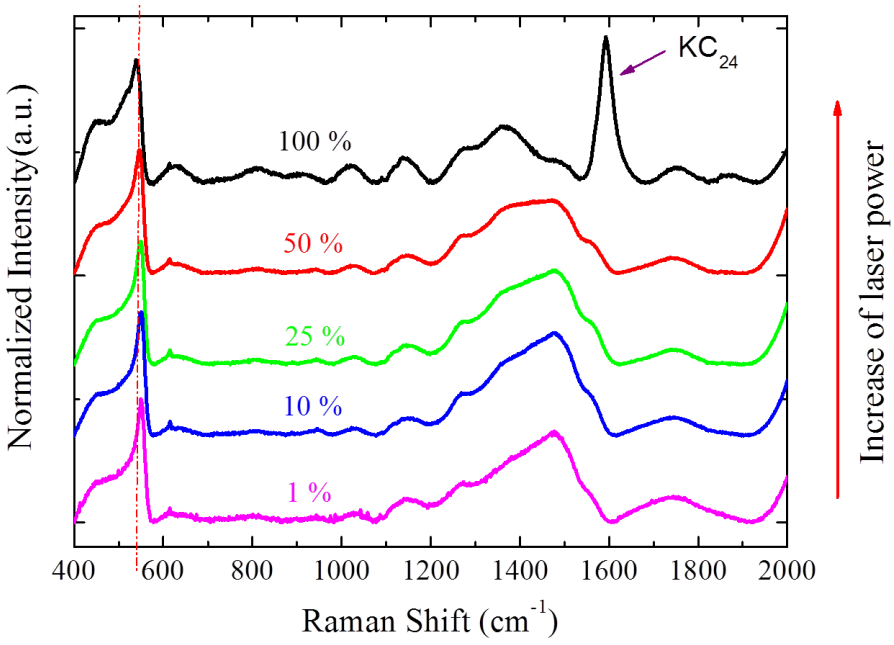

A

Figure 1A: Raman G band of laser induced deintercalation for stage-1 KC_8

In figure 1A, the D- to G-band region of stage-1 intercalation GICs KC_8 under different laser power excitation are shown. We can see that at lower laser power the G band has a Breit-Wigner-Fano (BWF) line shape. At high laser power excitation, one band appears around 1600 cm^{-1}, which is the G band of stage-2 GICs. Another band around 530 cm^{-1}, which is called as "C_z mode", [A2] didn't show any change even at high power excitation. Thus for Raman study of highly doped GICs, care must be taken in order to prevent the GICs specimens from laser induced deintercalation.

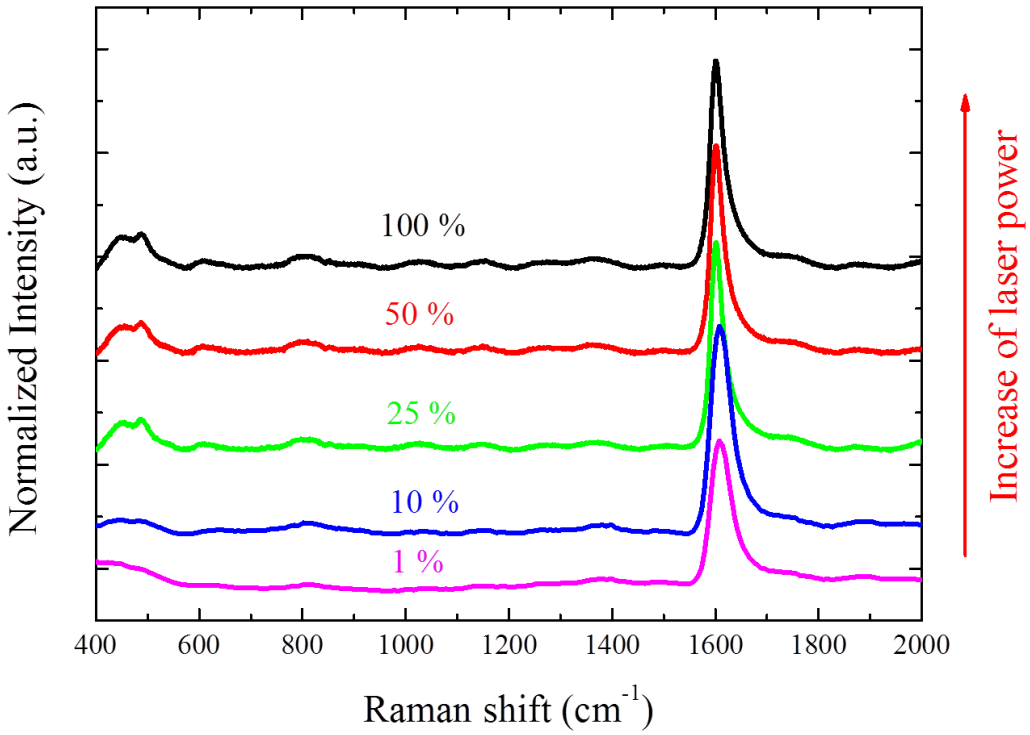

Figure 2A: Raman G band of laser induced deintercalation for stage-2 KC_{24}

The Raman spectra of the stage-2 GICs KC_{24}, which were acquired under excitation with different laser power, are shown in figure 2A. One G band having Fano form is around 1600 cm^{-1}, which doesn't change with increase of laser power. But we noticed a band located around 500 cm^{-1} displaying a visible change at high laser power.

B

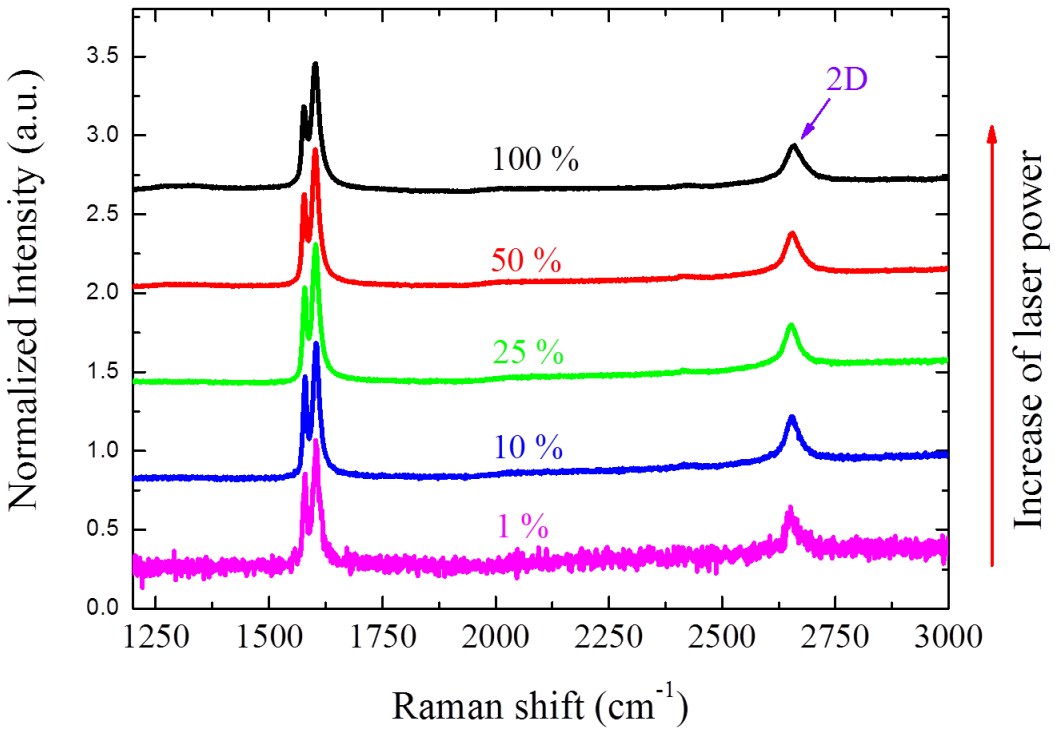

Figure 3A: Raman spectra of laser induced deintercalation for stage-3 KC_{36}

In stage 1 and stage 2, the graphene layers are doped by intercalated potassium layers. However, in stage 3, there is one graphene layer surrounded by two doped graphene layers. Since the charge transfers are mainly carried out between these two graphene layers and adjacent potassium layers, the interior graphyene layer is barely charged. In Raman spectra shown in figure 3A, the barely charged graphene layers give rise to the 2D band which is not present in stage 1 and stage 2 GICs. Under different laser power excitation, the Raman spectra of stage-3 GICs KC_{36} are shown in figure 3A. Two G band having Fano form are around 1600 cm^{-1}, which doesn't change with increase of laser power. And 2D band around 2660 cm^{-1} doesn't show any invisible change with increase of laser power. Even though stage 3 KC_{36} is less sensitive to laser induced heating, we still performed Raman study of KC_{36} under low laser power (<0.2 mW) as stage 1 and stage 2.

Annex 2

Thermal treatment of graphene film at low temperature (120°C for 2H)

1. Thermal treatment process

One film (diameter ~ 47mm) was prepared using a 30ml KC_8 + THF solution, and transferred onto glass substrates which had been washed with MillQ H_2O, acetone and isopropanol prior to the transfer step. The as-prepared film was then air dried under ambient lab conditions. The thermal treatment of the film was performed by thermogravimetry (TG, SETARAM Setsys) at 120 °C for 2 hours under constant Ar flow. Both heating rate and cooling rate were set at 5 °C/min.

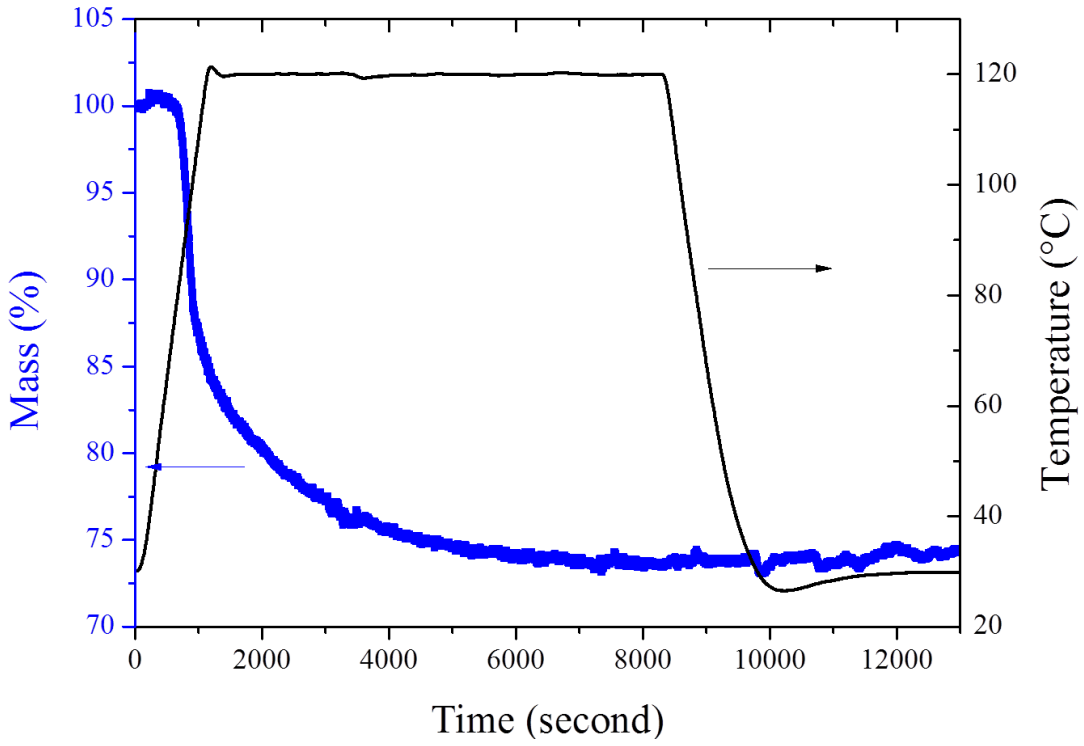

Figure 4A: Thermal treatment of graphene films treated at 120 °C for 2 hours

From figure 4A, we can see that the mass loss began around 100 °C, which is similar to the thermal treatment at 450 °C. After treatment, there was ~ 25 % of mass loss. After treatment,

the surface resistivity and transmittance at 550 nm of treated films were measured. The surface resistivity is 680 Ω/sq, the transmittance is ~ 30 % at 550 nm.

2. XPS and Raman analyses

Both the reference film and the film treated at 120°C were analyzed by XPS. The C1s peaks and O1s peaks concerning the reference film and the treated film are shown in figure 5A.

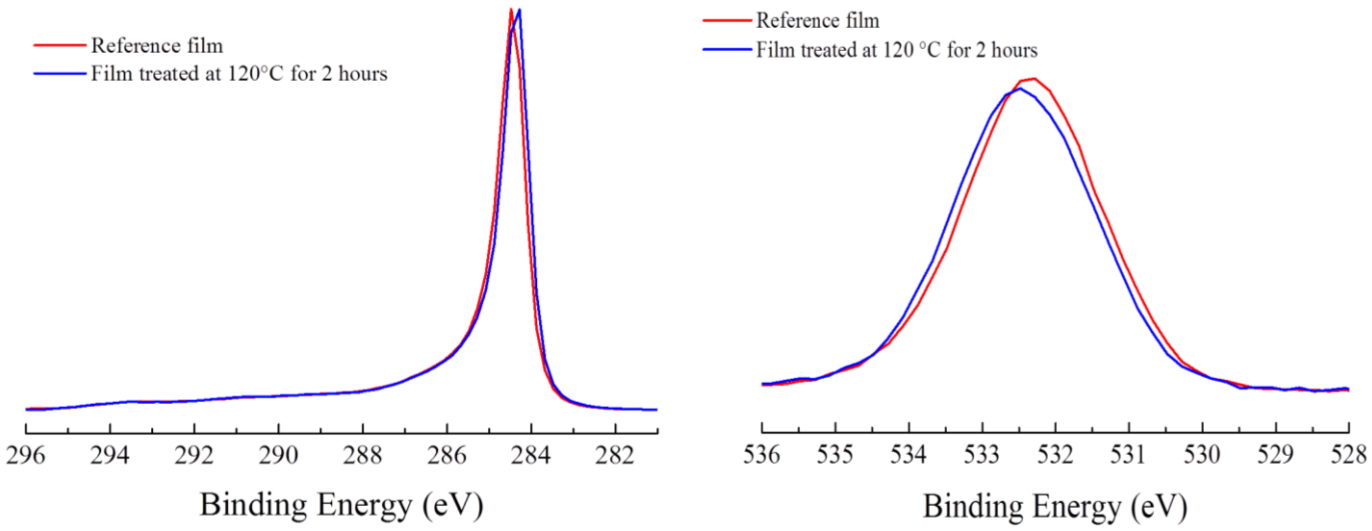

(a) (b)

Figure 5A: C1s and O1s of reference film (red) and treated film (blue).

From the figure 5A (a), we can see that the C1s peaks are superposed before and after treatment. The film was only mildly treated by annealing treatment at 120 °C, which is not sufficient to eliminate the oxygen-containing groups as we discussed in chapter 4. In figure B (b), the O1s peaks demonstrate similar form before and after treatment. With this low temperature treatment, we improve electrical properties of films without removing oxygen-containing groups, thus the reasonable interpretation of this improvement is that the annealing treatment can remove residual solvent and some ions like OH^- and H_3O^+ associated with water or solvent. These ions can be attached onto the film surface and act as scattering sources

which affect the charge transport behaviors, thus the film before treatment demonstrate a higher surface resistivity.

Raman mapping analyses were performed for the film after thermal treatment within 10x10µm area with 532nm wavelength incident laser light. The incident laser power is inferior to 1mW. After the treatment, the I_D/I_G ratio slightly decrease to 0.83, which indicates that after the treatment the film is less defective.

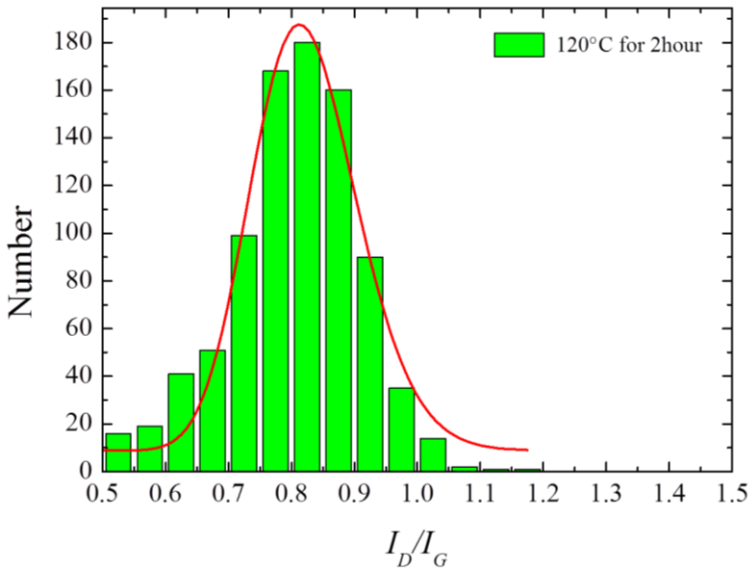

Figure 6A: Raman mapping analyses for the film after treatment

Annex 3

Film fabrication with spray and spin-coating methods

As discussed in chapter 1 and chapter 4, besides vacuum filtation, spray-coating and spin-coating have also been largely applied to produce large area graphene film with graphene produced by liquid-phase routes.

1. Spray-coating

The spray-coating process was practiced in glove box. The graphenide solution KC_8+THF was prepared by following production process presented in chapter 2. The substrate, polyethylene terephthalate (PET) substrate (PET, GoodFellow, biaxially oriented PET film), was used to perform spray-coating. The PET substrate was washed by MillQ H2O, acetone, isopropanol, and then dried in oven at 50 °C.

The spraying was done using a Preval ValPak sprayer onto the substrates which were preheated to ~ 60 °C in order to evaporate rapidly the THF solvent. 50 ml of graphenide solution was used to prepare a large-area graphene film (6 x 15 cm), as shown in figure C (b).

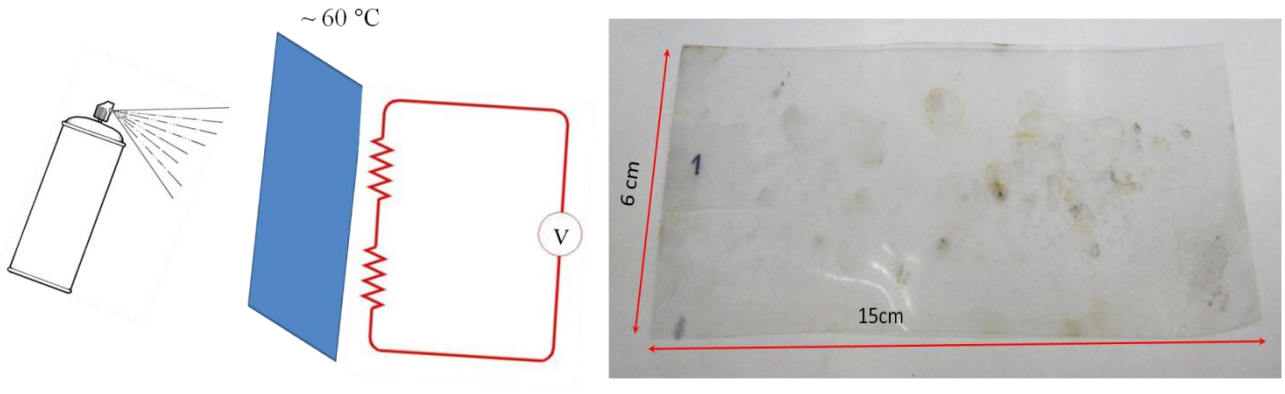

(a) (b)

Figure 7A: (a) Schematic image of spray-coating technique; (b) Image of spray-coated film (6x15 cm)

As we can see from figure 7A (b), the as-prepared film is inhomogeneous. There are visible spots on the film, which indicate that during spraying of KC_8+THF the in-homogeneity of spray distribution occurred. Instead of hand-made spraying, the automatic spray-coating system may prevent the appearance of spots.

The as-prepared film was then oxidized and dried outside the glovebox at 60 °C in an oven overnight. The surface resistivity was measured by four-point probing method. The surface resistivity is > 600000 Ω/sq. This large surface resistivity implies that at above-described condition the spray-coating could not make graphene sheets to cover homogeneously the PET substrate.

2. Spin-coating

The graphene films were prepared on glass substrate (18x18mm) and PET substrate by spin-coater (Novocontrol, SCC-200). The glass substrate and PET substrate were washed by MillQ H2O, acetone, isopropanol, and then dried in an oven at 50 °C. The spin-coating dispersion of graphenide solution KC_8+THF was performed in glove box.

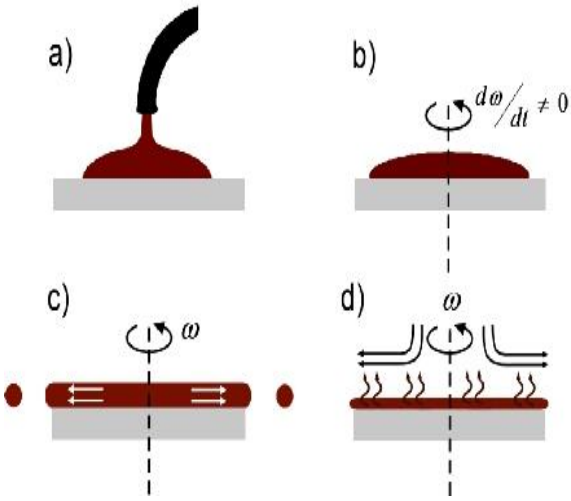

(a)

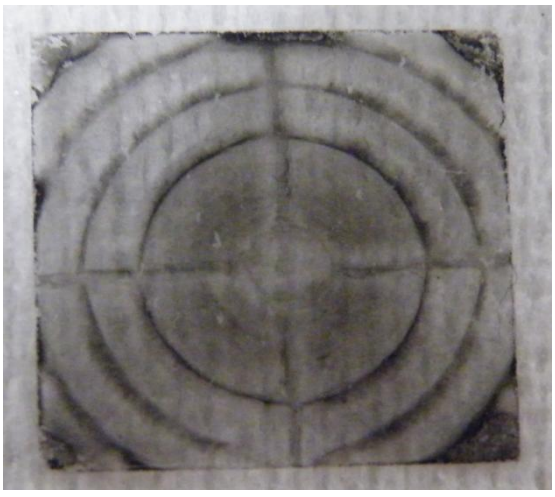

(b)

Figure 8A: (a) The different “stages” of spin coating a) Dispensation; b) acceleration; c) flow dominated; d) evaporation dominated. (b) Image of spin-coating of graphenide solution.

The spin-coating process, which is composed of 4 stages, is illustrated in figure D (a). From one image of as-prepared film on glass substrate, shown in figure 8A (b), we can see that the as-prepared film is inhomogeneous. This film was then oxidized and dried outside the glovebox at 50 °C in an oven overnight. The surface resistivity was measured using a four-point probe method. The surface resistivity is > 3000000 Ω/sq, which implies that it is hard to form a good film on glass substrate by spin-coating. The film spin-coated on PET substrate is hardly conductive no matter how much solution we used during spin-coating process. Actually, to get homogeneous and good quality films in spin-coating process, several important factors have to be considered: (a) evaporation rate of the solvent; (b) viscosity of the fluid; (c) concentration of the solution; (d) rotating speed; (e) spinning time. For the process it is necessary to have a solvent that evaporates fast at room temperature. For graphenide solution KC_8+THF, solvent THF is low boiling-point solvent. We varied rotating speed and spinning time to prepare the film, the results were similar. Thus, we think it could be helpful by changing the viscosity of the fluid to form a continuous and homogenous film.

Reference

[A1] R. J. Nemanich, S. A. Solin, D. Guerard, Raman scattering from intercalated donor compounds of graphite. Phys. Rev. B 1977, 16, 2965.

[A2] J. C. Chacon-Torres, A. Y. Ganin, M. J. Rosseinsky, T. Pichler. Raman response of stage-1 graphite intercalation compounds revisited. Phys. Rev. B 2012, 86, 075406.